Cosmic microwave background properties in a universe with simply or multiply connected topology

Martin Jacques France

N° d'ordre NNT : 2022LYSE1098

THÈSE de DOCTORAT DE L'UNIVERSITÉ DE LYON

opérée au sein de

l'Université Claude Bernard Lyon 1

École Doctorale 52
École doctorale de Physique et Astrophysique

Spécialité de doctorat : Physique
Discipline : Cosmologie

Soutenue publiquement le 28 Juin 2022, par :

Martin Jacques FRANCE

Cosmic microwave background properties in a universe with simply or multiply connected topology

—

Propriétés du Fond diffus cosmologique micro-ondes dans un univers à topologie simplement connexe ou multi-connexe

---

Devant le jury composé de :

de LAPPARENT Valérie, Directrice de Recherches (IAP)	Présidente
ROUKEMA Boudewijn, Professeur (NCU Toruń)	Rapporteur et Examinateur
WILTSHIRE David, Professeur (University of Canterbury)	Rapporteur
MAHMOUDI Nazila, Maîtresse de Conférences (UCBL - CERN)	Examinatrice
TRIAY Roland, Professeur (AMU - CPT)	Examinateur
BUCHERT Thomas, Professeur (UCBL - CRAL)	Directeur de thèse
TRESSE Laurence, Astronome (LAM - GECO)	Co-directrice de thèse

Remerciements

Mon travail numérique et de recherche en cosmologie accompli pendant cette thèse de doctorat fait partie d'un projet qui a reçu un financement de la part du Conseil Européen de la Recherche (ERC) pour le programme de recherche et d'innovation European Union's Horizon 2020 (Grant Agreement ERC adG No. 740021-ARThUs, chercheur principal: TB).

Merci en premier lieu a mon directeur de thèse Thomas Buchert pour m'avoir chaleureusement intégré dans son groupe de cosmologie dès 2008 et pour m'avoir conduit à tant de savoirs fondamentaux ou innovants et, m'avoir appris que faire de la science c'est en premier lieu prendre du recul et remettre en question les théories et les données.

Roland Bacon, Bruno Guiderdoni, Laurence Tresse et Matthew Lehnert (directeurs successifs du CRAL) m'ont prêté une oreille bienveillante et exigeante dans mon but et dans mes progrès à faire de la science et de la cosmologie. Merci Roland, Bruno, Laurence, Matthew et merci aussi Gilles Adam, Claus Beisbart, Hélène Courtois, Julien Devriendt, Boud Roukema et Frank Steiner pour m'avoir encouragé et conseillé tout au long de cette longue route !

Je voudrais remercier Asta Heinesen et les deux rapporteurs Boud Roukema et David L Wiltshire pour leur relecture approfondie de ce Manuscrit de thèse. Je souhaite aussi les remercier ainsi que Ralf Aurich, Claus Beisbart, Léo Brunswic, Gilles Chabrier, Timothée David-Cléris, Léo Michel-Dansac, Pierre Mourier, Jan Jakub Ostrowski, Pratyush Pranav, Frank Steiner, Laurence Tresse, Nezihe Uzun et Quentin Vigneron pour les très intéressantes discussions que nous avons échangé sur de multiples questions de cosmologie, de physique, de mathématiques et d'informatique. Ma gratitude va à la chaleureuse hospitalité accordée par Thomas Buchert, Gilles Chabrier, Guillaume Laibe ainsi que toute l'équipe AstroENS. Et non des moindres, bien des tâches administratives et pratiques sont rendues possibles ou simplifiées à l'ENS et au CRAL grâce à Stéphanie Vigner et au Service Informatique et grâce à Sylvie Réa. Mes remerciements vont aussi bien sûr à Arlette Pécontal et Laure Piqueras du Pôle d'expertise et Calcul Scientifique du CRAL. Une immense aide est fournie par Hervé Gilquin et Loïs Taulelle du PSMN, le Pôle Scientifique de Modélisation Numérique à l'ENS Lyon. Je veux les remercier de m'avoir accordé un accès à leurs clusters et de m'avoir permis d'obtenir quelques résultats importants présentés dans ce travail de thèse.

Acknowledgements

My work in computer science and research in cosmology made during this PhD thesis is part of a project that has received funding from the European Research Council (ERC) under the European Union's Horizon 2020 research and innovation programme (Grant Agreement ERC adG No. 740021-ARThUs, PI: TB).

I say thank you firstly to Thomas Buchert my PhD supervisor to have hosted my work in his cosmology group in 2008 and to teach me among other basic or innovative knowledges, that the hindsight and the reassessment of theories and data are premises of the good science.

Roland Bacon, Bruno Guiderdoni, Laurence Tresse and Matthew Lehnert (successive CRAL directors) offered me a benevolent and demanding ear in my goal and my progresses in making science and cosmology. Thank you Roland, Bruno, Laurence and Matthew and thank you also to Gilles Adam, Claus Beisbart, Hélène Courtois, Julien Devriendt, Boud Roukema and Frank Steiner for your support and your advices all along this long way!

I would like to thank Asta Heinesen and the two referees Boud Roukema and David L Wiltshire for their thorough readings of this thesis Manuscript. I wish also to thank them and Ralf Aurich, Claus Beisbart, Léo Brunswic, Gilles Chabrier, Timothée David-Cléris, Léo Michel-Dansac, Pierre Mourier, Jan Jakub Ostrowski, Pratyush Pranav, Frank Steiner, Laurence Tresse, Nezihe Uzun and Quentin Vigneron for the very interesting discussions we have had on many questions of cosmology, physics, mathematics and computer science. My gratitude goes to the warm hospitality granted by Thomas Buchert, Gilles Chabrier, Guillaume Laibe and the whole team at CRAL AstroENS. And not the least, many administrative and practical tasks are made easier or possible at ENS and at CRAL thanks to Stéphanie Vigner and the Informatic Division and Sylvie Réa. I want to thank also Arlette Pécontal and Laure Piqueras of the Computational Science Department. A great support is provided by Hervé Gilquin and Loïs Taulelle of the PSMN, the Scientific Pole of Numerical Modelling at ENS Lyon. I wish to thank them to having granted me access to their clusters and to allow me to get some important results presented in this PhD thesis work.

Résumé

Le modèle cosmologique standard, dans le cadre de la théorie de la Relativité Générale (notée GR), suppose que l'Univers est isotrope et homogène et que le principe copernicien est valide. Ce modèle ne prescrit pas explicitement si l'Univers est spatialement infini ou fini. En effet la GR ne contraint pas la topologie ou l'extension spatiale de l'Univers. Cependant, en pratique, un modèle de formation de structure et d'évolution globale de l'Univers, dérivé avec la GR à une résolution spatiale appropriée, requiert une connaissance à priori de la topologie globale. Les anisotropies de température du fond diffus cosmologique (ci-après CMB), dans le modèle standard, sont projetées sur la $2-$sphère qui détermine la limite spatiale finie comobile de notre Univers observable. L'observation du CMB, depuis notre planète, résulte des effets que, la géométrie de l'espace-temps local et global, et les sources d'énergie au sens des composantes du tenseur énergie-impulsion de la GR, ont sur la propagation des photons. Le modèle standard d'Univers est le modèle ΛCDM, dont le contenu en énergie, outre l'énergie associée à la matière ordinaire, inclut l'énergie sombre (DE) sous la forme d'une constante cosmologique Λ, et l'énergie de la matière sombre froide (CDM). ΛCDM est un modèle cosmologique paramétrique, basé sur six paramètres cosmologiques (voir appendice 8.2.2), quoique sa paramétrisation puisse être étendue à six paramètres additionnels. La paramétrisation du modèle ΛCDM permet d'en explorer les variantes. Chaque variante étant caractérisée par une modification du spectre de puissance angulaire des anisotropies de température du CMB. Ainsi, le CMB et son spectre de puissance offrent un diagnostic synoptique de l'Univers ΛCDM. Les prédictions de ce modèle sont globalement en excellente conformité avec la plupart des observations de notre Univers. Ces observations étant interprétées dans ce modèle. Cependant, plusieurs anomalies dans les observations cosmologiques, sont constatées par rapport aux prévisions du modèle ΛCDM. Notamment, le spectre du CMB de l'Univers ΛCDM infini diffère du spectre du CMB observé.

La carte de température du CMB est affectée de biais dus à la géométrie de l'espace-temps et aux sources traversées par les photons dans leur trajectoire depuis l'époque de dernière diffusion. Corrigée de ces effets, la carte de température du CMB primordial, montre plusieurs anomalies à grande échelle angulaire, par rapport au CMB du modèle ΛCDM. Ce modèle suppose une expansion adiabatique de l'Univers, et prescrit les propriétés d'isotropie, d'homogénéité et de gaussianité des anisotropies de température du CMB primordial.

Durant mon travail de thèse, et dans ce Manuscrit, je m'intéresse notamment à une particularité des données du CMB qui est en désaccord avec la prescription d'isotropie globale du CMB dans le modèle standard. En fait, la fonction de corrélation à deux points (ci-après 2-pcf) dans l'Univers ΛCDM, révèle des corrélations non nulles à toutes les échelles angulaires, soit de 0 à 180°. Cependant,

la 2-pcf du CMB observé affiche une absence de corrélation aux grandes échelles angulaires, c'est à dire pour les angles $> 60°$. Ce manque de corrélation sur les deux derniers tiers de la plage de 180° est en anomalie avec le résultat du modèle ΛCDM. De plus, aucun changement dans la valeur ou le choix des 6 paramètres du modèle standard ne conduit à ce défaut de corrélation angulaire. Mais, c'est en reconsidérant la topologie globale de l'Univers avec des variétés multi-connexes qu'une solution à ce problème est obtenue. Ainsi, des cartes de simulation du fond diffus cosmologique dans un Univers de modèle ayant une topologie multi-connexe, par exemple celle du dodécaèdre de Poincaré (dénomination courante de la variété topologique orientable précisément appelée sphère d'homologie de Poincaré) ou bien celle du $3-$tore, affichent également un manque de corrélation de la 2-pcf aux grands angles. Le dodécaèdre de Poincaré (de courbure intrinsèque positive constante) et le $3-$tore plat (de courbure intrinsèque constante nulle) sont deux variétés topologiques compactes, finies et sans bord. Durant mes recherches de thèse, je développe ou adapte plusieurs outils d'analyse morphologique et statistique (morpho-statistique) pour les cartes du CMB. J'analyse, en recourant à différentes stratégies, trois variétés de cartes de température du CMB, (i) observée par les sondes WMAP et Planck, (ii) générées à partir de modèle d'Univers à topologie multi-connexe tel que le $3-$tore et (iii) générées à partir du modèle d'Univers infini ΛCDM.

Ce qui est nouveau, c'est que les investigations accomplies pendant ma thèse, conduisent à développer et implémenter numériquement pour le CMB, une signature statistique ρ, d'Univers multi-connexe complémentaire de la fonction de corrélation à deux points décrite plus haut. Les travaux et résultats sont présentés en détail dans notre article d'équipe publié [2], (voir [1]), et dans le chapitre dédié de ce Manuscrit. Non seulement, l'article prouve que la signature de variance du gradient de température ρ permet de classer monotoniquement les modèles d'Univers en fonction de leur extension spatiale, mais encore montre que les cartes du CMB avec topologie trois-toroïdale restent statistiquement compatibles avec le haut niveau d'isotropie et d'homogénéité, défini au sens de ρ, des cartes de température du CMB du modèle standard infini.

Dans le second article publié, présenté dans ce Manuscrit, nous recherchons, de manière modèle-indépendante, les écarts à la gaussianité de cartes du CMB. Dans le modèle standard, le fond diffus cosmologique est supposé être isotrope, homogène et gaussien (donnant l'acronyme IHG) pour les échelles angulaires plus grandes que l'horizon primordial de 0.6°. Une violation de la gaussianité à ces échelles pour les dernières données CMB, pouvant signifier que les précédentes conclusions sur l'Univers primordial et les hypothèses de modèles standards avec

[2] ***The variance of the CMB temperature gradient: a new signature of a multiply connected Universe*** 2021. Aurich R, Buchert T, **France M J** et Steiner F (auteurs par ordre alphabétique).

inflation doivent être modifiés. Les analyses sont menées principalement avec une classe de descripteur à la fois statistique et morphologique, les Fonctionnelles de Minkowski (ci-après MFs), appliquées en cosmologie dès 1994 par Mecke, Buchert et Wagner.

Notre article d'équipe [3] (voir [2]) confirme le faible niveau de non-gaussianité (ci-après NG) de la carte d'anisotropie de température du CMB observé par Planck. Par conséquent, le développement perturbatif de la NG du CMB est justifié et appliqué tout au long de ce travail. Y est montré, que notre développement modèle indépendant de la non-gaussianité du CMB en polynômes d'Hermite, converge avec une précision croissante dépendant seulement de l'ordre du développement. Notre méthode s'appliquant aussi à toute forme et amplitude de non-gaussianité. Nous vérifions également que le développement modèle dépendant avec ordonnancement hiérarchique biaise la description de la non-gaussianité primordiale. De plus, nous observons que ces développements modèle dépendants en séries perturbatives sont faits en fonction du terme σ_0 qui est de valeur non négligeable. Enfin, nos calculs mettent en évidence la plus faible non-gaussianité, au sens des Fonctionnelles de Minkowski, de la carte de température du CMB observé par Planck en comparaison avec les cartes gaussiennes par construction du CMB du modèle ΛCDM.

[3] ***Model-independent analyses of non-Gaussianity in Planck CMB maps using Minkowski functionals*** 2017. Buchert T, **France M J** et Steiner F (auteurs par ordre alphabétique).

Plan de la thèse

Dans ce Manuscrit, je vise à présenter mes recherches et résultats d'analyse du CMB dans le cadre large, tout d'abord du modèle standard d'Univers ΛCDM. Puis, à la lumière de résultats récoltés ou obtenus pendant mon travail de thèse, je dessine quelques traits d'un modèle d'Univers plus réaliste, restant à construire, et plus à même de tenir compte, de l'inhomogénéité de l'Univers et de prédire ses propriétés aux grandes échelles spatiales. Je recense tout d'abord, dans la revue historique, les étapes du développement de la GR et de la cosmologie relativiste (voir section 2.1). J'introduis ensuite en 3.1, des observations majeures et les concepts physiques sous-tendant la construction de la cosmologie actuelle. Mon introduction décrit la progression conceptuelle partant des fondations générales relativistes du modèle ΛCDM d'un Univers homogène et isotrope (From the ΛCDM model), où je détaille l'équation de champ d'Einstein (EFE) en 3.1.1, puis je présente la solution exacte de l'EFE dite Friedmann-Lemaître-Robertson-Walker (FLRW) en 3.1.2. Ensuite, en 3.1.3, j'introduis les équations de Friedmann. Puisqu'il faut prendre en compte l'existence d'anomalies et d'éventuelles inconsistences ou contradictions du modèle standard; mon Manuscrit s'intéresse à quelques pistes possibles en vue d'amender le modèle ΛCDM. En 3.2 (...toward an inhomogeneous universe model), je présente au début, une difficulté conceptuelle de la GR que je nomme "incompatibilité d'échelle". En effet, la solution exacte de l'équation d'Einstein n'est, sauf en de rares cas, calculable qu'aux petites échelles spatiales cosmologiques ou en imposant l'homogénéité et l'isotropie prescrite dans le modèle FLRW. Or, comme je vais le quantifier plus loin, les observations cosmologiques montrent que notre Univers est anisotrope et inhomogène à ces petites échelles spatiales et c'est seulement à partir des grandes échelles spatiales que l'homogénéité est constatée.

Les méthodes permettant la géométrisation relativiste de la gravité à grande échelle spatiale par moyennage et la rétroaction inhérente aux distributions d'énergie inhomogènes sont discutées en 3.2.1. Et c'est en 3.2.2 que je fais une brève présentation de la Topologie Cosmique (ci-après CT) assortie d'une revue historique de la Topologie et de la CT. J'y présente, entre autres, un papier de Boud Roukema auquel je contribue sur la détectabilité de la topologie cosmique dans des relevés de galaxies à grand redshift [3]. En 3.2.4, "Relativité Générale et topologie globale de l'Univers", je discute les spécificités du problème de Cauchy (problème de la valeur initiale) et d'un problème bien posé (existence et unicité d'une solution) appliqués à la résolution exacte des équations aux dérivées partielles non linéaires constituant l'EFE. Je considère alors l'application des conditions périodiques de bord (conditions de Neumann et de Dirichlet) dans le cas d'un Univers à topologie multi-connexe pour la résolution de l'EFE. J'illustre en détaillant la méthodologie d'un article par Frank Steiner qui détermine au premier ordre le champ gravitationnel (globalement anisotrope) d'un trou noir statique dans un Univers à topologie $3-$toroïdale.

En section 3.2.5, je fais une brève présentation du CMB que j'approfondis dans l'appendice 8.2.2. Je développe alors au chapitre 4 notre article d'équipe sur la découverte d'une nouvelle signature d'Univers multi-connexe. L'introduction détaillée de la fonction de corrélation à deux points (2-pcf) du CMB et du manque de corrélation au delà d'un angle de 60° du CMB observé est faite en 4.1.1. Et l'anomalie vis à vis des corrélations non nulles partout du CMB du modèle ΛCDM est discutée en 4.1.2. Le calcul du spectre discret de l'opérateur de Laplace, c'est à dire de ses valeurs propres et de ses nombres d'onde est détaillé pour l'espace à topologie 3−tore plat, fini sans bord en 4.1.3.

En section 4.2.1, est explicité le calcul de ρ défini comme l'écart-type du champ de gradient normalisé de la température du CMB. Alors qu'en 4.2.2 est détaillé (en figures et tableaux), le résultat fondamental de notre papier, à savoir que ρ présente une signature hiérarchique monotonique de la taille de la variété topologique : "plus petit est le volume de la variété topologique, plus grande est la valeur de ρ associée". Et cette loi est même linéaire. Cet article illustre aussi l'effet que la taille du 3−tore à sur le manque de corrélation aux grands angles de la 2-pcf: "plus petit est le volume du tore, plus la disparition des corrélations survient à un petit angle". Enfin le dernier résultat de cet article est quantifié en 4.2.4, à savoir l'absence marquée d'anisotropie au sens de ρ pour le CMB avec topologie toroïdale. La conclusion de cet article souligne, (i) l'actuelle impossibilité de prédire physiquement la loi linéaire constatée entre ρ et L/L_H la taille du côté des tores cubiques, soit $L/L_H \sim -0.3\rho + 14$ tracée figure 5, et (ii) est compatible avec une taille comobile de topologie toroïdale cubique de notre Univers de environ 3 longueurs de Hubble (L_H) soit environ 13.3 gigaparsecs.

L'article développé au chapitre 5 vise à évaluer le degré de gaussianité des cartes du CMB dans le modèle standard infini spatialement vis à vis de la carte du CMB de Planck. La fonction de densité de probabilité (PDF) est définie en détail en 5.2. Les constructions des fonctions d'anomalie (discrepancy functions) quantifiant l'écart à la gaussianité, et les développements en polynômes orthogonaux d'Hermite sont explicités avec les moments et cumulants de la PDF en 5.2.2 avec les résultats pour les cartes du CMB du modèle ΛCDM infini. L'expression analytique de la première fonctionnelle de Minkowski v_0 est donnée en 5.2.3 ainsi que sa prédiction pour un champ scalaire aléatoire gaussien. La précision arbitrairement grande, permise par les développements modèle indépendants en polynômes d'Hermite de la non-gaussianité (NG), est vérifiée en 5.2.4. L'hypothèse modèle dépendante "d'ordonnancement hiérarchique" avec formulation perturbative de la NG est explicitée par des développements en séries hiérarchiques en 5.2.5, prouvant que la signature de NG est biaisée par la modèle dépendance. En 5.2.6, les fonctionnelles de Minkowski v_1 et v_2 sont définies et leurs représentations graphiques données pour les cartes du ΛCDM infini. Si, comme discuté en section 5.2.7, formellement, la définition des fonctions d'anomalies des fonctionnelles de Minkowski diffère dans

les recherches de NG de la collaboration Planck et dans nos recherches, notre article trouve des niveaux de NG similaires. Enfin en 5.2.8, la plus forte non-gaussianité du grand échantillon de cartes (100,000), gaussiennes par construction, du ΛCDM est comparée graphiquement à la plus faible NG de la carte d'observation de Planck pour la PDF et les 3 MFs (voir les graphiques en 21, 22, 23 et 24). En conclusion de cet article (voir sections $\geq$ 5.3.1), aux échelles angulaires supérieures à $\sim 2^\circ$ [4] la faible non-gaussianité de la carte d'anisotropies de température du CMB observé par Planck est confirmée mais il serait important que des investigations sur des cartes à plus haute résolution, celle de Planck et celles du modèle ΛCDM, soient menées.

Le chapitre 6 de mon Manuscrit présente la question de la non-gaussianité du CMB abordée sous différentes perspectives. Il s'agit d'un article [4] élaboré par notre équipe à l'invitation de la revue Classical and Quantum Gravity [5] après la publication de notre article "Model-independent analyses of non-Gaussianity in Planck CMB maps using Minkowski functionals" développé section 5).

[4] L'horizon causal sur le CMB est d'un rayon inférieur à $\sim 0.6^\circ$, cependant, la faible résolution de N_{side}=128 et le fort lissage gaussien de 2° f.w.h.m. appliqués aux cartes effacent les contributions d'anisotropie de température primordiales à petite échelle.

[5] **Focus issue: Planck and fundamentals of cosmology** est une revue en ligne étudiant l'impact sur la cosmologie théorique des données Planck réinterprétées et fournies en 2015 (voir **CQG+ https://cqgplus.com/2017/04/18/is-the-cosmic-microwave-background-gaussian/**).

Abstract

The standard cosmological model, in the frame of the General Theory of Relativity (hereafter GR), assumes that the Universe is isotropic and homogeneous and that the Copernican principle is valid. This model does not explicitly prescribe whether the Universe is spatially infinite or finite given that GR does not constrain the topology or the finiteness of the Universe. However, in practice, a model of structure formation and global evolution of the Universe derived with GR at an appropriate spatial resolution requires assumptions on the global topology. The Cosmic Microwave Background (CMB) temperature anisotropies in the standard model are projected over the 2-sphere which determines the comoving finite limit in space of our observable Universe. The CMB as observed from Earth accounts for the local spacetime geometry and energy-momentum sources. In the standard ΛCDM universe model, the energy-momentum content includes phenomenologic dark energy in the form of a cosmological constant Λ and cold dark matter (CDM). ΛCDM is a parametric cosmological model, based on six cosmological parameters (see appendix 8.2.2), although its parametrization could be extended up to six additional parameters. The parametrization of the ΛCDM model allows to explore the variants of this model. Each variant being characterized by a change in the CMB power spectrum, thus the CMB and its power spectrum offer a diagnosis picture of the ΛCDM Universe. These model predictions are globally in excellent conformity with most of the observations of our Universe, interpreted within this model. However, several anomalies of the cosmological observations are ascertained with respect to the forecasts of the ΛCDM model. Notably, the CMB spectrum of the infinite ΛCDM Universe differs from the spectrum of the observed CMB.

The CMB temperature map is impacted by biases due to spacetime geometry and sources traversed by the photons in their trajectory from the last scattering surface. Once corrected from these effects, the primordial CMB temperature map shows several anomalies at large angular scale with respect to the CMB map in the ΛCDM Universe. This model assumes adiabatic expansion of the Universe, and prescribes the properties of isotropy, homogeneity and Gaussianity of the primordial CMB temperature anisotropies.

In my thesis work and in this Manuscript I am interested, notably, in a peculiarity of the CMB data which is in disagreement with the prescription of global isotropy of the CMB. Indeed, the CMB two-point correlation function (hereafter 2-pcf) in the ΛCDM Universe presents non-zero correlations at any angular scale, i.e. from 0° to 180°. However, the 2-pcf of the CMB observation map displays a lack of correlation at large angular scale, for angles $> 60°$. This absence of correlation over the last two thirds of the range of 180° is in disagreement with the result of the ΛCDM model. Moreover, no change in the values of the 6 parameters of the standard model accounts for this discrepancy. But it is by reconsidering the global topology of the Universe with multiply connected manifolds that a solution to this problem appears. Indeed, simulation maps of the CMB in a model universe having the multiply connected topology, of e.g. the Poincaré dodecahedron (current name of the orientable topological manifold precisely named Poincaré's homology sphere) or the $3-$torus both show a lack of correlation of the 2-pcf at large angles. Both the dodecahedron (of constant positive intrinsic curvature) and the $3-$torus (of vanishing constant intrinsic curvature) are compact topological manifolds, finite and without boundary. During my PhD studies, I have analysed, using different

strategies and developing different tools, both statistical and morphological (thereafter morpho-statistical), three kinds of CMB temperature maps, (i) observed by the probes WMAP and Planck, (ii) generated from the universe model with 3−toroidal topology and (iii) generated from the infinite ΛCDM model.

What is new is that the investigations made during my PhD lead to develop and numerically implement a statistical signature ρ of a multiply connected universe model that is complementary to the signature of the 2-pcf. The work and the results are presented in detail in a published paper and in the dedicated chapter of this Manuscript. Our team paper [1] not only proves that the signature ρ allows to sort, monotonically, the universe models as a function of the spatial size, but yet shows that the CMB maps with 3−torus topology stay statistically consistent with the high level of isotropy and homogeneity, defined in the sense of ρ, of the CMB maps in the ΛCDM model.

In the second published article [2], presented in this Manuscript, we investigate in a model-independent way, the deviations from Gaussianity in the CMB maps. In the standard model, the temperature map of the Cosmic Microwave Background is assumed to be isotropic, homogeneous and Gaussian (giving the acronym IHG) at the angular scales larger than the primordial horizon of $\sim 0.6^\circ$. Violation of Gaussianity at these scales for the last CMB data available could mean that the previous conclusions on the primordial Universe and the hypothesis of the outcome of standard models of inflation have to be modified. The analyses in this work are chiefly based on a class of statistical and morphological descriptors, the Minkowski Functionals (thereafter MFs), applied first in cosmology in 1994 by Mecke, Buchert and Wagner and broadly used after. Our team paper confirms the weak level of non-Gaussianity (thereafter NG) of the CMB temperature anisotropy map as observed by Planck. As a consequence, the perturbative expansion of the CMB NG is justified and applied all along this investigation. It is shown that our model-independent development of the CMB non-Gaussianity in Hermite polynomials converges with an increasing precision depending only on the order of expansion. Our method applies as well to any form and amplitude of non-Gaussianity. We also verify that the model-dependent development with hierarchical ordering biases the description of the primordial NG. Moreover, we observe that these perturbative expansions are made in series of the term σ_0 which is not negligible. At last, our computations put into light the weak non-Gaussianity, in the sense of the Minkowski Functionals, of the CMB temperature map observed by Planck, in comparison with the higher NG of the ΛCDM CMB maps which are Gaussian by construction.

Summary of Contents

In this Manuscript, I aim at presenting my researches and results of analysis of the CMB in the wide framework, chiefly, of the standard universe model, the ΛCDM. Then, in light of the results harvested and obtained during my thesis work, I am sketching a few features of a universe model, more realistic, still to be constructed, and more able to take into account the inhomogeneities of the Universe, and to predict its properties at large spatial scale. In the historical overview, I make a review of the evolution of GR and the relativistic cosmology (see section 2.1). In 3.1, I introduce some important observations and the physical concepts underlying the construction of the current cosmology. My introduction aims at describing the conceptual progression starting from the general relativistic foundations of the ΛCDM model of a homogeneous and isotropic Universe (From the ΛCDM model...), where I present the Einstein Field Equation (EFE), in 3.1.1, then I introduce the Friedmann-Lemaître-Robertson-Walker (FLRW) solution in 3.1.2. The Friedmann equations appear in 3.1.3. Since one has to take into account the existence of anomalies and possible inconsistencies or contradictions of the standard model, I focus in my Manuscript on a few paths towards amendments of the ΛCDM model. In 3.2, (...toward an inhomogeneous universe model), I discuss at the beginning a conceptual difficulty of GR which I name "scale incompatibility". Indeed, the exact solution to the EFE is practically computable at small spatial cosmological scales assuming in addition homogeneity and isotropy prescribed in the FLRW model. But, as I shall quantify and detail further, cosmological observations display anisotropy and inhomogeneity at these small spatial scales and the homogeneity is ascertained only at large spatial scales.

The averaging methods allowing the relativistic geometrisation of gravity at large spatial scale, and the backreaction inherent to inhomogeneous energy distributions are reviewed in 3.2.1. It is in 3.2.2, that I make a brief introduction to Cosmic Topology (thereafter CT). The section continuing with an historical overview of Topology and then of CT. I present, inter alia, a paper by Boud Roukema to which I contribute on the statistical detectability of CT with high-redshift galaxies [3]. In 3.2.4, "General Relativity and global topology of the Universe", I discuss the Cauchy problem (initial value problem) and the well-posed problem (existence and uniqueness of a solution) applied to the exact resolution of the partial differential equations (PDE), non linear, of the EFE. I consider then the application of boundary conditions (Neumann and Dirichlet boundary conditions) in the case of the EFE for a Universe with multiply connected topology. I illustrate the effect of topology on GR, reviewing the methodology of an article by Frank Steiner that determines the (globally anisotropic) gravitational field of a static black hole to first order, in a Universe with 3−toroidal topology.

In section 3.2.5, I make a brief presentation of the CMB that I deepen in the appendice 8.2.2. I develop then in chapter 4 our team article on the discovery of a new statistical signature of a multiply connected universe model. A detailed introduction of the 2-point correlation function (2-pcf) of the CMB and of the lack of correlation beyond the angle of 60° in the observed CMB is made in 4.1.1. The anomaly of this result, with respect to the everywhere non-vanishing correlations of the CMB in the ΛCDM model is discussed in 4.1.2. The calculation of the discrete spectrum of the Laplace operator, and of its eigenvalues and its wave-numbers is presented for the universe model with 3−toroidal topology, flat, finite and without boundary (4.1.3).

In section 4.2.1 ρ is defined as standard deviation of the CMB temperature gradient field. It is in 4.2.2 that the important result of the paper is presented (in figures and tables). That is to say, ρ is a signature, monotonic and hierarchical of the size of the topological manifold: "the smaller the size of the topological manifold, the larger the associated ρ value". Furthermore, the relationship between the size of the Universe and and ρ turns out to be linear. This article illustrates also a result already known: "the smaller the sidelength of the torus, the more the lack of correlation begins at a small angle". At last, in section 4.2.4, our work shows the absence of anisotropy, in the sense of ρ, of the CMB in a toroidal topology. The conclusion of this article underlines, (i) the current impossibility to predict the linear law we verify between ρ and L/L_H, the size of the cubic tori. This linear law is $L/L_H \sim -0.3\rho + 14$, and it is shown in figure 5. (ii) our results are consistent with a comoving size of the 3−torus of ~ 3 Hubble lengths (L_H), corresponding to ~ 13.3 gigaparsecs.

The article developed in chapter 5 investigates the level of Gaussianity of the CMB simulation maps in the infinite Universe of the standard model, compared to the CMB map observed by Planck. The probability density function (PDF) of the CMB is defined in 5.2. The constructions of the discrepancy functions quantifying the CMB deviations from Gaussianity, and the developments in Hermite orthogonal polynomials are made explicit with the moments and the cumulants of the PDF in 5.2.2 along with results for the infinite model. The analytical expression of the first Minkowski Functional v_0 is given in 5.2.3 with its prediction for a Gaussian scalar random field. The arbitrarily high precision allowed by the model-independent expansions, in Hermite polynomials of the CMB non-Gaussianity is satisfied in 5.2.4. The model-dependent assumption of "hierarchical ordering" with perturbative formulation of the NG is developed in hierarchical series in 5.2.5, proving that the signature of NG is biased by the model dependence. In 5.2.6, the Minkowski Functionals v_1 and v_2 are defined and their graphical representations are given for the CMB in the infinite universe model. In section 5.2.7, we verify that the definition of discrepancy functions of the MFs differ in the investigations of the Planck collaboration and in our work. We check in our article that the two methods yield very similar levels of weak non-Gaussianity. At last, in 5.2.8, the stronger NG of large ensembles of maps (100,000), Gaussian by construction, of the ΛCDM, is compared, graphically, to the weaker NG of the Planck observation map. The smaller NG of the Planck map is observed in the figures of the PDF and the 3 MFs (see figures 21, 22, 23 and 24). In conclusion of this article (in sections $\geq$ 5.3.1), at angular scales larger than $\sim 2^\circ$ [6] , the weak level of non-Gaussianity in the Planck CMB map is confirmed but it would be important to make investigations on CMB maps at much higher angular resolution.

The chapter 6 of my Manuscript presents the question of the CMB non-Gaussianity examined under different insights. It is an article [4] devised by our team replying to the invitation of the editor Classical and Quantum Gravity [7] after publication of our article "Model-independent analyses of non-Gaussianity in Planck CMB maps using Minkowski functionals" developed in chapter 5.

[6] The causal horizon on the CMB is of radius smaller than $\sim 0.6^\circ$, nevertheless, the low resolution of N_{side}=128 and the Gaussian smoothing of 2° f.w.h.m. applied to the maps, erase the contribution of temperature anisotropy at small scales.

[7] **Focus issue: Planck and fundamentals of cosmology** is an online review studying the impact on theoretical cosmology of Planck data re-interpreted and released in 2015 (see **CQG+ https://cqgplus.com/2017/04/18/is-the-cosmic-microwave-background-gaussian/**).

References

[1] R Aurich, T Buchert, **M J France** and F Steiner 2021 The variance of the CMB temperature gradient: a new signature of a multiply connected Universe *Class. Quantum Grav.* **38** 225005 (arXiv:2106.13205)

[2] T Buchert, **M J France** and F Steiner 2017 Model–independent analyses of non-Gaussianity in Planck CMB maps using Minkowski functionals *Class. Quantum Grav.* **34** 094002 (arXiv:1701.03347)

[3] B F Roukema, **M J France**, T A Kazimierczak and T Buchert 2014 Deep redshift topological lensing: strategies for the $\mathcal{T}^3$ candidate *Mon. Not. Roy. Astr. Soc.* **437** 1096-1108 (arXiv:1302.4425)

[4] T Buchert, **M J France** and F Steiner 2017 Is the Cosmic Microwave Background Gaussian? *Class. Quantum Grav.* + **Focus issue: Planck**

Publications related to the content of this PhD thesis

Published during the PhD thesis (Sept. 1^{st}, 2018 - July 1^{st}, 2022):

Aurich R, Buchert T, **France M J** and Steiner F 2021 ***The variance of the CMB temperature gradient: a new signature of a multiply connected Universe***
(with authors by alphabetical order)
Class. Quantum Grav. **38** 225005 (arXiv:2106.13205)

Still under preparation:

Aurich R, Buchert T, **France M J** and Steiner F 2022 ***Minkowski functionals of CMB maps for cosmological models with hypertorus topology***
(with authors by alphabetical order)

Pranav P, Aurich R, Buchert T, **France M J** and Steiner F 2022 ***Homology of the Cosmic Microwave Background: Are finite universe models preferred over the infinite standard model?***

Published before the PhD thesis:

Buchert T, **France M J** and Steiner F 2017 ***Model-independent analyses of non-Gaussianity in Planck CMB maps using Minkowski functionals***
(with authors by alphabetical order)
Class. Quantum Grav. **34** 094002 (arXiv:1701.03347)

Buchert T, **France M J** and Steiner F 2017 ***Is the Cosmic Microwave Background Gaussian?***
(with authors by alphabetical order)
Class. Quantum Grav. + **Focus issue: Planck**

Roukema B F, **France M J**, Kazimierczak T A and Buchert T 2013 ***Deep redshift topological lensing: strategies for the $\mathcal{T}^3$ candidate***
Mon. Not. Roy. Astr. Soc. **437** 1096-108 (arXiv:1302.4425)

Teaching or lecturing related to this PhD thesis

Supervisor of a student in L3 Physique, period June-July 2019, subject

Caractérisation d'une anomalie du CMB dans le modèle ΛCDM:
Alignement des multipôles de rang faible avec le plan de l'écliptique

Contents

1 Notations

Acronyms

BBN	Big Bang Nucleosynthesis
CMB	Cosmic Microwave Background
COBE	COsmic microwave Background Explorer (space probe)
COBRA/SAMBA or Planck	COsmic Background Radiation Anisotropy (space probe) SAtellite for Measurement of Background Anisotropies
CITS	CIrcle-in-The-Sky (topological signal)
COSMOS	COSMic EvOlution Survey (using various large telescopes)
CT	Cosmic Topology
DE	Dark Energy
DM	Dark Matter
EFE	Einstein Field Equation
EP	Equivalence Principle
FIRAS	Far InfraRed Absolute Spectrophotometer (onboard COBE)
FLRW	Friedmann, Lemaître, Robertson, and Walker
GR	General Relativity
HFI	Planck bolometers covering 6 high microwave frequencies from 100GHz to 857GHz
IHG	Isotropic, homogeneous and Gaussian
ISW	Integrated Sachs-Wolfe (effect)
ΛCDM	Λ Cold Dark Matter
LFI	Planck bolometers covering 3 low microwave frequencies from 30GHz to 70GHz
LRG	Luminous Red Galaxies
LSS	Large Scale Structures
MCM	Multiply Connected Manifold
MCT	Multiply Connected Topology
MCU	Multiply Connected Universe
MFs	Minkowski Functionals
NG	Non-Gaussianity
PBC	Periodic Boundary Conditions
PDE	Partial Differential Equation
PDF	Probability Distribution Function
Planck	CMB observation space probe
SCM	Simply Connected Manifold
SDSS	Sloan Digital Sky Survey
SLS	Surface of Last Scattering
SNe Ia	Supernovae of type Ia
SR	Special Relativity
SW	Sachs-Wolfe (effect)
SZ	Sunyaev-Zel'dovich (effect)
WMAP	Wilkinson Microwave Anisotropy Probe

Mathematical conventions

I denote a first rank tensor (i.e. a vector) using a bold symbol or the upper arrow (example: the vector x can be denoted $\boldsymbol{x}$ or $\vec{x}$). And I denote a second or greater rank tensor using a bold symbol (example: the tensor G is denoted $\boldsymbol{G}$).

The adjective hierarchical is used in the two fields of investigation presented in my PhD thesis. i) In the chapter "A new signature of multiply connected Universe" the hierarchy of the 3−tori is sorted out by increasing side lengths L. The signature ρ is monotonically decreasing with respect to L. Also the maximum of the PDF of ρ is (excepted in one case) a monotonically decreasing function of ρ. We encase these two properties under the adjective hierarchical. ii) In the chapter "CMB non-Gaussianity: a model-independent analysis" the hierarchical ordering of the cumulants of the PDF (hierarchical ordering being a method to calculate the perturbative expansion of the CMB temperature non-Gaussianity) is discussed and compared to our model-independent approach of the CMB non-Gaussianity.

The term Gaussian premise (Gaußsche prämisse in german) adopted in some places in the thesis replaces the terms Gaussian hypothesis or Gaussian prior.

Variables, Functions and Functionals

Δ_{P}	discrepancy function of the PDF
Δ_{i}	discrepancy function of the i^{th} Minkowski Functional (i=0,1,2)
H_0	present-day Hubble constant
h	present-day reduced Hubble constant, $h{=}H_0/(100\ \mathrm{km\ s^{-1}\ Mpc^{-1}})$
L_H	Hubble length, $L_H{=}\mathrm{c}/H_0$
p (in GR)	relativistic pressure
P and $\mathrm{P^G}$	probability density function (PDF) and its Gaussian premise
ρ (in GR)	relativistic energy density
ρ (in the 2 CMB papers)	normalized standard deviation of the CMB temperature gradient field
σ_0^2	variance of the CMB temperature field
σ_1^2	variance of the CMB temperature gradient field
ST	spacetime section separating emitter from receiver
$ST\Lambda$	ST across the ΛCDM Universe
$\mathcal{T}^3$	3−torus or hypertorus multiply connected topological manifold
2-pcf	two-point correlation function
v_0 and v_0^{G}	first normalized Minkowski Functional and its Gaussian premise
v_1 and v_1^{G}	second normalized Minkowski Functional and its Gaussian premise
v_2 and v_2^{G}	third normalized Minkowski Functional and its Gaussian premise

2 Historical Overview

2.1 on General Relativistic Cosmology

The seminal papers of Albert Einstein on General Relativity "Covariance Properties of the Field Equations of the Theory of Gravitation Based on the Generalized Theory of Relativity" ("Kovarianzeigenschaften der Feldgleichungen der auf die verallgemeinerte Relativitätstheorie gegründeten Gravitationstheorie") and "The Formal Foundation of the General Theory of Relativity" ("Die formale Grundlage der allgemeinen Relativitätstheorie") were written in 1914 [1, 2]. These papers describe the geometric theory of gravity devised by Einstein and based on the principles of covariance [8], Special Relativity, the Equivalence Principle (EP)[9] and what Einstein will later name Mach's principle. I summarize the physical concepts underpinning these principles in section 3.1 of the Introduction (see 3). Einstein derived in these papers the covariant equations of the gravitational field and proved that the gravitational theory of Newton is an approximation of the General Relativity (GR). GR and the field equations of gravitation will be presented and developed with more details by Einstein in the subsequent papers written in 1915-1916 [3–6]. A comprehensive review of GR and its applications can be found in [7].

Einstein will identify three observational tests of GR: (i) The anomalous perihelion advance of Mercury (∼0.1arcsec per revolution) which he explains and confirms in [8]. (ii) The bending of light trajectories exerted by the gravitational field of a heavy celestial body which was predicted by Einstein in 1911 [9]. The bending of light due to the gravitational field of the Sun will be verified and measured by Dyson, Eddington and Davidson in 1919 (see [10]) thanks to the minute drift in position of stars they observed just next to the eclipsed Sun. (iii) The gravitational redshift of light propagating in a gravitational field. This gravitational redshift was first suggested by Einstein in [11], well before the formulation of GR, as a test of the Equivalence Principle. Einstein estimated at 1 part in 2 million the gravitational redshift of spectral lines of atoms at the sun's surface. However, Florides hinted in 2002 [12] that this gravitational redshift was predictable only using the full theory of General Relativity. And the first detection of this gravitational redshift, in rather good conformity with GR calculations, will be obtained in 1954 by Popper [13] comparing the redshift of a heavy white dwarf star to the redshifts of its lighter neighbouring stars. In the case of a massive object such as a white dwarf, the spectral lines of the light emitted by the object are shifted by two effects, the gravitational redshift as determined by the mass of the star and the "peculiar redshift" due to the radial velocity of the star.

From February 1917, in works such as "Cosmological Considerations in the General Theory of Relativity" [14] , Einstein discussed the dependence between the geometric structure of the spacetime and its energy-momentum content at the scale of the Universe

[8] The concept of covariance assumes that the form of the physical laws is invariant with respect to any differentiable and invertible coordinate transformation.

[9] The weak EP assumes identity of the inertial and gravitational masses. The strong EP assumes identity of results of a same experiment made in two distinct frames in free fall. The strong EP further asserts that at any event, always and everywhere, it is possible to choose a local inertial frame such that in a sufficiently small spacetime neighbourhood all non-gravitational laws of nature take on their familiar forms appropriate to the absence of gravity, namely the laws of special relativity.

as a whole (see also the historical review [15] by specialists and translators in English of Einstein's works). Einstein's initial ansatz was to "supplement the differential equations" of GR by "limiting conditions at spatial infinity", since at the time, the Universe was generally believed to be spatially infinite. However, Einstein identified huge difficulties in obtaining an infinite universe model where all frames of reference should be equivalent and where the inertia of any celestial body could exist. Einstein thus proposed a finite and bounded universe model, with spatial sections given by the 3 dimensional sphere $\mathcal{S}^3$ of constant positive curvature. Within this model, Einstein found that there were static non-vacuum solutions if an additional term was introduced in the system of differential equations. This term amounted to a universal constant Λ modifying Poisson's equation

$$\Delta\phi = \Lambda - 4\pi G\rho \ ; \tag{1}$$

with ϕ being the gravitational potential and ρ being the inhomogeneous density of matter in the Universe [10]. In analogy with the modified Poisson's equation, the full and general modified Einstein field equations (EFE) become

$$\boldsymbol{G}_{\mu\nu} - \Lambda \boldsymbol{g}_{\mu\nu} = \kappa \boldsymbol{T}_{\mu\nu} \ . \tag{2}$$

where $\kappa = 8\pi G/c^4$, and G is the universal constant of gravitation. The cosmological constant Λ was introduced by Einstein to ensure that the spacetime solution was static; however, it turned out that this static property was unstable. The system of equations (2) has a static dust solution with constant and uniform density field ρ_0 if Λ satisfies

$$\Lambda = \frac{\kappa\rho_0}{2} = \frac{1}{R^2} \ , \tag{3}$$

where R is the radius of the spatial sections of $\mathcal{S}^3$, and its volume being $V = 2\pi^2 R^3$.

The question of applying the field equations of gravitation to regions of the Universe showing a lack of uniformity of the matter distribution was a concern for Albert Einstein in [14], since in the physical Universe the "metrical structure of the continuum must necessarily be extremely complicated". He reasoned that it was a question of scale, since at large scale the matter distribution could be represented as uniformly distributed "over enormous spaces".

However, the questions to know,

1)– how to account for the matter distribution over a very large spatial volume, to determine the stress-energy-momentum tensor within small sub-regions of this volume, and

2)– how to arrive at a uniform universe description at large spatial scale from a spacetime solution on the small scales of GR (which is a local theory in virtue of its differential nature, but non local due to propagating constraints equations.),

were not asked or clarified yet.

After Einstein's founding work "Cosmological Considerations in the General Theory of Relativity", Alexander Friedmann derived non- static exact solutions to the EFE with $k > 0$ in his paper of 1922 (see [16] and [17] for the English translation). The model

[10] In the article "Cosmological Considerations..." [14], equations (1), (2) and (3) were written differently by Einstein. Einstein used definitions and conventions of notation slightly different of the ones used in GR today.

universes studied by Friedmann were homogeneous and isotropic with strictly positive or negative constant curvature of space (1924 [18], translated in English [19]). These solutions were the spherical Universe (curvature $k > 0$) and the hyperbolic Universe ($k < 0$) but Friedmann never considered the simplest flat models with $k = 0$. These works of Friedmann went against Einstein, who at the time considered the non static solutions unrealistic.

In 1927, George Lemaître derived differential equations for the radius of the spherical and non static Universe. The first observations of recessing nebulae by Slipher were known by Lemaître who suggested that large volumes of the Universe could be in global expansion in conformity with his solutions to the EFE (original French version [20] of 1927 and English translation in [21]). In the same paper Lemaître gave an observational estimate of the value of the Hubble constant $H_0 \approx 625$ km/s/Mpc. The reader may refer also to the editorial note of Jean-Pierre Luminet pp1619-33 of [21]. In 1929, Hubble established a linear relation between recession velocity and distance of spiral nebulae (galaxies) [22]. This relation was compatible with a general expansion law predicted by the Friedmann's and Lemaître's solutions to the EFE [11]. Robertson in 1929 [23] and Walker in 1933 [24, 25] also worked out a homogeneous and isotropic expanding solution to the EFE, slightly after the ones of Friedmann and Lemaître. Today, the spatially homogeneous and isotropic spacetime exact solutions to the EFE are known as the FLRW metric solutions. Confronted with the observational evidence, "The redshift of the distant nebulae have smashed my old construction like a hammer blow" said Einstein in 1931. And he published several works accounting for the 'new deal' of an expanding Universe (see the Einstein's bibliography of the early 1930's in [15]). The two main General Relativistic models of an expanding Universe devised by Einstein were, one model with non-vanishing positive spatial curvature and one model flat, both without the cosmological constant because Λ is not needed to formalise an expanding Universe.

Since these first applications of GR to cosmology by Einstein, Friedmann, Lemaître, Robertson, Walker and others at the beginning of the twentieth century, many attempts have been made to refine and to interpret existing derivations of exact solutions to the EFE, and to devise new exact solutions. One can refer to the review by [26] made in 2015 and the exploration of the more than 4,000 papers reviewing these solutions in [27]). Algebraic Classifications of the exact solutions were developed by Petrov (1957) and Segre (1964). Among these exact solutions, a vast majority of them concern either isolated astrophysical objects or the cosmological scales. Schwarzschild (1916) [28], Kerr (1963) [29] derived exact solutions for static or rotating black holes. Tolman (1939), Buchdahl (1967) studied exact solutions for star interiors and neutron stars. At the cosmological scales, attempts were made by Baldwin (1926) to build exact solutions in the case of the plane gravitational wave (propagation of gravitational radiation). Among the most important exact solutions to the EFE in cosmology going beyond the FLRW model, are the following inhomogeneous or anisotropic models. The LTB that is to say Lemaître-Tolman-Bondi (from 1933) spherically symmetrical inhomogeneous models are dust models [30] (see [31] for a definition of dust in cosmology). One strain of spatially homogeneous, anisotropic universe model with dust and perfect fluid source was devised by Kantowski and Sachs in [32] (1966). The spatially homogeneous, but anisotropic

[11] This general expansion law was named Hubble's law though the chronology should have given precedence to Lemaître by 2 years.

Bianchi models (1969) with perfect fluid sources were ascertained and studied in [33]. The inhomogeneous universe models of Oleson (1971) [34] have the source of gravitational field which is a perfect fluid (i.e. with vanishing anisotropic dissipative terms). The Stephani-Barnes [35] inhomogeneous models (from 1967) are with energy density and pressure in the stress-energy tensor but with barotropic equation of state, i.e. where pressure is a function of the restmass density. The Szekeres models [36] (dating back to 1975) are spatially inhomogeneous and without pressure. While the Szekeres-Szafron (1977) range of inhomogeneous models is with homogeneous pressure [37].

These theoretical progressions to model an inhomogeneous or anisotropic Universe were aimed at finding a better conformity with the observed Universe. The standard ΛCDM cosmological paradigm (based on the flat FLRW solution) constitutes today a largely consistent fit to the key cosmological observations. Since this model presents the least unacceptable concordance to the whole set of observational data, it is granted the title of Concordance model. Nevertheless, several of these observational data interpreted in the framework of the ΛCDM model are not compatible with its predictions. This leads to conclude to serious specific or statistical inconsistencies of this model. For instance, the FLRW model proposes no physical mechanism to describe nature and origin of Dark Energy (DE) and of Dark Matter (DM). DE and DM are two physical unknowns, energy sources in the EFE, inherent to the way the observations are interpreted in the FLRW model; see section 3.1 in the chapter 3 for explanations on DE and DM. Moreover, the CMB temperature anisotropies observed by Planck and the previous CMB radiotelescopes display several anomalies [38] with respect to the predictions of the standard model of cosmology relying on the FLRW solutions to the EFE. One of this anomalies is of course "the lack of correlation at large angular scale" of the CMB 2-pcf. Furthermore, the value of H_0, the Hubble parameter today, evaluated from observations of nearby regions of the Universe, and estimates of H_0 from the angular diameter distance of the first acoustic peak of the CMB, are in strong tension. I invite the reader to refer to the initial paper of 2020 on the tension on H_0 [39], and to the beginning of section 3.1 for more references and discussion on the foundational problems of the ΛCDM paradigm and the anomalies of the observational data w.r.t. this model.

I shall close here the historical overview on General Relativistic Cosmology. I will extend this discussion in section 3.2.1 of chapter 3 concerning the averaging problem of Einstein's equations and the resulting backreaction of inhomogeneities on global properties of universe models.

2.2 and on Cosmic Topology

The history of **Cosmic Topology**, in its definition of science studying the global structure of spacetime with the mathematical tools of geometry and topology begins at the end of the 20^{th} century. Cosmic Topology (denoted CT) is therefore a very young science. Its main historical facts and the theory will be developed in my subsection "A brief introduction to Cosmic Topology" 3.2.2 and in the chapter 4 presenting the results obtained for "The CMB in the multiply connected Universe $\mathcal{T}^3$".

References

[1] A Einstein and M Grossmann 1914 Kovarianzeigenschaften der Feldgleichungen der auf die verallgemeinerte Relativitätstheorie gedründeten Gravitationstheorie *Zeischrift für Mathematik und Physik* **63** 215-225

[2] A Einstein 1914 Die formale Grundlage der allgemeinen Relativitätstheorie *Mitth. phys.-math. Cl.* 1030-1085 *Comm. phys.-math. section* 1030-1085

[3] A Einstein 1915 Zur allgemeinen Relativitätstheorie *Sitzungb. König. Preuß. Akad. Wissens.* 778-786

[4] A Einstein 1915 Zur allgemeinen Relativitätstheorie (Nachtrag) *Sitzungb. König. Preuß. Akad. Wissens.* 799-801

[5] A Einstein 1915 Die Feldgleischungen der Gravitation *Sitzungb. König. Preuß. Akad. Wissens.* 844-847

[6] A Einstein 1916 Die Grundlage der allgemeinen Relativitätstheorie *Annalen der Physik* **49** 769-822

[7] C W Misner, K S Thorne and J A Wheeler 2018 Gravitation *Princeton University Press* ISBN 9780691177793

[8] A Einstein 1915 Erklärung der Perihelionbewegung der Merkur aus der allgemeinen Relativitätstheorie *Sitzungb. König. Preuß. Akad. Wissens.* 831-839

[9] A Einstein 1911 Über den Einfluß der Schwerkraft auf die Ausbreitung des Lichtes *Annalen der Physik* **340** 898-908

[10] F W Dyson, A S Eddington and C Davidson 1919 A Determination of the Deflection of Light by the Sun's Gravitational Field, from Observations made at the Total Eclipse of May 29, 2019 *Philos. Trans. R. Soc.* **220** 291-333

[11] A Einstein 1907 Über das Relativitätsprinzip und die aus demselben gezogene Folgerungen *Jahrb. Radioakt. Elektron.* Translation in *The collected papers of Albert Einstein* **2** 252-311, 316-317

[12] P S Florides 2002 Einstein's Equivalence Principle and the Gravitational Red Shift *School Math.* 1-25

[13] D M Popper 1954 Red Shift in the Spectrum of 40 Eridani B *Astrophys. J.* **120** 316-321

[14] A Einstein 1917 Kosmologische Betrachtungen zur allgemeinen Relativitätstheorie *Sitzungb. König. Preuß. Akad. Wissens.* 142-152

[15] C O'Raifeartaigh, M O'Keeffe, W Nahm and S Mitton 2017 Einstein's 1917 Static Model of the Universe: A Centennial Review (arXiv:1701.07261)

[16] A Friedmann 1922 Über die Krümmung des Raumes *Zeitschrift für Physik* **10** 377-86

[17] A Friedmann 1922 On the Curvature of Space (engl. translation of 1999) *Gen. Relat. Gravit.* **31** 1991-2000

[18] A Friedmann 1924 Über die Möglichkeit einer Welt mit konstanter negativer Krümmung des Raumes *Zeitschrift für Physik* **21** 326-32

[19] A Friedmann 1924 On the Possibility of a World with Constant Negative Curvature of Space (engl. translation of 1999) *Gen. Relat. Gravit.* **31** 2001-8

[20] G Lemaître 1927 Un Univers homogène de masse constante et de rayon croissant, rendant compte de la vitesse radiale des nébuleuses extra-galactiques *Ann. Soc. Scient. Bruxelles* **A47** 49-59

[21] Abbé G Lemaître 1927 A homogeneous Universe of constant mass and increasing radius accounting for the radial velocity of extra-galactic nebulae *Golden Oldies in General Relativity and Gravitation 2013* **45** 1635-46

[22] E Hubble 1929 A relation between distance and radial velocity among extra-galactic nebulae *Proc. Natl. Acad. Sci.* **15** 168-73

[23] H P Robertson 1929 On the foundations of relativistic cosmology *Proc. Natl. Acad. Sci.* **15** 822-29

[24] A G Walker 1933 Spatial distance in general relativity *Quart. J. Math.* **os-4** 71-80

[25] A G Walker 1934 On Riemannian spaces with spherical symmetry about a line, and the conditions for isotropy in general relativity *Quart. J. Math.* **os-6** 81-93
[26] M Ishak 2015 Exact Solutions to Einstein's Equations in Astrophysics *Texas Symp. Rel. Astr.*
[27] H Stephani, D Kramer, M MacCallum, C Hoenselaers and E Herlt 2003 Exact Solutions to Einstein's Field Equations (2^{nd} edition) ISBN-13 9780521461368
[28] K Schwarzschild 1916 Über das Gravitationsfeld eines Massenpunktes nach der Einsteinschen Theorie *Sitzungb. König. Preuß. Akad. Wissens.* **german version** 189-196
On the gravitational field of a mass point according to Einstein theory (arXiv:physics/9905030)
[29] Kerr R P 1963 Gravitational Field of a Spinning Mass as an Example of Algebraically Special Metrics *Phys. Rev. Lett.* **11** 237-238
[30] H Bondi 1947 Spherically Symmetrical Models in General Relativity *Mon. Not. Roy. Astr. Soc.* **107** 410-425
[31] D Wiltshire 2011 What is dust? – Physical foundations of the averaging problem in cosmology *Class. Quantum Grav.* **28** 164006 (arXiv:1106.1693)
[32] R Kantowski and R K Sachs 1966 Some Spatially Homogeneous Anisotropic Relativistic Cosmological Models *J. Math. Phys.* **7** 443
[33] G F R Ellis and M A H MacCallum 1969 A Class of Homogeneous Cosmological Models *Commun. math. Phys.* **12** 108-141
[34] M Oleson 1971 A Class of Type [4] Perfect Fluid Space-Times *J. Math. Phys.* **12** 666
[35] H Stephani 1967 Über Lösungen der Einsteinschen Feldgleichungen, die sich in einen fünfdimensionalen flachen Raum einbetten lassen *Commun. math. Phys.* **4** 137-142
[36] P Szekeres 1975 A Class of Inhomogeneous Cosmological Models *Commun. math. Phys.* **41** 55-64
[37] D A Szafron 1977 Inhomogeneous cosmologies: New exact solutions and their evolution *J. Math. Phys.* **18** 1673
[38] Schwarz D J, Copi C J, Huterer D and Starkman G D 2016 CMB anomalies after Planck *Class. Quantum Grav.* **33** 184001 (arXiv:1510.07929)
[39] Di Valentino E, Melchiorri A and Silk J 2020 Planck evidence for a closed Universe and a possible crisis for cosmology *Nature Astron.* **4** 196–203 (arXiv:1911.02087)

3 Introduction

3.1 From the ΛCDM model...

Cosmology studies the origin, the birth and the evolution of the Universe considered as a whole (see also e.g. [1]). As in any field of physics, in cosmology one wants to make observations and experiments and to obtain predictions on the evolution of the Universe. The Universe at cosmological scales, because of the huge distances separating an observer from the stars, galaxies, galaxy clusters, gas and dust clouds and the Cosmic Microwave Background, leaves no possibility to make experiments on these objects. Cosmology must therefore rely on the occurence of spatially and temporally non-controlled phenomena offering the opportunity to proceed to observations. The periodicity of many cosmological phenomena seen from Earth has permitted to systematize observation methods and to design always refined means of observation of the Universe. The repeatability of the physical experiments and the accuracy of the observations made on or around our planet Earth allows to build and develop the modern physics and supported by a robust and evolutive mathematical framework to frame the physical laws and the predictability of the experiments on fiducial physical models. The story goes differently for cosmology for which the standard cosmological model (SCM) is highly satisfactory in its globality and its predictions but faces several problems: inconsistencies, discrepancies or anomalies of observations compared to its expectations, such as the recent tension assessed between two different methods of evaluation for the value of H_0 the Hubble constant today, from the measurements in the large scale structures, or from the first acoustic peak of the Cosmic Microwave Background (see e.g. [2–4]). Other problems of the SCM have been at the origin of the development of three theories in cosmology which are the Inflation scenario (for an exploration of many variants of Inflation mechanisms see e.g. [5]), and the dark sources, i.e. Dark Matter [6] and Dark Energy [7, 8]. These problems were brought to light from the interpretation of CMB or large scale structure observations within the framework of the standard model. Two such problems see [10] are for instance the "horizon problem" [11] and the "singularity problem". As in the case of the Inflation, Dark Matter and Dark Energy theories are based on phenomenological mechanisms proposed as an attempt to elucidate observations made and interpreted with the prescriptions of the standard model that is to say homogeneity and isotropy of the Universe. Earth or solar system scaled phenomena are rather well described and predicted by the Newtonian gravity but the application of physical laws at cosmological scales could be impaired by the difficulty to apply the General Relativity at large scale to a Universe showing a big complexity due to the presence of spatial inhomogeneities.

The proposition of a realistic cosmological model must be made knowing that the spacetime where we make the observations can be twisted, stretched, compressed or even torn by the gravitational field and therefore the geodesics taken by the light during its propagation from emitter to receiver may be warped continuously before the light reaches the telescope. I shall define the light cone as the ensemble of geodesics associated to the observation of a sky object having a non zero transverse physical size subtending an angular size depending on the travel made by the photons along the different geodesics. In a Euclidean space of constant curvature $k = 0$ and a homogeneous and isotropic medium

the light cone is described by the usual geometric cone, but in the most general case the space curvature and the cut across medium may vary all along the travel of the source photons resulting in an anamorphic distortion of the light cone. The apparent direction, luminosity and angular size of the object differing from the ones observed in the Euclidean case.

The concept of "fair observation" in cosmology is therefore dependent on the level of knowledge the observer has on the spacetime ST separating the instrument from the light source object and on the physical nature of the object itself. The model hypothesis of an ideal Newtonian spacetime Euclidean, homogeneous and isotropic on average at large scale (named cosmological principle and denoted CP thereafter) makes far easier the estimation (always model-dependent) of distances since the angular diameter distance or the luminosity distance are supposed to be not affected by variations of the angle subtended by the object or by drifts of homogeneity all along the light cone propagation. Obviously for the determination of angular diameter distance or luminosity distance, the absolute diameter or the absolute luminosity of the source are required. The ansatz of assuming the most simple properties of geometry, that is to say constant zero curvature and homogeneous and isotropic matter distribution in the Universe allows to get a first (Euclidean model weighted) picture of our Universe. Step by step, once absolute diameter, absolute luminosity, mass and spectrum of the sun in our solar system are measured or determined applying the Newtonian dynamics (through the Kepler laws) and the Doppler-Fizeau effect, the sun-like stars velocities and distances and the galaxies velocities, distances, absolute luminosities and masses can be estimated. It is important to characterize the results, the limits, and the problems due to these assumptions of Newtonian geometry and CP applied to the whole Universe with the standard cosmological model, and to compare to the outcomes of non homogeneous models with Einsteinian gravity, more realistic, far more complex and which the global implementation at cosmological scales seems out of reach today.

I endeavour in this Manuscript of PhD thesis, to present my work of investigation on the CMB, first in the light of the achievements and the possibilities of evolution and enhancement offered by the ΛCDM model. The ΛCDM model is one of the most comprehensive universe models. This model imposes the prescriptions of spatial homogeneity, isotropy and takes into account the phenomenologies of the Big Bang, primordial Inflation, cold Dark Matter (CDM) and Dark Energy (associated to the cosmological constant denoted Λ). But it appeared also as a necessity and a motivation to keep into mind the possibility to explore and probe the Universe in all its apparent complexity with the physical laws inherent to a gravity dominated spacetime. The non-exhaustive inventory I am now making presents the interpretations of key observations, some are elaborated within the ΛCDM model under the assumptions of homogeneous and isotropic Universe, while some do not depend on the ΛCDM model.

- The Universe is in global expansion even at cosmological distances (up to $z \sim 11$ or beyond, see e.g. [12]). The expansion following the Hubble-Lemaître law satisfied by the recessional component of velocity of the galaxies ($v_{\rm rec}$ or Doppler-Fizeau redshift $z = v_{\rm rec}/c$) as a function of the Hubble constant H_0 and the luminosity distance r_L (see [13], [14] p15 fig8 or [15]). The approximate Hubble-Lemaître law, valid at small redshift (see section 3.1.2 for more details), reads

$$\dot{r} = H_0 r + a(t)\dot{\varsigma} \, , \tag{4}$$

if $|\dot{r}| \ll c$ while the comoving objects have the relative peculiar motion (using comoving distance units and proper time as defined in (6)) $\dot{\varsigma}$ for e.g. a galaxy. The relation between physical distance $r = r(t)$ and comoving distance ς through the scale factor $a(t)$ is

$$r = a(t)\varsigma \ , \tag{5}$$

while proper time t and conformal time η follow the relation

$$dt = a(t)d\eta \ . \tag{6}$$

The value taken by the Hubble parameter H being estimated from the first acoustic peak of the CMB and its angular diameter distance, at a value today of H_0=(67.66±0.42)km s^{-1} Mpc^{-1} [17].

- The distribution of nearby objects around our planet in the solar system (spatial scale = $sc \sim$ a few astronomical units) and up to the nearby stars ($sc \sim$ a few lightyears) looks very different according to the direction of observation, which answers to the definition of anisotropy. An anisotropy is also observed at larger distances ($sc \sim$ a few kilo-parsecs) in the various and motley shapes, sizes and separations of the constellations in the Milky way and the anisotropy appears also in the spatial dispersal of close galaxies ($sc \sim$ a few million parsecs). Overally the anisotropy seems to decrease for larger and larger spatial scales. Thus [18] presents a "transition to large-scale homogeneity" measured in the distribution of galaxies with the 2-point correlation function (2-pcf) estimating this way a minimum comoving scale of homogeneity $sc \sim 70$ mega parsecs ($70h^{-1}$Mpc). Though [19] suggests using number counts statistics a large scale convergence to spatial homogeneity leading to a larger by 40 % "transition to large-scale homogeneity". Moreover, [20] using the morpho-statistical "Germ-grain" Minkowski Functionals (denoted MFs) [12] on the luminous red galaxies (LRG) of the SDSS-DR7 catalogue, obtains departure $> 3\sigma$ from the homogeneity compared to a ΛCDM mock catalogue even at spatial scales of $500h^{-1}$Mpc and 2σ for $700h^{-1}$Mpc scales.

- Slice-shaped (at constant galactic declination) and projected distribution maps of galaxies (up to 7031 objects) are presented by de Lapparent et al. in 1986 [21] using the survey of Zwicky and the CfA redshift survey. "The galaxies appear to be on the surfaces of bubble-like structures", posing a riddle about the mechanisms of structure formation. In 2007, de Lapparent et al. using their ESO-Sculptor galaxy survey (ESS) confirm the scenario that structures form by gravitational instability "driven by the hierarchical merging of dark matter halos" [22]. More specifically, that early-type galaxies are located near the center of dark matter halos, while late-type galaxies (spiral) are located around the center of less massive dark matter halos. The clustering by hierarchical formation of structures such as galaxies and clusters is observed and confirmed [23]. A cosmological consistency relation quantifies the effects of structures on the validity of hypothesis of a homogeneous and isotropic Universe [24]. What comes out is that Universe matter is structured into voids

[12] The MFs of a random field are a set of morpho-statistical descriptors integrating all the orders of correlation functions, 2-pcf, 3-pcf, ...

separating galaxies organised in filaments, clusters and superclusters mapped by surveys such as COSMOS and SDSS [25, 26] which detect the baryon acoustic peak in the clustering of galaxies.

- The long term observations and measurements made on the kinematics and the dynamics of the sun and the planets in our solar system are in agreement with the predictions of General Theory of Relativity (read e.g. [27]).

- The relative abundance of light elements in our galaxy is measured in halo stars at low-metallicity, it amounts to 25% for the helium while the expected helium abundance assuming that initially stars were made of pure hydrogen should be only 2% today. The excess in helium and light elements is assumed to be produced during a primordial period said Big Bang Nucleosynthesis or BBN (see e.g. [28], [29], [30] and [31]). The observed relative abundances of deuterium, D/H and of helium 3, ^{3}He/H are in conformity with the predictions of production obtained during the primordial nucleosynthesis. However, the abundance of ^{7}Li/H measured in low-metallicity stars is 3 to 4 times lower than predicted with the BBN with a difference of 5σ (see e.g. [32]).

- The Cosmic Microwave Background is observed as highly homogeneous, isotropic and Gaussian [33, 34] with a nearly ideal blackbody radiation spectrum (see [35] for a review and [36]) at a temperature today T_0=(2.7255±0.0006)K [37]. CMB anisotropies hold within $|\Delta T/T_0|$ $\sim 10^{-5}$. The CMB angular power spectrum is nearly flat at angular distances larger than 3°, shows a dominant acoustic peak around 0.55° and several secondary peaks at smaller angles [38].

- Given the prescriptions of the Virial theorem is observed a too high velocity dispersion of the luminous matter (stars) at the edge of the galaxies. This is accounted for an invisible matter named Dark Matter (DM) dominating in mass the luminous matter said baryonic [6].

- Supernovae of type Ia (SNe Ia) are dimmer and therefore farther away than estimated from their redshift recession velocity and luminosity distance [7,8]. It is in the specific Universe of the ΛCDM model which prescribes spatial homogeneity and isotropy at large scale that this could be interpreted as the effect of an accelerated expansion occuring since ∼5Gyr. A Dark Energy (DE) with equation of state $\omega=\frac{p}{\rho c^2} < -1/3$ is in this case phenomenologically considered as being the cause of this acceleration. In 2005, Triay discusses the issue of the Cosmological Constant Problem. In [9], Triay argues that the vacuum energy density $\rho_{\rm vac}$ of quantum fluctuations is expected to amount to ($2\ 10^{-4} \leq \rho_{\rm vac} \leq 2\ 10^{89}$) g cm^{-3} however, in comparison, the Dark Energy density

$$\rho_{\rm DE} = \frac{\Lambda c^2}{8\pi G} \ , \tag{7}$$

measured in cosmological observations in comoving units amounts only to $\rho_{\rm DE}$ $\sim 10^{-29}$ g cm^{-3}. As a consequence, Dark Energy cannot be attributed to the vacuum energy of quantum fluctuations.

Apart from the cosmological principle I discussed before, I explain now under which conditions and under which other fundamental principles these cosmological observations

are made. The conditions and principles are part of the model would it be the ΛCDM model or other challenging models.

- In absence of any reference point and energy source around even at the remotest distances, Mach's principle assumes that an observer cannot determine if he is at rest or in motion or in rotation on himself, given that a non vanishing inertial frame is needed to feel the inertial forces. Many different observers live each in a non zero inertial frame made up of all the surrounding Universe energy and matter and make experiments, observations and measurements [39]. In [51] Einstein summarizes what will be named the Mach's principle, stating "there can be no inertia relatively to space but only inertia of masses relatively to one another".

- The Copernican principle is assumed, meaning that there is no privileged location in the Universe. Wherever the observer sits, he or she observes on average the same objects and properties whatever the direction of observation. Remark: except for the case of the CMB the Copernican principle cannot be verified given the requirement to extend the set of experiments and observations in as many as possible different remote locations in the Universe. This requirement has still not been fulfilled, though observations from Earth may help to decide to what degree the Copernican principle is valid [40]. From our Earth-centered vantage point, it is made far easier to verify the spatial isotropy of the large scale structures (LSS) of the Universe rather than their homogeneity.

  Although the following assertions: "isotropy implies space homogeneity if the Copernican principle is valid", "Spatial isotropy everywhere ≡ spatial homogeneity" and "high isotropy of the CMB plus Copernican principle prove the homogeneity of the Universe", are not true in general and are very interesting to open the discussion (see e.g. [41]). I am illustrating with the example of the Bianchi universe models which spatially are prescribed as being homogeneous but anisotropic and the example explored in the chapter 4, the flat 3−torus topology which spatially is globally homogeneous but is not globally isotropic.

  The Cosmic Microwave Background observed in the spacetime of the ΛCDM model universe seems to be highly isotropic and homogeneous at all spatial scales, this illustrates the period when the Universe would verify the Copernican principle. Since the subsequent LSS formation, the distribution of matter in the Universe is observed from Earth across the ΛCDM spacetime ($ST\Lambda$) to be much less isotropic at small spatial scale.

- The equivalence principle in its weak acception stipulates that inertial mass m_{in} and gravitational mass m_{gr} of a body are identical. More generally in its strong acception, the equivalence principle states that a same physical experiment embedded in two different frames in free fall will produce the same results. Remark: the weak equivalence principle (denoted EP) is quantified with the Eötvös parameter which allows many experiments to confirm the weak EP at higher and higher precision. The strong EP edicting that a physical experiment, involving negligible masses in free fall, is subjected to no gravitational field [42].

- The principle of Special Relativity (denoted SR) is based upon 1) the strong EP, i.e. physical laws are invariant with respect to the inertial frames, and 2) in a given medium c the speed of light is invariant. Specifically, c is the same whatever the velocity of the source or of the observer until the light experiences a change of medium in its propagation [43].

- General Relativity (denoted GR) is a geometric and tensor theory of gravity extending the Special relativistic resolution of the physical problems in curved spacetimes with a source of gravitational field represented by a stress-energy-momentum tensor $\boldsymbol{T}_{\mu\nu}$ as input to the Einstein Field Equation (the Einstein Field Equation denoted thereafter EFE): a 10 nonlinear partial differential equations system. The solution to EFE are the components of the metric tensor $\boldsymbol{g}_{\mu\nu}$ [44]. Remarks: the exact solution of EFE is extremely difficult to derive and is made far easier using simplifying physical hypotheses e.g. assuming properties of symmetry of the metric. Also, by definition, the solutions to partial differential equations are local. Thus a fundamental question is to know if the global solution of EFE in an extended spacetime neighborhood can be treated at a relevant spatial scale by e.g. scalar averaging on the volume element of the metric.

3.1.1 The Einstein Field Equation

The Einstein Field Equation of General Relativity relying on the principles seen above and on the covariance principle of the tensor formalism of physical laws is the tensor equation

$$\boldsymbol{G}_{\mu\nu} + \Lambda \boldsymbol{g}_{\mu\nu} = \frac{8\pi G}{c^4} \boldsymbol{T}_{\mu\nu} \, , \tag{8}$$

where the Einstein tensor representing the term of spacetime curvature reads

$$\boldsymbol{G}_{\mu\nu} = \boldsymbol{R}_{\mu\nu} - \frac{1}{2} R \boldsymbol{g}_{\mu\nu} \, . \tag{9}$$

$\boldsymbol{R}_{\mu\nu}$ is the Ricci tensor and R the Ricci scalar curvature (i.e. the Riemann tensor contracted to its trace part) and $\boldsymbol{g}_{\mu\nu}$ is the metric tensor. Notice that the Weyl tensor, the trace-free part of the Riemann tensor, does not enter EFE. $\Lambda \boldsymbol{g}_{\mu\nu}$ is the cosmological constant tensor, it accounts for an amount of positive or negative energy due to the Dark Energy in addition of the stress-energy-momentum tensor $\boldsymbol{T}_{\mu\nu}$ which describes the content in energy of the Universe. $\boldsymbol{T}_{\mu\nu}$ satisfies the fundamental principle of conservation

$$\boldsymbol{\nabla}_{\mu} \boldsymbol{T}^{\mu\nu} = 0 \, . \tag{10}$$

In the case of the DE inferred from the SNeIa light curve measurements, DE plays the role of a positive cosmological constant Λ corresponding to a repulsive force counteracting the attractive gravity. An expanding Universe with cosmological constant Λ is described by the partial differential equation

$$\boldsymbol{G}_{\mu\nu} = \frac{8\pi G}{c^4} (\boldsymbol{T}_{\mu\nu} - \rho_{\mathrm{DE}} \boldsymbol{g}_{\mu\nu}), \tag{11}$$

$\boldsymbol{T}_{\mu\nu} - \rho_{DE} \boldsymbol{g}_{\mu\nu}$ accounting for all the matter and energy content in the Universe with $\rho_{\mathrm{DE}} = \frac{\Lambda c^2}{8\pi G}$ of equation of state $\omega_{\mathrm{DE}} = \frac{p_{\mathrm{DE}}}{\rho_{\mathrm{DE}}\, c^2} = -1$. Dark Energy is also termed vacuum energy.

EFE is decomposed into 16 coupled equations (although the tensors in EFE are evaluated point wise in tangent spaces, the physical setup can be illustrated by considering the changes of geometry between the 4 spacetime coordinates $x^i = (x^0, x^1, x^2, x^3)$ of a point coupled to the 4 spacetime coordinates' $x^{i'} = (x^{0'}, x^{1'}, x^{2'}, x^{3'})$ of a neighboring point) but the Einstein tensor $\boldsymbol{G}_{\mu\nu}$ is symmetric implying that among the 16 possible pairs between x^i and $x^{i'}$ the couples $(x^\mu, x^{\nu'}) = (x^\nu, x^{\mu'})$ so that EFE should be reduced to 10 independent differential equations. Furthermore the four Bianchi identities that couple together the curvature in each of the 2 points allow to limit EFE to 6 independent equations (see also further discussions on the Cauchy problem and EFE in section 3.2.4). The drawback of EFE system of these 6 differential equations is that it is not linear, meaning that the superposition principle doesn't hold. The sum of two different solutions to EFE is not solution of EFE in general. Actually, because of this non linearity and for other technical reasons the resolution of EFE system of differential equations is made overwhelmingly difficult.

3.1.2 The FLRW solution to the Einstein Field Equation

The assumption that the Universe is spatially homogeneous and isotropic at large scales, implies interesting simplifications when using the symmetry properties of the metric (the symmetries appear in the matrix form of the metric which behaves like a symmetric and second-rank tensor) to get exact solutions to the Einstein Field Equation. These exact solutions are the Friedmann-Lemaître-Robertson and Walker (abridged FLRW) metrics of an expanding, homogeneous and isotropic Universe. Such metrics invariant under spatial translations (homogeneity) and invariant under spatial rotations (isotropy) take the general form

$$\mathrm{d}s^2 := -dt^2 + a^2(t)\left[\mathrm{d}\varsigma^2 + S^2(\varsigma, k)(\mathrm{d}\theta^2 + \sin^2\theta \mathrm{d}\phi^2)\right] , \tag{12}$$

in spherical coordinates $(\varsigma, \theta, \phi)$ where ς is the dimensionfull comoving radial distance defined in equation (5). If $K(t)$ is the time-dependent curvature, the curvature scalar of the three-dimensional surfaces is $k = K(t)a^2(t)$. The three FLRW metrics are defined according to the parameter $S(\varsigma, k)$ as follows

$$S(\varsigma, k) := \begin{cases} k^{-1/2}\sin(\sqrt{k}\,\varsigma), & \text{if } k > 0 \quad \text{, spherical topological manifolds} \\ \varsigma, & \text{if } k = 0 \quad \text{, flat topological manifolds} \\ |k|^{-1/2}\sinh(\sqrt{|k|}\,\varsigma), & \text{if } k < 0 \quad \text{, hyperbolic topological manifolds} \end{cases} \tag{13}$$

These FLRW metrics are conformally flat (i.e. the angles are conserved by a flat space mapping over infinitesimal areas). On the 2-sphere $\mathcal{S}^2$ of radius R the curvature is $K \equiv 1/R^2$ and for manifolds of spatially constant curvature $K = K(t)$ Carroll and Ostlie (see [45]) propose the formula

$$K = \frac{3}{\pi}\lim_{R_{\text{equ}}\to 0}\frac{2\pi R_{\text{equ}} - C_{\text{meas.}}}{R_{\text{equ}}^3} , \tag{14}$$

where $C_{\text{meas.}}$ is the measured boundary length of a closed curve used to make a diagnostic of the given manifold. R_{equ} is the radius of the equivalent circle having circumference $C_{\text{meas.}}$. The infinitesimal distance element $\mathrm{d}s$ of any metric provides only a local description of the spacetime geometry. Thus, each of the three FLRW metrics is compatible with different global topologies of constant curvature:

met(+1)– The FLRW metric with $S(\varsigma, k>0) = k^{-1/2}\,\sin(\sqrt{k}\,\varsigma)$ belongs to the topological set of homogeneous spherical spaces (of constant and non vanishing positive curvature) which are all finite and in infinite number (classified by [46, 47], and see also [48]). The simply connected sphere $\mathcal{S}^3$ is one of this spherical solutions.

met(+0)– The FLRW metric with $S(\varsigma, k=0) = \varsigma$ belongs to the topological set of the 18 homogeneous flat spaces (of vanishing curvature), some are finite (e.g. the multiply connected 3-torus $\mathcal{T}^3$), some are non-orientable, but of which for instance the Euclidean 3−space $\mathbb{E}^3$ is spatially infinite (see the chapter on Cosmic Topology in 3.2.2).

met(−1)– The FLRW metric with $S(\varsigma, k<0) = |k|^{-1/2}\,\sinh(\sqrt{|k|}\,\varsigma)$ belongs to the topological set of the homogeneous hyperbolical spaces (of constant and non vanishing negative curvature) which are in infinite number and are not yet exhaustively classified. Certain of such hyperbolical spaces are compact e.g. the simply connected Picard horn of finite volume and infinite length along its axis of symmetry.

In an expanding and spatially isotropic Universe the Hubble-Lemaître expansion is isotropic.

The physical distance between light emitter and receiver (the receiver is conventionally at the origin of the coordinate system) is defined here with the radial part of the FLRW distance element

$$r(\varsigma) = a(t)\int_0^{\varsigma} \frac{dS}{\sqrt{1-kS^2}}. \tag{15}$$

The physical distance being r and the comoving distance ς. In the case of a flat FLRW space ($k=0$) the integral (15) yields the result seen above in equation (5)

$$r = a(t)\varsigma\ . \tag{16}$$

For $k>0$ (spherical spaces) the integration gives

$$r = \frac{a(t)}{\sqrt{k}}\,\arcsin\left(S\sqrt{k}\right)\ , \tag{17}$$

while one has for the hyperbolic spaces ($k<0$)

$$r = \frac{a(t)}{\sqrt{|k|}}\,\mathrm{arcsinh}\left(S\sqrt{|k|}\right)\ . \tag{18}$$

The quantities involved in (15) are not directly reachable while the redshift of most of the cosmological light sources can be obtained knowing their chemical composition since the fiducial emission lines of elements at rest are measured with high precision on Earth. The Doppler shift of the emission lines $\Delta\lambda = \lambda_{\rm rec} - \lambda_{\rm emi}$ satisfying $z = \Delta\lambda/\lambda_{\rm rec}$. The scale factor and the redshift at two different periods of proper time t an t' satisfy the ratio

$$\frac{a(t)}{a(t')} = \frac{1+z'}{1+z}\ , \tag{19}$$

and for $t' = t_0$=today we have $a(t') = a_0 = 1$, $z' = z_0 = 0$ and $a(t) = \frac{1}{1+z}$. The four-velocity vector of a distant object can be parallel transported to the receiver and then

there exists a physically meaningful Minkowski spacetime velocity v between object and receiver four-velocities in the same tangent spacetime. v and redshift z are related by

$$1+z=\sqrt{\frac{1+v/c}{1-v/c}}. \tag{20}$$

A relation between redshift z and proper distance r is proposed in [45] for redshifts $z<2$ (error on $r<5\%$)

$$r=\left[\frac{(z+1)^2-1}{(z+1)^2+1}\right]\frac{c}{H_0}\ , \tag{21}$$

with $c=299\ 792.458$ km s^{-1} (c the speed of light in vacuum, the Planck constant and the electron charge are the fundamental physical constants considered as exact i.e. with a zero uncertainty [49]), the Hubble constant today (see 2019 results by [50]) $H_0=67.44\pm0.58$ km s^{-1} Mpc^{-1} giving the proper distance r in Mpc.

3.1.3 The Friedmann equations

GEOMETRY and kinematics of an expanding, isotropic and homogeneous Universe are governed by a FLRW metric. The remaining unknowns of the FLRW metric, the scale factor a(t) and its evolution are obtained by solving EFE. The CP is inherent with stringent simplifications and imposes to the stress-energy tensor the most general form of a multicomponent ideal fluid source entirely described by the total energy density [13] ρ (assuming linear superposition of all the energy densities ρ_i and $\rho_{\rm DE}$ due to Dark Matter, radiation, ..., and Dark Energy) and the pressure p (assuming linear superposition of all the pressures p_i and $p_{\rm DE}$ due to DM, radiation, ..., and DE). If in addition is assumed that ρ and p share a same velocity field and depend on the time only we get a single fluid described by

$$\boldsymbol{T}_{\mu\nu}=(\rho c^2+p)\boldsymbol{u}_\mu\boldsymbol{u}_\nu+p\boldsymbol{g}_{\mu\nu}\ , \tag{22}$$

with $\boldsymbol{u}^\mu$ the fluid four-velocity field. The resolution of EFE for this fluid gives the two Friedmann equations as a function of $a(t)$ and the energy density $\rho=\rho_{\rm DE}+\sum_i\rho_i$ and pressure $p=p_{\rm DE}+\sum_i p_i$

$$\left(\frac{\dot a}{a}\right)^2:=H^2=\frac{8\pi G}{3}(\rho_{\rm DE}+\sum_i\rho_i)-\frac{Kc^2}{a^2}\ , \tag{23}$$

$$\frac{\ddot a}{a}:=-\frac{4\pi G}{3c^2}\left[(\rho_{\rm DE}+\sum_i\rho_i)c^2+3(p_{\rm DE}+\sum_i p_i)\right]\ . \tag{24}$$

The equation of state, needed to close the system, is for instance a single-valued function $p=f(\rho)$, e.g. $p=0$ for pressureless models or barotropic equations of state with $p=\omega\rho$ or $p=\rho/3$ (for purely radiative models).

One has a source being reduced to an ideal single fluid characterized by 3 quantities, $a(t)$, the density ρ, the pressure p and 4 constraints which are the 2 Friedmann equations, the continuity equation $(\dot\rho+3\frac{\dot a}{a}(\rho+p/c^2)=0$ calculated with $\boldsymbol{T}^{0\nu}_{\ ;\nu})$ and the equation of

[13] I shall use the same unique notation ρ for the restmass density of matter and the energy density (or specific internal energy density often denoted by ϵ/c^2 in GR, see e.g. Ellis in [41] p93 or Einstein in [51] the footnote p143).

state (relating ρ to p). However, the continuity equation is contained in the 2 Friedmann equations. This reduces the number of constraints to 3 meaning that the two Friedmann equations are redundant. The second Friedmann equation can be obtained from the time derivative of the first imposing energy conservation, i.e. $\dot{\rho} + 3H(\rho + p/c^2) = 0$.

Equation (23) fixes the constraints on the energy and equation (24) which depends only on the global equation of state of all the fluid components can be derived also in the FLRW conditions without pressure (equation of state $p = 0$) from the Raychaudhuri's equation [52].

3.2 ...toward an inhomogeneous universe model

The evidence is presented in my introductory section 3.1 that the transition to large scale homogeneity is statistically satisfied at increasing spatial scales. The homogeneity scale starts from $70h^{-1}$Mpc (2-pcf of galaxy distributions). Recent works of analysis, for instance of the SDSS-IV DR16 quasar survey (see [53]) report an homogeneity scale $\sim 90h^{-1}$Mpc at redshift z=2.30 and $\sim 71h^{-1}$Mpc at redshift z=2.85 using the scaled count-in-spheres ansatz. The homogeneity scale is evaluated up to $700h^{-1}$Mpc (Minkowski Functionals of luminous red galaxies).

Our Universe does not look very isotropic and homogeneous. Observations and measurements suggest that the smaller the spatial scale the larger the inhomogeneity. It is likely that this property also holds for other locations in the Universe, and not just our Earth-centred vantage point. Even if the Universe satisfies the CP at increasingly large spatial scales, a difficulty arises from the fact that EFE are only directly tested on the scales of few body systems such as stellar systems and black holes. These represent small spatial scales by cosmological standards. The conditions of ideal fluid (idealized in subsection 3.1.3) allowing to calculate the stress-energy tensor are not fullfiled at the small spatial scales of the Universe. The consequence is that the Friedmann equations may be not representative of the physical reality. Applying an homogeneous and isotropic FLRW metric to small cosmological scales from the interpretation of observations and measurements made at large scales is not appropriate. However, despite this tension, which I shall name "scale incompatibility" between GR and transition scale to homogeneity, one may wonder how is the FLRW model comparable to a more realistic universe model? Ellis and Stoeger discussed in [54] "the best way to fit" the idealised FLRW model to a model more representative of the "lumpy" Universe not FLRW in its time-evolution. In "What is dust?" (see [55]) Wiltshire studies "The fitting problem: On what scale are Einstein's equations valid?". He developes the concept of the "timescape" scenario, a step toward the possibility of applying GR beyond the local scales, as I shall discuss in the next subsection.

3.2.1 Relativistic geometrisation of gravity at large scale

The resolution of EFE provides a local description of the spacetime since the infinitesimal distance element of the metric determines exactly the local scalar

curvature k. This local characterisation could be extended to arbitrarily large regions in a Universe which is ideally homogeneous and isotropic everywhere, since the metric is in this case spatially invariant. In a more realistic description of the Universe showing drifts from the CP (medium to large scale inhomogeneity) the fluid and $\boldsymbol{T}_{\mu\nu}$ should be reevaluated locally to allow to solve EFE in a few places. In the most stringent case one would aim at describing the real observed Universe over all its spatial inhomogeneities at sharp resolution. In such a case the resolution of EFE should be made in a countless number of places. The other way around is to average spatially over the distinct sources. The question being, can one work out a "macroscopic" theory of the General Relativity (see e.g. [56])? For an inhomogeneous Universe there are two competing solutions, i.e. respectively to make a "temporal evolution of spatial averages" (operator denoted AE) or to make an "average of evolved spatial metrics" (operator EA) [57, 58]. For pressureless fluids ($p \equiv 0$) [14], in the first case $\boldsymbol{T}_{\mu\nu}$ can be determined at proper time t from the spatially weighted averaging of the scalar variables like the densities ρ_i, the expansion rate or the scalar curvature (for regions of size below the transition scale to large-scale homogeneity L_Υ i.e. estimated to be 70 to 100Mpc wide according to the evaluations made using the 2-pcf) and EFE is solved once to give the evolution. In the second case $\boldsymbol{T}^{(i)}_{\mu\nu}$ obtained from the ρ_i's and the velocities $\boldsymbol{v}_i$ serves to solve EFE in each point indexed i within the selected spatial region (reg) to calculate the local metrics which are averaged into one metric. In general, because of the non-linearity of EFE, in an inhomogeneous Universe the two operators AE and EA do not commute as illustrated by the two cases below

$$\frac{d}{dt}\langle\zeta\rangle_{\rm reg} - \left\langle\frac{d}{dt}\zeta\right\rangle_{\rm reg} = \left\langle\zeta^2\right\rangle_{\rm reg} - \langle\zeta\rangle^2_{\rm reg} \neq 0 \ , \tag{25}$$

with the scalar function ζ (see [57]), or given that

$$\left\langle\left(\boldsymbol{R}_{\mu\nu} - \frac{1}{2}R\boldsymbol{g}_{\mu\nu}\right)[\boldsymbol{g}_{\mu'\nu'}]\right\rangle \neq \left(\langle\boldsymbol{R}_{\mu\nu}\rangle - \frac{1}{2}\left\langle R\boldsymbol{g}_{\mu\nu}\right\rangle\right)[\left\langle\boldsymbol{g}_{\mu'\nu'}\right\rangle] \ , \tag{26}$$

where $< . >$ stands for an operator of spatial averaging suitably defined. This equation illustrates that the average Einstein tensor differs, in general, from the Einstein tensor constructed from the average of the metric. What comes out, is that applied over a spatially inhomogeneous region the "averaging does modify Einstein's equations by an effective energy term" [59]. The difference between the two operators AE and EA is called "backreaction" of the inhomogeneities (see [60], [61] and [62]) appearing as an additional source term in EFE and the Friedmann's equations.

But of course, energy density gradients and pressure gradients cannot be smoothed and averaged too much without erasing or changing the micro-geometry and micro-local evolution of the Universe, since for the classical matter, the motion of inertial mass density of matter follows the gradients of pressure, moving in their direction if the inertial mass density of matter is positive. The *weak energy condition*, if $\rho \geq 0$, is obtained with

$$\rho + p/c^2 > 0 \ . \tag{27}$$

While if the gravitational mass density is positive, one has the strong energy condition (see e.g. [41]) verified if both the weak energy condition and

$$\rho + 3p/c^2 > 0 \ , \tag{28}$$

are true. $\rho + 3p/c^2$ is also named active gravitational mass density. Even if these energy conditions are valid locally, it is possible that a scalar spatial averaging might

[14] The pressureless matter is also termed "dust" in cosmology (see the discussion in [55]).

yield a negative effective energy density, showing that on average we do not have energy conditions as the local ones.

In a CDM model (without DE source) expanding, perturbatively inhomogeneous and anisotropic, the "macroscopic" Friedmann evolution equations closed with an equation of state $p = 0$ (for ideal pressureless fluids) are derived according to the Buchert scheme (see [63]). The following procedure is extended now over a non infinitesimal spatial domain $\mathcal{D}$ of volume $V_{\mathcal{D}}$, in general non spherical and of arbitrarily complex shape in an inhomogeneous Universe, so that the cosmological variables corresponding to the local EFE are now spatially averaged variables over the comoving domain $\mathcal{D}$. The scale factor $a(t)$ becomes the volume scale factor $a_{\mathcal{D}}(\mathrm{t})$ during the time of expansion between the moments t_{ini} and t

$$a_{\mathcal{D}}(t) := \left(\frac{V_{\mathcal{D}}(t)}{V_{\mathcal{D}_{\mathrm{ini}}}}\right)^{1/3} \quad , \tag{29}$$

and the averaged Ricci scalar curvature is $\langle R\rangle_{\mathcal{D}}$. The Friedmann equations over the non homogeneous and non isotropic domain $\mathcal{D}$ become on average on the volume $V_{\mathcal{D}}$

$$\left(\frac{\dot{a}_{\mathcal{D}}}{a_{\mathcal{D}}}\right)^2 := H_{\mathcal{D}}^2 = \frac{8\pi G}{3}\langle\rho\rangle_{\mathcal{D}} - \frac{(\langle R\rangle_{\mathcal{D}} + \mathcal{Q}_{\mathcal{D}})c^2}{6} \quad , \tag{30}$$

$$\frac{\ddot{a}_{\mathcal{D}}}{a_{\mathcal{D}}} = -\frac{4\pi G}{3}\langle\rho\rangle_{\mathcal{D}} + \frac{\mathcal{Q}_{\mathcal{D}}}{3} \quad , \tag{31}$$

where $\langle\rho\rangle_{\mathcal{D}}$ is the average of the densities $\sum_i \rho_i$ (which are scalars quantities as in equations (23) and (24)) obtained by the covariant mean values

$$\langle\rho_i\rangle_{\mathcal{D}} = \frac{1}{V_{\mathcal{D}}}\int_{\mathcal{D}} \rho_i \, dV \quad . \tag{32}$$

$\mathcal{Q}_{\mathcal{D}}$ is the *kinematical backreaction* term which arises in equations (30) and (31) when the domain $\mathcal{D}$ does not satisfy the principle of homogeneity and isotropy, i.e. in the domain $\mathcal{D}$, local expansion called θ may differ from average expansion $\langle\theta\rangle_{\mathcal{D}}$ and a shear (σ which preserves the volume but not the distance) effect may appear. The vorticity term ω doesn't enter this *kinematical backreaction* since dust is assumed to be irrotational in this averaging scheme, and therefore one has

$$\mathcal{Q}_{\mathcal{D}} := \frac{2}{3}\left\langle(\theta - \langle\theta\rangle_{\mathcal{D}})^2\right\rangle_{\mathcal{D}} - 2\left\langle\sigma^2\right\rangle_{\mathcal{D}} \quad . \tag{33}$$

In the case of an ideal pressureless fluid with four-velocity field corresponding to a homogeneous and isotropic Hubble flow field, [58] demonstrated that under periodic boundary conditions of the three space sections of an inhomogeneous Universe Newtonian and of Euclidean metric, the backreaction term cancels out for an averaging made over the whole volume. The spacetime $\mathcal{S}$ considered is toroidal based on the 3−torus (which is flat i.e. of intrinsic curvature equal to zero), $\mathcal{S} = \mathcal{T}^3 x\mathbb{R}$. [58] proves that a unique kind of homogeneous and isotropic Hubble flow exists for a 3-torus which expands then self-similarly without rotation. The absence of backreaction doesn't depend on the proportions or volume of the closed topological manifold (compact and without boundaries). Notice that most of the numerical simulations in cosmology and astrophysics run within a virtual space, of Euclidean geometry, staked out by a parallelepiped rectangle volume imposing practically the same periodic boundary conditions (PBC) mentioned above to

data and physics. Such $N-$body simulations with homogeneous distribution of points are globally anisotropic because of the breaking of rotational SO(3) symmetry due to the PBC of the virtual parallelepiped rectangle volume where the physical model is simulated. $N-$body general relativistic simulations of inhomogeneous distribution of points with PBC and their analyses in the frame of GR are made by [64,65]. Besides [66] proposes a $N-$body method numerically simulating an expanding and infinite Universe with Newtonian gravity and without such PBC while the periodic effects due to PBC on the Newtonian gravity have been tested in $N-$body simulations of a patch of the ΛCDM Universe in [67].

3.2.2 A brief introduction to Cosmic topology...

It was in 1995 that Lachièze-Rey and Luminet applied the term Cosmic Topology (thereafter CT) to the science studying the "spacetime global structure" (see [68] p138), that is to say the global geometry and topology of the Universe. Lachièze-Rey and Luminet describe spatial topology as unevolving with time within the class of FLRW models, the term topology being generally used to apply to the topology of the spatial sections, not to that of global spacetime. Global geometry and topology (see [68–70]) of the spacetime are not dictated by the resolution of the Einstein Field Equation of General Relativity.

However, global geometry and topology constrain spatial curvature, connectedness and compactness of the Universe. Since GR takes the inputs of EFE from the various gravity sources, at various spatial scales, a knowledge a priori of the spacetime geometry and topology is very important to get, in order to build an initial estimator of $\boldsymbol{T}_{\mu\nu}$ the stress-energy-momentum tensor and an equation of state both representative of the chosen universe model.

In the ΛCDM model of cosmology the global properties of the spacetime are provided beforehand by the FLRW prescriptions of an homogeneous and isotropic in average, expanding and infinite Universe. As presented in 3.1.2 each one of the FLRW metrics is consistent with one of the 3 simply connected topological manifolds (SCM) of constant curvature which are either $\mathcal{M} = \mathbb{R}^3$ the Euclidean manifold of vanishing curvature, or the spherical one $\mathcal{M} = \mathcal{S}^3$ with $k > 0$ or the hyperbolic one $\mathcal{M} = \mathbb{H}^3$ with $k < 0$. The spacetime, endowed with a unidimensional time, being the $4-$manifold $\mathcal{M} \times \mathbb{R}$. But many other types of topologies exist, thus multiply connected topologies (MCT) are possible candidates for interesting simulations of universe models which for some of them bring interesting similarities with the observations (see the similarity of the 2-point correlation functions of the CMB temperature anisotropies for the Planck map compared to the $3-$torus CMB model maps in chapter 4).

A Universe with multiply connected spatial sections is based on a multiply connected manifold (MCM), quotient space $\mathcal{M}/\Gamma$ of a simply connected space by Γ. Γ belongs to the group of isometries, or holonomy group (see e.g. the work of Thurston in [71–73]). The $3-$torus $\mathcal{T}^3$ (also said hypertorus) is a flat MCM, finite and without boundaries. $\mathcal{T}^3 = \mathbb{R}^3/\Gamma_{cg}$, where Γ_{cg} is one of the three-dimensional symmetry groups said crystallographic groups (see Steiner in [74]). A $3-$torus is compact, defined by a fundamental domain represented by a polyhedron, parallelepiped rectangle (the hexahedron, made of 12 edges, 8 vertices and 6 faces), regular in the case of the cubic $3-$torus. The identification of

the opposite faces is the generator of the holonomy group of $\mathcal{T}^3$. The displacements allowing the identification of homologous points are isometries. The 3−torus (E_1) is one of the 10 three-dimensional flat manifolds, orientable since its holonomy group preserves an orientation curve (e.g. materializing a rotation sense in the plane of a face) after identification of opposite faces. The classification of flat 3−manifolds [75–77] counts 18 manifolds going from E_1 the 3−torus, to the only simply connected manifold E_{18}, the Euclidean space $\mathbb{E}^3$. The manifold orientability is best defined by counter-examples such as the Klein space (E_7) which contains an orientation-reversing curve (in analogy with the Möbius band, its flip impose a reversal to an orientation curve) is therefore a nonorientable flat 3−manifold. The half-turn space (E_2) is obtained from a 3−torus where a plane rotation of $\pi/2$ is made after identification of the opposite faces, this preserves the orientation. This is why E_2 which doesn't contain an orientation-reversing curve is an orientable flat 3−manifold.

The tesselation (term covering the concepts of tiling or paving) corresponds to the juxtaposition of an infinite numbers of copies of the fundamental hexahedron which tiles $\mathbb{E}^3$. The universal covering space $\mathbb{E}^3$ of the 3−torus practically corresponds to an observational space. Any point in the covering space of $\mathcal{T}^3$ can be localized in a right-handed trihedron by its rectangular cartesian coordinates defining a 3−vector $\vec{x}$ of coordinates x_i, for i running on (1,2,3). Even if the 3−torus has no boundaries, the periodicities due to the symmetry group yield periodic boundary conditions. The 3−torus is intrinsically flat, locally and globally homogeneous, locally isotropic but is globally anisotropic since the global periodic identifications of the group Γ_{cg} break the rotational symmetries of the group $SO(3)$. $\mathcal{T}^3$ is characterized by an infinite number of discrete eigenmodes specific of the 3 finite side lengths L_1, L_2, L_3. In comparison, E_{16} the slab space with one compact direction and the 2 other infinite is characterized by a discrete spectrum of eigenmodes along its finite direction and a continuum along the 2 other directions. A discussion about the 17 flat multiply connected 3−manifolds, quotient spaces of the Euclidean space $\mathbb{E}^3$ by Γ_i, $E_i = \mathbb{E}^3/\Gamma_i$, for i=1,17, is made in [78] in relation with the numerical simulations in cosmology.

3.2.3 ...and an Historical Overview of Topology

The historical overview I present here, on topology, integral geometry, and Cosmic Topology, is intended to complete the specific bibliographies made in the 2 team articles presented in this Manuscript (see these peer reviewed articles [79] and [34]).

It was from 1895 that Henri Poincaré condensed his preliminary investigations in a series of articles entitled "Analysis Situs" (the Latin term for topology). In these articles Poincaré established topology as a field of mathematics, pioneering the algebraic topology, introducing the concepts of homology, and for instance, the Kronecker integral and the Kronecker index (see [80]). Many earlier mathematical works such as by Euler (∼1735, solution to the Königsberg bridge problem and the fundamental formula of convex polyhedra), Listing (1847, concept of connectivity and the first use of the word topology in a scientific publication), Riemann (connectivity of Riemann surfaces, 1851), Möbius (1865, publication of the work on the Möbius band and the non-orientability), and Klein (1872, the Erlangen program; 1921, fundamental group of a topological space, classification of geometries [81]), contributed to the construction of the theories of Integral Geometry and

of Topology in their current definitions. The mathematical definition of the 2−torus $\mathcal{T}^2$, embedded in $\mathbb{E}^3$, was explicitly given in French by the engineer Armengaud (1848) in the book [82] translated in English (1851) by Johnson [83].

I arrive then to the topology of spacetime, as in 1949 Infeld predicted the infrared cut-off as signature of a finite Universe with 3−torus topology [84]. In "Topology and Cosmology" [85], 1971, Ellis asked the question whether the Universe had compact spatial sections. Since this hypothesis was compatible with each of the three Friedmann solutions, $k = -1$, $k = 0$ or $k = +1$. In 1984, Zel'dovich considered the dynamical evolution of a locally open region in a closed inhomogeneous Tolman's Universe [86] without pressure.

The first predictions of detectability of a non trivial topology of the Universe on the cosmic microwave background, such as the hypertorus $\mathcal{T}^3$, were developed, investigated and confirmed in 1993 by [87,88]. In 1994 Jing et al. detected an infrared cutoff in the two-point correlation function of the CMB temperature anisotropies observed by COBE [89]. Jing et al. concluded to a possible finiteness of our Universe having the topology of a 3−torus. It was one hundred years after the Poincaré's "Analysis Situs" that "Cosmic Topology", the Physics Report published in 1995 by Lachièze-Rey and Luminet, specified the definition of Cosmic Topology as being the field of study of the spacetime global structure [68].

Starting in 1995 were made the pioneering works of de Oliveira and Smoot [90, 91] (CMB constraints on CT), Lehoucq [92] (applying methods of crystallography to detect a non-trivial CT in LSS) and Cornish [93] (predicting that pairs of circles of correlated radiation would be observable on the CMB as signature of a Universe with multiply connected topology). Several investigations were made by Roukema et al. in observational and numerical CT. His studies aimed at "determining the topology of the observable Universe via" different strategies of analysis of the matter distribution at large scale. In a Universe having a MCT such as the 3−toroidal one, multiple images of a same astrophysical object could be observed in different directions of the sky (ghost images). "A cosmic hall of mirrors" [94], although ahead in the chronology (2005), illustrated well the way ghost images of a test object form in a Universe with flat 3−torus topology. The observer would see one direct image and six images by first reflection on each torus face. In 1996 was explored the quasars distribution in the NED catalogue to search for isometries of QSOs quintuplets in comparison with the results of Monte-Carlo 3D simulations [95]. The observation of only two QSOs quintuplets in the data was statistically not sufficient to conclude to a positive detection of the hypertorus topology. Another investigation was made by Roukema in [96] applying a similar strategy to find ghost images of a few highly luminous X-ray clusters of galaxies at predicted sky locations. However, the observed physical properties of the ghost candidates did not support identity with the original X-ray cluster.

In 1998 other general or topology-independent methodologies were considered by Roukema in order to detect or constrain the global topology of our Universe (see [97–100]). Thus, in 2013 I contributed to the paper [101] evaluating the detectability of a $\mathcal{T}^3$ topology in the observational surveys of high-redshift galaxies (7>z>4). The method compared the quadruple statistics,(i) of the observed galaxy catalogue to which was applied the 3−torus holonomy (based on the geometric construction of matched disks) to (ii) a corresponding galaxy catalogue with simply connected topology. Both catalogues constructed in a

spacetime having a flat FLRW metric. However, the statistical validity of the catalogue comparison needed a higher photometric redshift accuracy given the small number of high-redshift galaxies at the time. Therefore, one could not confirm or reject the detectability of the toroidal topology with this method.

To complete the bibliography on Cosmic Topology made in the section 4.1.3 of this Manuscript, reviews of conceptual and observational investigations made in Cosmic Topology can be found for instance in [102] (period going up to year 2000), and in the Planck collaboration paper [17] (2016). In the next section "General Relativity and global topology of the Universe" 3.2.4, I shall present the investigations made by Roukema and others concerning the effects a MCT may have on the gravitational field of a test object. I am closing this historical review of the CT mentioning the many thorough investigations of Ralf Aurich et al. regarding the computing of CMB temperature anisotropies in universe models having different multiply connected topologies. The main works and results of Aurich in CT, starting in 1999, are discussed in the section 4.1.3 presenting the paper I wrote in collaboration with Ralf Aurich, Thomas Buchert and Frank Steiner during my PhD thesis, "The variance of the CMB temperature gradient: a new signature of a multiply connected topology".

3.2.4 General Relativity and global topology of the Universe

For a PDE, the solution which satisfies the initial conditions (initial value problem) and the boundary conditions (boundary value problem) is the general form of the Cauchy problem (see a review of the extremely rich mathematical work of Cauchy in [104] and the original French texts of Cauchy on the website *Gallica*). According to the definition of Hadamard, a ***well-posed*** problem of a mathematical model describing physical phenomena satisfies: 1) one solution exists and 2) this solution is unique [105]. In General Relativity EFE is a system of PDEs reducible to a set of nonlinear hyperbolic partial differential equations for which the local solutions are completely determined by the initial conditions. Existence and uniqueness of an analytic solution to a partial differential equation in a close neighborhood of a spacetime point $x^i = (x^0, x^1, x^2, x^3)$ is guaranteed if the PDE satisfies the conditions of the Cauchy-Kowalevski theorem (C-K theorem). Though C-K theorem applies in arbitrarily large dimension, GR applies in a $4-$manifold, smooth in addition. This C-K theorem requires that all the functions describing the PDE and all the functions describing the initial conditions are analytic in the vicinity of x^i. In the $4-$dimension spacetime of GR, x^0 has the dimension of a time element times c, the speed of light, while the 3 other components are the space elements. Since GR is a causal theory, EFE is solved on a $3-$dimensional hypersurface, the Cauchy surface C_S.

The boundary value problem imposes in addition the resolution of the PDE on a spatial domain $\mathcal{D}$ of C_S delimited by a boundary $\partial\mathcal{D}$. In this case, the value taken by the solution (Dirichlet conditions) and, or the derivatives of the solution (Neumann conditions) on the boundary $\partial\mathcal{D}$ of the domain are imposed. Having in mind the questions: for which kind of boundary the problem of resolution of EFE is well-posed? A smooth, axially or centrally symmetric boundary? And in the contrary, for which kind of boundary EFE yields several distinct solutions (ill-posedness)? With a boundary not smooth, or asymmetrical, or anisotropic? One can refer to e.g. the works of Frittelli on the issue of

boundary in the resolution of EFE and the concept of initial-boundary value problem in numerical GR in [106,107]. Choquet-Bruhat and Ringström [108–110] study, theoretically, the resolution of the Cauchy problem and the issue of existence and uniqueness of a solution to EFE in relation with the topology.

A question which is of interest for both CT and the resolution of the field equations of GR is to study the effect the periodic boundary conditions, for instance inherent to a 3-torus multiply connected topology, have on the resolution of EFE in comparison with a spatially infinite and flat Universe which presents no boundary value problem. Since we already know that EFE doesn't determine the curvature or the topology at large scale, the issue is to know how CT affects the inputs of EFE, the components of the stress-energy-momentum tensor and the equation of state? And as a consequence, how the prescriptions of a non-trivial topology change the results of EFE? Thus, the assumption is made in cosmology that a "topological acceleration" could result from the property of periodicity of a MCM. That is to say that the Einsteinian gravity of an isolated massive object should be modified in a Universe having, for instance, the topology of an hypertorus or a Poincaré dodecahedron. Since in such a Universe, an object could interact with itself, and could interact differently with another object, and this in term of any interaction. In 1989, Farrar and Melott discuss the periodic boundary conditions inherent to the virtual space, finite with boundaries imposed to the numerical simulations made in cosmology. They show that the local physical properties of the model do not depend on the topology [111]. Notably, they probe a very peculiar topology: the non-orientable Klein space (E7). I already pointed out the 1997 work of Buchert and Ehlers in sub-section 3.2.1. They conclude to the cancelation of the globally averaged backreaction [58] in a spacetime of flat toroidal topology and this for inhomogeneous Newtonian universes with Euclidean metric and isotropic expansion.

Roukema et al. published a work studying the Newtonian causal gravity (for which the interaction of gravitation propagates at the speed of light, and not instantaneously as it is inherent to the original Newton's gravity) in a Universe with spatial periodic boundary conditions [112].

Steiner asks in [74], "Do black holes exist in a finite Universe having the topology of a flat 3−torus?". I.e., what is the static gravitational field of a black hole or a star of mass M, at rest, in a flat 3−toroidal Universe? As cited above in 2.1, Schwarzschild calculates the exact solution to EFE for a static, spherically symmetric black hole in an infinite Universe. But, does an approximate solution to EFE exists for this object, in the boundless, finite and homogeneous 3−torus, where, in virtue of $\mathcal{T}^3$ symmetries (quantified above in 3.2.2), the weak and static gravitational field of the black hole should be a triply-periodic function? In absence of availability of an exact solution, Steiner devises an iterative and perturbative approach to get an approximate solution to the full non-linear EFE for a weak gravitational field. The Hadamard condition, seen above, of existence and uniqueness of solutions to EFE, satisfying the $\mathcal{T}^3$ periodic boundary conditions, is guaranteed here by the theorem said Fredholm alternative. Concretely, in the fundamental domain of the 3−torus, the source, i.e. the active gravitational mass density $\rho + 3p/c^2$ of the star has to be a triply-periodic function $S(\vec{x})$ (see definitions in 3.2.2). In virtue of the Fredholm alternative, a non-trivial and unique solution $u_0(\vec{x})$ to the Poisson's equation must be orthogonal to S, i.e. has to satisfy the integrability condition $\langle S, u_0 \rangle = 0$ (the operator $\langle , \rangle$ denotes the inner product). Unfortunately, Steiner arrives

first to a divergent solution for the Newton's gravitational potential and furthermore the integrability condition is not satisfied. However, adopting three regularization methods based (i) on the Appell Zeta function, (ii) on the Epstein Zeta function, and (iii) on the generalized Green's function, Steiner solves the first order Einstein-Poisson equation using these three different ansatzes. Thus, Steiner proves that for a cubic torus, three equivalent, non-trivial, convergent and exact first-order solutions to the Einstein-Poisson equation exist. In view of these results, Steiner conjectures that the gravitational field of a black hole in a Universe with 3−toroidal topology is in the far-field limit [15] well approximated by this 1^{st} order solution. This solution is globally anisotropic and is unique up to an additive constant field.

An illustration of the effects of the global topology on the resolution of the relativistic geometrisation of gravity over large spatial scales by averaging methods is made in [113]. Hypotheses on the topology of the Universe allow to consider solutions to the closure problem of the spatially averaged 3+1 Einstein Field Equations. Thus, Brunswic and Buchert use the Gauss-Bonnet-Chern theorem (GBC). GBC formalises a relationship between the topological Euler characteristic (of 4D spaces) of the Cauchy hypersurface and the extrinsic curvature of its boundary. This method consists in shrinking the 4D tube to 3D to relate GBC to 3D space sections. This ansatz yields a supplementary equation connecting the expansion tensor and the Weyl tensor. However, the resolution of the averaged EFE cannot predict the change of the global topology of the Universe, while the formation of singularities in the spacetime (such as new black holes puncturing the Cauchy hypersurface) could induce dynamical intrinsic changes of topology over time.

3.2.5 A short introduction to the Cosmic Microwave Background

The CMB was discovered in 1965 by Penzias and Wilson [114] in a study of noise backgrounds in a microwave receiver as a nearly isotropic radiation with antenna temperature (3.5±1.0)K at a wave-length of 7.5 cm.[16] But from this they could not conclude that they were observing a black-body spectrum as predicted by the Big-Bang paradigm. It was 25 years later that the satellite COBE (Cosmic Microwave Background Explorer, active life-time 1989-1993) [117] could show with the FIRAS instrument that the CMB data follow an almost perfect Planck spectrum with the present mean value of

[15] In the far-field limit, the distance r to the star with mass M is such that its gravitational field is weak and the star can be treated as a point-like object, having $r_s \ll R < r \ll L$, where $r_s = \frac{2GM}{c^2}$ is the Schwarzschild radius, R is the radius of the star and L is the side length of the cubic 3−torus.

[16] "In between the star ζ Oph (Ophiuchi) and the earth there is a cloud of cold molecular gas, whose absorption of light produces dark lines in the spectrum of the star. In 1941, Adams [115], following a suggestion of McKellar, found two dark lines in the spectrum of ζ Oph that could be identified as due to absorption of light by cyanogen (CN) in the molecular cloud ... From this, McKellar concluded [116] that a fraction of the CN molecules in the cloud were in the first excited rotational component of the vibrational ground state, ... and from this fraction he estimated an equivalent molecular temperature of 2.3 K. Of course, he did not know that the CN molecules were being excited by radiation, much less by black-body radiation. After the discovery by Penzias and Wilson, several astrophysicists independently noted that the old Adams-McKellar result could be explained by radiation with a black-body temperature at wave-length 0.264 cm in the neighborhood of 3 K." (Citation from [31].)

the CMB temperature $T_{\rm CMB}$=(2.735±0.060)K. Nine years later, COBE finally obtained $T_{\rm CMB}$=(2.725±0.002)K [118] (see section 4.2.1 for the present best value). In 1992 , COBE discovered with the DMR instrument the CMB temperature anisotropies [119–121], subsequently measured with more and more precision by the space probe missions WMAP (Wilkinson Microwave Anisotropy Probe, active life-time 2001-2010) [122–125] and Planck (Planck probe active life-time 2009-2013) [126–131].

The observable part of the CMB covers, typically, depending on the frequency, up to 70% of the celestial sphere, and one has to assume what the properties of the remaining invisible CMB are. For this problem there is no model–independent analysis of the CMB—a model is required to infer and build the CMB regions hidden beyond the galaxy mask and beyond each field source out of the main foreground mask. It is interesting to see that some of the CMB anomalies reviewed in [132], such as the cold spot or the hemispherical asymmetry, are very likely independent of the masked CMB reconstruction model. But, most of the various CMB anomalies, even of this magnitude, are consistent with a certain level of Gaussianity (p–value $>$ 99%). Some of these anomalies are detected with the 2–point correlation function; some anomalies could be remedied by a cutoff between 60 and 160° as in [133], statistically favouring multiply connected universe models with finite volume [134, 135]. Besides assumptions on the topology of the Universe, an assumption is needed for the geometry of the CMB support manifold, commonly thought of as being an ideal sphere. This is related to the estimate of the relative motion vector of the observer to the CMB. Will peculiar–velocity analyses of larger and larger catalogues converge to this motion, or is there a global dipole of a non–idealized space form? What is the correct definition of "peculiar–velocities"? There can be significant differential expansion of space that is not allowed for in a Newtonian model of structure formation [136]. Another challenge to the CMB non–Gaussianity is the way to link the specific CMB intensity, $I(\nu)$, to the CMB temperature anisotropy, δT [137], using the Taylor expansion at first order only; higher orders may eventually impair the evaluation of the primordial non–Gaussianity.

References

Bibliography on the observations

[1] Hetherington N S and Balashov Y V 2014 *Amer. J. Phys.***62** 475 Encyclopedia of Cosmology: Historical, Philosophical, and Scientific Foundations of Modern Cosmology ISBN 978-1-317-67766.6

[2] Di Valentino E, Melchiorri A and Silk J 2020 Planck evidence for a closed Universe and a possible crisis for cosmology *Nature Astron.* **4** 196–203 (arXiv:1911.02087)

[3] Di Valentino E, Melchiorri A and Silk J 2021 Investigating Cosmic Discordance *The Astrophys. J.* **908** L9 (arXiv:2003.04935)

[4] Di Valentino E, Mena O, Pan S, Visinelli L, Yang W, Melchiorri A, Mota D F, Riess A G and Silk J 2021 In the realm of the Hubble tension—a review of solutions *Class. Quantum Grav.* **38** 153001 (arXiv:2103.01183)

[5] Martin J, Ringeval C and Vennin V 2014 Encyclopaedia Inflationaris *Elsevier* **5-6** 75–235 (*Preprint* arXiv:1303.3787)

[6] N A Bahcall and A Kulier 2014 Tracing mass and light in the Universe: where is the dark matter? *Mon. Not. Roy. Astr. Soc.* **439** 2505-14 (arXiv:1310.0022)

[7] A G Riess et al. 1998 Observational evidence from supernovae for an accelerating universe and a cosmological constant *Astron. J.* **116** 1009-1038 (arXiv:astro-ph/9805201)

[8] S Perlmutter et al. 1999 Measurement of Ω and Λ from 42 high-redshift supernovae *Astrophys. J.* **517** 565-586 (arXiv:astro-ph/9812133)

[9] R Triay 2005 a Solution to the Cosmological Constant Problem *Int. J. Mod. Phys. D* **14** 1667-73 (arXiv:gr-qc/0510088)

[10] M Giovannini A Primer on the Physics of the Cosmic Microwave Background 2008 *World Scientific Publishing Co.* (https://doi.org/10.1142/6730)

[11] T Padmanabhan and T R Seshadri 1987 Horizon Problem and Inflation *J. Astrophys. Astr.* **8** 275-280

[12] L Jiang et al. 2021 Evidence for GN-z11 as a luminous galaxy at redshift 10.957 *Nat. Astron.* **5** 256-261 (arXiv:2012.06936)

[13] R P Kirshner 2004 Hubble's diagram and cosmic expansion *Proc. Natl. Acad. Sci.* **101** 8-13

[14] M Betoule et al. 2014 Improved cosmological constraints from a joint analysis of the SDSS-II and SNLS supernova samples *Astron. Astrophys.* **568** A22 (arXiv:1401.4064)

[15] A Heinesen 2021 Multipole decomposition of the general luminosity distance "Hubble law" - a new framework for observational cosmology (arXiv:2010.06534)

[16] Ade P A R et al. 2016 Planck 2015 results XVIII. Background geometry and topology of the universe *Astron. Astrophys.* **594** A18(*Preprint* arXiv:1502.01593)

[17] N Aghanim et al. 2020 Planck 2018 results. VI. Cosmological parameters *Astron. Astrophys.* **641** A6 (arXiv:1807.06209)

[18] Scrimgeour M I et al. 2012 The WiggleZ Dark Energy Survey: the transition to large-scale cosmic homogeneity *Mon. Not. Roy. Astr. Soc.* **425** 116-134 (arXiv:1205.6812)

[19] A Heinesen 2020 Cosmological homogeneity scale estimates are dressed *J. Cosmol. Astropart. Phys.* **JCAP12(2020)052** (arXiv:2006.15022)

[20] A Wiegand, T Buchert and M Ostermann 2014 Direct Minkowski Functional analysis of large redshift surveys: a new high-speed code tested on the luminous red galaxy SDSS-DR7 catalogue *Mon. Not. Roy. Astr. Soc.* **443** 241-259 (arXiv:1311.3661)

[21] V de Lapparent, M J Geller and J P Huchra 1986 A SLICE OF THE UNIVERSE *The Astrophys. J.* **302** L1-L5

[22] V de Lapparent and E Slezak 2007 Spatial clustering in the ESO-Sculptor survey: two-point correlation functions by galaxy type at redshifts 0.1-0.5 *Astron. Astrophys.* **472** 29-42 (arXiv:0707.4354)

[23] H Mo, F van den Bosch and S White 2010 Galaxy Formation and Evolution *Cambridge University Press* eISBN 9780511807244
[24] V Rustagi and R Durrer 2019 The Cosmological Consistency Relation in a Universe with Structure *J. Cosmol. Astropart. Phys.* **JCAP12(2019)034** (arXiv:1907.11101)
[25] S Nadathur et al. 2020 The completed SDSS-IV extended Baryon Acoustic Oscillation Spectroscopic Survey: geometry and growth from the anisotropic void-galaxy correlation function in the luminous red galaxy sample *Mon. Not. Roy. Astr. Soc.* **499** 4140-57 (arXiv:2008.06060)
[26] S Alam et al. 2021 Completed SDSS-IV extended Baryon Oscillation Spectroscopic Survey: Cosmological implications from two decades of spectroscopic surveys at the Apache Point Observatory *Phys. Rev. D* **103** 083533 (arXiv:2007.08991)
[27] G V Kraniotis and S B Whitehouse 2003 Compact calculation of the perihelion precession of Mercury in general relativity, the cosmological constant and Jacobi's inversion problem *Class. Quantum Grav.* **20** 4817 (arXiv:astro-ph/0305181)
[28] S Weinberg 1977 The first three minutes. A modern view of the origin of the universe ISBN 0465024351
[29] A M Boesgaard and G Steigman 1985 Big Bang Nucleosynthesis: Theories and Observations *Ann. Rev. Astron. Astrophys.* **23** 319-78
[30] P Peter and J-P Uzan 2005 Cosmologie primordiale ISBN 978-2-7011-7824-0
[31] S Weinberg Cosmology 2008 *Oxford University Press* eISBN 9780198526827
[32] R G Pizzone et al. 2014 Big Bang Nucleosynthesis Revisited via Trojan Horse Method Measurements *Astrophys. J.* **786** 112 (arXiv:1403.4909)
[33] Akrami Y et al. 2020 Planck 2018 results. VII. Isotropy and Statistics of the CMB *Astron. Astrophys.* **641** A7 (arXiv:1906.02552)
[34] Buchert T, France M J and Steiner F 2017 Model–independent analyses of non-Gaussianity in Planck CMB maps using Minkowski functionals *Class. Quantum Grav.* **34** 094002 (arXiv:1701.03347)
[35] A Kogut et al. 2019 CMB Spectral Distortions: Status and Prospects *Bull. Am. Astr. Soc.* **51** 7 (arXiv:1907.13195)
[36] K Konar, K Bose and R K Paul 2021 Revisiting cosmic microwave background radiation using blackbody radiation inversion *Sci. Rep.* **11** 1008
[37] Fixsen D J 2009 The Temperature of the Cosmic Microwave Background *Astrophys. J.* **707** 916-920 (arXiv:0911.1955)
[38] Aghanim N et al. 2020 Planck 2018 results. V. CMB power spectra and likelihoods *Astron. Astrophys.* **641** A5 (arXiv:1907.12875)

Bibliography on the principles

[39] I Szapudi 2021 Constraining Mach's principle with high precision astrometry (arXiv:2105.05337)
[40] D Camarena, V Marra, Z Sakr and C Clarkson 2021 The Copernican principle in light of the latest cosmological data (arXiv:2107.02296)
[41] G F R Ellis, R Maartens and M A H MacCallum 2012 Relativistic Cosmology *Cambridge University Press* ISBN-13 9780521381154
[42] A Kapustin and M Touraev 2021 Non-relativistic geometry and the equivalence principle *Class. Quantum Grav.* **38** 135003 (arXiv:2101.04153)
[43] G Koekoek, J W van Holten and U Wyder 2021 The path to Special Relativity (arXiv:2109.11925)
[44] I R Kenyon 1990 General Relativity *Oxford Science Publications* ISBN 0198519966

Bibliography on the FLRW solution to the Einstein Field Equation

[45] B W Carroll and D A Ostlie 2007 An Introduction to Modern Astrophysics *Pearson Addison-Wesley* ISBN 9780321442840
[46] W Threlfall and H Seifert 1931 Topologische Untersuchung der Diskontinuitätsbereiche endlicher Bewegungsgruppen des dreidimensionalen sphärischen Raumes *Math. Ann.* **104** 1
[47] W Threlfall and H Seifert 1932 Topologische Untersuchung der Diskontinuitätsbereiche endlicher Bewegungsgruppen des dreidimensionalen sphärischen Raumes (Schluß) *Math. Ann.* **107** 543
[48] J A Wolf 1984 Spaces of Constant Curvature *Publish or Perish, Inc.* ISBN 0914098071
[49] P A Zyla et al. 2020 Review of Particle Physics *Prog. Theor. Exper. Phys.* **2020** 083C01
[50] G Efstathiou and S Gratton 2020 A Detailed Description of the CamSpec Likelihood Pipeline and a Reanalysis of the Planck High Frequency Maps *O. J. Astrophys.* **4** (arXiv:1910.00483)

Bibliography on the Friedmann equations

[51] A Einstein 1917 Kosmologische Betrachtungen zur allgemeinen Relativitätstheorie *Sitzungb. König. Preuß. Akad. Wissens.* 142-152
[52] G F R Ellis 2007 On the Raychaudhuri equation *Pramana - J. Phys.* **69** 15-22

Bibliography on ...toward an inhomogeneous Universe

[53] R S Gonçalves, G C Carvalho, U Andrade, C A P Bengaly, J C Carvalho and J Alcaniz 2021 Measuring the cosmic homogeneity scale with SDSS-IV DR16 Quasars *J. Cosmol. Astropart. Phys.* **JCAP03(2021)029** (*Preprint* arXiv:2010.06635)
[54] G F R Ellis and W Stoeger 1987 The "fitting problem" in cosmology *Class. Quantum Grav.* **4** 1697-1729
[55] D Wiltshire 2011 What is dust? – Physical foundations of the averaging problem in cosmology *Class. Quantum Grav.* **28** 164006 (arXiv:1106.1693)

Bibliography on Relativistic geometrisation of gravity at large scale

[56] R M Zalaletdinov 1992 Averaging out the Einstein equations *Gen. Relat. Gravit.* **24** 1015-31
[57] T Buchert 1997 Averaging Inhomogeneous Cosmologies – a Dialogue (arXiv:astro-ph/9706214)
[58] T Buchert and J Ehlers 1997 Averaging inhomogeneous Newtonian cosmologies *Astron. Astrophys.* **320** 1-7 (arXiv:astro-ph/9510056)
[59] R M Zalaletdinov 2007 Averaging Problem in Cosmology and Macroscopic Gravity (arXiv:gr-qc/0701116)
[60] T Buchert 2007 Dark Energy from structure: a status report *Gen. Relat. Gravit.* **40** 467-527 (arXiv:0707.2153)
[61] G F R Ellis 2011 Inhomogeneity effects in cosmology *Class. Quantum Grav.* **28** 164001 (arXiv:1103.2335)
[62] T Buchert 2018 Is Dark Energy Simulated by Structure Formation in the Universe ? *PoS* **(EDSU2018)** 038 (arXiv:1810.09188)
[63] T Buchert, P Mourier and X Roy 2020 On average properties of inhomogeneous fluids in general relativity III: general fluid cosmologies *Gen. Relat. Gravit.* **52** (arXiv:1912.04213)

[64] H J Macpherson, D J Price and P D Lasky 2019 Einstein's Universe: Cosmological structure formation in numerical relativity *Phys. Rev. D* **99** 063522 (arXiv:1807.01711)
[65] H J Macpherson and A Heinesen 2021 Luminosity distance and anisotropic sky-sampling at low redshifts: A numerical relativity study *Phys. Rev. D* **104** 023525 (arXiv:2103.11918)
[66] G Rácz, I Szapudi, I Csabai and L Dobos 2018 Compactified Cosmological Simulations of the Infinite Universe *Mon. Not. Roy. Astr. Soc.* **477** 1949-57 (arXiv:1711.04959)
[67] G Rácz, I Szapudi, I Csabai and L Dobos 2021 The anisotropy of the power spectrum in periodic cosmological simulations *Mon. Not. Roy. Astr. Soc.* **503** 5638-45 (arXiv:2006.10399)

Bibliography on A brief introduction to Cosmic Topology

[68] M Lachièze-Rey and J P Luminet 1995 Cosmic Topology *Phys. Reports* **254** 135-214 (arXiv:gr-qc/9605010)
[69] J P Uzan 1997 What Do We Know and What Can We Learn About the Topology of the Universe? *Int. J. Theor. Phys.* **36** 2439-50
[70] J P Luminet and B F Roukema 1999 Topology of the Universe: Theory and Observations (arXiv:astro-ph/9901364)
[71] W P Thurston 1979 The geometry and topology of three manifolds ISBN 9780691083049 *Princeton Lecture Notes* 1-379
[72] W P Thurston 1982 Three dimensional manifolds, Kleinian groups and hyperbolic geometry *Bull. Am. Math. Soc.* **6** 357-381
[73] W P Thurston 1988 How to see 3-manifolds *Class. Quantum Grav.* **15** 2545 (arXiv:1103.2335)
[74] F Steiner 2016 Do black holes exist in a finite Universe having the topology of a flat 3−torus? (arXiv:1608.03133)
[75] A Riazuelo, J Weeks, J P Uzan, R Lehoucq and J P Luminet 2004 Cosmic microwave background anisotropies in multiconnected flat spaces *Phys. Rev. D* **69** 103518 (arXiv:astro-ph/0311314)
[76] R Aurich and S Lustig 2011 Cosmic microwave background anisotropies in an inhomogeneous compact flat universe *Class. Quantum Grav.* **28** 085017 (arXiv:1009.5880)
[77] R Aurich and S Lustig 2014 The Hantzsche-Wendt manifold in cosmic topology *Class. Quantum Grav.* **31** 165009 (arXiv:1403.2190)
[78] B Mota, M J Rebouças and R Tavakol 2010 Circles-in-the-sky searches and observable cosmic topology in a flat universe *Phys. Rev. D* **81** 103516 (arXiv:1002.0834)
[79] R Aurich, T Buchert, M J France and F Steiner 2021 The variance of the CMB temperature gradient: a new signature of a multiply connected Universe *Class. Quantum Grav.* **38** 225005 (*Preprint* arXiv:2106.13205)
[80] H Poincaré 1895 Analysis Situs *J. École Polytech.* **Analysis Situs**
[81] F Klein 1918 Collected Mathematical Treatises (Foundation of the Geometry of the Erlanger Program) *Verlag Von Julius Springer* **erster Band**
[82] J E Armengaud 1848 Nouveau cours raisonné de dessin industriel appliqué principalement à la mécanique et à l'architecture (1ière édition) *Bur. Publ. Industr.* **Nouveau cours raisonné de dessin industriel**
[83] W Johnson 1851 The Practical Draughtsman's Book of Industrial Design: Forming a Complete Course of Mechanical, Engineering, and Architectural Drawing *Franklin Classics* ISBN 9780341948605
[84] Infeld L 1949 On The Structure of Our Universe, in: Albert Einstein: Philosopher-Scientist 2000 (The Library of Living Philosophers, Vol. VII (New York: MFJ Books, ed. Schilpp P A), pp.475-499. See also Einstein's reply, l.c. p.686. eISBN 9780875482866
[85] G F R Ellis 1971 Topology and Cosmology *Gen. Relat. Gravit.* **2** 7-21

[86] I B Zel'dovich and L P Grishchuk 1984 Structure and future of the 'new' universe *Mon. Not. Roy. Astr. Soc.* **207** 23P-28P
[87] Stevens D, Scott D and Silk J 1993 Microwave background anisotropy in a toroidal universe *Phys. Rev. Lett.* **71** 20-23
[88] Starobinsky A A 1993 New restrictions on spatial topology of the universe from microwave background temperature fluctuations *JETP Letters* **57** 622-625 (arXiv:gr-qc/9305019)
[89] Y P Jing and L Z Fang 1994 An Infrared Cutoff Revealed by the Two Years of COBE observations of Cosmic Temperature Fluctuations *Phys. Rev. Lett.* **73** 1882 (arXiv:astro-ph/9409072)
[90] A de Oliveira-Costa and G F Smoot 1995 Does COBE rule out a toroidal Universe? *Nucl. Phys. B* **43** 299-302(*Preprint* arXiv:astro-ph/9601034)
[91] A de Oliveira-Costa and G F Smoot 1995 Constraints on the Topology of the Universe from the 2 Year COBE Data *Astrophys. J.* **448** 477-481 (*Preprint* arXiv:astro-ph/9412003)
[92] R Lehoucq, M Lachièze-Rey and J P Luminet 1996 Cosmic Crystallography *Astron. Astrophys.* **313** 339-346(*Preprint* arXiv:gr-qc/9604050)
[93] Cornish N J, Spergel D N and Starkman G D 1996 Does Chaotic Mixing Facilitate Ω <1 Inflation? *Phys. Rev. Lett.* **77** 215-218(*Preprint* arXiv:astro-ph/9601034)
[94] J P Luminet 2005 A cosmic hall of mirrors arXiv:physics/0509171
[95] B F Roukema 1996 On determining the topology of the observable Universe via three-dimensional quasar positions *Mon. Not. Roy. Astr. Soc.* **283** 1147–1152 (*Preprint* arXiv:astro-ph/9603052)
[96] B F Roukema and C E Alastair 1997 Constraining cosmological topology via highly luminous X-ray clusters *Mon. Not. Roy. Astr. Soc.* **292** 105–112 (*Preprint* arXiv:astro-ph/9706166)
[97] B F Roukema 1998 Cosmological Topology 4 Observational Methods, Constraints and Candidates *ADS* **4** 23-27
[98] B F Roukema 1998 Méthodes aux grandes échelles pour mesurer la topologie globale de l'Univers *Acta Cosmol.* **XXIV-1** 117-125 (*Preprint* arXiv:astro-ph/9801125)
[99] B F Roukema 1998 Dwarf Galaxies from Cosmology (*Preprint* arXiv:astro-ph/9806111)
[100] B F Roukema 1998 Three-dimensional topology-independent methods to look for global topology *Class. Quantum Grav.* **15** 2645 (*Preprint* arXiv:astro-ph/9802083)
[101] B F Roukema, M J France, T A Kazimierczak and T Buchert 2014 Deep redshift topological lensing: strategies for the $\mathcal{T}^3$ candidate *Mon. Not. Roy. Astr. Soc.* **437** 1096-1108 (arXiv:1302.4425)
[102] B F Roukema 2000 The topology of the universe *Bull. Astr. Soc. Ind.* **28** 483-497(*Preprint* arXiv:astro-ph/0010185)
[103] R Aurich 1999 The fluctuations of the Cosmic Microwave Background for a compact hyperbolic universe *Astrophys. J.* **524** 497-503(*Preprint* arXiv:astro-ph/9903032)

Bibliography on General Relativity and global topology of the Universe

[104] A Papadopoulos 2018 Cauchy and Puiseux: Two precursors of Riemann *HAL* **01674509** 1-24
[105] M Hadamard 1907 Les problèmes aux limites dans la théorie des équations aux dérivées partielles *J. Phys. Theor. Appl.* **6** 202-241
[106] S Frittelli and R Gómez 2003 Boundary conditions for hyperbolic formulations of the Einstein Equations *Class. Quantum Grav.* **20** 2379-92 (arXiv:gr-qc/0302032)
[107] S Frittelli and R Gómez 2006 On Boundary Conditions for the Einstein Equations In: Frauendiener J., Giulini D.J., Perlick V. (eds) Analytical and Numerical Approaches to Mathematical Relativity *Lect. Notes Phys.* **692** 205-222
[108] Y Choquet-Bruhat and R Geroch 1969 Global aspects of the Cauchy problem in general relativity *Commun. Math. Phys.* **14** 329-335

[109] H Ringström 2013 On the Topology and Future Stability of the Universe *Oxford Science Publications* ISBN 9780199680290
[110] H Ringström 2013 The Cauchy Problem in General Relativity *Acta Phys. Pol.* **B 44** 2621-41
[111] K A Farrar and A L Melott 1989 Gravity in twisted space *Comp. Phys.* **4** 185-189
[112] B F Roukema, S Bajtlik, M Besiada, A Szaniewska and H Jurkiewicz 2007 A weak gravity acceleration effect due to residual gravity in a multiply connected universe *Astron. Astrophys.* **463** 861-71 (arXiv:astro-ph/0602159)
[113] L Brunswic and T Buchert 2020 Gauss-Bonnet-Chern approach to the averaged Universe *Class. Quantum Grav.* **37** 215022 (arXiv:2002.08336)

Bibliography on A short introduction to the Cosmic Microwave Background

[114] Penzias A A and Wilson R W 1965 A Measurement of Excess Antenna Temperature at 4080 Mc/s *Astrophys. J.* **142** 419-421
[115] Adams W S 1941 Some Results with the COUDÉ Spectrograph of the Mount Wilson Observatory *Astrophys. J.* **93** 11
[116] McKellar A 1941 Molecular lines from the lowest states of diatomic molecules composed of atoms probably present in interstellar space *Publ. Domin. Astrophys. Obs.* **7** 251-272
[117] Mather J et al. 1990 A preliminary measurement of the Cosmic Microwave Background spectrum by the *Cosmic Background Explorer (COBE)* satellite *Astrophys. J.* **354** L37-L40
[118] Mather J et al. 1999 Calibrator design for the *COBE* far infrared absolute spectrophotometer (FIRAS) *Astrophys. J.* **512** 511-520 (arXiv:astro-ph/9810373)
[119] Smoot G F et al. 1992 Structure in the *COBE* Differential Microwave Radiometer first-year Maps *Astrophys. J.* **396** L1-L5
[120] Wright E L et al. 1992 Interpretation of the Cosmic Microwave Background Radiation Anisotropy Detected by the *COBE* Differential Microwave Radiometer *Astrophys. J.* **396** L13-L18
[121] Hinshaw G, Banday A J, Bennett C L, Górski K M, Kogut A, Lineweaver C H, Smoot G F and Wright E L 1996 Two-Point Correlations in the *COBE* DMR Four-Year Anisotropy Maps *Astrophys. J.* **464** 25-28 (arXiv:astro-ph/9601061)
[122] Bennett C L et al. 2003 First-year Wilkinson Microwave Anisotropy Probe (WMAP) Observations: Preliminary maps and basic results *Astrophys. J. Suppl.* **148** 1-27 (arXiv:astro-ph/0302207)
[123] Hinshaw G et al. 2003 First-year Wilkinson Microwave Anisotropy Probe (WMAP) Observations: The angular power spectrum *Astrophys. J. Suppl.* **148** 135-159 (arXiv:astro-ph/0302217)
[124] Spergel D N et al. 2003 First-year Wilkinson Microwave Anisotropy Probe (WMAP) Observations: Determination of Cosmological Parameters *Astrophys. J. Suppl.* **148** 175-194 (arXiv:astro-ph/0302209)
[125] Bennett C L et al. 2011 Seven-Year Wilkinson Microwave Anisotropy Probe (WMAP) Observations: Are There Cosmic Microwave Background Anomalies? *Astrophys. J. Suppl.* **192** 1-19 (arXiv:1001.4758)
[126] Ade P A R et al. 2014 Planck 2013 results. XXIII. Isotropy and statistics of the CMB *Astron. Astrophys.* **571** A23 (arXiv:1303.5083)
[127] Ade P A R et al. 2016 Planck 2015 results. XVI. Isotropy and statistics of the CMB *Astron. Astrophys.* **594** A16 (arXiv:1506.07135)
[128] Ade P A R et al. 2016 Planck 2015 results. XIII. Cosmological parameters *Astron. Astrophys.* **594** A13 (arXiv:1502.01589)

[129] Ade P A R et al. 2016 Planck 2015 results XVIII. Background geometry and topology of the universe *Astron. Astrophys.* **594** A18 (arXiv:1502.01593)
[130] Aghanim N et al. 2020 Planck 2018 results. V. CMB power spectra and likelihoods *Astron. Astrophys.* **641** A5 (arXiv:1907.12875)
[131] Akrami Y et al. 2020 Planck 2018 results. VII. Isotropy and Statistics of the CMB *Astron. Astrophys.* **641** A7 (arXiv:1906.02552)
[132] Schwarz D J, Copi C J, Huterer D and Starkman G D 2016 CMB anomalies after Planck *Class. Quantum Grav.* **33** 184001 (arXiv:1510.07929)
[133] Aurich R, Janzer H S, Lustig S and Steiner F 2008 Do we live in a "small Universe"? *Class. Quantum Grav.* **25** 125006 (arXiv:0708.1420)
[134] Aurich R and Lustig S 2013 A search for cosmic topology in the final WMAP data *Mon. Not. Roy. Astr. Soc.* **433** 2517–2528 (*Preprint* arXiv:1303.4226)
[135] Aurich R 2008 A spatial correlation analysis for a toroidal universe *Class. Quantum Grav.* **25** 225017 (*Preprint* arXiv:0803.2130)
[136] Bolejko K, Nazer M A and Wiltshire D L 2016 Differential cosmic expansion and the Hubble flow anisotropy *J. Cosmol. Astropart. Phys.* **JCAP06(2016)035** (*Preprint* arXiv:1512.07364)
[137] Notari A and Quartin M 2016 CMB all–scale blackbody distortions induced by linearizing temperature *Phys. Rev. D* **94** 043006 (*Preprint* arXiv:1603.02996)

4 A new signature of multiply connected Universe

I arrive now at the first research paper presented in this PhD thesis. Very preliminary calculations made by Sven Lustig, Frank Steiner and me suggested an interesting property of the CMB maps calculated by Ralf Aurich for a Universe having the topology of the 3−torus. These maps seemed to satisfy a general property that we qualify of hierarchical, i.e. the smaller the size of the 3−torus the larger the variance of the CMB temperature gradient map. I confirmed the result applying the systematic study to large ensembles of maps (100 000) for each torus size L. Ralf Aurich suggested to calculate the probability distribution function (PDF) of ρ over each map ensemble. The PDFs confirmed the hierarchical result. Furthermore I found that the law of L with respect to the variance of the CMB temperature gradient was linear. Given the interesting results we found, I began writing the paper (published in 2021) named **The variance of the CMB temperature gradient: a new signature of a multiply connected Universe** (see references page xvi). Even if my contributions to this paper and to the results were important and numerous (various investigations, algorithmics, computing, bibliography, redaction), it was decided to apply the alphabetical order of the authors (Ralf Aurich, Thomas Buchert, Martin J France and Frank Steiner) and keeping this way the logic of displaying Ralf Aurich as first author of the series of cosmic topology papers involving him and Frank Steiner.

4.1 The CMB in the multiply connected Universe $\mathcal{T}^3$

4.1.1 Two-point correlation function

A basic quantity characterizing the anisotropies of the CMB and probing the primordial seeds for structure formation is the full-sky two-point correlation function (hereafter 2–pcf) of the temperature fluctuation $\delta T(\hat{\boldsymbol{n}})$, observed for our actual sky in a direction given by the unit vector $\hat{\boldsymbol{n}}$, defined by

$$C^{\rm obs}(\vartheta) := \langle \delta T(\hat{\boldsymbol{n}}) \delta T(\hat{\boldsymbol{n}}') \rangle \quad \text{with} \quad \hat{\boldsymbol{n}} \cdot \hat{\boldsymbol{n}}' = \cos\vartheta \ , \tag{34}$$

where the brackets denote averaging over all directions $\hat{\boldsymbol{n}}$ and $\hat{\boldsymbol{n}}'$ (or pixel pairs) on the full sky that are separated by an angle ϑ. Since $C^{\rm obs}(\vartheta)$ corresponds to *one* observation of the actual CMB sky from our particular position in the Universe, the average in equation (34) should not be confused with an ensemble average. The ensemble average could be either an average of the observations from every vantage point throughout the Universe, or the average of an ensemble of realizations of the CMB sky in a given cosmological model.

$C^{\rm obs}(\vartheta)$ has been measured for the first time in 1992 by COBE [1, 2] from the 1–year maps, and in 1996 from the 4–year maps [3]. The COBE data revealed small correlations in the large angular range Υ delimited by $70° \leq \vartheta \leq 150°$ which later has been confirmed with high precision by WMAP [4–7] and Planck [8–13]. COBE compared the observed correlation functions with a large variety of theoretical predictions within the class of FLRW (Friedmann-Lemaître-Robertson-Walker) cosmologies, including flat

and non-zero constant-curvature models with radiation, massive and massless neutrinos, baryonic matter, cold dark matter (CDM), and a cosmological constant Λ, using both adiabatic and isocurvature initial conditions, see e.g. [14, 15]. From COBE observations it was concluded [1] that the two-point correlations, including the observed small values of $C^{\rm obs}(\vartheta)$ in the range Υ, are in accord with scale-invariant primordial fluctuations (Harrison-Zel'dovich spectrum with spectral index $n = 1$) and a Gaussian distribution as predicted by models of inflationary cosmology. Thus, there was no indication that the small correlations measured in the angular range Υ could hint to a serious problem, or even to new physics. The situation changed drastically with the release of the first-year WMAP observations that will be discussed below.

At this point it is worth to mention that at the time of COBE, i.e. before 1998, the Hubble constant was not well-determined (the uncertainty amounting to a factor of 2 or more); the acceleration of the time-evolution of the scale-factor of a FLRW cosmology [16, 17] was not yet discovered and thus the value of the cosmological constant was not known. Also the low quadrupole was already clearly seen by COBE, but was usually dismissed due to cosmic variance or foreground contamination.

COBE observations were used in 1993 in an attempt [18, 19] to detect CMB temperature fluctuations specific of the discrete spectrum of metric perturbations of a Universe with 3−torus topology. And several other authors emphasized that the COBE observations might hint to a non-trivial topology of our Universe and called this field of research Cosmic Topology [20]. Another signature of multiply connected universes on the CMB, based on the identified circles principle was proposed since 1996 [21, 22] and observational analyses of the COBE data were made using this principle [23, 24].

The first-year data by WMAP led to today's standard model of cosmology [4–6], a spatially flat Λ−dominated universe model seeded by nearly scale-invariant adiabatic Gaussian fluctuations, the ΛCDM model with cold dark matter and a positive cosmological constant Λ. The fact that the non-Gaussianities of the primordial gravitational fluctuations are very small is nicely confirmed by the recent Planck data [25].

There remain, however, intriguing discrepancies between predictions of the ΛCDM model and CMB observations: one of them is the lack of any correlated signal on angular scales greater than 60° [6], [26], [27], [28], [29], [30], [31], [32], [33], [34], [35], [36], [37], [38]. Further anomalies are e.g. the low quadrupole and a strange alignment of the quadrupole with the octopole [39–41]. These anomalies were still questioned on the basis of the seven-year WMAP data [7], and it is only with the sharper spatial and thermal resolution of Planck that their existence in the CMB data have a robust statistical standing [8]. The observed severe suppression of correlations at large scales does not appear in the simulated sky map examples of the CMB in a ΛCDM model. Figure 1 shows the average 2–pcf of the four Planck foreground corrected CMB observation maps without mask, NILC, SEVEM, SMICA and Commander-Ruler (their ensemble hereafter named NSSC) compared to the average 2–pcf of one hundred thousand ΛCDM CMB maps at a resolution $N_{\rm side} = 128$, with $l_{\rm max} = 256$ and a Gaussian smearing (defined in equation (63)) of 2° (full width at half maximum). The calculation of the 2–pcfs is made in the spherical harmonic space imposing isotropy and homogeneity for the Planck NSSC 2–pcf which shows no correlation between 80° and 150°. Also the 2–pcf average behaviour of the ΛCDM ensemble differs strongly from the one of the CMB observation maps by WMAP and Planck. Approximately 0.025% of the ΛCDM realizations have a 2–pcf displaying the same large-angles suppression as the 5−year WMAP map [34].

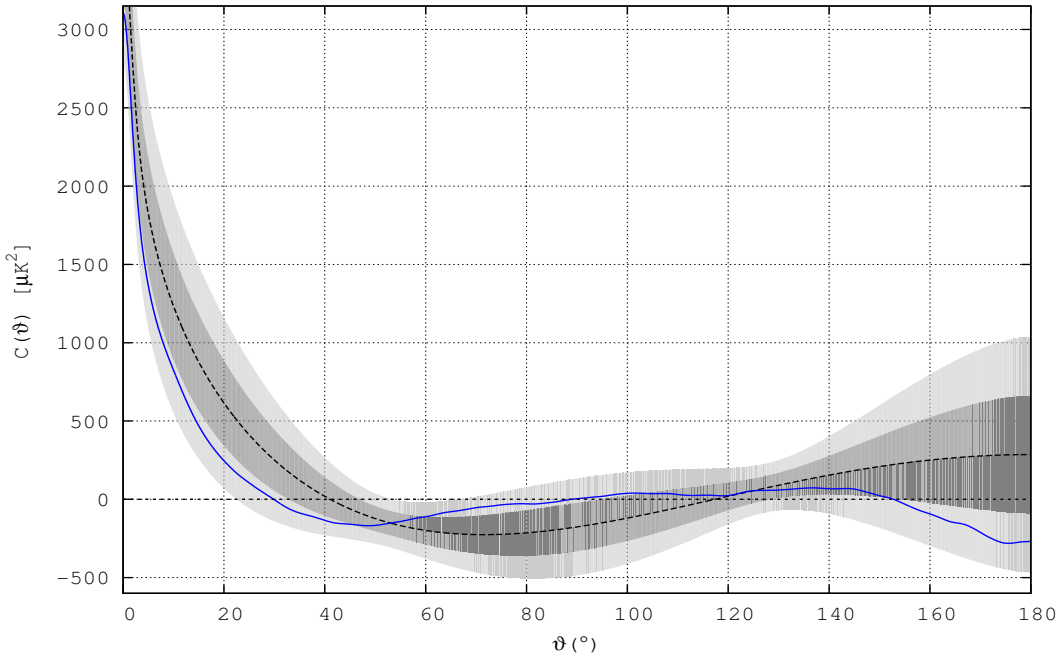

Figure 1: The average two-point correlation function of 100 000 CMB simulation maps without mask in the infinite ΛCDM model according to Planck 2015 [9] cosmological parameters (in black dash line), $\pm 1\sigma$ in the dark shaded area, and $\pm 2\sigma$ in the light shaded area (68 and 95 percent confidence levels, respectively). This is compared to the average two-point correlation function of the four foreground corrected Planck maps, NILC, SEVEM, SMICA and Commander-Ruler (NSSC) in solid blue line.

A further discrepancy occurs on scales below $\vartheta \approx 50°$, where the ΛCDM simulations also reveal, on average, larger correlations than those observed by WMAP and Planck (see figure 1 and, e.g., figure 3 in [41]). The angular range $\vartheta \leq 50°$ of the 2–pcf depends on all multipoles ($l \geq 2$) of the observed power spectrum (see e.g. the Planck spectrum, figure 57) [9]) in the case of no or very small smoothing (see equation (63)). There is a large contribution from the first acoustic peak and also from the higher peak structure which appears up to the large l's (i.e. the smallest angles limited by the instrument resolution). Note, however, that the very large multipoles ($l \geq 900$) are strongly suppressed by Silk damping. The 'high' multipole moments ($l \geq 30$) do not differ very much for ΛCDM and the 'topological' models, the crucial contribution to $C(\vartheta)$, which leads to the discrepancy for $\vartheta \leq 50°$, comes from the 'low' multipoles (mainly for $l \leq 29$) where the power spectrum shows a lack of power for the quadrupole and a characteristic 'zig-zag structure' (see, e.g., [6], [26], [27], [28], [29], [30], [31], [32], [34], [35], [36], [37], [38]).

In addition, the 2–pcf $C(\vartheta)$ of the ΛCDM model reveals a negative dip between 50° and 100° and a positive slope beyond and up to 180°. Thus, on average, these CMB sample maps for an isotropic and homogeneous infinite ΛCDM model display a non zero 2–pcf for any separation angle ϑ except those in the two narrow regions of cancellation around 40° and 120°.

4.1.2 **2-pcf hinting at a difficulty**

For the observed CMB by Planck, WMAP or COBE the lack of correlations at large angular scales finds a natural explanation in cosmic topology: compared to the CMB simulation maps of the ΛCDM model in an infinite Universe, the suppression of the 2–pcf at large angular scales of the Planck CMB maps is consistent with finite spatial sections of the Universe.

Before 1998 there was the theoretical prejudice that the Universe is flat (total density parameter Ω_{tot}=1), while the data pointed to a negatively curved spatial section $\Omega_{\text{tot}} < 1$. In [42, 43] the CMB was investigated for a small compact hyperbolic universe model (an orbifold) with $0.3 \leq \Omega_{\text{tot}} \leq 0.6$, and for the nearly flat case with $\Omega_{\text{tot}} \leq 0.95$, respectively, containing radiation, baryonic, cold dark matter and Λ. It was shown that the low multipoles are suppressed even for nearly flat, but hyperbolic models with $\Omega_{\text{tot}} \leq 0.9$. For even larger values of $\Omega_{\text{tot}} \approx 0.95$, fluctuations of the low multipole moments C_l occur, which are typical in the case of a finite volume of the Universe. In [44, 45] the first-year WMAP data and the magnitude-redshift relation of Supernovae of type Ia have been analyzed in the framework of quintessence models and it has been shown that the data are consistent with a nearly flat hyperbolic geometry of the Universe if the optical depth τ to the surface of last scattering is not too big.

Furthermore it has been shown [26–28] that the hyperbolic space form of the Picard universe model, defined by the Picard group which has an infinitely long horn but finite volume, leads e.g. for $\Omega_{\text{matter}} = 0.30$ and $\Omega_\Lambda = 0.65$, to a very small quadrupole and displays very small correlations at angles $\vartheta \geq 60°$. Even at small angles, $\vartheta \approx 10°$, $C(\vartheta)$ agrees with the observations much better than the ΛCDM model.

Depending on certain priors, the WMAP team reported in 2003 from the first-year data [6] for the total energy density $\Omega_{\text{tot}} = 1.02 \pm 0.02$ together with $\Omega_{\text{baryon}} = 0.044 \pm 0.004$, $\Omega_{\text{matter}} = 0.27 \pm 0.04$, and $h = 0.71^{+0.04}_{-0.03}$ for the present-day reduced Hubble constant $h = H_0/(100\text{km s}^{-1}\ \text{Mpc}^{-1})$ (the errors give the 1σ-deviation uncertainties). Taken at face value, these parameters hint at a positively curved Universe. Luminet et al. [46] studied the Poincaré dodecahedral space which is one of the well-known space forms with constant positive curvature. In [46] only the first three modes of the Laplacian have been used (comprising in total 59 eigenfunctions), which in turn restricted the discussion to the multipoles $l \leq 4$. Normalizing the angular power spectrum at $l = 4$, they found for $\Omega_{\text{tot}} = 1.013$, a strong suppression of the quadrupole and a weak suppression of the octopole. The 2–pcf $C(\vartheta)$ could not be calculated.

A thorough discussion of the CMB anisotropy and of $C(\vartheta)$ for the dodecahedral topology was carried out in [29] based on the first 10 521 eigenfunctions. An exact analytical expression was derived for the mean value of the multipole moments C_l ($l \geq 2$) for the ordinary Sachs-Wolfe contribution (i.e. without the integrated Sachs-Wolfe effect and the Doppler contribution), which explicitly shows that the lowest multipoles are suppressed due to the discrete spectrum of the vibrational modes. The discrete eigenvalues for all spherical spaces are in appropriate units given by $E_\beta = \beta^2 - 1$, where the dimensionless wave numbers β run through a subset of the natural numbers. (Only in the case of the simply connected sphere $\mathcal{S}^3$, β runs through all natural numbers.) In the case of the dodecahedral space there exist no even wave numbers, and the odd wave numbers have large gaps since, e.g., the allowed β-values up to 41 are given by $\{1, 13, 25, 31, 33, 37, 41\}$, where $\beta = 1$, corresponding to the zero mode $E_1 = 0$, is subtracted since it gives the monopole. Thus, the spectrum is not only discrete but has in addition large gaps

('missing modes') which lead to an additional suppression. The analytical expression for the C_l's also leads to an analytical expression for the correlation function (due to the ordinary Sachs-Wolfe contribution) which shows the suppression at large scales [29]. The remaining contributions from the integrated Sachs-Wolfe and Doppler effect were computed numerically. A detailed analysis of the CMB anisotropy for all spherical spaces was carried out in [30], and it was shown that only three spaces out of the infinitely many homogeneous spherical spaces are in agreement with the first-year WMAP data.

The question of the strange alignment of the quadrupole with the octopole, and the extreme planarity or the extreme sphericity of some multipoles has been investigated in [47] with respect to the maximal angular moment dispersion and the Maxwellian multipole vectors for five multiply connected spaces: the Picard topology in hyperbolic space [26–28], three spherical spaces (Poincaré dodecahedron [29, 46], binary tetrahedron and binary octahedron [30]) and the cubic torus [32]. Although these spaces are able to produce the large-scale suppression of the CMB anisotropy, they do not describe the CMB alignment. From the models considered, the Picard space form reveals the strongest alignment properties.

Already the 3−year data of WMAP provided a hint that our Universe might be spatially flat [31]. The 2018 results reported by the Planck team [48], combining Planck temperature and polarization data and BAO (baryon acoustic oscillation) measurements, give for the curvature parameter $\Omega_K := 1 - \Omega_{\rm tot}$ the small value $\Omega_K = 0.0007 \pm 0.0019$, suggesting flatness to a 1σ accuracy of 0.2%. Recently, however, a different interpretation has been presented claiming that the data show a preference for a positively curved Universe, noted also in [48] (for references see [49]). This problem has been revisited in [49], and when combining with other astrophysical data, it is concluded that spatial flatness holds to extremely high precision with $\Omega_K = 0.0004 \pm 0.0018$ in agreement with Planck [48]. But, also recently, it has been pointed out [50–54] that there are inconsistencies between cosmological datasets arising when the FLRW curvature parameter Ω_K is determined from the data rather than constrained to be zero *a priori*. Relaxing this prior also increases the already substantial discrepancy between the Hubble parameter as determined by Planck and local observations to the level of 5σ. These different outcomes originate from the comparison of data at the CMB epoch and data from the present-day Universe providing 'tensions' for the ΛCDM model [55], [56], [57]. Resolving these tensions appears to need a fully general-relativistic description of the curvature evolution [58].

Assuming that the spatial section of our Universe is well-approximated by a flat manifold that is furthermore simply connected, it follows that its topology is given by the infinite Euclidean 3−space $\mathbb{E}^3$. This is exactly the assumption made in the ΛCDM model which leads to the intriguing discrepancies in the range Υ of large angular scales as discussed above (see figure 1). It has been shown in [32, 35, 37, 59] that the simplest spatially flat finite-volume manifold with non-trivial topology i.e. the multiply-connected cubic 3−torus $\mathcal{T}^3$ with side length L having the finite volume L^3, leads in a natural way, without additional assumptions, to the observed suppression at large scales if only the volume is not too large. For the many previous works on a toroidal Universe model, see the references in [32].

A modified correlation function, the spatial correlation function, was suggested in [33], which takes the assumed underlying topology of the dodecahedron into account and provides estimates for the orientation of the manifold. This method was applied to the 3−torus topology in [37]. Another example of topology is provided by the flat slab

space [38] with one compact direction and two infinite directions. A further example is provided by the compact Hantzsche-Wendt manifold for which the ensemble averages of statistical quantities such as the 2–pcf depend on the position of the observer in the manifold, which is not the case for the 3−torus topology $\mathcal{T}^3$. The suppression of correlations of the 2–pcf is studied in [36]. For this topology, the 'matched circles-in-the-sky' signature is much more difficult to detect because there are much fewer back-to-back circles compared to the $\mathcal{T}^3$ topology.

4.1.3 The CMB of a Universe with 3−torus topology

While the infinite ΛCDM model is homogeneous and isotropic, the multiply connected torus Universe $\mathcal{T}^3$ is still homogeneous and locally isotropic, but no more globally isotropic. In a flat Universe having three infinite spatial directions such as for the ΛCDM model, the spectrum of the vibrational modes (i.e. the eigenvalues and eigenfunctions) of the Laplacian is continuous. In the case of the 3−torus topology $\mathcal{T}^3$, the CMB temperature anisotropies δT over the 2−sphere $\mathcal{S}^2$ are calculated by using the vibrational modes of the Laplacian with periodic conditions imposed by the cubic fundamental domain without boundary [32]. The discrete eigenvalues of the Laplacian are then given by

$$E_{\boldsymbol{n}} = \left(\frac{2\pi}{L}\right)^2 \boldsymbol{n}^2 \quad \text{with } \boldsymbol{n} = (n_1, n_2, n_3) \in \mathbb{Z}^3 \ . \tag{35}$$

Thus, the wave number spectrum of $\mathcal{T}^3$ is discrete and countably infinite consisting of the distinct wave numbers

$$k_m = \frac{2\pi}{L}\sqrt{m} \ , \ m = 0, 1, 2, \dots \ , \tag{36}$$

i.e. there is no ultraviolet cut-off at large wave numbers. There are gaps between consecutive wave numbers,

$$k_{m+1} - k_m = \frac{\pi}{L}\frac{1}{\sqrt{m}}\left[1 - \frac{1}{4m} + \mathcal{O}\left(\frac{1}{m^2}\right)\right] \ , \ m \to \infty \ , \tag{37}$$

which tend to zero asymptotically. However, the wave numbers are degenerate, i.e. they possess multiplicities $r_3(m)$, where $r_3(m)$ is a very irregular, number-theoretical function with increasing mean value, which counts the number of representations of $m \in \mathbb{N}_0$ as a sum of 3 squares of integers, where representations with different orders and different signs are counted as distinct. For example, $r_3(0) = 1$, $r_3(1) = 6$, $r_3(2) = 12$, $r_3(3) = 8$, $r_3(4) = 6$, $r_3(5) = 24$. ($r_3(m)$ has been already studied by Gauss.) Weyl's law provides the asymptotic growth of the number $N(K)$ of all vibrational modes in the 3−torus with $|\boldsymbol{k_n}| := \sqrt{E_{\boldsymbol{n}}} \leq K$,

$$N(K) \sim \frac{V}{6\pi^2}K^3 \ , \ K \to \infty \ , \tag{38}$$

where $V = L^3$ is the volume of the torus manifold (see for instance [29, 30, 43] and the review [60]). For example, in [59], the first 50 000 distinct wave numbers were taken into account comprising in total 61 556 892 vibrational modes which allowed to compute the multipoles up to $l = 1\,000$. There is, however, in the case of the CMB anisotropy in a torus universe model, a cut-off at small wave numbers, i.e. an infrared cut-off, $|\boldsymbol{k_n}| \geq 2\pi/L = k_1$, since the zero mode $|\boldsymbol{k_0}| = 0$ has been subtracted, as was first pointed out by Infeld in the late forties [61].

In this part of my manuscript, the cosmological lengths are expressed in terms of the Hubble length denoted $L_H = c/H_0$ as in [32, 37]. The value of the reduced Hubble constant today according to Planck 2015 [9] was $h = (0.6727 \pm 0.0066)$ (68% limits) , giving a Hubble length of $L_H = (4.4453^{+0.0386}_{-0.0379})$ Gpc. The value determined from the most recent analysis of Planck from the ΛCDM model in 2019 [62] is very close, i.e. at $h = (0.6744 \pm 0.0058)$ (68% limits). The 3−torus and ΛCDM simulations presented in my thesis manuscript are calculated using the Planck 2015 cosmological parameters. But, given the small $N_{\rm side} = 128$ and $l_{\rm max} = 256$ and the strong Gaussian smoothing scale of 2° f.w.h.m., suppressing the sharp CMB structures at the first acoustic peak and beyond, differences between using the Planck 2015 or the Planck 2019 cosmological parameters to generate the CMB temperature maps are not expected in terms of cosmic topology. It is only when considering the improved polarization data of Planck legacy 2018 that differences might be expected for cosmic topology.

For the CMB in a universe model with 3−torus topology and with an optimally determined torus side length of $L \approx 3.69 L_H$, the 2–pcf is nearly vanishing for large angles [32, 37], fitting much better to the 2–pcf of the observed maps than those of the ΛCDM model. In the case of the slab space manifold (only one compact direction [38]) the match with the Planck 2015 CMB maps 2–pcf is good, once the slab is optimally oriented with respect to our galactic plane and for an optimal slab thickness close to $4.4 L_H$ (for the same H_0 of Planck 2015). Also good is the 2–pcf match for any angle separation [38], except for the angles beyond 150° where the remnants of galactic foreground pollution in the Planck maps could explain the non-zero and negative value of the correlation at the largest scales.

Another signature of multiply connected topology, the 'matched circles-in-the-sky' (thereafter CITS) was and is much tested on the COBE, WMAP and Planck CMB temperature and polarization maps (see [11], [21–24], [32] and [63–66]). The CITS signal is based on the fact that the metric perturbation at the surface of last scattering (SLS) is responsible for a large part of the CMB signal, since the metric perturbation is mapped by the 3−torus group to the identified points on the SLS. Other contributions to the CMB signal deteriorate the CITS signal, such as the Doppler contribution which is projected from different lines of sight. Another deteriorating effect is due to the integrated Sachs-Wolfe (ISW) effect, which describes the changes along the photon path from the SLS to the observer, where again the points along the path are not identified due to the topology. There are hints that this contribution is larger than expected from the ΛCDM model, so that the CITS signal might be less pronounced than derived from ΛCDM simulations. The late time ISW effect due to the supervoids is stronger than expected from the ΛCDM model measured by $A_{\rm ISW} = \Delta T^{\rm data}/\Delta T^{\rm theory}$ [67] which should be close to 1. The Dark Energy Survey (DES) collaboration finds an excess amplitude $A_{\rm ISW}$=4.1 ±2.0 [67] and when they combine their data with the independent Baryon acoustic Oscillations Spectroscopic Survey (BOSS) data, even an excess ISW signal of supervoids with $A_{\rm ISW}$=5.2 ±1.6 is revealed. For a summary, see figure 5 in [67] and references in this publication. It thus seems to be premature to exclude non-trivial topologies due to the non-observations of the CITS signal on the SLS.

The other tested signature of a 3−torus multiply connected topology, the covariance matrix, entails no conclusive results, e.g. [32]. It is then of great importance to confirm the possibly multiply connected nature of our Universe suggested by the vanishing 2–pcf through complementary methods using different observables and implemented with other morphological or topological descriptors.

It is clear that the Cosmic topology of multiply connected manifolds brings to a universe model an intrinsic signature at any spatial scale since the whole spectrum of eigenmodes of the Laplacian characterizes unambiguously shape and volume of each different manifold up to its maximum size(s) while in a 3−spatially infinite Universe such as the Universe of the ΛCDM model, there are no eigenmodes. The intrinsic discretization of the eigenmodes due to the finite section(s) of a Universe with multiply connected topology would have important consequences on the observable shape of structures and would also play a major role on the structure formation (see e.g. [68] for a study considering the effect of the 3−torus multiple connectedness and inherent periodic boundary conditions on the gravity and a possible weak topological acceleration) and evolution in conjunction with the role played by the geometrisation of the gravity. Cosmic topology of MCM allows a spatial discretization which is not accounted for by the General Theory of Relativity formalism. Although "observable" is a concept one sometimes use in cosmology, I shall therefore not generalize the term of "observable" in the present PhD thesis manuscript since its application to observational cosmology needs clarifications because of the incompatibility between Quantum Mechanics and GR and a Quantum Gravity Theory still to be build.

I shall now introduce an important result reached during the period of my PhD thesis work while analysing large ensembles of CMB simulation maps for a Universe with multiply connected topology with a new statistical tool:

4.2 CMB temperature gradient map and cosmic topology

4.2.1 The standard deviation ρ of the temperature gradient field

The CMB temperature fluctuation $\delta T(\hat{\boldsymbol{n}}) := T(\hat{\boldsymbol{n}}) - T_0$ is defined as the difference between the direction-dependent temperature $T(\hat{\boldsymbol{n}})$ and the monopole $T_0 := T_{\rm CMB}$, with $T_{\rm CMB} = (2.7255 \pm 0.0006K)$ [9, 69]. On the unit sphere $\mathcal{S}^2$, we write the metric in spherical coordinates (ϑ, φ),

$$\mathrm{d}s^2 := \mathrm{d}\vartheta^2 + \sin^2\vartheta\,\mathrm{d}\varphi^2 \ , \tag{39}$$

and denote the unit vector by $\hat{\boldsymbol{n}} = \hat{\boldsymbol{n}}(\vartheta, \varphi)$. The angular average of $\delta T(\hat{\boldsymbol{n}})$ vanishes,

$$\frac{1}{4\pi}\int_{\mathcal{S}^2} \mathrm{d}^2\hat{\boldsymbol{n}}\ \delta T(\hat{\boldsymbol{n}}) = 0 \ . \tag{40}$$

Averaging also over the possible positions from which the CMB is observed, one obtains:

$$\int_{\mathcal{S}^2} \mathrm{d}^2\hat{\boldsymbol{n}}\ \mu(\hat{\boldsymbol{n}}) = 0 \ , \tag{41}$$

with $\mu(\hat{\boldsymbol{n}}) := \langle \delta T(\hat{\boldsymbol{n}}) \rangle$. Here, the brackets denote an ensemble average at fixed $\hat{\boldsymbol{n}}$. Similarly, we define the ensemble average of the variance of $\delta T(\hat{\boldsymbol{n}})$,

$$\sigma_0^2(\hat{\boldsymbol{n}}) := \left\langle [\delta T(\hat{\boldsymbol{n}}) - \mu(\hat{\boldsymbol{n}})]^2 \right\rangle \ . \tag{42}$$

Assuming that the Universe is homogeneous and isotropic *on average*, all averages $\langle \delta T(\hat{\boldsymbol{n}}) \delta T(\hat{\boldsymbol{n}}') \delta T(\hat{\boldsymbol{n}}'') \cdots \rangle$ are rotationally invariant functions of $\hat{\boldsymbol{n}}, \hat{\boldsymbol{n}}', \hat{\boldsymbol{n}}'', \cdots$, and thus μ and σ_0^2 are independent of $\hat{\boldsymbol{n}}$. In this case it follows that $\mu = 0$ [17] and

$$\sigma_0^2 = \langle [\delta T(\hat{\boldsymbol{n}})]^2 \rangle \ . \tag{43}$$

Since the correlation function (34) is a function of $\hat{\boldsymbol{n}} \cdot \hat{\boldsymbol{n}}' = \cos\vartheta$, it can be expanded in Legendre polynomials,

$$\begin{aligned} C^{\mathrm{obs}}(\vartheta) &= \frac{1}{8\pi^2} \int_{\mathcal{S}^2} \mathrm{d}^2\hat{\boldsymbol{n}}_1 \int_{\mathcal{S}^2} \mathrm{d}^2\hat{\boldsymbol{n}}_2 \ \delta\left(\hat{\boldsymbol{n}}_1 \cdot \hat{\boldsymbol{n}}_2 - \cos\vartheta\right) \delta T(\hat{\boldsymbol{n}}_1) \delta T(\hat{\boldsymbol{n}}_2) \\ &= \frac{1}{4\pi} \sum_{l=1}^{\infty} (2l+1) C_l^{\mathrm{obs}} \ P_l(\cos\vartheta) \ , \end{aligned} \tag{44}$$

with the multipole moments

$$C_l^{\mathrm{obs}} := \frac{1}{4\pi} \int_{\mathcal{S}^2} \mathrm{d}^2\hat{\boldsymbol{n}} \int_{\mathcal{S}^2} \mathrm{d}^2\hat{\boldsymbol{n}}' \ P_l(\hat{\boldsymbol{n}} \cdot \hat{\boldsymbol{n}}') \ \delta T(\hat{\boldsymbol{n}}) \delta T(\hat{\boldsymbol{n}}') = \frac{1}{2l+1} \sum_{m=-l}^{l} |a_{lm}|^2 \ , \tag{45}$$

and where the complex coefficients $\{a_{lm}\}$ are the coefficients of the expansion of $\delta T(\hat{\boldsymbol{n}})$ into spherical harmonics, ${Y_l}^m(\hat{\boldsymbol{n}})$, on the full sky. The observed angular power spectrum is then given by

$$\left(\delta T_l^{\mathrm{obs}}\right)^2 := \frac{l(l+1)}{2\pi} C_l^{\mathrm{obs}} \ . \tag{46}$$

Note that equations (44) and (45) hold without any theoretical assumptions on $\delta T(\hat{\boldsymbol{n}})$ (provided the integrals and series converge).

Assuming that the Universe is homogeneous and isotropic on average, the ensemble average of the full-sky correlation function is rotationally invariant and satisfies

$$C(\vartheta) := \langle \delta T(\hat{\boldsymbol{n}}) \delta T(\hat{\boldsymbol{n}}') \rangle = \frac{1}{4\pi} \sum_{l=1}^{\infty} (2l+1) C_l \ P_l(\hat{\boldsymbol{n}} \cdot \hat{\boldsymbol{n}}') \ , \tag{47}$$

with the multipole moments

$$C_l := \langle |a_{lm}|^2 \rangle \tag{48}$$

(independent of m). From (45) and (48) follows that

$$\langle C_l^{\mathrm{obs}} \rangle = C_l \ . \tag{49}$$

From (48) and (49) one finds the normalized variance of $C_l - C_l^{\mathrm{obs}}$, i.e. the cosmic variance:

$$\left\langle \left(\frac{C_l - C_l^{\mathrm{obs}}}{C_l} \right)^2 \right\rangle = -1 + \frac{1}{(2l+1)^2 C_l^2} \sum_{m=-l}^{l} \sum_{m'=-l}^{l} \langle |a_{lm}|^2 |a_{lm'}|^2 \rangle \ . \tag{50}$$

If we furthermore assume that $\delta T(\hat{\boldsymbol{n}})$ is a Gaussian random field on $\mathcal{S}^2$, it follows that the $\{a_{lm}\}$ are complex Gaussian random variables which, however, does not imply that also the C_l's are Gaussian random variables. The cosmic variance (50) simplifies in the Gaussian case and is given by

$$\left\langle \left(\frac{C_l - C_l^{\mathrm{obs}}}{C_l} \right)^2 \right\rangle = \frac{2}{2l+1} \ . \tag{51}$$

[17] For an ensemble of n maps we have $\langle \mu \rangle := (1/n) \sum_{j=1}^{n} \mu_j$. After subtraction of the monopole and the dipole (this is done for all the maps studied in this work), we can verify that over the 100 000 simulation maps of the ΛCDM and the 3−torus models, $|\langle \mu \rangle|$ is numerically extremely small $\mathcal{O}(10^{-7}\mu K)$ without mask and $\mathcal{O}(10^{-4}\mu K) - \mathcal{O}(10^{-3}\mu K)$ after mask pixel suppression.

(For the case with mask, the reader is directed to equations (22)-(24) in [36].)

Over the 2−sphere support of the CMB temperature anisotropy map we also define $\boldsymbol{G}$, the gradient field, dependent on the spherical coordinates ϑ and φ. In terms of its components,

$$G_{\vartheta} := \frac{\partial \delta T}{\partial \vartheta} \ , \tag{52}$$

and

$$G_{\varphi} := \frac{1}{\sin \vartheta} \frac{\partial \delta T}{\partial \varphi} \ . \tag{53}$$

The variance σ_1^2 of the local temperature gradient is defined by an average over the directions,

$$\sigma_1^2 := \left\langle \nabla_1 \delta T(\hat{\boldsymbol{n}}) \nabla^1 \delta T(\hat{\boldsymbol{n}}) + \nabla_2 \delta T(\hat{\boldsymbol{n}}) \nabla^2 \delta T(\hat{\boldsymbol{n}}) \right\rangle \ , \tag{54}$$

where in spherical coordinates the covariant derivatives are given by

$$\nabla_1 \delta T(\hat{\boldsymbol{n}}) \nabla^1 \delta T(\hat{\boldsymbol{n}}) = \delta T_{,\vartheta} \delta T^{,\vartheta} = G_{\vartheta}^2 = \left(\frac{\partial \delta T}{\partial \vartheta} \right)^2 \ , \tag{55}$$

and

$$\nabla_2 \delta T(\hat{\boldsymbol{n}}) \nabla^2 \delta T(\hat{\boldsymbol{n}}) = \delta T_{,\varphi} \delta T^{,\varphi} = G_{\varphi}^2 = \left(\frac{1}{\sin \vartheta} \frac{\partial \delta T}{\partial \varphi} \right)^2 \ . \tag{56}$$

If the CMB sky map is an isotropic and homogeneous Gaussian random field having a negligible mean μ (hereafter IHG properties, IHG standing for isotropic, homogeneous and Gaussian of zero mean), the ensemble average of the CMB is statistically determined by its 2–pcf $C(\vartheta)$, equations (47) and (48). Under this condition the components G_{ϑ} and G_{φ} of the gradient vector $\boldsymbol{G}$, equations (52) and (53), are Gaussian random variables with zero mean and identical variance $\sigma_1^2/2$.

The field of CMB temperature anisotropies $\delta T(\hat{\boldsymbol{n}})$ is discretized into pixels of the HEALPix tessellation $\delta T_i := \delta T(\hat{\boldsymbol{n}}_i)$, and for the purpose of this investigation, σ_1^2 is calculated in pixel space in spherical coordinates (see also the formulas in the non-discretized case, equations (29) and (30) in [70]) as the average[18] expanded into

$$\sigma_1^2 := \left\langle G_{\vartheta}^2 + G_{\varphi}^2 \right\rangle = \frac{\sum_{i=0}^{\mathrm{npixels}-1} \left[\left(\frac{\partial \delta T_i}{\partial \vartheta} \right)^2 + \left(\frac{1}{\sin \vartheta} \frac{\partial \delta T_i}{\partial \varphi} \right)^2 \right]}{\mathrm{npixels}} \ . \tag{57}$$

The reader may refer to mathematical definitions, developments and discussions related to scalar statistics on the CMB spherical support manifold in [14], [71], [70], [59]. Under the assumption that $\delta T(\hat{\boldsymbol{n}})$ is an isotropic and homogeneous random field on average, σ_1^2 can be calculated in the spherical harmonic space as

$$\sigma_1^2 := \sum_{l=l_{\mathrm{min}}}^{l_{\mathrm{max}}} C_l \frac{l(l+1)(2l+1)}{4\pi} \ , \tag{58}$$

where C_l are the multipole moments (48), monopole and dipole are subtracted (i.e. $l_{\mathrm{min}} = 2$) and $l_{\mathrm{max}} = 256$. Under the same isotropy condition, the variance of $\delta T(\hat{\boldsymbol{n}})$ reads:

$$\sigma_0^2 := \sum_{l=l_{\mathrm{min}}}^{l_{\mathrm{max}}} C_l \frac{2l+1}{4\pi} \ . \tag{59}$$

[18] This is implemented using a modified version of the HEALPix Fortran subroutine 'alm2map_der' and its function 'der1'.

If the CMB sky maps possess the IHG properties, they are statistically completely determined by the multipoles C_l. Also, the equivalence between the 2–pcf $C(\vartheta)$ and the power spectrum ($\delta T_l^2 := l(l+1)C_l/2\pi$) only holds if the CMB over the whole 2−sphere is observable.

We define ρ as the normalized standard deviation of the gradient field $\boldsymbol{G}$ of temperature anisotropy over a single map,

$$\rho := \sqrt{\frac{\left\langle G_\vartheta^2 + G_\varphi^2 \right\rangle}{\sigma_0^2}} = \sqrt{\frac{\sigma_1^2}{\sigma_0^2}} \quad , \tag{60}$$

while the mean in terms of ρ for an ensemble of n maps is given by

$$\langle \rho \rangle := \frac{\sum_{j=1}^{n} \rho_j}{n} \quad . \tag{61}$$

While searching for possible non-Gaussianities in the CMB maps using Minkowski functionals [25], one of us (FS) proposed in 2012 the normalized variance of the CMB gradient as a new signature of a multiply connected nature of the Universe. Note that the ratios σ_1/σ_0 and respectively σ_1^2/σ_0^2, appear in the definition of the Gaussian prediction of the second Minkowski functional (MF) and respectively the third MF of a random field on the 2−sphere $\mathcal{S}^2$. For comprehensive definitions of random fields and Minkowski functionals of excursion sets, see [72], [73, 74], [14], [71, 75], [59], [25].

Obviously, ρ defined as a ratio does not depend on an overall normalization constant of the temperature field. While a comparison of maps using only σ_0 or σ_1 or the 2–pcf requires the normalization of the temperature anisotropy field. We shall develop on this application of normalization for our ensembles of 3−torus maps in section 4.2.5.

In order to provide an illustration of the quantity from which ρ is derived by averaging $\boldsymbol{G}$, figure 2 shows in Mollweide projection the map of

$$\rho_i := \sqrt{\frac{G_{\vartheta,i}^2 + G_{\varphi,i}^2}{\sigma_0^2}} = \sqrt{\frac{\sigma_{1,i}^2}{\sigma_0^2}} \quad , \tag{62}$$

where i denotes a pixel index, for one CMB map of the 3−torus simulations at a side length of $L = 1.0 L_H$. The resolution parameters are the ones applied to all the maps all along the present study i.e. $N_{\text{side}} = 128$, $l_{\text{range}} = [2, 256]$ and a Gaussian smoothing $\vartheta_G = 2^\circ$ f.w.h.m. The Gaussian smoothing is defined by $C_l \to C_l |F_l|^2$ with

$$F_l = \exp\left(-\frac{\alpha^2 \vartheta_G^2}{2}\, l(l+1) \right) \tag{63}$$

and $\alpha = \pi/(180\sqrt{8 \ln 2})$, which is obtained in the limit $\alpha\vartheta_G \ll 1$ from the Gaussian kernel on $\mathcal{S}^2$.

4.2.2 Hierarchical dependence: size of fundamental cell versus ρ

The following analysis is based on five ensembles of the cubic 3−torus $\mathcal{T}^3$ topology belonging to different sizes of the fundamental cell, and one ensemble of the infinite ΛCDM model (with a simply connected topology). The five 3−torus ensembles belong to the side lengths $L/L_H = 0.5, 1.0, 1.5, 2.0$ and 3.0. Each ensemble consists of 100 000

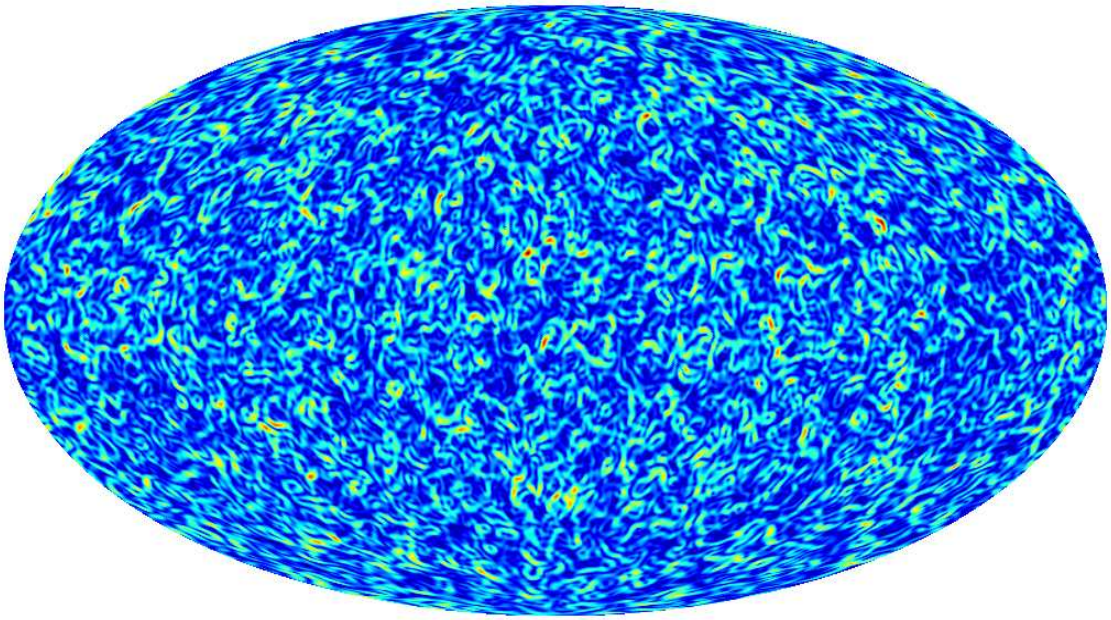

Figure 2: The map of the normalized norm of the temperature gradient field $\boldsymbol{G}$, as defined in equation (62) and calculated from a CMB map of the 3−torus at $L = 1.0L_H$ at a resolution of $N_{\text{side}} = 128$, $l_{\text{range}} = [2, 256]$ and $\vartheta_G = 2°$. The strongest local gradients appear in red and the weakest gradients in dark-blue. While the most interesting features, the numerous iso-contour patterns, are shown in light-blue.

realizations leading to 100 000 CMB sky maps.[19] In order to generate a realization of the ensemble, a Gaussian random number of unit variance and zero mean is multiplied by each eigenmode belonging to a wavenumber $\boldsymbol{k_n}$, see equation (36). The CMB maps of the 3−torus and the infinite ΛCDM model are computed using the cosmological parameters according to Planck 2015 [9]. The CMB maps are analyzed at a HEALPix resolution of $N_{\text{side}} = 128$ (196608 pixels of diagonal 27.5′, i.e. a pixel side length of 19.4′) with $l_{\text{max}} = 256$, and are smoothed with $\vartheta_G = 2°$.

For each set of 100 000 maps, the probability distribution functions (PDFs) of ρ are shown for the five cubic 3−torus side lengths L, and for the infinite ΛCDM model, as histograms in figure 3 (unmasked case) and figure 4 (masked case). All distributions are unimodal with a pronounced peak. We present in tables 1 and 2 the mean value $\langle\rho\rangle$, the median ρ-value (hereafter denoted median), the standard deviation Σ, the skewness coefficient

$$\gamma_1 := \frac{m_3}{\Sigma^3} \ , \tag{64}$$

and the excess kurtosis

$$\gamma_2 := \frac{m_4}{\Sigma^4} - 3 \ , \tag{65}$$

where m_n denotes the n^{th} central moment of a given distribution (see e.g. [25]).

The PDFs of the random variables σ_0 and σ_1, respectively, can be approximated by truncated Gaussian distributions (see Appendix 8.1). The deviations from the actual

[19] The simulation of the map ensembles for larger side lengths of the torus is computationally expensive, typically months for a hundred core cluster.

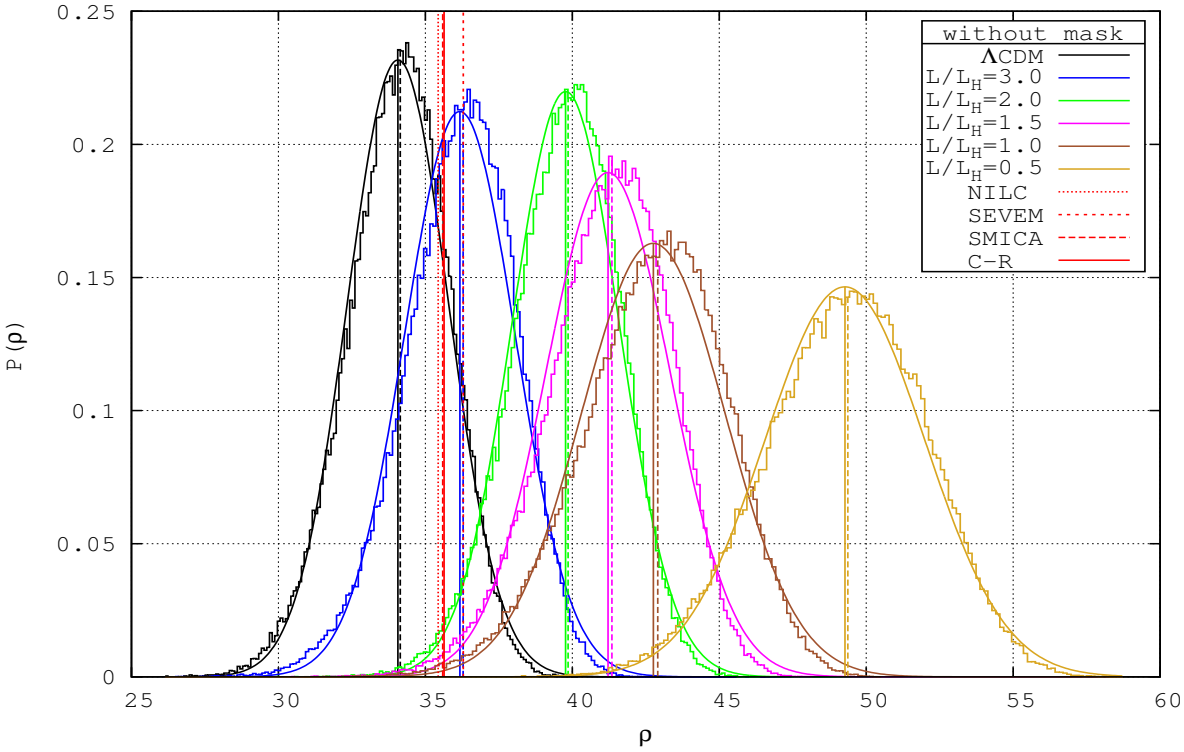

Figure 3: The histograms of ρ without foreground mask. Presented in solid lines are the PDF histograms and the Gaussian distributions for the ensembles of 100 000 model maps. From right to left: the 3−torus at $L = 0.5L_H$ in light brown, $L = 1.0L_H$ in brown, $L = 1.5L_H$ in magenta, $L = 2.0L_H$ in green, $L = 3.0L_H$ in blue and the ΛCDM model in black. The Gaussian PDFs are computed from the means and the variances given in table 1 and illustrate the deviation of the PDFs from a symmetrical distribution. The means are shown with a vertical solid line and the medians with a vertical dashed line. The mean $\langle\rho\rangle$ for each of the four Planck maps is shown with a vertical red line (NILC in small dots, SEVEM in small dashes, SMICA in large dashes and Commander-Ruler as a solid line).

histograms is due to the fact that the PDF of σ_0 possesses a definite non-Gaussian component, whereas the PDF of σ_1 only shows a small deviation from a Gaussian behaviour. The histograms presented in figure 3 are indeed unimodal, but not Gaussian[20]. In order to visualize a possible non-Gaussianity of $P(\rho)$, we shall compare in figures 3 and 4 the histograms with a Gaussian PDF.

Since ρ is by definition a strictly positive random variable, the appropriate Gaussian PDF to compare with is not the standard normal distribution defined on the whole line but rather a truncated normal distribution defined only on the positive half-line. Thus, the Gaussian PDF to be applied in this situation should *a priori* be a one-sided truncated Gaussian probability distribution function. For the construction of the truncated Gaussian we refer to the Appendix in 8.1. There it is shown that the deviations of the truncated Gaussian PDF from the standard normal distribution are, however, extremely small in the case considered here. Therefore, we compare the histograms in figures 3 and 4 with the standard Gaussian PDF fixed by the mean values $\langle\rho\rangle$ and the variance Σ^2 given in tables 1 and 2.

[20] The deviation from Gaussianity does not necessarily imply a violation of the IHG properties.

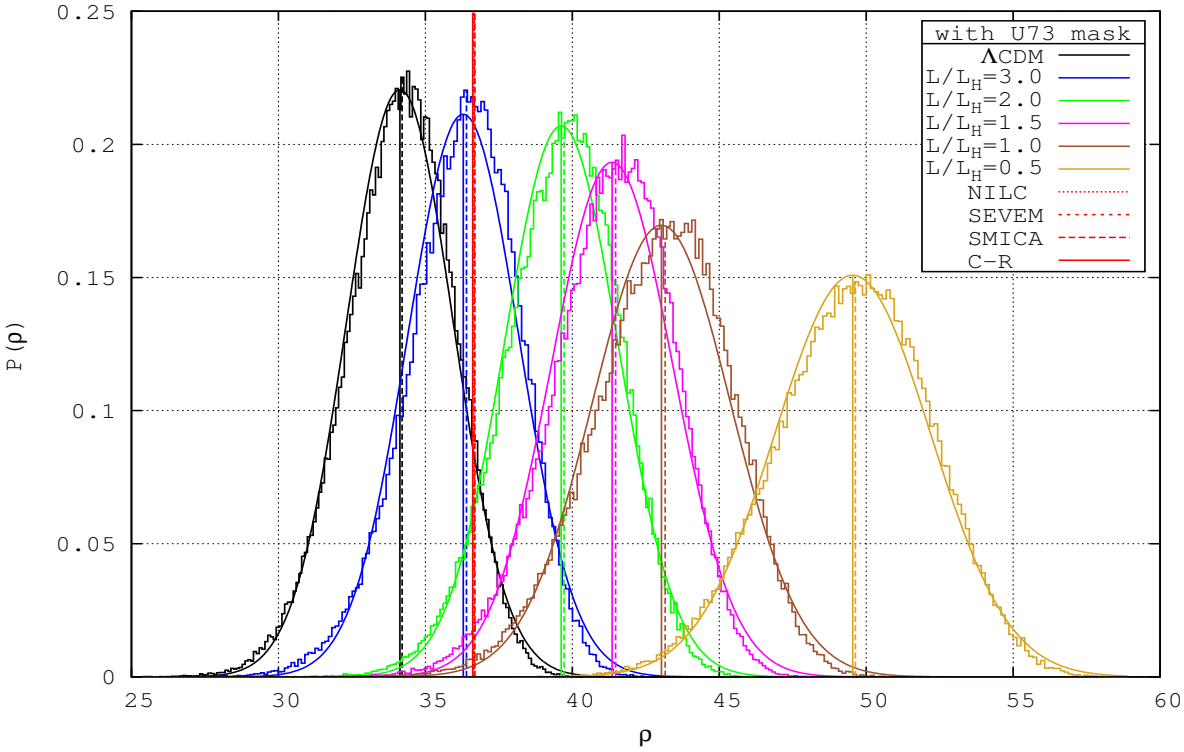

Figure 4: Same as figure 3 for the histograms of ρ, here with exclusion of the U73 mask pixels. The Gaussian PDFs are computed from the means and the variances given in table 2.

A Gaussian random variable has the following unique characteristic properties:

- Its PDF maximizes the (differential) entropy among all probable continuous distributions with fixed first and second moment, and in general among all unimodal distributions.
- All higher odd moments and all cumulants with $n \geq 3$ are identically zero, i.e. in particular $\gamma_1 = \gamma_2 = 0$.
- Furthermore, one can show (Marcinkiewicz's theorem [76]) that the normal distribution is the only distribution having a finite number of non-zero cumulants.
- The equality 'mean' = 'median' = 'mode' holds (where 'mode' is defined as the location of the maximum of the unimodal PDF).

Thus, γ_1, γ_2 as well as all higher cumulants and the differences

$$\delta_1 := \text{median} - \langle\rho\rangle \quad ; \quad \delta_2 := \text{mode} - \langle\rho\rangle \ , \tag{66}$$

can serve as indicators of non-Gaussianity of $P(\rho)$. There exists the general bound (Mallows' bound) for all PDFs with $\Sigma < \infty$:

$$|\delta_1| \leq \Sigma \ , \tag{67}$$

and for any unimodal PDF there is the sharper bound

$$|\delta_1| \leq \sqrt{\frac{3}{5}}\, \Sigma \approx 0.775\, \Sigma \ . \tag{68}$$

Tables 1 and 2 show that $\delta_1 > 0$ for all tori, and thus we can consider the normalized ratio δ_1/Σ as another measure of non-Gaussianity. A possible non-Gaussianity may be considered as small, if δ_1/Σ is smaller by a factor of 10 than the upper bound (68), i.e. if $\delta_1/\Sigma \leq 0.078$ holds.

Some general properties of these histograms of ρ arise, independently of taking into account the U73 union mask:

- All PDFs of ρ show a systematically weak negative skewness γ_1 which is true also for the infinite ΛCDM sample. This skewness is less pronounced for the torus at $L = 0.5L_H$.
- The PDFs for the 3−torus at $L = 0.5L_H$ are platykurtic, i.e. with a small negative excess kurtosis $\gamma_2 = -0.115$ (no mask) and $\gamma_2 = -0.109$ (U73 mask).
- The PDFs of $L = 1.0,\ 2.0L_H$ and the ΛCDM are almost mesokurtic with γ_2 very small and positive ($\gamma_2 \leq 0.085$).
- The PDFs of $L = 1.5$ and $3.0L_H$ are leptokurtic i.e. with γ_2 positive between $\gamma_2 = 0.138$ and $\gamma_2 = 0.245$.

L/L_H	L(Gpc)	R	$\langle\rho\rangle$	median	δ_1	Σ	δ_1/Σ	γ_1	γ_2
0.5	2.2227	12.57	49.275	49.376	0.101	2.723	0.037	−0.202	−0.115
1.0	4.4453	6.29	42.755	42.907	0.152	2.45	0.062	−0.339	0.085
1.5	6.6680	4.19	41.215	41.347	0.132	2.106	0.063	−0.372	0.175
2.0	8.8906	3.15	39.771	39.858	0.087	1.815	0.048	−0.273	0.085
3.0	13.3359	2.10	36.173	36.285	0.112	1.879	0.060	−0.356	0.201
NILC			35.434						
SEVEM			36.290						
SMICA			35.591						
C-R			35.635						
NSSC			35.738	35.613	−0.125	0.327	−0.380	0.971	−0.781
∞	∞	0	34.067	34.143	0.076	1.722	0.044	−0.248	0.035

Table 1: Table of ρ (no mask), $\langle\rho\rangle$ (ρ for the four Planck maps), median, δ_1, standard deviation Σ, δ_1/Σ, skewness γ_1 and excess kurtosis γ_2 for each of the 3−torus side lengths and the infinite ΛCDM. NSSC stands for the ensemble of the four Planck maps NILC, SEVEM, SMICA and Commander-Ruler. The 3−torus comoving side length L is given in units of the Hubble length L_H, and $R = 2r_{\rm SLS}/L$ is twice the ratio comoving CMB angular diameter distance to the comoving side length of the fundamental cell, with a distance to the CMB of $r_{\rm SLS} = 14.0028$ Gpc corresponding to $3.15L_H$.

L/L_H	L(Gpc)	R	$\langle\rho\rangle$	median	δ_1	Σ	δ_1/Σ	γ_1	γ_2
0.5	2.2227	12.57	49.542	49.634	0.092	2.645	0.035	−0.184	−0.109
1.0	4.4453	6.29	43.031	43.161	0.130	2.352	0.055	−0.304	0.054
1.5	6.6680	4.19	41.351	41.471	0.120	2.064	0.058	−0.339	0.138
2.0	8.8906	3.15	39.622	39.720	0.098	1.928	0.051	−0.274	0.069
3.0	13.3359	2.10	36.288	36.400	0.112	1.888	0.059	−0.360	0.245
NILC			36.639						
SEVEM			36.662						
SMICA			36.688						
C-R			36.612						
NSSC			36.650	36.650	$6.9\ 10^{-5}$	$2.8\ 10^{-2}$	0.002	$-6.2\ 10^{-3}$	−1.304
∞	∞	0	34.132	34.206	0.074	1.809	0.041	−0.244	0.050

Table 2: Same as table 1 but with U73 mask.

no mask	$L/L_H = 3$	NSSC	ΛCDM
$\langle\rho\rangle$	36.173	35.738	34.067
δs	$-0.232\Sigma_{L3}$		$+0.970\Sigma_{\Lambda}$
median	36.285	35.613	34.143
δs	$-0.358\Sigma_{L3}$		$+0.854\Sigma_{\Lambda}$
U73 mask	$L/L_H = 3$	NSSC	ΛCDM
$\langle\rho\rangle$	36.288	36.650	34.132
δs	$+0.192\Sigma_{L3'}$		$+1.392\Sigma_{\Lambda'}$
median	36.400	36.650	34.206
δs	$+0.132\Sigma_{L3'}$		$+1.351\Sigma_{\Lambda'}$

Table 3: Table of the statistical deviations δs (see equations (69) and (70)), comparing $\langle\rho\rangle$ and median of the Planck NSSC maps with the 3−torus at $L/L_H = 3$, also denoted $L3$ ($L3'$ with mask), and with the ΛCDM model, also denoted Λ (Λ' with mask).

In tables 1 and 2 one observes that the largest value for δ_1/Σ is in the no mask case 0.063, and in the U73 mask case 0.059, which clearly indicates that the non-Gaussianities of $P(\rho)$ are small.[21]

Despite the overlap between the adjacent PDFs of each different 3−torus, one notices that, to a given ρ-range, one can associate a given 3−torus side length following a hierarchical ordering, i.e. the smaller the 3−torus, the larger the ρ-value. In addition, the PDF of ρ for the infinite ΛCDM model is located beyond the PDF of the largest chosen 3−torus at $L = 3.0L_H$. This trend confirms the hierarchical dependence between the size of the fundamental cell of the universe model and the value of the normalized standard deviation ρ of the temperature gradient. Figure 4 shows, in contrast to figure 3, the distributions obtained from the CMB maps with the application of the U73 mask, i.e. the pixels behind the U73 mask are ignored. It reveals a similar hierarchical ordering with the mean and median ρ-values somewhat shifted to higher ρ-values for a given torus ensemble, see also table 2.

The two figures 3 and 4 also display the value of ρ for each of the four foreground-corrected Planck 2015 maps, NILC, SEVEM, SMICA and Commander-Ruler. In addition, the arithmetic average $\langle\rho\rangle$ for these four Planck maps (NSSC) is shown (see tables 1 and 2). Their individual ρ-values are indicated by the four vertical lines in the two plots. These ρ-values can be clearly distinguished in figure 3, where the foreground-contaminated pixels are present. These ρ-values, however, nearly converge to the arithmetic average $\langle\rho\rangle$, when the U73 mask pixels are rejected, as can be appreciated in figure 4. The arithmetic average $\langle\rho\rangle = 35.738$ of the four Planck maps is rather close to the arithmetic average $\langle\rho\rangle \sim 36.173$ of the 3−torus ensemble $L = 3.0L_H$ at $-0.232\Sigma_{L3}$ (see equations (69) and (70) for definition of the statistical deviations) when no mask is used, see table 1, and, with the U73 union mask, the arithmetic average $\langle\rho\rangle = 36.650$ of the four Planck maps is $+0.192\Sigma_{L3'}$ above the arithmetic average at 36.288 of the 3−torus sample $L = 3.0L_H$, see table 2.

Without mask (see table 1), the median value 35.613 of the four Planck maps is slightly below the median at 36.285 of the 3−torus ensemble, i.e. at $-0.358\Sigma_{L3}$. With the U73 mask (see table 2), the median of the NSSC maps at 36.650 is a little above, i.e. at $+0.132\Sigma_{L3'}$ of the median 36.400 of the 3−torus sample $L = 3.0L_H$. These results of the statistical deviation δs of $\langle\rho\rangle$ and median for the four NSSC Planck maps compared with the 3−torus at $L = 3.0L_H$ are shown in the synoptic table 3. This table applies the same method to compare the NSSC maps with the ΛCDM maps, and we discuss these further results at the end of section 4.2.5.

The statistical deviation δs of the NSSC ensemble (denoted NSSC' with mask) in comparison with the 3−torus at $L/L_H = 3$ (denoted $L3$ or $L3'$ with mask) or the ΛCDM

[21] In table 2, the very tiny values of Σ, δ_1/Σ and γ_1 obtained for the NSSC maps using the U73 mask are due to the fact that the observed maps constitute only one realization for a single observer position, evaluated with different pipelines of analysis. If the observations and the different pipelines were perfect, one would obtain a zero value. So, these tiny values are a measure of the consistency of the four pipelines used by Planck in the case of the U73 mask and should not be compared with the results obtained over the ensemble of 100 000 realizations (different universe models or different observer positions separated by cosmological scales) for the $\mathcal{T}^3$ models and the ΛCDM model. For the same reason, the corresponding NSSC values in table 1 should not be compared with the ensemble-derived values.

model ensembles (denoted Λ or Λ' with mask) is defined the following way without mask:

$$\delta s := \begin{cases} \frac{\langle\rho\rangle_{\mathrm{NSSC}}-\langle\rho\rangle_{L3}}{\Sigma_{L3}} & \text{, for } \langle\rho\rangle \text{ and the 3}-\text{torus at } L/L_H = 3 \\ \frac{\langle\rho\rangle_{\mathrm{NSSC}}-\langle\rho\rangle_{\Lambda}}{\Sigma_{\Lambda}} & \text{, for } \langle\rho\rangle \text{ and } \Lambda\mathrm{CDM} \\ \frac{\mathrm{median}_{\mathrm{NSSC}}-\mathrm{median}_{L3}}{\Sigma_{L3}} & \text{, for the median and the 3}-\text{torus at } L/L_H = 3 \\ \frac{\mathrm{median}_{\mathrm{NSSC}}-\mathrm{median}_{\Lambda}}{\Sigma_{\Lambda}} & \text{, for the median and } \Lambda\mathrm{CDM} \ , \end{cases} \tag{69}$$

and with U73 mask:

$$\delta s := \begin{cases} \frac{\langle\rho\rangle_{\mathrm{NSSC}'}-\langle\rho\rangle_{L3'}}{\Sigma_{L3'}} & \text{, for } \langle\rho\rangle \text{ and the 3}-\text{torus at } L/L_H = 3 \\ \frac{\langle\rho\rangle_{\mathrm{NSSC}'}-\langle\rho\rangle_{\Lambda'}}{\Sigma_{\Lambda'}} & \text{, for } \langle\rho\rangle \text{ and } \Lambda\mathrm{CDM} \\ \frac{\mathrm{median}_{\mathrm{NSSC}'}-\mathrm{median}_{L3'}}{\Sigma_{L3'}} & \text{, for the median and the 3}-\text{torus at } L/L_H = 3 \\ \frac{\mathrm{median}_{\mathrm{NSSC}'}-\mathrm{median}_{\Lambda'}}{\Sigma_{\Lambda'}} & \text{, for the median and } \Lambda\mathrm{CDM} \ . \end{cases} \tag{70}$$

The ρ-statistics is thus favouring a 3−torus size slightly larger than $3L_H$ in the case without mask and is consistent with a 3−torus of side length $3L_H \approx 13.336\,\mathrm{Gpc}$ in the case with U73 mask. The analysis of ρ median and $\langle\rho\rangle$ with respect to the 3−torus side length L clearly shows (see the figures 3 and 4) that the derivatives are negative, $\mathrm{d}(\mathrm{median})/\mathrm{d}L < 0$ and $\mathrm{d}\langle\rho\rangle/\mathrm{d}L < 0$, as it is quantified by the linear equations (71), (72), (73) and (74) obtained by linear least square fitting (thereafter LSF). Figure 5 shows the relation between the side length L of the cubic 3−torus and the median or the arithmetic mean of ρ obtained from the samples consisting of 100 000 maps.

Except below $L = 1.0L_H$, the curves of $L = f(\mathrm{median})$ and $L = f(\langle\rho\rangle)$ look close to linear between $L = 1.0L_H$ and the three larger side lengths up to $L = 3.0L_H$. In the case without a mask, the linear least square fitting for the median case in the interval $36.285 \leq \mathrm{median}_{\mathrm{nomask}} \leq 42.907$ yields

$$\frac{L_{\mathrm{nomask}}(\mathrm{median})}{L_H} \approx -0.302\ \mathrm{median}_{\mathrm{nomask}} + 13.981\ , \tag{71}$$

and for the $\langle\rho\rangle$ case in the interval $36.173 \leq \langle\rho\rangle_{\mathrm{nomask}} \leq 42.755$, the LSF gives

$$\frac{L_{\mathrm{nomask}}(\langle\rho\rangle)}{L_H} \approx -0.304\ \langle\rho\rangle_{\mathrm{nomask}} + 14.021\ . \tag{72}$$

With applying the U73 mask, the LSF for the median case in the interval $36.400 \leq \mathrm{median}_{\mathrm{U73}} \leq 43.161$ yields

$$\frac{L_{\mathrm{U73}}(\mathrm{median})}{L_H} \approx -0.295\ \mathrm{median}_{\mathrm{U73}} + 13.751\ \ , \tag{73}$$

and for the $\langle\rho\rangle$ case in the interval $36.288 \leq \langle\rho\rangle_{\mathrm{U73}} \leq 43.031$, the LSF gives

$$\frac{L_{\mathrm{U73}}(\langle\rho\rangle)}{L_H} \approx -0.296\ \langle\rho\rangle_{\mathrm{U73}} + 13.750\ . \tag{74}$$

One may visually observe in figure 5 the better agreement with the linear behaviour of the curves with U73 mask (small dotted line for the median-case or small dashed line for the $\langle\rho\rangle$-case) in comparison to the slightly twisted curve (solid line or dotted dash line for the $\langle\rho\rangle$-case) obtained without mask pixel suppression. The χ^2 comparing the data points to the LSF's being with U73 mask $1.72\ 10^{-6}$ for the median and $7.5\ 10^{-7}$ for $\langle\rho\rangle$, while the χ^2 without mask is $2.929\ 10^{-5}$ for the median and $4.040\ 10^{-5}$ for $\langle\rho\rangle$. These χ^2-values are $\sim$17 (for the median) and ~ 54 (for $\langle\rho\rangle$) times larger without mask than with U73 mask. Thus, given the median and average ρ values of the four Planck NSSC maps, these LSF's of the data points yield, with the hypothesis of a flat 3−toroidal topology of our Universe,

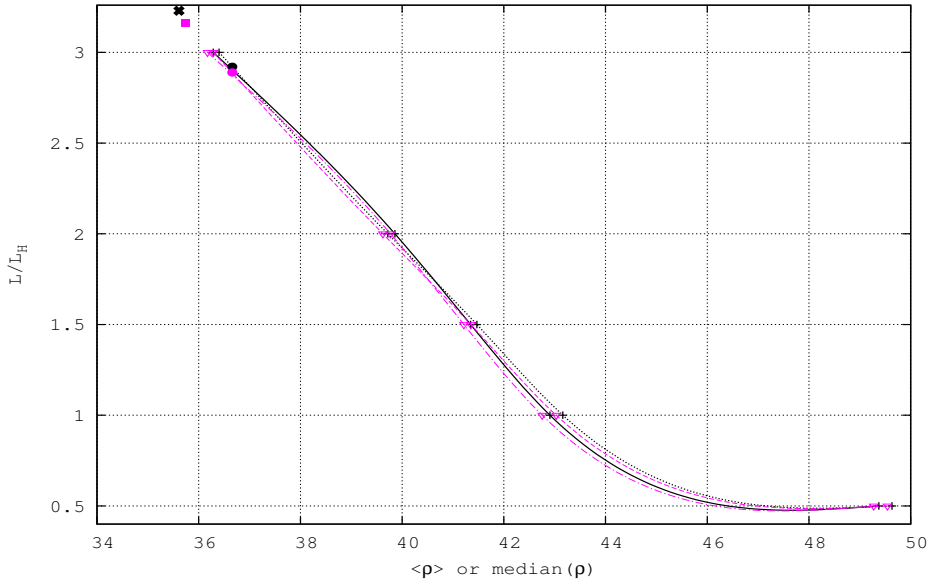

Figure 5: The side length L/L_H of the 3−torus as a function of the median of ρ in black and of $\langle\rho\rangle$ in magenta, for $L/L_H = [0.5, 1.0, 1.5, 2.0, 3.0]$. The median case without mask is in black solid line, and in black small-dotted line with U73 mask; the $\langle\rho\rangle$ case without mask is in dotted-dashed line, and in small-dashed line with U73 mask. For the median case, the thick black cross in the upper left at $L/L_H \approx 3.229$, respectively the thick black dot at $L/L_H \approx 2.920$, point at the side length of the $\mathcal{T}^3$ estimated from equation (71), respectively equation (73), using as argument the $\langle\rho\rangle$ of the NSSC Planck maps without mask, respectively with U73 mask. Similarly, for the $\langle\rho\rangle$ case of the Planck maps, the equation (72) without mask points at a side length of $L/L_H \approx 3.164$ (the solid square in the upper left), respectively the equation (74) with U73 mask pointing at a side length of $L/L_H \approx 2.889$ (the thick inferior dot).

a side length between 2.89 and 3.23 ($3.16 \leq L/L_H$ (no mask) ≤ 3.23 and $2.89 \leq L/L_H$ (U73 mask) ≤ 2.92).

According to the works [11], [38] and [77], 3−torus side lengths that are barely bigger than the CMB diameter ($L_{\text{limit}} = 2.2 r_{\text{SLS}}$, which translates to $6.93 L_H$, corresponding to a threshold ratio $R = 0.91$), do not allow for a clear detection of a multiply connected topology in the sense of the Kullback–Leibler divergence. A reasonable spatial section size that results in no difference with the infinite Universe was proposed in [38] to be $L_\infty = 4 r_{\text{SLS}} = 12.6 L_H$ giving $R = 0.5$. For this chapter we did not calculate ρ-values for L bigger than three Hubble radii to analyze the asymptotic behaviour of $L = f(\rho)$ presented in figure 5.

4.2.3 Comparison of two tori: $\mathbf{L = 0.5\,L_H}$ and $\mathbf{L = 3.0\,L_H}$

The CMB map for a 3−torus topology at $L = 0.5 L_H$ is shown in figure 6 and reveals that the small–scale structures are dominant, i.e. the anisotropy gradients at the smallest scales are strong almost everywhere, while no obvious structure at large scales appears. This contrasts to the CMB map for a six times larger 3−torus at $L = 3.0 L_H$ (figure 7), where the small–scale structures are superposed by large–scale structures, i.e. larger areas with similar temperatures are patching the CMB map. This is caused by the decreasing suppression of large–scale fluctuations with increasing size of the fundamental

cell, which is also revealed by the multipole spectrum C_l or the 2–pcf $C(\vartheta)$. The small smoothing scale of $\vartheta_G = (1/3)°$, which is applied in the CMB maps shown in figures 6 and 7, does not influence those features.

In both cases, a scale typical for the underlying 3−torus size visually betrays the topology (see the 2–pcf signature of each of these side lengths in figures 8 and 9). This visual illustration is in accordance with the conclusions in section 4.2.2 that the normalized local CMB gradient ρ characterizes and quantifies the 3−torus side length.

The CMB maps of different 3−torus sizes and of the infinite ΛCDM model have to be normalized in order to get the first acoustic peak of the power spectrum at the same level as in the Planck observation map. To this aim, the transfer function is computed for each averaged torus model, and the 1^{st} acoustic peak of the corresponding C_l spectrum is fitted to the 1^{st} peak of the Planck spectrum.

Figure 8 (respectively figure 9) display, for the case without mask, the average 2–pcf (over 100 000 simulation maps) of the torus at $L = 0.5L_H$ (respectively at $L = 3.0L_H$), compared with the average 2–pcf of the ensemble of 100 000 ΛCDM simulation maps and to the average 2–pcf of the four NSSC Planck maps.

An examination of the 2–pcfs of the cubic torus with $L = 0.5$ (shown in figure 8), and $3.0L_H$ (shown in figure 9) reveals the following:

- the torus with $L = 0.5L_H$ has no correlation for the pairs of pixels separated by more than 30°, on average;
- between 10° and 30°, and between 60° and 145°, the average 2–pcf for $L = 3.0L_H$ fits well the average 2–pcf of the Planck NSSC, better than the average 2–pcf of the ΛCDM model;
- for the small angles ϑ below 30° also the $\pm 1\sigma$ confidence region of the 3−torus at $L = 3.0L_H$ does not overlap with the corresponding region of the ΛCDM model.

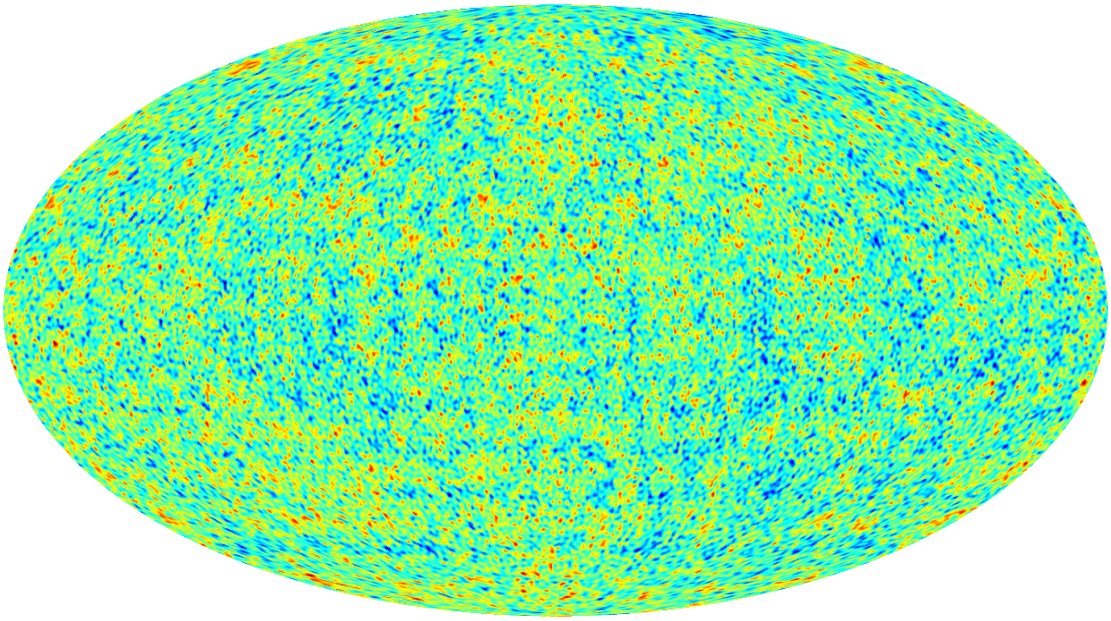

Figure 6: This figure shows a simulated CMB sky map (having the monopole and dipole subtracted) for a small cubic 3−torus fundamental cell of $L = 0.5L_H$. The resolution parameters are $N_{\text{side}} = 256$, $l_{\text{range}} = [2, 256]$ and $\vartheta_G = (1/3)^\circ$.

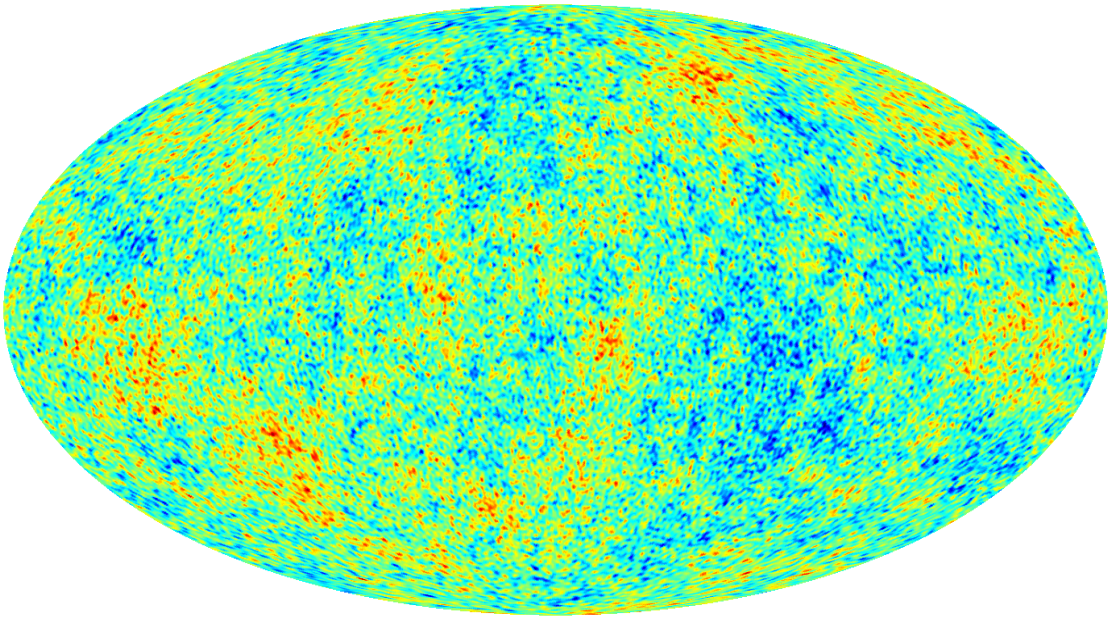

Figure 7: Figure showing a simulated CMB sky map (having the monopole and dipole subtracted) for a cubic 3−torus fundamental cell of $L = 3.0L_H$, which is six times larger than the one used for figure 6. The resolution parameters are those of the figure 6.

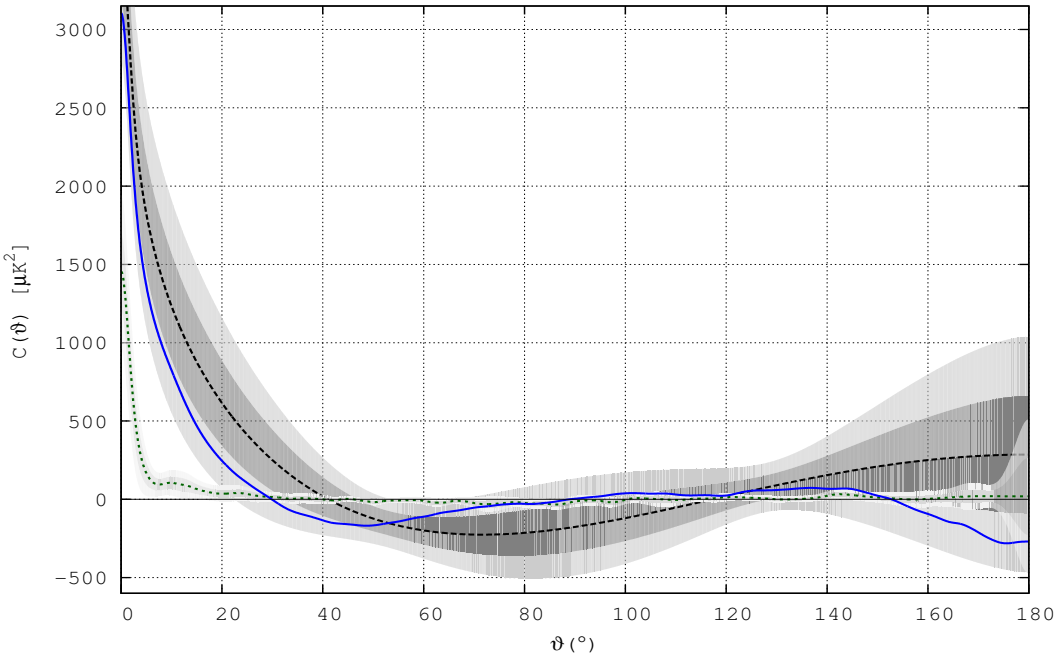

Figure 8: For 100 000 CMB maps without mask, at $N_{side} = 128$, $l_{max} = 256$ and a Gaussian smoothing of 2°fwhm: the average two-point correlation functions of the ΛCDM ensemble in large-dashed black line, of the torus at $L = 0.5L_H$ in green small-dashed line; $\pm 1\sigma$ in dark shaded area and $\pm 2\sigma$ in light shaded area are shown versus the average 2–pcf of the four Planck NSSC maps in solid blue line.

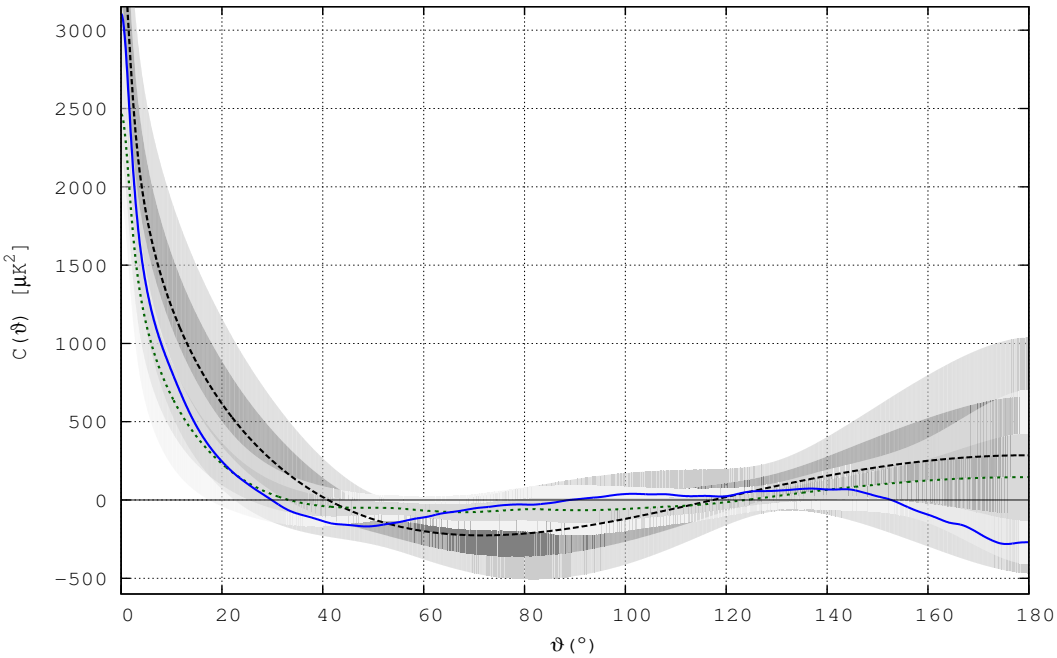

Figure 9: Same as figure 8, but for the torus at $L = 3.0L_H$.

4.2.4 Isotropy and homogeneity of the CMB with torus topology

We define a discrepancy function of the histogram of $P(\rho)$ shown in figure 3 by

$$\Delta P(\rho) := \frac{P_{\mathrm{IHG}}(\rho) - P(\rho)}{\max(P_{\mathrm{IHG}})} \ , \tag{75}$$

where the histogram $P_{\mathrm{IHG}}(\rho)$ is determined from the equations (58) and (59), while the histogram $P(\rho)$ is determined using equations (57) and (42). This quantifies the drift of the 3−torus CMB maps from the hypothesis of isotropy and homogeneity. We present in figure 10 the shape of the function (75) for the map ensembles of the ΛCDM and the 3−torus.

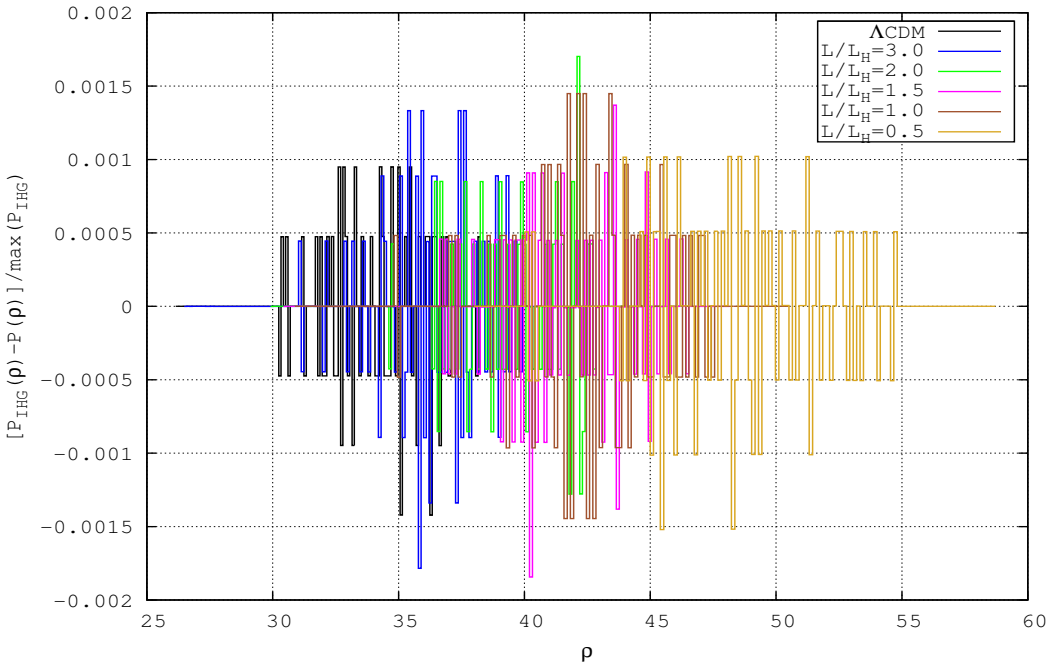

Figure 10: The level of isotropy and homogeneity of the CMB in a Universe with 3−torus topology is quantified with the discrepancy functions $\Delta P(\rho)$ of the histogram of $P(\rho)$ without mask. This figure is presented in solid lines with from left to right the ΛCDM in black, the 3−torus at $3.0L_H$ in blue, $2.0L_H$ in green, $1.5L_H$ in magenta, $1.0L_H$ in brown and at $0.5L_H$ in light brown.

The discretization of figure 10 is due to the very close values taken by the two histograms in each bin so that the discrepancy function progresses by leaps, because the histograms with IHG or without IHG differ only by zero or by a few multiples of unity before normalization. Despite the large number of 100 000 maps used for this ρ-statistics, figure 10 does neither present a smooth behaviour nor shape similarities from one 3−torus to another. Finally, this test proves the extremely high level of isotropy and homogeneity (in the sense of the formulas (58) and (59)) of all the ensembles of maps. This test over 100 000 maps allows to draw a firm conclusion, confirming that the ΛCDM CMB map ensemble is closer to the perfect IH (this is not a test of IHG but only of IH). The violation of the isotropy in the sense of ρ is nearly as small as for the five CMB map ensembles of the 3−torus under scrutiny given that $|\Delta P(\rho)| < 0.18\%$ for all the map ensembles. Thus, the relative global anisotropy of the 3−torus models barely appears here and we

will come later to methods able to detect it. Very likely, a similar analysis applied to the same large sample sizes but with a higher spatial resolution would lead to the same weak anisotropy and inhomogeneity.

4.2.5 **Discussion and outlook on ρ**

The 3−torus simulations of the CMB temperature anisotropies were computed by implementing the following effects of the Boltzmann physics and the influence of the discrete spectrum of vibrational modes dictated by the topology: the roster of physical ingredients of the 3−torus simulations includes the ordinary and integrated Sachs-Wolfe effects, the Doppler effect, Silk damping, reionization, photon polarization and neutrinos. The computation of the CMB anisotropies (CMB power spectrum) is carried out along the lines presented in [78]. We use as in [12] the definition of low-l values $l \in [2, 29]$ (see e.g. their figures 2 and 3 on page 6 of [12]) and high-l values for $l \geq 30$. At high-l values, the angular power spectrum $\delta T_l^2 := l(l+1)C_l/2\pi$ gets smoother and smoother and approaches for instance, near the first acoustic peak at $l = 221$ and for all the different 3−torus side lengths, the ΛCDM result (shown in [12], figure 57).

For the CMB simulations in the ΛCDM model, in addition to the effects enumerated above, lensing is present too. However, the impact of lensing would be sensitive for maps with $l_{max} \geq 400$ (see [79]) but all of our maps are limited to $l_{max} = 256$, and are furthermore smoothed to a resolution of 2° f.w.h.m. Because of this smoothing we have almost no power above $l = 100$ ... 150. Thus, the comparison between the 3−torus and the ΛCDM CMB maps remains unaffected by the effect of weak lensing in the ΛCDM simulation maps. Fully accounting for all these effects in a universe model with multiply or even simply connected topology for an *analytic* prediction of CMB observables such as ρ, or for a statistics such as the 2–pcf, is for the moment out of reach. The σ_n's defined for $n = 0, 1, 2, ...$ by [59],

$$\sigma_n^2 := \sum_{l=2}^{\infty} \frac{2l+1}{4\pi} C_l |F_l|^2 \frac{(l+n)!}{(l-n)!} \ , \tag{76}$$

are decreasing functions of ϑ_G, the scale of Gaussian smoothing (full width at half maximum), defined in equation (63). However, the decrease of (76) does not imply that the normalized variance of the gradient field, $\rho = \sqrt{\sigma_1^2/\sigma_0^2}$, of a CMB map is also everywhere a decreasing function of the smoothing angle ϑ_G.

In a flat Universe having three infinite spatial directions such as the ΛCDM model the spectrum is continuous. The average 2–pcf of the CMB map sample in the ΛCDM model (large-dashed line e.g. in figure 9) shows correlations at all angular scales.

Our investigation shows that ρ is a powerful signature probe that is sensitive to the size and the compactness of the spatial sections of the Universe. The ρ-statistics allows to hierarchically discriminate compact fundamental cells having the same 3−torus topology but different volumes. A clear distinction between a multiply connected flat universe model (the cubic 3−torus) and a simply connected flat universe model with infinite spatial sections (the ΛCDM model) is nicely verified for torus side lengths smaller than $L \sim 3L_H$ as shown in figures 3 and 4. For tori larger than about $L = 3.0L_H$ (see the discussion at the end of section 4.2.2), the calculation of a more refined grid of models would be needed. Different observables allow to detect a given multiply connected topology in a different way. On the one hand, the 2–pcf is able to detect on the CMB map the different

angular scales and the size of a given fundamental domain. On the other hand, ρ is by definition extremely sensitive to a change of the normalized CMB gradient as a function of the domain size and of the smoothing angle and amplitude. The ρ-statistics furnishes a complementary test of the multiply connected nature of the Universe along with the 2–pcf. The present results based on samples of 100 000 CMB maps with cubic torus topology are consistent with a Dirichlet domain side length of our Universe of $\sim 3.20 L_H$, or $\sim 2.90 L_H$ when the Planck and torus maps are cleaned up from the contaminated mask pixels. The investigated ρ-test may be included in future Bayesian analyses of model selection, with the expectation that a torus model in the above size range with the U73 mask might be favoured over the flat infinite model.

For the Planck maps, the 3−torus size around three Hubble radii or below, inferred from this ρ-study, is therefore slightly smaller than the torus size of $3.69 L_H$ inferred from the 2–pcf investigations. It remains to be seen whether other statistics like the Minkowski functionals, may lead to a slightly different optimal torus size. The sources of such a difference as well as the systematically negative skewness are currently investigated and thoroughly probed in other projects that employ the Minkowski functionals and topological characterization using Betti numbers and homological concepts such as hierarchical persistence, e.g. [80]. It will have to be verified that ρ could more generally detect size changes in finite fundamental cells of any geometry and topology. The vibrational modes (wave numbers and eigenfunctions of the Laplacian) along each compact spatial section and the interference (destructive or constructive) of these vibrational modes reveal the possible shapes of the underlying topological manifold. The 2–pcf says nothing about the non–Gaussianity of a random field. For some compact manifolds there are analytic premises of the CMB 2–pcf for the Sachs-Wolfe contribution, e.g. for the Poincaré dodecahedron [29], and general spherical spaces [29, 30]. Thus, the 2–pcf and ρ lead to identical diagnoses in two conceptually different ways.

The possibility of detecting the circle-in-the-sky (CITS) signal of a multiply connected topology has been discussed at the end of section 4.1.3. It is a geometric signal, while the 2–pcf and ρ are statistical observables. In [11], ΛCDM temperature simulation maps (with noise and Gaussian smoothing of the Planck SMICA map) with cubic 3−torus topology at $L/L_H = 2$ present all the pairs of matched circles that are expected. Also for the associated simulation maps of E-mode polarization, the multiply connected topology is detected with the $S^-_{\max}(\alpha)$ statistics. However, the same detection tools applied to the Planck 2015 observation maps for different circle patterns show no evidence of multiply connected topology with a size smaller than the distance to the CMB, i.e. $L \approx 3.15 L_H$. In view of recent survey results regarding the strong ISW effect, it is possible that this ISW signal (which is stronger than in the ΛCDM 3−torus simulations) impairs the detection of the CITS signal.

References

[1] Smoot G F et al. 1992 Structure in the *COBE* Differential Microwave Radiometer first-year Maps *Astrophys. J.* **396** L1-L5

[2] Wright E L et al. 1992 Interpretation of the Cosmic Microwave Background Radiation Anisotropy Detected by the *COBE* Differential Microwave Radiometer *Astrophys. J.* **396** L13-L18

[3] Hinshaw G, Banday A J, Bennett C L, Górski K M, Kogut A, Lineweaver C H, Smoot G F and Wright E L 1996 Two-Point Correlations in the *COBE* DMR Four-Year Anisotropy Maps *Astrophys. J.* **464** 25-28 (arXiv:astro-ph/9601061)

[4] Bennett C L et al. 2003 First-year Wilkinson Microwave Anisotropy Probe (WMAP) Observations: Preliminary maps and basic results *Astrophys. J. Suppl.* **148** 1-27 (arXiv:astro-ph/0302207)
[5] Hinshaw G et al. 2003 First-year Wilkinson Microwave Anisotropy Probe (WMAP) Observations: The angular power spectrum *Astrophys. J. Suppl.* **148** 135-159 (arXiv:astro-ph/0302217)
[6] Spergel D N et al. 2003 First-year Wilkinson Microwave Anisotropy Probe (WMAP) Observations: Determination of Cosmological Parameters *Astrophys. J. Suppl.* **148** 175-194 (arXiv:astro-ph/0302209)
[7] Bennett C L et al. 2011 Seven-Year Wilkinson Microwave Anisotropy Probe (WMAP) Observations: Are There Cosmic Microwave Background Anomalies? *Astrophys. J. Suppl.* **192** 1-19 (arXiv:1001.4758)
[8] Ade P A R et al. 2014 Planck 2013 results. XXIII. Isotropy and statistics of the CMB *Astron. Astrophys.* **571** A23 (arXiv:1303.5083)
[9] Ade P A R et al. 2016 Planck 2015 results. XIII. Cosmological parameters *Astron. Astrophys.* **594** A13 (arXiv:1502.01589)
[10] Ade P A R et al. 2016 Planck 2015 results. XVI. Isotropy and statistics of the CMB *Astron. Astrophys.* **594** A16 (arXiv:1506.07135)
[11] Ade P A R et al. 2016 Planck 2015 results XVIII. Background geometry and topology of the universe *Astron. Astrophys.* **594** A18 (arXiv:1502.01593)
[12] Aghanim N et al. 2020 Planck 2018 results. V. CMB power spectra and likelihoods *Astron. Astrophys.* **641** A5 (arXiv:1907.12875)
[13] Akrami Y et al. 2020 Planck 2018 results. VII. Isotropy and Statistics of the CMB *Astron. Astrophys.* **641** A7 (arXiv:1906.02552)
[14] Bond J R and Efstathiou G 1987 The statistics of cosmic background radiation fluctuations *Mon. Not. Roy. Astr. Soc.* **226** 655-687
[15] Holtzman J A 1989 Microwave background anisotropies and large-scale structure in Universes with cold dark matter, baryons, radiation, and massive and massless neutrinos *Astrophys. J. Suppl.* **71** 1-24
[16] Riess A G et al. 1998 Observational evidence from supernovae for an accelerating universe and a cosmological constant *Astron. J.* **116** 1009-1038 (arXiv:astro-ph/9805201)
[17] Perlmutter S et al. 1999 Measurement of Ω and Λ from 42 high-redshift supernovae *Astrophys. J.* **517** 565-586 (arXiv:astro-ph/9812133)
[18] Stevens D, Scott D and Silk J 1993 Microwave background anisotropy in a toroidal universe *Phys. Rev. Lett.* **71** 20-23
[19] Starobinsky A A 1993 New restrictions on spatial topology of the universe from microwave background temperature fluctuations *JETP Letters* **57** 622-625 (arXiv:gr-qc/9305019)
[20] Lachièze-Rey M and Luminet J P 1995 Cosmic Topology *Phys. Reports* **254** 135-214 (arXiv:gr-qc/9605010)
[21] Cornish N J, Spergel D N and Starkman G D 1996 Does Chaotic Mixing Facilitate $\Omega < 1$ Inflation? *Phys. Rev. Lett.* **77** 215-218 (arXiv:astro-ph/9601034)
[22] Cornish N J, Spergel D N and Starkman G D 1998 Circles in the sky: finding topology with the microwave background radiation *Class. Quantum Grav.* **15** 2657-2670 (arXiv:gr-qc/9602039)
[23] Roukema B F 2000 COBE and global topology: an example of the application of the identified circles principle *Mon. Not. Roy. Astr. Soc.* **312** 712-723 (arXiv:astro-ph/9910272)
[24] Roukema B F 2000 A counterexample to claimed COBE constraints on compact toroidal universe models *Class. Quantum Grav.* **17** 3951-3963 (arXiv:astro-ph/0007140)
[25] Buchert T, France M J and Steiner F 2017 Model–independent analyses of non-Gaussianity in Planck CMB maps using Minkowski functionals *Class. Quantum Grav.* **34** 094002 (arXiv:1701.03347)

[26] Aurich R, Lustig S, Steiner F and Then H 2004 Hyperbolic universes with a horned topology and the cosmic microwave background anisotropy *Class. Quantum Grav.* **21** 4901-4925 (arXiv:astro-ph/0403597)
[27] Aurich R, Steiner F and Then H 2012 Numerical Computation of Maass Waveforms and an Application to Cosmology. In: *Hyperbolic Geometry and Applications in Quantum Chaos and Cosmology* (eds. Bolte J and Steiner F) *London Math. Soc. Lecture Notes Series* **397**, 229-269, Cambridge Univ. Press (arXiv:gr-qc/0404020)
[28] Aurich R, Lustig S, Steiner F and Then H 2005 Indications about the shape of the universe from the Wilkinson Anisotropy Probe data *Phys. Rev. Lett.* **94** 021301 (arXiv:astro-ph/0412407)
[29] Aurich R, Lustig S and Steiner F 2005 CMB anisotropy of the Poincaré dodecahedron *Class. Quantum Grav.* **22** 2061 (arXiv:astro-ph/0412569)
[30] Aurich R, Lustig S and Steiner F 2005 CMB anisotropy of spherical spaces *Class. Quantum Grav.* **22** 3443 (arXiv:astro-ph/0504656)
[31] Spergel D N et al. 2007 Three-year Wilkinson Microwave Anisotropy Probe (WMAP) Observations: Implications for Cosmology *Astrophys. J. Suppl.* **170** 377-408 (arXiv:astro-ph/0603449)
[32] Aurich R, Janzer H S, Lustig S and Steiner F 2008 Do we live in a "small Universe"? *Class. Quantum Grav.* **25** 125006 (arXiv:0708.1420)
[33] Roukema B F, Buliński Z, Szaniewska A and Gaudin N E 2008 The optimal phase of the generalised Poincaré dodecahedral space hypothesis implied by the spatial cross–correlation function of the WMAP sky maps *Astron. Astrophys.* **486** 55-72 (arXiv:0801.0006)
[34] Copi C J, Huterer D, Schwarz D J and Starkman G D 2009 No large–angle correlations on the non–Galactic microwave sky *Mon. Not. Roy. Astr. Soc.* **399** 295-303 (arXiv:0808.3767)
[35] Aurich R, Lustig S and Steiner F 2010 Hot pixel contamination in the CMB correlation function? *Class. Quantum Grav.* **27** 095009 (arXiv:0903.3133)
[36] Aurich R and Lustig S 2014 The Hantzsche-Wendt manifold in cosmic topology *Class. Quantum Grav.* **31** 165009 (arXiv:1403.2190)
[37] Aurich R 2015 A spatial–correlation analysis of the cubic 3−torus topology based on the Planck 2013 data *Mon. Not. Roy. Astr. Soc.* **452** 1493-1501 (arXiv:1412.5355)
[38] Bernui A, Novaes C P, Pereira T S and Starkman G D 2018 Topology and the suppression of CMB large-angle correlations (arXiv:1809.05924)
[39] Tegmark M, de Oliveira-Costa A and Hamilton J S 2003 High resolution foreground cleaned CMB map from WMAP *Phys. Rev. D* **68** 123523 (arXiv:astro-ph/0302496)
[40] de Oliveira-Costa A et al. 2004 Significance of the largest scale CMB fluctuations in WMAP *Phys. Rev. D* **69** 063516 (arXiv:astro-ph/0307282)
[41] Schwarz D J, Copi C J, Huterer D and Starkman G D 2016 CMB anomalies after Planck *Class. Quantum Grav.* **33** 184001 (arXiv:1510.07929)
[42] Aurich R 1999 The Fluctuations of the Cosmic Microwave Background for a Compact Hyperbolic Universe *Astrophys. J.* **524** 497-503 (arXiv:astro-ph/9903032)
[43] Aurich R and Steiner F 2001 The Cosmic Microwave Background for a Nearly Flat Compact Hyperbolic Universe *Mon. Not. Roy. Astr. Soc.* **323** 1016-1024 (arXiv:astro-ph/0007264)
[44] Aurich A and Steiner F 2003 Quintessence with a constant equation of state in hyperbolic universes *Phys. Rev. D* **67** 123511 (arXiv:astro-ph/0212471)
[45] Aurich R and Steiner F 2004 Quintessence and the curvature of the universe after WMAP *Int. J. Mod. Phys. D* **13** 123-136 (arXiv:astro-ph/0302264)
[46] Luminet J P et al. 2003 Dodecahedral space topology as an explanation for weak wide-angle temperature correlations in the cosmic microwave background *Nature* **459** 593-595 (arXiv:astro-ph/0310253)
[47] Aurich R, Lustig S, Steiner F and Then H 2007 Cosmic microwave background alignment

in multi-connected spaces *Class. Quantum Grav.* **24** 1879 (arXiv:astro-ph/0612308)
[48] Aghanim N et al. 2020 Planck 2018 results. VI. Cosmological parameters *Astron. Astrophys.* **641** A6 (arXiv:1807.06209)
[49] Efstathiou G and Gratton S 2020 The evidence for a spatially flat Universe *Mon. Not. Roy. Astr. Soc.* **496** 91-95 (arXiv:2002.06892)
[50] Di Valentino E, Melchiorri A and Silk J 2020 Planck evidence for a closed Universe and a possible crisis for cosmology *Nature Astron.* **4** 196–203 (arXiv:1911.02087)
[51] Vagnozzi S, Loeb A and Moresco M 2021 Eppur è piatto? The Cosmic Chronometers Take on Spatial Curvature and Cosmic Concordance *Astrophys. J.* **908** 84 (arXiv:2011.11645)
[52] Di Valentino E, Melchiorri A and Silk J 2021 Investigating Cosmic Discordance *The Astrophys. J.* **908** L9 (arXiv:2003.04935)
[53] Vagnozzi S, Di Valentino E, Gariazzo S, Melchiorri A, Mena O and Silk J 2021 The galaxy power spectrum take on spatial curvature and cosmic concordance *Phys. Dark Univ.* **33** 100851 (arXiv:2010.02230)
[54] Handley W 2021 Curvature tension: Evidence for a closed universe *Phys. Rev. D* **103** L041301 (arXiv:1908.09139)
[55] Buchert T, Coley A, Kleinert H, Roukema B F and Wiltshire D L 2016 Observational challenges for the standard FLRW model *Int. J. of Mod. Phys. D* **25** 1630007 (arXiv:1512.03313)
[56] Perivolaropoulos L and Skara F 2021 Challenges for ΛCDM: An update (arXiv:2105.05208)
[57] Di Valentino E, Mena O, Pan S, Visinelli L, Yang W, Melchiorri A, Mota D F, Riess A G and Silk J 2021 In the realm of the Hubble tension—a review of solutions *Class. Quantum Grav.* **38** 153001 (arXiv:2103.01183)
[58] Heinesen A and Buchert T 2020 Solving the curvature and Hubble parameter inconsistencies through structure formation-induced curvature *Class. Quantum Grav.* **37** 164001 *Erratum*: 229601 (arXiv:2002.10831)
[59] Aurich R, Janzer H S, Lustig S and Steiner F 2011 Ellipticity of Structures in CMB Sky Maps *Int. J. Mod. Phys. D* **20** 2253-2280 (arXiv:1007.2722)
[60] Arendt W, Nittka R, Peter W and Steiner F 2009 Weyl's Law: Spectral Properties of the Laplacian in Mathematics and Physics, in: Mathematical Analysis of Evolution, Information, and Complexity (eds Arendt W and Schleich W P) Wiley-VCH eISBN 9783527408306 1-71
[61] Infeld L 1949 On The Structure of Our Universe, in: Albert Einstein: Philosopher-Scientist 2000 (The Library of Living Philosophers, Vol. VII (New York: MFJ Books, ed. Schilpp P A), pp.475-499. See also Einstein's reply, l.c. p.686. eISBN 9780875482866
[62] Efstathiou G and Gratton S 2020 A Detailed Description of the CamSpec Likelihood Pipeline and a Reanalysis of the Planck High Frequency Maps (arXiv:1910.00483)
[63] Cornish N J, Spergel D N, Starkman G D and Komatsu E 2004 Constraining the Topology of the Universe *Phys. Rev. Lett.* **92** 201302 (arXiv:astro-ph/0310233)
[64] Aurich R, Lustig S and Steiner F 2006 The circles-in-the-sky signature for three spherical universes *Mon. Not. Roy. Astr. Soc.* **369** 240-248 (arXiv:astro-ph/0510847)
[65] Vaudrevange P M, Starkman G D, Cornish N J and Spergel D N 2012 Constraints on the topology of the Universe: Extension to general geometries *Phys. Rev. D* **86** 083526 (arXiv:1206.2939)
[66] Gomero G I, Mota B and Rebouças M J 2016 Limits of the circles–in–the–sky searches in the determination of cosmic topology of nearly flat universes *Phys. Rev. D* **94** 043501 (arXiv:1604.02179)
[67] Kovács A et al. 2019 More out of less: an excess integrated Sachs-Wolfe signal from supervoids mapped out by the Dark Energy Survey *Mon. Not. Roy. Astr. Soc.* **484** 5267-5277 (arXiv:1811.07812)
[68] F Steiner 2016 Do black holes exist in a finite Universe having the topology of a flat 3−torus?

(arXiv:1608.03133)
[69] Fixsen D J 2009 The Temperature of the Cosmic Microwave Background *Astrophys. J.* **707** 916-920 (arXiv:0911.1955)
[70] Monteserín C, Barreiro R B, Sanz J L and Martínez-Gonzaléz E 2005 Scalar statistics on the sphere: application to the cosmic microwave background *Mon. Not. Roy. Astr. Soc.* **360** 9–26 (arXiv:astro-ph/0511308)
[71] Schmalzing J and Górski K M 1998 Minkowski Functionals used in the morphological analysis of Cosmic Microwave Background anisotropy maps *Mon. Not. Roy. Astr. Soc.* **297** 355–365 (arXiv:astro-ph/9710185)
[72] Adler R J 1981 The Geometry of Random Fields *SIAM edition* eISBN 9780898718980
[73] Tomita H 1986 Statistical Properties of Random Interface System *Prog. Theor. Phys.* **75** 952
[74] Tomita H 1986 Curvature Invariants of Random Interface Generated by Gaussian Fields *Prog. Theor. Phys.* **76** 4
[75] Schmalzing J and Buchert T 1997 Beyond genus statistics: a unifying approach to the morphology of cosmic structure *Astrophys. J.* **482** L1–L4 (arXiv:astro-ph/9702130)
[76] Marcinkiewicz J 1939 Sur une propriété de la loi de Gauß *Math. Z.* **44** 612-618
[77] Fabre O, Prunet S and Uzan J-P 2015 Topology beyond the horizon: How far can it be probed? *Phys. Rev. D* **92** 043003 (arXiv:1311.3509)
[78] Aurich R and Lustig S 2016 Early-matter-like dark energy and the cosmic microwave background *J. Cosmol. Astropart. Phys.* **JCAP01(2016)021** (arXiv:1511.01691)
[79] Durrer R The Cosmic Microwave Background 2008 *Cambridge University Press* eISBN 9780511817205
[80] Pranav P, Adler R J, Buchert T, Edelsbrunner H, Jones B J T, Schwartzman A, Wagner H and van de Weygaert R 2019 Unexpected topology of the temperature fluctuations in the cosmic microwave background *Astron. Astrophys.* **627** A163 (arXiv:1812.07678)

5 CMB non-Gaussianity: a model-independent analysis

This second research paper presented in my PhD thesis investigates the non-Gaussianity of the CMB temperature map a model-independent way. Thomas Buchert, my PhD supervisor, suggested that for the purpose of a paper we go further in the application, to the CMB map, of the morphological and statistical descriptors said Minkowski functionals (MFs). MFs have been first applied to cosmology by Mecke, Buchert and Wagner then implemented by Schmalzing and Buchert using excursion sets and adapted to the analysis of the CMB temperature anisotropy by Schmalzing and Górski (see the bibliography in this chapter).

In the literature the weak non-Gaussianity (weak NG) of the CMB temperature map was often probed a model-dependent way. Indeed, Thomas Buchert, Frank Steiner and me were intrigued by papers of T Matsubara working out analytical formulae of the MFs of the CMB using perturbation theory and imposing hierarchical ordering of the PDF cumulants (this hierarchical ordering was assumed in some models of inflation). These perturbative expansions of the CMB NG were developed as power series of σ_0 the standard deviation of the CMB temperature anisotropy. But σ_0 was not small, as it should be for such perturbative expansions which are valid in the neighbourhood of zero.

Frank Steiner devised model-independent expansions of the CMB non-Gaussianity without use of the perturbation theory and for arbitrarily large NG. We calculated the signatures of CMB deviation from Gaussianity by expressing them in terms of discrepancy functions (normalized difference of each given descriptor and its Gaussian premise) and this for the PDF and the 3 MFs. Our expansions of the CMB NG made use of the Hermite orthogonal polynomials (method of Gauss-Hermite quadrature denoted thereafter GHQ). I developed and adapted the formalisms giving me a base to write numerically implementable algorithms. Thus my computations allowed us to analyse large ensembles of CMB maps (100 000 to 200 000) in terms of discrepancy functions of the PDF and the three MFs and to calculate the GHQ expansions and the model-dependent expansions with hierarchical ordering. Our comparative results showed that our model-independent method was, for a given order of expansion, a better fit to the CMB non-Gaussianity than the model-dependent expansion with hierarchical ordering. I wrote the draft of the paper in LaTeX and we iterated with Buchert and Steiner to finalize and submit **Model-independent analyses of non-Gaussianity in Planck CMB maps using Minkowski functionals** (published in 2017) (see references page xvi). I contributed much to the investigations, algorithmics, computing, bibliography and redaction but the alphabetical authorship (Thomas Buchert, Martin J France and Frank Steiner), adopted generally for papers in e.g. high-energy physics, was decided.

5.1 CMB statistics in the infinite ΛCDM Universe

Probing the non–Gaussianity of the CMB temperature map

In his March 26, 2010 talk (Observational Constraints on Primordial Non–Gaussianity) during the 'Non–Gaussian Universe' workshop at the Yukawa institute (YITP), Eiichiro Komatsu [1] concluded about the statistical analysis of the Cosmic Microwave

Background (CMB): "So far, no detection of primordial non–Gaussianity of any kind by any method"[22]. This conclusion, strengthened by the analysis of the last available CMB data at the time ($WMAP$ 7yr)—and the reader may judge, after reading this chapter and in the future, whether we can say more after *Planck*—sounded like a challenge to the cosmological community. An ongoing challenge, because the high–precision *Planck* CMB data are certainly not exhaustively analysed today. A challenge also as there are as many analytical definitions of 'non–Gaussianity' as there are different statistical descriptors calling for the application of unified statistical analysis tools. But mostly a challenge, because in the frame of the ΛCDM model and various inflationary models, a non–detectable up to a non–negligible primordial non–Gaussianity may be expected [2–4], as measured by bi– and tri–spectra [5]. In various other models of primordial physics we may expect different kinds of primordial non–Gaussianity for the CMB as, e.g., in string gas cosmology [6], or even large non–Gaussianity such as in some ekpyrotic phase models [7]. Furthermore, it is a challenge given that a sufficiently high tensor–to–scalar ratio r should allow for a slight detection of primordial gravitational waves with the non–Gaussianity of the CMB polarization (B–mode) and temperature maps correlation function ($\langle BTT \rangle$ bispectrum)[23] [9,10] and see (inter alia) the chapter 7 "Lensing and the CMB" in the book by Durrer [8].

Given the variety of potential contaminations in the cosmic microwave background map, a good strategy to analyse it and discriminate primordial non–Gaussianity from secondary effects is not only to multiply the statistical methods, but to head for model–independent estimators. For that, integral geometry provides us with a general mathematical framework where a small set of descriptors allows for a complete morphological analysis over random fields such as the CMB temperature maps. The descriptive power of integral geometry relies on the polynomial of convex bodies in three dimensions, introduced by J. Steiner (1840) [17], its generalization to the mixed volume associated to a convex body by Minkowski [18], and the Blaschke problem and diagram. Then, the Bonnesen enhanced isoperimetric inequality (1921), the Aleksandrov (Fenchel) inequalities (1937), the Hadwiger works and theorem (1955, 1957) [19], the studies by Santaló (1976) [20], the statistical predictions for random fields by Adler (1981) [21] and the work by Tomita (1986) [22,23] bring the key mathematical foundations to the Minkowski Functionals (henceforth 'MFs'). Interesting theoretical and applied developments are found in the mathematical reviews by Groemer [24], Schneider [25] and Mecke [26].

The theory of $2D$ Gaussian random fields on the CMB 2–sphere was developed by Bond and Efstathiou (1987) [27]. They applied it to the number density of hot and cold spots and to the ellipticity of peaks. This has later been generalized for extrema counts and ellipticity contour lines by Aurich et al. [28] and also by Pogosyan et al. [29–31].

Minkowski Functionals comprise the by now well–known set of scalar functionals, being rotation and translation invariant, Minkowski additive[24], and conditionally continuous. This set of MFs describes the morphology of any convex body[25] in a

[22] http://wwwmpa.mpa-garching.mpg.de/~komatsu/talks.html .

[23] However, small angular scales (l>200) temperature anisotropies have to be analysed to reach the convergence power spectrum of the B–modes; unfortunately, at such scales the Sunyaev–Zel'dovich effect and reionization scattering pollute the temperature lensing reconstruction.

[24] Minkowski additivity assigns a functional of the union of bodies to the functionals of the individual bodies minus the functionals of their intersection.

[25] Even more generally, the morphology of non–convex bodies is made possible using the property

complete and unique way in the sense of Hadwiger's theorem. The explicit introduction of the MFs into cosmology (describing the morphology of galaxy distributions) was made in statistics of large–scale structure using the Boolean grain description by Mecke et al. (1994) [32] with follow–up studies of galaxy catalogues [33–35]; Kerscher wrote a review on the MFs including applications to cosmology [36]. In 1997, Schmalzing and Buchert introduced the MFs for the excursion set approach, suitable for any density or temperature contour maps [37]. In 1998, Schmalzing and Górski are the first to apply the set of $3+1$ MFs of the CMB 2–sphere (curvature=+1) to COBE DMR data excursion sets on a quadriteralized spherical cube tesselation (6 $[2^{2(N-1)}]$ pixels) [38], implementing also the Gaussian premises predicted in 1990 by Tomita [39]. (See also [40].) Also, galaxy catalogues have been analysed with the excursion set approach [41, 42], and a generalization to vector–valued MFs has been proposed [43] and applied to the morphological evolution of galaxy clusters [44].

At present, many fundamental tools are available to take up the challenge in the broad sense of several different but unified statistical descriptors to ask: is the cosmic microwave background Gaussian? Looking at CMB non–Gaussianity within the MF approach was first undertaken by Winitzki and Kosowsky [45], and by Novikov et al [46]. Following work by Takada *et al.* [47] on the detectability of the weak lensing with the two–point correlation function, a further study predicts that the weak lensing effect could be detected directly with the MFs v_1 and v_2 [48]. Not only this capability of the MFs was confirmed in later work, but also the lensing–induced morphology changes in modified gravity theories could be detected. Furthermore, the lensing and the Sunyaev–Zel'dovich non–Gaussianity can be separately detected with MFs, all of this for CMB temperature maps at high resolution (up to $\ell = 3000$) [49]. Specific, regional morphological features like the *Cold Spot* could be detected by local analyses with MFs [50].

Since then the majority of works rely on model assumptions, either by testing a given inflationary model as in [46], or explicitly replacing the analytic Gaussian premises for the MFs by the MFs of a grid of ΛCDM model maps: the so–evaluated deviations from non–Gaussianity yield what we below call the 'difference of the normalized MFs' (abridged by Df) (see [51–56], to mention only a few works in this context). These authors argue that the noise, the mask and the pixel effects are better taken into account by using a model ensemble rather than using analytical predictions for evaluating the data map non–Gaussianity.

Ade et al. [56] propose a rather exhaustive (claimed model–independent) investigation of the CMB isotropy and statistics and neither reach a clear rejection nor a confirmation of the standard FLRW cosmological model. It is then a natural next step to investigate perturbative models at a FLRW background (here the works by Matsubara [57, 57, 59] stand out as a sustained such attempt). In this chapter we follow another route. We focus on and specify model–independent methods to quantify non–Gaussianity, and we compare with what is obtained when applying the standard model–dependent perturbative ansatz. General perturbative expansions are based on series of terms, some of which are solely specified in terms of the chosen model [60–62], leaving a certain degree of arbitrariness in the application of perturbation theory. Beyond perturbation theory taken in this broad sense, we can fundamentally explore the non–Gaussianity only when using non–perturbative expansions. We shall introduce these latter paying careful attention to some methodological details that may have a strong impact

of Minkowski additivity, extending the analysis to the convex ring.

on the extremely weak level of CMB non–Gaussianity.

5.2 PDF and Minkowski Functionals of the CMB map

The CMB anisotropy δT is described by a scalar random field on the surface of last scattering. The CMB support manifold is idealized by the constant curvature 2−sphere $\mathcal{S}^2$, but different supports of variable curvature may be envisaged for the CMB. Furthermore, the thickness of the surface of last scattering is not taken into account. The manifold $\mathcal{S}^2$ is very convenient and universally adopted and we use it in the present work too. Upon this chosen manifold, any statistical descriptor such as the Minkowski Functionals is otherwise model–independent.

5.2.1 Probability density function of the CMB temperature map

An important statistical descriptor of the random variable δT is its *probability density function* (PDF) or *frequency function* $P(\tau) \geq 0$, where we assume that τ can take on any real value, and $P(\tau)$ is continuous. (The more general case will be discussed below.) $P(\tau)\mathrm{d}\tau$ gives the probability of finding δT in between τ and $\tau + \mathrm{d}\tau$. Hence, $P(\tau)$ is normalized to unity.
Figure 11 shows the 10^5 histograms envelope of the individual PDFs in the ΛCDM sample over a total temperature range $\pm 396.5 \mu K$, divided into 61 bins of $13 \mu K$. Detailed informations regarding the ΛCDM map sample generation, the numerical methodology, and the conventions adopted for the analysis all along this work are given in Appendix 8.2.
From $P(\tau)$ one obtains the *cumulative distribution function* $F(\tau)$ (CDF),

$$F(\tau) := \mathrm{prob}(\delta T < \tau) = \int_{-\infty}^{\tau} P(\tau')\mathrm{d}\tau' \quad , \tag{77}$$

respectively, the *complementary cumulative distribution function* $F_C(\tau)$ (CCDF)[26],

$$F_C(\tau) := \mathrm{prob}(\delta T \geq \tau) = \int_{\tau}^{\infty} P(\tau')\mathrm{d}\tau' = 1 - F(\tau) \quad , \tag{78}$$

satisfying $F(-\infty) = 0$, $F(\infty) = 1$, respectively, $F_C(-\infty) = 1$, $F_C(\infty) = 0$. Note that $F(\tau)$ is non–decreasing and $\mathrm{prob}(\tau_1 \leq \tau < \tau_2) = F(\tau_2) - F(\tau_1)$.

For a continuous function $f : \mathbb{R} \to \mathbb{R}$, $f(\delta T)$ is again a random field whose *expectation value* is defined as:

$$\langle f(\delta T) \rangle := \int_{-\infty}^{\infty} f(\tau) P(\tau) \mathrm{d}\tau \quad , \tag{79}$$

if the integral exists. An important role is played by the *moments* α_n of δT,

$$\alpha_n := \langle (\delta T)^n \rangle := \int_{-\infty}^{\infty} \tau^n P(\tau) \mathrm{d}\tau \quad ; \quad n = 0, 1, 2, \cdots \quad , \tag{80}$$

[26] It will turn out that $F_C(\tau)$ is identical to the *Minkowski Functional* v_0 (see below).

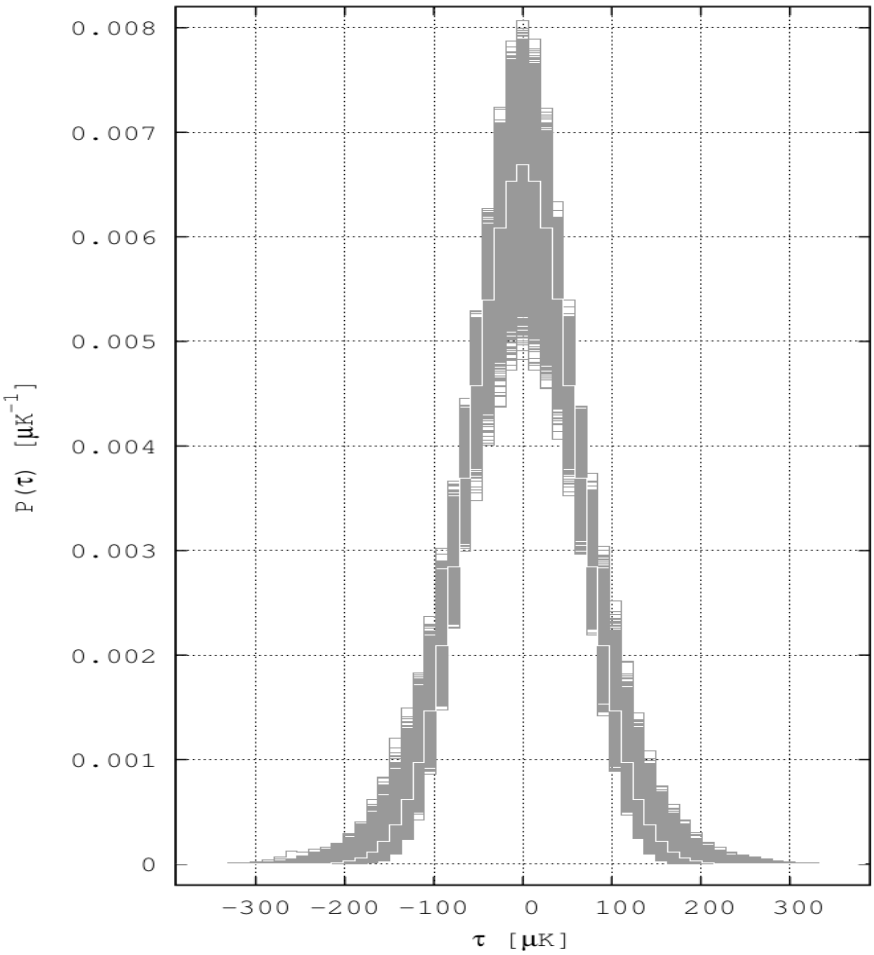

Figure 11: ΛCDM map sample, $N_{\rm side}$=128, $\ell_{\rm range}$=[2,256] without mask, 2° fwhm, for a 13μK temperature bin width over the largest temperature range of the sample ($\pm 396.5 \mu K$). We plot the envelope of P(τ) histograms for the ensemble of 10^5 simulation maps. Each PDF histogram is normalized to 1 (the cosmic variance being not shown here as it is not normalized to 1). The small asymmetries of this envelope reflect a non–vanishing skewness. The average of all the individual PDFs is the white histogram from which the centre τ_ℓ of each white horizontal segment serves as comparison point with the Gaussian hypothesis (of the averages), used to calculate the discrepancy function. (Model and computational details are given in Appendix 8.2).

the *central moments* m_n (i.e., the moments about the *mean* $\mu := \alpha_1$),

$$m_n := \langle (\delta T - \mu)^n \rangle := \int_{-\infty}^{\infty} (\tau - \mu)^n P(\tau) \mathrm{d}\tau \ , \tag{81}$$

and the *cumulants* $\varkappa_n := \langle (\delta T)^n \rangle_C$. The *generating function of the moments* α_n is given by:

$$M(x) := \left\langle \mathrm{e}^{x \delta T} \right\rangle = \int_{-\infty}^{\infty} \mathrm{e}^{x\tau} P(\tau) \mathrm{d}\tau = \sum_{n=0}^{\infty} \alpha_n \frac{x^n}{n!} \ , \tag{82}$$

from which one obtains the *generating function of the cumulants* $\varkappa_n$,

$$C(x) := \ln M(x) = \sum_{n=1}^{\infty} \varkappa_n \frac{x^n}{n!} \quad . \tag{83}$$

The first few moments and cumulants are $\alpha_0 = m_0 = 1$, the *mean values* $\mu := \alpha_1 = \varkappa_1$, respectively, $m_1 = 0$, and the *variance* σ_0^2,

$$\sigma_0^2 := \left\langle (\delta T - \mu)^2 \right\rangle = m_2 = \alpha_2 - \mu^2 = \varkappa_2 \quad , \tag{84}$$

respectively, the *standard deviation* (uncertainty) $\sigma_0 = \sqrt{\alpha_2 - \mu^2}$. There are the following *recurrence relations*:

$$m_n = \sum_{r=0}^{n} \left(\begin{array}{c} n \\ r \end{array} \right) (-1)^{n-r} \mu^{n-r} \alpha_r \quad ; \quad n = 0, 1, 2, \cdots \quad , \tag{85}$$

and, for $n \geq 2$:

$$\varkappa_n = m_n - \sum_{r=1}^{n-1} \left(\begin{array}{c} n-1 \\ r-1 \end{array} \right) \varkappa_r m_{n-r} \quad . \tag{86}$$

Any odd non–vanishing central moment m_{2n+1} of the CMB anisotropy δT is a measure of the *skewness* of $P(\tau)$; the simplest of these is

$$m_3 = \varkappa_3 = \alpha_3 - 3\mu\alpha_2 + 2\mu^3 \quad , \tag{87}$$

respectively, the dimensionless *skewness coefficient*

$$\gamma_1 := \frac{m_3}{\sigma_0^3} \quad . \tag{88}$$

This latter indicates a possible asymmetry of $P(\tau)$, i.e., whether the left tail ($\gamma_1 < 0$) or the right tail ($\gamma_1 > 0$) is more pronounced. Another important measure of the "tailedness" of $P(\tau)$ is the dimensionless *excess kurtosis* (sometimes simply called kurtosis or excess),

$$\gamma_2 := \frac{m_4}{\sigma_0^4} - 3 \quad . \tag{89}$$

It should be stressed that the basic equations (77), (78), and (79) will in general only hold for the theoretical continuous limit distributions of the CMB anisotropy in the sense of ensemble averages in the limit of an infinite ensemble (infinitely many realizations). For a single realization, as it is the case for the data obtained by *WMAP* or *Planck*, or in computer simulations using a large but finite number of realizations, the distributions will in general not be continuous but rather discrete and, thus, the PDF will not satisfy $P(\tau) = \mathrm{d}F/\mathrm{d}\tau = -\mathrm{d}F_C/\mathrm{d}\tau$, as is implied by (77), respectively (78). Instead, the above Riemann integrals have to be replaced by Riemann–Stieltjes integrals such that, for example, the *expectation value* (79) is given by:

$$\langle f(\delta T) \rangle := \int_{-\infty}^{\infty} f(\tau) \mathrm{d}F(\tau) \quad . \tag{90}$$

The last relation even holds in cases where $F(\tau)$ is ill–behaved, for example, if $F(\tau)$ has at most enumerably many jumps at the discrete points τ_ℓ, and as long as $F(\tau)$ is a CDF. In this case one has (if the integral and the sum over ℓ converge):

$$\langle f(\delta T) \rangle := \int_{-\infty}^{\infty} f(\tau) F'(\tau) \mathrm{d}\tau + \sum_{\ell} f(\tau_\ell) [F(\tau_\ell + 0) - F(\tau_\ell - 0)] \quad , \tag{91}$$

where $F'(\tau)$ is the almost everywhere existing derivative of $F(\tau)$. An example is the case where $F(\tau)$ is given as a *histogram*, i.e., it is a step function and, thus, $F'(\tau) \equiv 0$ almost everywhere.

The non–Gaussianities, which are the subject of this chapter, are defined as deviations from the analytically known Gaussian prediction for the PDF and for the Minkowski Functionals that we shall introduce below. In the case of the PDF, the *Gaussian prediction* (G) is given by the normal distribution,

$$P^{\mathrm{G}}(\tau) = \frac{1}{\sqrt{2\pi}\sigma_0} \mathrm{e}^{-\frac{(\tau-\mu)^2}{2\sigma_0^2}} \quad , \tag{92}$$

which has mean μ and variance σ_0^2. From (92) one derives with (82) the moment generating function,

$$M^{\mathrm{G}}(x) = \mathrm{e}^{\,\mu x + \frac{\sigma_0^2}{2} x^2} \quad , \tag{93}$$

and with (83) the generating function for the Gaussian cumulants,

$$C^{\mathrm{G}}(x) = \mu x + \frac{\sigma_0^2}{2} x^2 \quad . \tag{94}$$

Our numerical results for the CMB anisotropy are based on an ensemble of 10^5 realizations (for details, see Appendix 8.2). It turns out that the mean value $\mu = \langle \delta T \rangle$ (calculated from pixels) is negligibly small, $\mu = \mathcal{O}(10^{-7}\mu K)$ for sky maps that cover the full sky. Since typical values for the standard deviation σ_0 are $\sigma_0 \cong 59\mu K$, the ratio μ/σ_0 is much smaller than τ/σ_0 and, thus, we can put $\mu = 0$ in (92) when comparing with the full PDF. We then obtain from equations (82) and (93) the well–known result that all odd moments of the Gaussian prediction $P^{\mathrm{G}}(\tau)$ vanish, $\alpha^{\mathrm{G}}_{2n+1} = 0$, and that the even moments are given by:

$$\alpha^{\mathrm{G}}_{2n} = \frac{2^n}{\sqrt{\pi}} \Gamma\left(n + \frac{1}{2}\right) \sigma_0^{2n} = \frac{(2n)!}{2^n n!} \sigma_0^{2n} \quad , \tag{95}$$

and increase with increasing n. (Note that $m^{\mathrm{G}}_n = \alpha^{\mathrm{G}}_n$.) Equation (95) gives $\alpha^{\mathrm{G}}_4 = 3\sigma_0^4$ and, thus, one obtains from (88) and (89) $\gamma^{\mathrm{G}}_1 = \gamma^{\mathrm{G}}_2 = 0$, which shows that a non–vanishing value of the skewness coefficient γ_1 and/or of the excess kurtosis γ_2 are quantitative measures of non–Gaussianity. A comparison of equation (94) with equation (83) shows that all Gaussian cumulants vanish apart from $\varkappa^{\mathrm{G}}_2 = \sigma_0^2$ and, therefore, any non–vanishing cumulant with $n \geq 3$ is a measure of non–Gaussianity.

5.2.2 Discrepancy functions and Hermite expansions

In the present chapter we pursue a general model–independent approach to the PDF and to the Minkowski Functionals (MF) that depends, in general, on all higher–order poly–spectra. As a measure of non–Gaussianity using the PDF, we consider the dimensionless *discrepancy function* $\Delta_P(\tau)$, defined by:

$$\Delta_P(\tau) := \frac{P(\tau) - P^{\rm G}(\tau)}{P^{\rm G}(0)} \quad , \tag{96}$$

with $P^{\rm G}(0) = (\sqrt{2\pi}\sigma_0)^{-1} = \max\{P^G(\tau)\}$. Here, $P(\tau)$ denotes the ensemble average over a large number of realizations (10^5 in our case), compatible with $\mu = \langle \delta T \rangle = 0$, and possessing the standard deviation σ_0. The Gaussian prediction is defined by equation (92) for $\mu = 0$, and by identifying the standard deviation with the value σ_0 that is numerically obtained from $P(\tau)$, i.e., $\alpha_n^{\rm G} = \alpha_n$ for $n = 0, 1, 2$, respectively $\varkappa_1 = 0$ and $\varkappa_2 = \sigma_0^2$.

Although some models of inflation predict large non–Gaussianities for $P(\tau)$, there is clear evidence from *WMAP* and *Planck* data, [51, 52, 55, 56], that possible deviations from the Gaussian prediction $P^{\rm G}(\tau)$ are very small. Under very general conditions (for details see 8.5), $\Delta_P(\tau)$ can be written as a product of a Gaussian and a function $h(\nu) \in L^2(\mathbb{R}, w(\nu)\mathrm{d}\nu)$, where $w(\nu)$ denotes the weight function, $w(\nu) = \exp(-\nu^2/2)$, expressed in terms of the dimensionless scaled temperature variable $\nu := \tau/\sigma_0 \in \mathbb{R}$.

The *Hermite polynomials* $\mathrm{He}_n(\nu)$ provide a complete orthogonal basis in the Hilbert space $L^2(\mathbb{R}, w(\nu)\mathrm{d}\nu)$. Therefore, $h(\nu)$ possesses a convergent Hermite expansion (see 8.5) and we are led to

$$\Delta_P(\tau) = \mathrm{e}^{-\tau^2/2\sigma_0^2} \sum_{n=3}^{\infty} \frac{a_P(n)}{n!} \mathrm{He}_n\left(\frac{\tau}{\sigma_0}\right) \quad , \tag{97}$$

which describes the non–Gaussian "modulations" of the PDF. Possible non–Gaussianities are parametrized by the real dimensionless coefficients $a_P(n)$, where the non–vanishing of any of them is a clear signature of non–Gaussianity. We would like to point out that the $\mathrm{He}_n(\nu)$ are the "probabilist's Hermite polynomials" that are different from the Hermite polynomials $H_n(\nu)$ commonly used in physics and which are defined with respect to the weight function $\exp(-\nu^2)$. In the cosmology literature the $\mathrm{He}_n(\nu)$ are used, but unfortunately denoted as $H_n(\nu)$! The relation between the two is $\mathrm{He}_n(\nu) = 2^{-n/2} H_n(\nu/\sqrt{2})$, (see, e.g., [63]). Our condition on $h(\nu)$ is satisfied as long as $P(\tau)$ and, thus, also $\Delta_P(\tau)$ are piecewise continuous, and if $h(\nu) = o(\exp(\nu^2/4)/\sqrt{|\nu|})$ for $|\nu| \to \infty$ (see 8.5). It is clear that the expansion (97) is particularly useful if only a few terms have to be taken into account such that the series can be cut off at a low value $n = N$, i.e., can be well–approximated by a polynomial of degree N.

In order to obtain a physical interpretation of the non–Gaussianity (NG) parameters $a_P(n)$, we insert $P(\tau) = P^{\rm G}(\tau) + [1/(\sqrt{2\pi}\sigma_0)]\Delta_P(\tau)$ into the definition (82) of the moment generating function $M(x)$, which in turn gives with (83) the following *generating function of the cumulants* $\varkappa_n$ *of* $P(\tau)$ (see 8.3):

$$C(x) = \frac{\sigma_0^2}{2}\, x^2 + \Delta C(x) \quad , \tag{98}$$

with

$$\Delta C(x) := \ln\left[1 + \sum_{n=3}^{\infty} \frac{a_P(n)\sigma_0^n}{n!}\, x^n\right] = \sum_{n=3}^{\infty} \frac{\varkappa_n}{n!}\, x^n \quad . \tag{99}$$

Then, the cumulants are $\varkappa_1 = 0$, $\varkappa_2 = \sigma_0^2$, and the higher cumulants, for $n \geq 3$, are uniquely determined by (99). Here are the first coefficients $a_P(n)$, expressed in terms of the skewness coefficient γ_1, equation (88), the excess kurtosis γ_2, equation (89), and the dimensionless *normalized cumulants*,

$$C_n := \frac{\varkappa_n}{\sigma_0^n} = \frac{\langle (\delta T)^n \rangle_C}{\sigma_0^n} \quad : \tag{100}$$

$$\begin{aligned}
&a_P(3) = \gamma_1 \quad ; \quad a_P(4) = \gamma_2 \quad ; \quad a_P(5) = C_5 \quad ; \quad a_P(6) = 10\gamma_1^2 + C_6 \quad ; \\
&a_P(7) = 35\gamma_1\gamma_2 + C_7 \quad ; \quad a_P(8) = 56\gamma_1 C_5 + 35\gamma_2^2 + C_8 \quad ; \\
&a_P(9) = 280\gamma_1^3 + 126\gamma_2 C_5 + 84\gamma_1 C_6 + C_9 \quad ; \\
&a_P(10) = 2100\gamma_1^2\gamma_2 + 120\gamma_1 C_7 + 210\gamma_2 C_6 + 126 C_5^2 + C_{10} \quad ; \\
&a_P(11) = 5775\gamma_1\gamma_2^2 + 4620\gamma_1^2 C_5 + 165\gamma_1 C_8 + 330\gamma_2 C_7 + 462 C_5 C_6 + C_{11} \quad ; \\
&a_P(12) = 15400\gamma_1^4 + 5775\gamma_2^3 + 27720\gamma_1\gamma_2 C_5 + \\
&\qquad 9240\gamma_1^2 C_6 + 220\gamma_1 C_9 + 495\gamma_2 C_8 + 792 C_5 C_7 + 462 C_6^2 + C_{12} \quad .
\end{aligned} \tag{101}$$

Note that there is the general closed expression in terms of the normalized cumulants ($n \geq 3$):

$$a_P(n) = B_n(0, 0, \gamma_1, \gamma_2, C_5, \cdots, C_n) \quad , \tag{102}$$

where $B_n(x_1, x_2, \cdots, x_n)$ denotes the n^{th} complete *Bell polynomial* (see 8.4). An equivalent closed expression in terms of the moments is given in equation (219).

Table 4 shows the moments α_n (main term, equation (201) in 8.2.5), the cumulants $\varkappa_n$ and the dimensionless normalized cumulants C_n of $P(\tau)$. We here give the three first orders of each for the sample without mask, $\alpha_{0,1,2} = 1,\ 0\mu\text{K},\ 3558.31519\mu\text{K}^2$; $\varkappa_{0,1,2} = 1,\ 0\mu\text{K},\ 3558.31519\mu\text{K}^2$ and $C_{0,1,2} = 1, 0, 1$, and we obtain $\sigma_0 = 59.65166\mu\text{K}$, $\gamma_1 = -5.1872 \times 10^{-4}$ and $\gamma_2 = 5.825 \times 10^{-5}$.

(Units of μK^n) ΛCDM sample Full individual map range, no mask, 2°fwhm, bin 13μK *c.f.* 8.2										
n	3	4	5	6	7	8	9	10	11	12
α_n	−110.103727	37985558.5	−4040069.36	6.8×10^{11}	-1.5×10^{11}	1.7×10^{16}	-6.6×10^{15}	5.4×10^{20}	-3.1×10^{20}	2.1×10^{25}
$\varkappa_n$	−110.103727	737.480513	−122231.715	−108751936.	785344215.	8.2×10^{11}	1.1×10^{14}	-1.1×10^{16}	2.4×10^{18}	8.4×10^{20}
C_n	-5.187×10^{-4}	5.82×10^{-5}	-1.618×10^{-4}	-2.4138×10^{-3}	2.922×10^{-4}	5.1255×10^{-3}	1.14291×10^{-2}	-1.96036×10^{-2}	7.14927×10^{-2}	0.4147370

(Units of μK^n) ΛCDM sample Equal temperature range (ETR ± 201μK), U73 mask, 2°fwhm, bin 6μK										
n	0	1	2	3	4	5	6	7	8	9
α_n	1.0001469	-1.4912×10^{-3}	3515.73711	−113.475560	36119872.5	−2963938.41	5.9×10^{11}	-7.8×10^{10}	1.2×10^{16}	-2.2×10^{15}
$\varkappa_n$	1.0	-1.4912×10^{-3}	3515.73710	−97.7480482	−961350.317	741927.368	-1.3×10^{10}	-3.4×10^{9}	1.8×10^{14}	-1.6×10^{14}
C_n	1.0	-2.51×10^{-5}	1.0	-4.689×10^{-4}	-7.77766×10^{-2}	1.0123×10^{-3}	−0.2973678	-1.3108×10^{-3}	1.1699687	-1.76138×10^{-2}

Table 4: Table of the moments α_n (main term, equation (201)), cumulants $\varkappa_n$, and dimensionless normalized cumulants C_n of the probability density function $P(\tau)$.

With the help of the orthogonality relation (see [63], p.775, and 8.5),

$$\int_{-\infty}^{\infty} \mathrm{e}^{-\nu^2/2}\, \mathrm{He}_m(\nu)\mathrm{He}_n(\nu)\, \mathrm{d}\nu = \sqrt{2\pi}\, n!\, \delta_{mn} \quad , \tag{103}$$

one derives from (97) the following integral representation for the $a_P(n)$'s ($n \geq 3$):

$$a_P(n) = \frac{1}{\sqrt{2\pi}} \int_{-\infty}^{\infty} \Delta_P(\sigma_0\nu)\, \mathrm{He}_n(\nu)\, \mathrm{d}\nu \quad . \tag{104}$$

If the discrepancy function Δ_P is known, one can compute from (104) the non–Gaussianity parameters $a_P(n)$ and then, from (101) and (102), the normalized cumulants γ_1, γ_2, C_n. Vice versa, one can compute the $a_P(n)$'s from (101) once the cumulants have been computed from the moments $\alpha_n = m_n$ of the PDF $P(\tau)$, using equations (80) and (86), or directly from a theory of the primordial CMB fluctuations as, e.g., given by the ansatz (170). With $\mathrm{He}_{2n+1}(0) = 0$ and $\mathrm{He}_{2n}(0) = [(-1)^n(2n)!]/2^n n!$, we obtain from (97) and (101) for the discrepancy function at $\tau = 0$:

$$\begin{aligned}\Delta_P(0) &= \sum_{n=2}^{\infty} \frac{(-1)^n a_P(2n)}{2^n\, n!} = \frac{a_P(4)}{8} - \frac{a_P(6)}{48} + \frac{a_P(8)}{384} - \frac{a_P(10)}{3840} + \frac{a_P(12)}{46080} \mp \cdots \\ &= \frac{\gamma_2}{8} - \frac{5}{24}\gamma_1^2 - \frac{C_6}{48} + \frac{35}{384}\gamma_2^2 + \frac{7}{48}\gamma_1 C_5 + \frac{C_8}{384} \mp \cdots \quad . \end{aligned} \tag{105}$$

In table 5 we present the values for the first $a_P(n)$'s (see equations (101) and (104)), respectively for γ_1, γ_2, and C_5 for the ΛCDM model (model and computational details are given in 8.2).

ΛCDM sample Full individual map range, no mask, 2°fwhm, bin 13μK *c.f.* eqs. (101), (104) and model in 8.2										
n	3	4	5	6	7	8	9	10	11	12
$a_P(n)$	-5.1872×10^{-4}	5.825×10^{-5}	-1.6184×10^{-4}	-2.41112×10^{-3}	2.9116×10^{-4}	5.13035×10^{-3}	1.153302×10^{-2}	-1.964794×10^{-2}	7.123993×10^{-2}	0.41622908
$a_P(n)$	-5.1872×10^{-4}	5.830×10^{-5}	-1.6184×10^{-4}	-2.40919×10^{-3}	2.9116×10^{-4}	5.19401×10^{-3}	1.153302×10^{-2}	-1.785385×10^{-2}	7.123994×10^{-2}	0.45721793
ΛCDM sample Equal temperature range (ETR ± 201μK), U73 mask, 2°fwhm, bin 6μK										
n	0	1	2	3	4	5	6	7	8	
$a_P(n)$				-5.4435×10^{-4}	-7.777654×10^{-2}	1.01233×10^{-3}	$-2.9736480 \times 10^{-1}$	1.7101×10^{-4}	1.38165948	
$a_P(n)$	9.9534×10^{-4}	-2.8×10^{-7}	1.002019×10^{-2}	-4.7175×10^{-4}	5.20385×10^{-3}	1.00469×10^{-3}	-1.989114×10^{-2}	9.19×10^{-6}	$-2.1129824 \times 10^{-1}$	

Table 5: Table of coefficients $a_P(n)$ for the ΛCDM model, computed from table 4 using equation (101) in 1^{st} line, then using equation (104) in 2^{nd} line.

One observes that $a_P(6) = 10\gamma_1^2 + C_6 < 0$ implying $C_6 < 0$ in agreement with table 4. This is in contrast to hierarchical ordering (as assumed in perturbation theory [58]) where $a_P^{\mathrm{HO}}(J,6) = 6a_0^{\mathrm{HO}}(J,5) = 10\gamma_1^2 > 0$ in second– and third–order ($J = 2, 3$) (see equations (136) and (137). Only at fourth and higher order (i.e. $J \geq 4$) does that $a_P^{\mathrm{HO}}(J,6) = a_P(6)$ (see (138)). This will be discussed more in detail in subsection 5.2.5.

Figure 12 displays the discrepancy function Δ_P of the averaged PDF (10^5 map sample). Δ_P is calculated by equation (96) over the lattice defined by the mid–points of each segment in the histogram of $P(\tau)$ using σ_0 defined as the "main term" of α_2 in equation (200). This figure also displays the expansion in Hermite polynomials (equation (97) limited to the order 8).

Figure 13 shows the envelope of the 10^5 discrepancy functions of the map sample.

5.2.3 The first Minkowski Functional v_0

Let us discuss now the simplest morphological descriptor which is given by the first Minkowski Functional (MF). We consider the compact *excursion set* $\mathcal{Q}_\nu \in \mathcal{S}^2$ with boundary $\partial\mathcal{Q}_\nu (\nu := \tau/\sigma_0)$:

$$\mathcal{Q}_\nu := \{\hat{\boldsymbol{n}} \in \mathcal{S}^2 \;\Big|\; \delta T(\hat{\boldsymbol{n}}) \geq \sigma_0 \nu\} \quad . \tag{106}$$

We define the MF $V_0(\nu)$ as follows:

$$V_0(\mathcal{Q}_\nu) := \int_{\mathcal{Q}_\nu} \mathrm{d}a = \mathrm{area}(\mathcal{Q}_\nu) \quad , \tag{107}$$

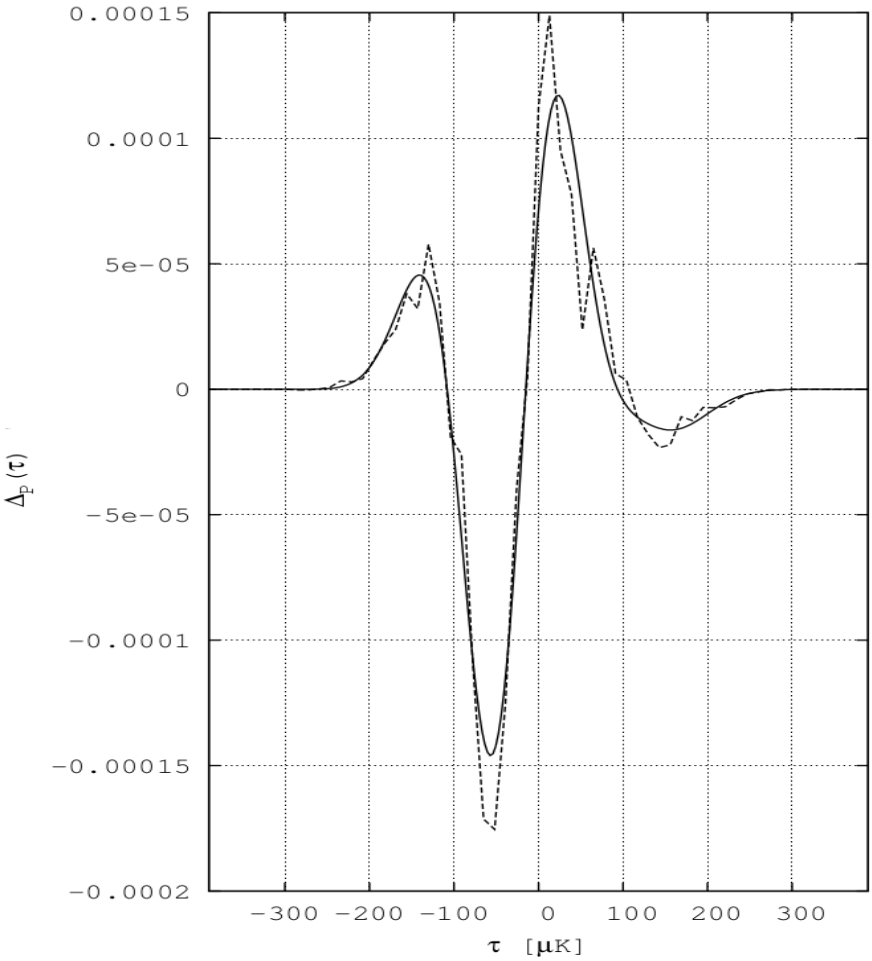

Figure 12: ΛCDM map sample, $N_{\rm side}$=128, $\ell_{\rm range}$=[2,256] without mask, 2° fwhm, for a 13μK temperature bin width over the smallest temperature range covering all the sample maps ($\pm 396.5 \mu K$). We plot the discrepancy function (black dashed line) of the PDF for the 10^5 maps ensemble ($\sigma_0' = \sqrt{\alpha_2'} = 59.65166 \mu$K being used here to calculate Δ_P – see 8.2.5 for details). The black solid line shows the Hermite expansion according to equation (97) for $n = 3$ to $n = 8$.

with da denoting the surface element on $\mathcal{S}^2$. In the following we shall be using the *normalized MF* $v_0(\nu)$ that is normalized with respect to area($\mathcal{S}^2$) $= 4\pi$, i.e.:

$$v_0(\nu) := \frac{1}{4\pi} V_0(\nu) = \mathrm{prob}(\delta T \geq \sigma_0 \nu) = F_C(\sigma_0 \nu) = \int_{-\infty}^{\infty} \Theta(\tau' - \sigma_0 \nu) P(\tau')\, \mathrm{d}\tau' \quad , \tag{108}$$

where F_C is the complementary cumulative distribution function (78). From the definition (108) follows also the relation

$$P(\tau) = -\frac{1}{\sigma_0} \frac{\mathrm{d}v_0(\nu)}{\mathrm{d}\nu}\Big|_{\nu=\tau/\sigma_0} \quad . \tag{109}$$

Thus, the MF $v_0(\nu)$ can be seen as a "smoothed" (cumulative) version of the PDF $P(\tau)$. Using the Gaussian prediction $P^{\rm G}(\tau)$ in equation (92), we obtain the *Gaussian prediction*

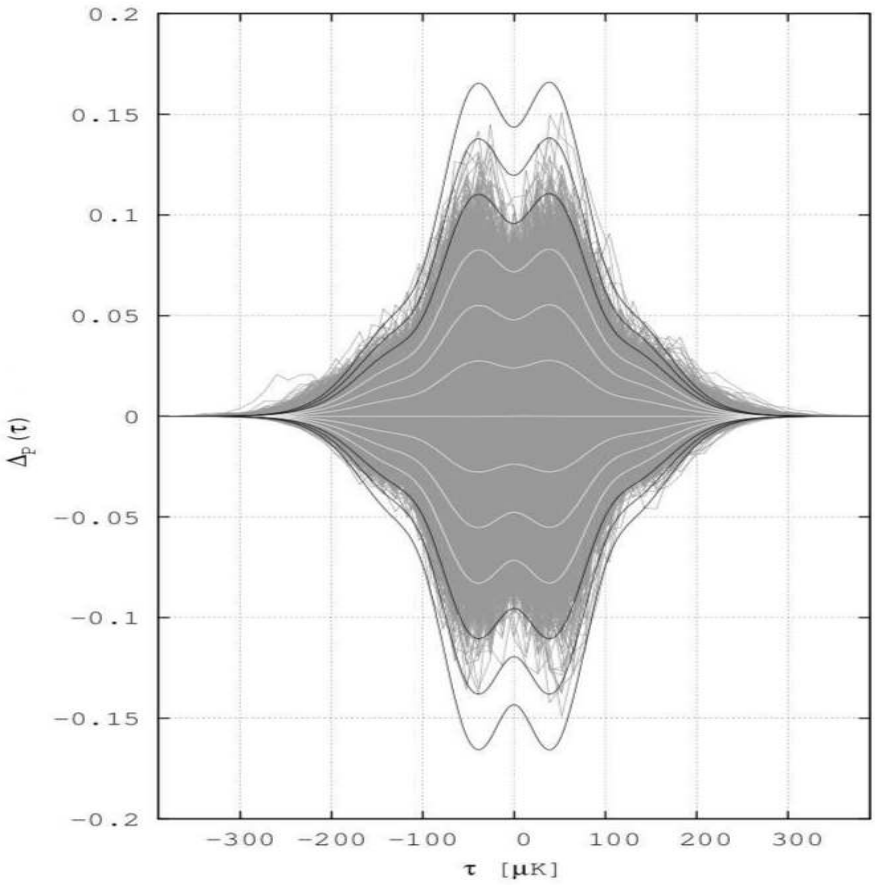

Figure 13: ΛCDM map sample, $N_{\rm side}$=128, $\ell_{\rm range}$=[2,256] without mask, 2° fwhm, for a 13μK temperature bin width over the largest temperature range of the sample ($\pm 396.5 \mu K$). We plot the envelope of the 10^5 individual discrepancy functions of the PDFs of figure 11. The cosmic variance curves of the 10^5 maps sample appear in white or in black from 1σ up to 6σ. This proves the high level of non–Gaussianity of several maps. The quasi straight, white horizontal central line is the PDF discrepancy function of the ensemble average.

for $v_0(\nu)$ (setting $\mu = 0$):

$$v_0^{\rm G}(\nu) := \frac{1}{2}{\rm erfc}\left(\frac{\nu}{\sqrt{2}}\right) \quad , \tag{110}$$

in terms of the complementary error function [63], from which one derives $v_0^{\rm G}(-\infty) = 1$, $v_0^{\rm G}(\infty) = 0$, $v_0^{\rm G}(0) = 1/2$, and the symmetry relation $v_0^{\rm G}(-\nu) = 1 - v_0^{\rm G}(\nu)$. Furthermore, one has the asymptotic behaviour for $\nu \to \infty$,

$$v_0^{\rm G}(\nu) = \frac{1}{\sqrt{2\pi}} \frac{{\rm e}^{-\nu^2/2}}{\nu} \left[1 - \frac{1}{\nu^2} + \mathcal{O}\left(\frac{1}{\nu^4}\right)\right] \ . \tag{111}$$

In analogy to equation (96), we define the dimensionless *discrepancy function* $\Delta_0(\nu)$ as follows:

$$\Delta_0(\nu) := \sqrt{2\pi}\left(v_0(\nu) - v_0^{\rm G}(\nu)\right) \quad , \tag{112}$$

which in turn is expanded into Hermite polynomials,

$$\Delta_0(\nu) := \mathrm{e}^{-\nu^2/2} \sum_{n=2}^{\infty} \frac{a_0(n)}{n!} \mathrm{He}_n(\nu) \quad , \tag{113}$$

with the coefficients

$$a_0(n) = \frac{1}{\sqrt{2\pi}} \int_{-\infty}^{\infty} \Delta_0(\nu) \mathrm{He}_n(\nu) \, \mathrm{d}\nu \quad . \tag{114}$$

The above coefficients $a_0(n)$, $n \geq 2$, measure a possible non–Gaussianity described by the MF $v_0(\nu)$. With

$$\frac{\mathrm{d}}{\mathrm{d}\nu} \left[\mathrm{e}^{-\nu^2/2} \, \mathrm{He}_n(\nu) \right] = -\mathrm{e}^{-\nu^2/2} \, \mathrm{He}_{n+1}(\nu) \quad , \tag{115}$$

and the relation (see equations (97) and (109)),

$$\frac{\mathrm{d}}{\mathrm{d}\nu} \Delta_0(\nu) = -\Delta_P(\sigma_0 \nu) \quad , \tag{116}$$

one obtains the following relation between the coefficients $a_0(n)$ and $a_P(n)$:

$$a_0(n) = \frac{a_P(n+1)}{n+1} \quad (n \geq 2) \quad , \tag{117}$$

and, thus, we arrive at the following exact coefficients (see equations (101) and (102)):

$$\begin{aligned}
&a_0(2) = \frac{\gamma_1}{3} \quad ; \quad a_0(3) = \frac{\gamma_2}{4} \quad ; \quad a_0(4) = \frac{C_5}{5} \quad ; \quad a_0(5) = \frac{5}{3}\gamma_1^2 + \frac{C_6}{6} \quad ; \\
&a_0(6) = 5\gamma_1\gamma_2 + \frac{C_7}{7} \quad ; \quad a_0(7) = 7\gamma_1 C_5 + \frac{35}{8}\gamma_2^2 + \frac{C_8}{8} \quad ; \\
&a_0(8) = \frac{280}{9}\gamma_1^3 + 14\gamma_2 C_5 + \frac{28}{3}\gamma_1 C_6 + \frac{C_9}{9} \quad ; \\
&a_0(9) = 210\gamma_1^2\gamma_2 + 12\gamma_1 C_7 + 21\gamma_2 C_6 + \frac{63}{5}C_5^2 + \frac{C_{10}}{10} \quad ; \\
&a_0(10) = 525\gamma_1\gamma_2^2 + 420\gamma_1^2 C_5 + 15\gamma_1 C_8 + 30\gamma_2 C_7 + 42 C_5 C_6 + \frac{C_{11}}{11} \quad ; \\
&a_0(11) = \frac{3850}{3}\gamma_1^4 + \frac{1925}{4}\gamma_2^3 + 2310\gamma_1\gamma_2 C_5 + \\
&\qquad 770\gamma_1^2 C_6 + \frac{55}{3}\gamma_1 C_9 + \frac{165}{4}\gamma_2 C_8 + 66 C_5 C_7 + \frac{77}{2}C_6^2 + \frac{C_{12}}{12} \quad .
\end{aligned} \tag{118}$$

In table 6 we present the values for the first $a_0(n)$'s of the ΛCDM model.

ΛCDM Full individual map range, no mask, 2°fwhm, bin 13μK *c.f.* equation (118) and model in 8.2									
n	0	1	2	3	4	5	6	7	8
$a_0(n)$			-1.7295×10^{-4}	1.456×10^{-5}	-3.237×10^{-5}	-4.0185×10^{-4}	4.159×10^{-5}	6.4130×10^{-4}	1.28145×10^{-3}

ΛCDM Equal temperature range (ETR $\pm$ 201μK), U73 mask, 2°fwhm, bin 6μK									
n	0	1	2	3	4	5	6	7	8
$a_0(n)$			-1.8145×10^{-4}	-1.944413×10^{-2}	2.0247×10^{-4}	-4.95608×10^{-3}	2.443×10^{-5}	1.7270744×10^{-1}	-1.54858×10^{-3}

Table 6: Table of coefficients $a_0(n)$, computed from table 4 using equation (118).

Figure 14 shows the first Minkowski Functional $v_0(\nu)$ of the ΛCDM sample without mask, and figure 15 its discrepancy function $\Delta_0(\nu)$ together with the Hermite expansion (113) of $\Delta_0(\nu)$ (order 2 to 5) in $a_0(n)$.

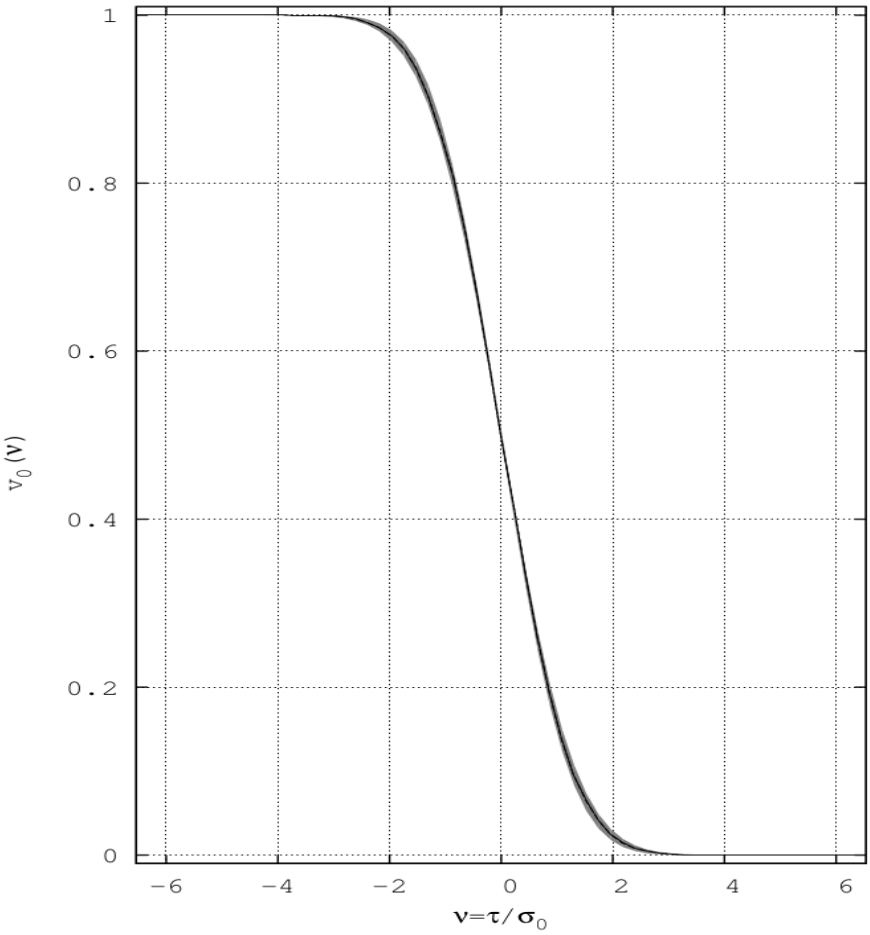

Figure 14: ΛCDM map sample, $N_{\rm side}$=128, $\ell_{\rm range}$=[2,256] without mask, 2° fwhm, for a 13μK temperature bin width over the largest temperature range of the sample ($\pm 396.5\mu K$). We plot the first Minkowski functional $v_0(\nu)$ as a black dashed line with its Gaussian premise in black solid line (almost coincident). The 1σ cosmic variance is displayed as a grey shaded area.

5.2.4 Accuracy of Hermite expansions

The Hermite expansions (97) and (113) for the discrepancy functions $\Delta_P(\tau)$ and $\Delta_0(\nu)$, respectively, provide very convenient parametrizations and quantitative measures of the CMB non–Gaussianities. They hold under very general conditions (as discussed in 8.5) and do not require that the NGs have to be small. The main assumption is the existence of a unique probability density function $P(\tau)$ (a very natural assumption, indeed, from a physical point of view), which is equivalent to demanding that the "Hamburger moment problem" is determinate (see e.g. [78, 79]). It is then guaranteed that the Hermite expansions are absolutely convergent. In subsections 5.2.2 and 5.2.3 we considered polynomial approximations of degree N in τ, respectively in ν of $\Delta_P(\tau)$ and $\Delta_0(\nu)$ by truncating the Hermite expansions at $n = N$. A nice property of this truncation is that the accuracy of the approximation is well under control, since there is, for example

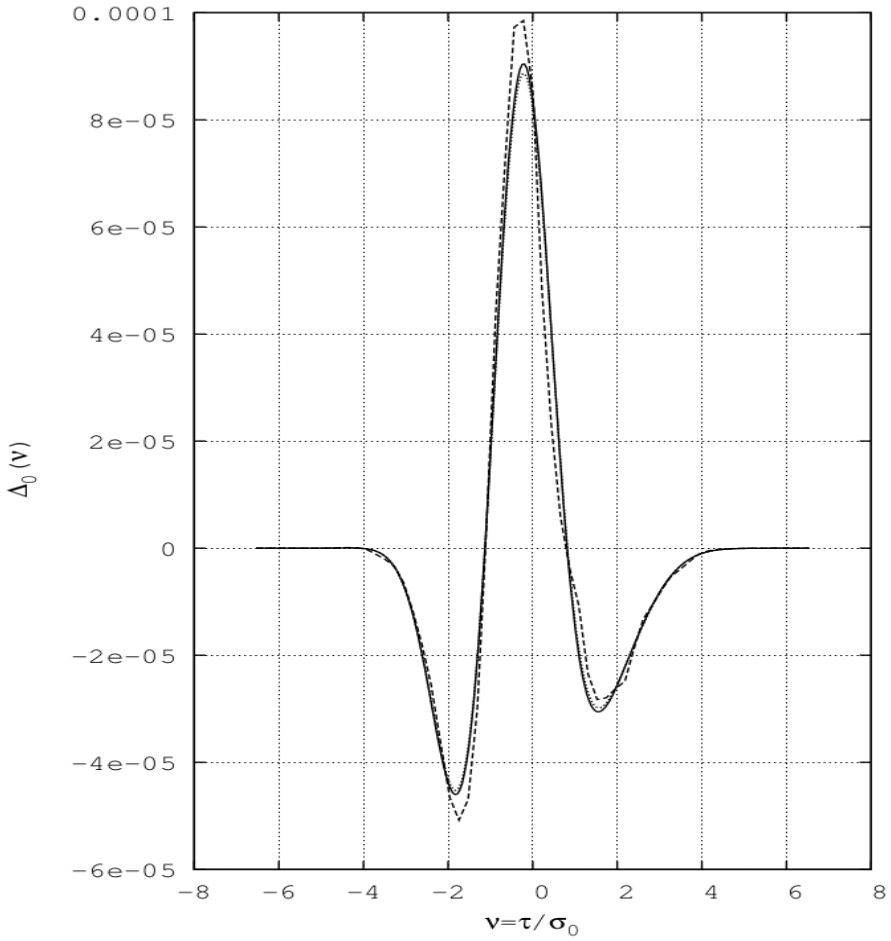

Figure 15: We plot $\Delta_0(\nu)$, the discrepancy function of v_0 in dashed line ($\sigma_{0px} = 59.53348\mu$K, the variance from the moments of pixels being used here to calculate Δ_0). The Hermite expansions (order 2 to 5) appear in black solid line using the coefficients $a_0(n)$ computed from equation (114), and in dotted line from equation (118). Coefficients are shown in table 6.

for $\Delta_0(\nu)$, the exact *mean square error* of equations (226) and (227),

$$\mathcal{E}_N := ||h_0 - \sum_{n=2}^{N} \frac{a_0(n)}{n!} \mathrm{He}_n||^2 \;=\; ||h_0||^2 - \sum_{n=2}^{N} \frac{(a_0(n))^2}{n!} \;, \tag{119}$$

for $h_0(\nu) := e^{\nu^2/2}\Delta_0(\nu)$. The error $\mathcal{E}_N$ gets smaller and smaller if the degree N increases and finally approaches zero in the limit $N \to \infty$ as a consequence of the completeness relation (Parseval's equation),

$$\sum_{n=2}^{\infty} \frac{(a_0(n))^2}{n!} = ||h_0||^2 := \frac{1}{\sqrt{2\pi}} \int_{-\infty}^{+\infty} e^{-\nu^2/2} (h_0(\nu))^2 \mathrm{d}\nu \;, \tag{120}$$

(here we use the weight function $w(\nu) = \frac{1}{\sqrt{2\pi}} e^{-\nu^2/2}$ in the definition of the inner product of the Hilbert space $\mathbb{H} = L^2(\mathbb{R}, w(\nu)\mathrm{d}\nu)$, see 8.5.) As an example, let us consider the

approximation of degree $N = 5$ applied to $\Delta_0(\nu)$ for which the *mean square error* is explicitly given in terms of the skewness coefficient γ_1, the excess kurtosis γ_2 and the higher cumulants C_5 and C_6 by

$$\mathcal{E}_5 = ||h_0||^2 - \left[\frac{\gamma_1^2}{18} + \frac{\gamma_2^2}{96} + \frac{C_5^2}{600} + \frac{(10\gamma_1^2 + C_6)^2}{4320}\right] , \tag{121}$$

using the coefficients $a_0(2, 3, 4, 5)$ of (118). Figure 15 nicely illustrates that the polynomial approximation of degree 5 provides an excellent description of the discrepancy function $\Delta_0(\nu)$. Similar results exist for the discrepancy function $\Delta_P(\tau)$ as shown already in figure 12 at order 8.

5.2.5 Hierarchical ordering and perturbation theory

Most of the commonly studied models of inflation predict weak primordial non–Gaussianities. Among these models there is a wide class where the normalized cumulants C_n obey the additional property of *hierarchical ordering* (indexed below by HO), i.e., $C_n \sim \sigma_0^{n-2}, n \geq 2$ (where we assume $C_1 = 0, C_2 = 1$). This suggests to expand the discrepancy function not into Hermite polynomials, but rather at fixed ν into a power series (perturbation theory) in σ_0. This approach has been pioneered by Matsubara [57,58] who has derived second–order *perturbative formulae* in σ_0 for the discrepancy functions of the MFs. In the following, we show that the perturbation theory applied to $\Delta_0(\nu)$ is a direct consequence of the general Hermite expansion (113) that can be easily carried out to any order J in σ_0, i.e., to the NG of order σ_0^J (indexed below by HO$(J), J \geq 1$). It turns out that the perturbation expansion HO(J) corresponds, at a given order J, to a double truncation of the Hermite expansion: i) a truncation of the Hermite expansion at $n = M_0(J) := 3J - 1$, ii) a truncation of the expansion coefficients $a_0(n)$ at order J with respect to their expansion into a power series in σ_0. As an example, we give below the explicit formulae at second, third and fourth order, where the second–order formula is identical to Matsubara's result. Analogous perturbative formulae hold for $\Delta_P(\tau)$, which have not been given before. As another new result we also present the exact *mean square error* of the perturbative formulae and compare it with the corresponding error (119) of the original Hermite expansion.

Let us assume that the hierarchical ordering holds and introduce the "renormalized cumulants" (or "HO–cumulants"),

$$S_n := \frac{C_n}{\sigma_0^{n-2}}, n \geq 3 , \tag{122}$$

which are assumed to be of zeroth order in σ_0. Using the relation (117) and the explicit expression (102) for the coefficients $a_P(n)$ in terms of the complete Bell polynomials B_n, we obtain for $n \geq 2$,

$$\begin{aligned} a_0(n) &= \frac{a_P(n+1)}{n+1} = \frac{1}{n+1} B_{n+1}(0, 0, \gamma_1, \gamma_2, C_5, C_6, \cdots, C_{n+1}) \\ &= \frac{1}{n+1} B_{n+1}(0, 0, S_3\sigma_0, S_4\sigma_0^2, \cdots, S_{n+1}\sigma_0^{n-1}) \text{ , } i.e. \\ a_0(n) &= D_{n-1}(\sigma_0), n \geq 2 , \end{aligned} \tag{123}$$

where $D_n(z)$ is a polynomial of degree n in z with $D_0(z) := 1$ and

$$D_n(-z) = (-1)^n D_n(z) \; . \tag{124}$$

Thus, $a_0(n)$ is a polynomial of degree $n-1$ in σ_0,

$$a_0(n) = \sum_{j=j_0(n)}^{n-1} D_{n-1,j}(S_3, S_4, \cdots, S_{n+1}) \sigma_0^j \;\; , \; n \geq 2 \; . \tag{125}$$

Here, $j_0(n)$ denotes the smallest power of σ_0 which contributes to $a_0(n)$ and is given for $n \geq 2$ by

$$j_0(n) := n(k,l) - (2l+1) = k + l - 1 \geq l + 1 \;\; , \tag{126}$$

where n is parametrized as $n = n(k,l) := k + 3l$ with $k = 2, 3, 4$ and $l = 0, 1, 2, \cdots$. (As a consequence of the symmetry relation (124), the coefficients $D_{n-1,j}$ vanish for j even or odd depending on whether n is even or odd.) The first few polynomials are explicitly given by:

$$\begin{aligned} D_n(z) &= \frac{S_{n+2}}{n+2} z^n \;\; (n = 1, 2, 3) \;\; ; \;\; D_4(z) = \frac{5}{3} S_3^2 z^2 + \frac{S_6}{6} z^4 \;\; ; \\ D_5(z) &= 5 S_3 S_4 z^3 + \frac{S_7}{7} z^5 \;\; ; \;\; D_6(z) = (7 S_3 S_5 + \frac{35}{8} S_4^2) z^4 + \frac{S_8}{8} z^6 \;\; . \end{aligned} \tag{127}$$

(Note that the highest power in σ_0 is for all D_n given by $\frac{S_{n+2}}{n+2} z^n$ for $n \geq 1$.) Explicit expressions for the polynomials $D_n(z)$ for $n \geq 7$ are easily obtained either from the recurrence relation (212) or from the combinatorial expression (213).

In order to derive the perturbative expansion HO(J) for the discrepancy function Δ_0 at any order $J \geq 1$, we insert in the Hermite expansion (113) the polynomial relation (123) for the expansion coefficients $a_0(n)$. At lowest order, $J = 1$, one immediatly obtains from (123) and (125–127) the simple result:

$$\Delta_0^{\mathrm{HO}(1)}(\nu) = e^{-\nu^2/2} \frac{a_0(2)}{2} \mathrm{He}_2(\nu) = \frac{\gamma_1}{6} (\nu^2 - 1) e^{-\nu^2/2} \;\; , \tag{128}$$

which is completely determined by the skewness coefficient $\gamma_1 = S_3 \sigma_0$. To obtain the HO(J)–expansion for $J \geq 2$, we decompose the exact (general) Hermite expansion into three terms ($M_0(J) = 3J - 1$):

$$\begin{aligned} \Delta_0(\nu) = e^{-\nu^2/2} \Bigg[& \sum_{n=2}^{J+1} \frac{D_{n-1}(\sigma_0)}{n!} \mathrm{He}_n(\nu) + \sum_{n=J+2}^{M_0(J)} \frac{D_{n-1}(\sigma_0)}{n!} \mathrm{He}_n(\nu) \\ & + \sum_{n=M_0(J)+1}^{\infty} \frac{D_{n-1}(\sigma_0)}{n!} \mathrm{He}_n(\nu) \Bigg] \; . \end{aligned} \tag{129}$$

Since $D_{n-1}(\sigma_0)$ is a polynomial of degree $n-1$ in σ_0, the first sum in (129) represents (having ν fixed) a polynomial of degree J in σ_0 and thus contributes to the HO(J)–expansion. The last infinite series in (129), which is absolutely convergent, does not contribute at all to the HO(J)–expansion, since the smallest power of σ_0 appearing in this series is already larger than J; (with $M_0(J) + 1 = n(3, J-1)$, equation (126) gives $j_0(M_0(J)+1) = J + 1 > J$.) We thus obtain the important result that the perturbative expansion at order J necessarily implies a *truncation of the Hermite expansion* at $n = M_0(J) = 3J - 1$. It remains to discuss the second finite sum in (129) where the summation runs over $J + 2 \leq n \leq M_0(J)$. Inspection of the expression (125) for the polynomials $D_{n-1}(\sigma_0)$ (see also the explicit expressions (127)) shows that they will

contribute (for $n \geq J+2$ and $j_0(n) \leq J$) to this sum not only with powers $j \leq J$, but also with higher powers that are not admitted in the HO(J)–expansion. Thus, the polynomials D_{n-1} have to be replaced by truncated ones. In the case where $j_0(n) > J$, the polynomials D_{n-1} do not contribute at all. This leads us to define, for $n \geq J+2$, the *truncated polynomials* $D_{n-1}^{\mathrm{HO}(J)}(z)$, which now depend also on J:

$$D_{n-1}^{\mathrm{HO}(J)}(z) := \begin{cases} \sum_{j=j_0(n)}^{J} D_{n-1,j}(S_3, S_4, \cdots, S_{n+1}) z^j & , \ j_0(n) \leq J \\ 0 & , \ j_0(n) > J \ . \end{cases} \tag{130}$$

We now explicitly give the *truncated polynomials* at order $J = 2, 3$ and 4:
$J = 2, M_0(2) = 5$:

$$\begin{aligned} D_3^{\mathrm{HO}(2)}(z) &= 0 \\ D_4^{\mathrm{HO}(2)}(z) &= \frac{5}{3} \ S_3^2 z^2 \ ; \end{aligned} \tag{131}$$

$J = 3, M_0(3) = 8$:

$$\begin{aligned} D_4^{\mathrm{HO}(3)}(z) &= D_4^{\mathrm{HO}(2)}(z) \\ D_5^{\mathrm{HO}(3)}(z) &= 5 \ S_3 S_4 z^3 \\ D_6^{\mathrm{HO}(3)}(z) &= 0 \\ D_7^{\mathrm{HO}(3)}(z) &= \frac{280}{9} \ S_3^2 z^3 \ ; \end{aligned} \tag{132}$$

$J = 4, M_0(4) = 11$:

$$\begin{aligned} D_5^{\mathrm{HO}(4)}(z) &= D_5^{\mathrm{HO}(3)}(z) \\ D_6^{\mathrm{HO}(4)}(z) &= (7 \ S_3 S_5 + \frac{35}{8} \ S_4^2) z^4 \\ D_7^{\mathrm{HO}(4)}(z) &= D_7^{\mathrm{HO}(3)}(z) \\ D_8^{\mathrm{HO}(4)}(z) &= 210 \ S_3^2 S_4 z^4 \\ D_9^{\mathrm{HO}(4)}(z) &= 0 \\ D_{10}^{\mathrm{HO}(4)}(z) &= \frac{3850}{3} \ S_3^4 z^4 \ . \end{aligned} \tag{133}$$

We then obtain from (129) the general *perturbative formula* for the discrepancy function $\Delta_0(\nu)$ valid *at any order* $J \geq 1$:

$$\Delta_0^{\mathrm{HO}(J)}(\nu) := e^{-\nu^2/2} \sum_{n=2}^{M_0(J)} \frac{a_0^{\mathrm{HO}}(J,n)}{n!} \mathrm{He}_n(\nu) \ , \tag{134}$$

in terms of the HO–Hermite expansion coefficients $a_0^{\mathrm{HO}}(J,n)$, which now also depend on J,

$$a_0^{\mathrm{HO}}(J,n) := \begin{cases} a_0(n) = D_{n-1}(\sigma_0) & , \text{for } 2 \leq n \leq J+1 \\ D_{n-1}^{\mathrm{HO}(J)}(\sigma_0) & , \text{for } J+2 \leq n \leq M_0(J) \ . \end{cases} \tag{135}$$

As an example, we give the expansion coefficients of the hierarchical ordering at second, third and fourth order:
$J = 2, M_0(2) = 5$:

$$\begin{aligned} a_0^{\mathrm{HO}}(2,2) &= a_0(2) = \frac{\gamma_1}{3} \\ a_0^{\mathrm{HO}}(2,3) &= a_0(3) = \frac{\gamma_2}{4} \end{aligned}$$

$$a_0^{\mathrm{HO}}(2,4) = 0$$
$$a_0^{\mathrm{HO}}(2,5) = \frac{5}{3}\gamma_1^2 \ . \tag{136}$$

$J = 3, M_0(3) = 8$:

$$a_0^{\mathrm{HO}}(3,2) = a_0(2) = \frac{\gamma_1}{3}$$
$$a_0^{\mathrm{HO}}(3,3) = a_0(3) = \frac{\gamma_2}{4}$$
$$a_0^{\mathrm{HO}}(3,4) = a_0(4) = \frac{C_5}{5}$$
$$a_0^{\mathrm{HO}}(3,5) = \frac{5}{3}\gamma_1^2$$
$$a_0^{\mathrm{HO}}(3,6) = 5\gamma_1\gamma_2$$
$$a_0^{\mathrm{HO}}(3,7) = 0$$
$$a_0^{\mathrm{HO}}(3,8) = \frac{280}{9}\gamma_1^3 \ . \tag{137}$$

$J = 4, M_0(4) = 11$:

$$a_0^{\mathrm{HO}}(4,n) = a_0(n) \quad (n = 2,3,4,5)$$
$$a_0^{\mathrm{HO}}(4,6) = 5\gamma_1\gamma_2$$
$$a_0^{\mathrm{HO}}(4,7) = 7\gamma_1 C_5 + \frac{35}{8}\gamma_2^2$$
$$a_0^{\mathrm{HO}}(4,8) = \frac{280}{9}\gamma_1^3$$
$$a_0^{\mathrm{HO}}(4,9) = 210\gamma_1^2\gamma_2$$
$$a_0^{\mathrm{HO}}(4,10) = 0$$
$$a_0^{\mathrm{HO}}(4,11) = \frac{3850}{3}\gamma_1^4 \ . \tag{138}$$

(Here, we have replaced the $S_n's$ by the cumulants C_n according to equation (122).)

Being a direct consequence of the general Hermite expansion (113), the perturbative formula (134), valid at arbitrary order J in σ_0, has still the form of a Hermite expansion (truncated at $n = M_0(J)$). If we insert, however, for the Hermite coefficients $a_0^{\mathrm{HO}}(J,n)$ their definition (135) in terms of polynomials in σ_0, we obtain, by combining all terms of same power, the *alternative version of the perturbative formula*:

$$\Delta_0^{\mathrm{HO}(J)}(\nu) = e^{-\nu^2/2}\sum_{j=1}^{J} v_0^{\mathrm{HO}(J)}(j,\nu)\sigma_0^j \ , \tag{139}$$

which has now (at fixed ν) the form of a power series in σ_0 with coefficient functions $v_0^{\mathrm{HO}(J)}(j,\nu)$. (Since the series in (134) is finite, the rearrangement as a power series in σ_0 is of course always possible.) The coefficient functions $v_0^{\mathrm{HO}(J)}(j,\nu)$ are given as a linear combination of a finite number of Hermite polynomials. Up to the second order, they have been calculated by Matsubara [57, 58]. It is straightforward to obtain them at arbitrary order J using the equations (125), (130) and (135). Here we give the coefficient functions up to fourth order:

$$J = 1 : v_0^{\mathrm{HO}(1)}(1,\nu) = \frac{S_3}{6}\mathrm{He}_2(\nu) \ , \tag{140}$$

$$J = 2 : v_0^{\mathrm{HO}(2)}(1,\nu) = v_0^{\mathrm{HO}(1)}(1,\nu)$$
$$v_0^{\mathrm{HO}(2)}(2,\nu) = \frac{S_4}{24}\mathrm{He}_3(\nu) + \frac{S_3^2}{72}\mathrm{He}_5(\nu) \ , \tag{141}$$

$$
\begin{aligned}
J=3: v_0^{\mathrm{HO}(3)}(1,\nu) &= v_0^{\mathrm{HO}(1)}(1,\nu) \\
v_0^{\mathrm{HO}(3)}(2,\nu) &= v_0^{\mathrm{HO}(2)}(2,\nu) \\
v_0^{\mathrm{HO}(3)}(3,\nu) &= \frac{S_5}{120}\mathrm{He}_4(\nu) + \frac{S_3 S_4}{144}\mathrm{He}_6(\nu) + \frac{S_3^2}{1296}\mathrm{He}_8(\nu)\,, \qquad (142)
\end{aligned}
$$

$$
\begin{aligned}
J=4: v_0^{\mathrm{HO}(4)}(1,\nu) &= v_0^{\mathrm{HO}(1)}(1,\nu) \\
v_0^{\mathrm{HO}(4)}(2,\nu) &= v_0^{\mathrm{HO}(2)}(2,\nu) \\
v_0^{\mathrm{HO}(4)}(3,\nu) &= v_0^{\mathrm{HO}(3)}(3,\nu) \\
v_0^{\mathrm{HO}(4)}(4,\nu) &= \frac{S_6}{720}\mathrm{He}_5(\nu) + \frac{1}{720}(S_3 S_5 + \frac{5}{8}S_4^2)\mathrm{He}_7(\nu) \\
&\quad + \frac{S_3^2 S_4}{1728}\mathrm{He}_9(\nu) + \frac{S_3^4}{31104}\mathrm{He}_{11}(\nu)\,. \qquad (143)
\end{aligned}
$$

The second–order formulae (141) agree with Matsubara's result [57, 58] (who writes $S := S_3$ and $K := S_4$).

It is worthwhile to mention that the perturbative formula (139) closely resembles the so–called Edgeworth expansion (240) which gives a refinement of the classical central limit theorem (for details and references, see 8.5). However, (240) is an asymptotic expansion in the sense of Poincaré where the role of σ_0 is played by the small dimensionless parameter $1/\sqrt{n}$ which can be made arbitrarily small and does not have a fixed finite value as in the case of the standard deviation σ_0 of the CMB anisotropy. In fact, the central limit theorem is precisely the statement that the limit $n \to \infty$ is asymptotically exactly Gaussian and thus the NGs in the Edgeworth expansions have no fundamental meaning, they just determine the rate of convergence to the Gaussian limit. In contrast, the NGs of the CMB—if they are non–zero and of primordial origin—contain genuine information on the underlying model of inflation.

Having shown that the two perturbative formulae (134) and (139) are identical, we discuss in the following only the Hermite expansion (134).

Let us compare the perturbative NG–coefficients, (136) respectively (137), with the complete NG–coefficients $a_0(n)$ given in equation (118). At *second order* ($J = 2$) we see that the first two coefficients are identical to the complete coefficients $a_0(n)$, i.e., $a_0^{\mathrm{HO}}(2,n) = a_0(n)$ for $n = 2, 3$. The coefficient $a_0^{\mathrm{HO}}(2,4)$ vanishes because its complete value $C_5/5$ is of third order. Finally, the last coefficient $a_0^{\mathrm{HO}}(2,5)$ differs from $a_0(5)$ by the term $C_6/6$, which is of fourth order. At *third order* ($J = 3$) one observes that now the first three coefficients are identical to the complete expressions, i.e., $a_0^{\mathrm{HO}}(3,n) = a_0(n)$ for $n = 2, 3, 4$; $a_0^{\mathrm{HO}}(3,5) = a_0^{\mathrm{HO}}(2,5)$ still does not contain the term $C_6/6$; the coefficient $a_0^{\mathrm{HO}}(3,7)$ vanishes because the complete value for $a_0(7)$ is of order σ_0^4; $a_0^{\mathrm{HO}}(3,6)$ does not contain the term $C_7/7$ (of order 5), and $a_0^{\mathrm{HO}}(3,8)$ does not contain the terms of order 5, respectively 7. Note, in particular, that a vanishing coefficient $a_0^{\mathrm{HO}}(J,n)$ implies that the associated contribution from the Hermite polynomial $\mathrm{He}_n(\nu)$ is absent in $\Delta_0^{\mathrm{HO(J)}}$ compared to Δ_0. This is the case at second order with $\mathrm{He}_4(\nu)$, and at third order with $\mathrm{He}_7(\nu)$. Since the $\mathrm{He}_n(\nu)$'s have exactly n distinct zeros, the omission of one or several of them can have an important influence on the shape of the discrepancy function.

Finally, we come to the important question about the accuracy of the perturbative expansion. To this purpose we consider in analogy to equation (119) the *mean square*

error of the HO(J)*–expansion*:

$$\mathcal{E}^{\mathrm{HO}(J)} := ||h_0 - \sum_{n=2}^{M_0(J)} \frac{a_0^{\mathrm{HO}}(J,n)}{n!}\mathrm{He}_n||^2$$
$$= ||h_0||^2 - \sum_{n=2}^{M_0(J)} \frac{(a_0(n))^2}{n!} + \sum_{n=2}^{M_0(J)} \frac{(a_0(n) - a_0^{\mathrm{HO}}(J,n))^2}{n!} \ , \qquad (144)$$

where we have used the identity (227). Here, the first two terms are identical to the error $\mathcal{E}_{M_0(J)}$, i.e. the error of the complete Hermite expansion truncated at order $N := M_0(J)$ (see equation (119)), which leads to the interesting formula:

$$\mathcal{E}^{\mathrm{HO}(J)} = \mathcal{E}_{M_0(J)} + \sum_{n=J+2}^{M_0(J)} \frac{(a_0(n) - a_0^{\mathrm{HO}}(J,n))^2}{n!} \ . \qquad (145)$$

Here, we have used in the last sum $a_0(n) - a_0^{\mathrm{HO}}(J,n) \equiv 0$ for $2 \leq n \leq J+1$ (see (135)). Since the last sum in (145) is strictly positive, one infers that we have at any order in perturbation theory:

$$\mathcal{E}^{\mathrm{HO}(J)} > \mathcal{E}_{M_0(J)} \ , \qquad (146)$$

i.e., the *mean square error* of the HO(J)–expansion is always larger than the *mean square error* of the complete Hermite expansion truncated at $n = M_0(J)$. For instance, at second–order of perturbation theory, $J = 2$, we have $\mathcal{E}^{\mathrm{HO}(2)} > \mathcal{E}_5$, where $\mathcal{E}_5$ is explicitly given in (121). Precisely, we obtain from (145) through (118) and (136):

$$\mathcal{E}^{\mathrm{HO}(2)} = \mathcal{E}_5 + \frac{C_5^2}{600} + \frac{C_6^2}{4320} \ . \qquad (147)$$

One observes that both errors approach zero in the limit $J \to \infty$ which reflects the fact that the perturbative expansion becomes identical to the general untruncated Hermite expansion in this limit.

Test of the hierarchical ordering in perturbation theory

In figure 16 we compare the discrepancy function Δ_P with its Hermite expansion in terms of the coefficients $a_P(n)$ (computed from (101) and table 4) for $n = 3$ to 6, according to the following equation:

$$\Delta_P(\tau) = \mathrm{e}^{-\tau^2/2\sigma_0^2} \sum_{n=3}^{n=6} \frac{a_P(n)}{n!} \mathrm{He}_n(\tau/\sigma_0) \ . \qquad (148)$$

In addition, in figure 16, we show the expansion of Δ_P with the assumption of hierarchical ordering (HO) in fourth–order perturbation theory, according to

$$\Delta_P^{\mathrm{HO}(4)}(\tau) = \mathrm{e}^{-\tau^2/2\sigma_0^2} \sum_{n=3}^{12} \frac{a_P^{\mathrm{HO}}(4,n)}{n!} \mathrm{He}_n(\tau/\sigma_0) \ , \qquad (149)$$

where the NG–coefficients $a_P^{\mathrm{HO}}(4,n)$ are obtained from equations (117) and (138) using γ_1, γ_2 and the cumulants C_n in table 4.

We verified that, at second and third–order, the HO–expansion displays an almost purely odd function (central symmetry), while Δ_P (black dashed line) does not pass by the central point ($\tau = 0$, $\Delta_P(0)$, see equation (105)), and we note that $\Delta_{Px}(\tau)$ derived from moments of pixels, not shown here, confirms this behaviour.

At fourth–order, however, the HO–expansion fits well the non–Gaussianity of the sample and reveals the same shift from perfect central symmetry. (For some further

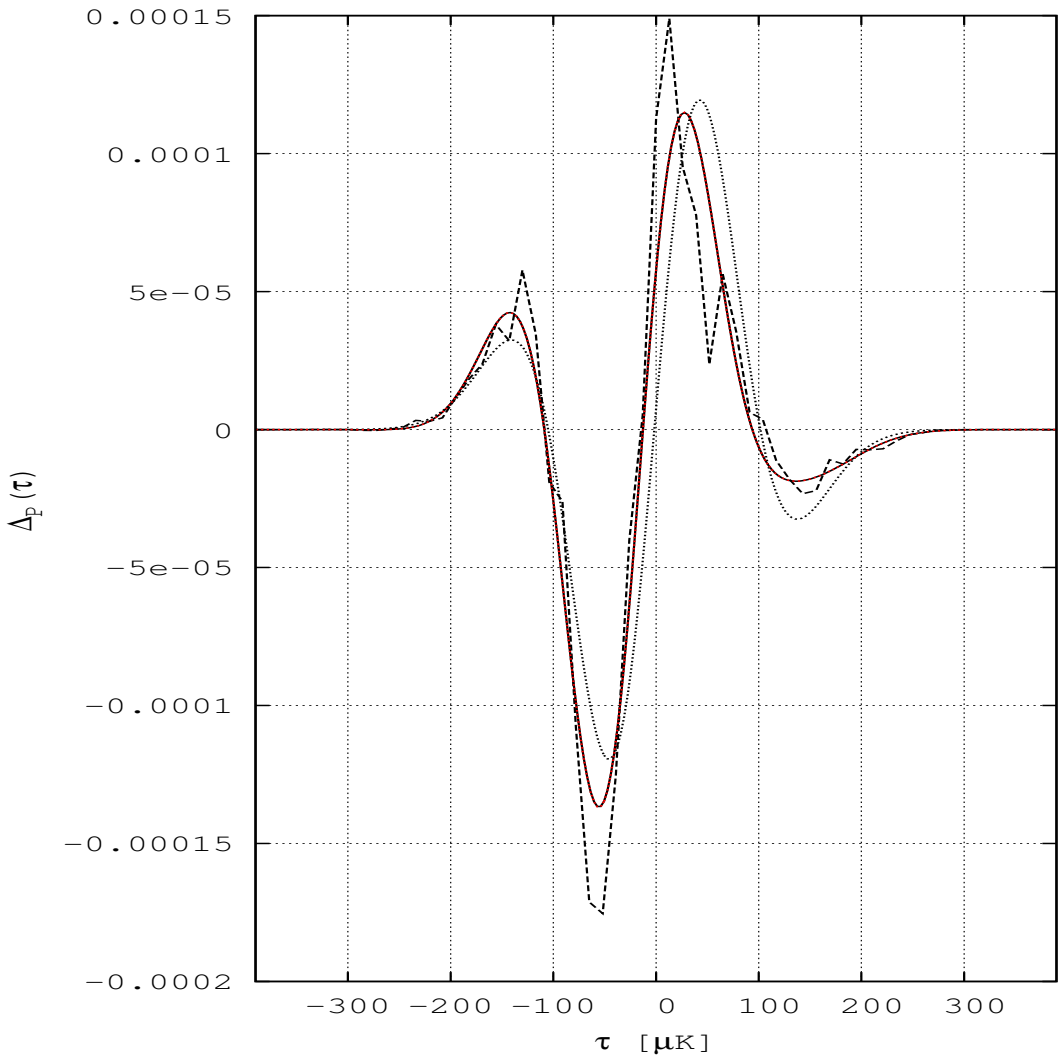

Figure 16: ΛCDM map sample, N_{side}=128, ℓ_{range}=[2,256] without mask, 2° fwhm, for a 13μK temperature bin width over the largest temperature range of the sample ($\pm 396.5 \mu K$). We plot the discrepancy function (black dashed line) of the PDF for the 10^5 maps ensemble. As a black dotted line we show the perturbative expansion according to equation (149) limited to $n = 6$ (hierarchical ordering and second–order perturbation theory); the red line shows the result for the HO($J = 4$) expansion of equation (149) up to $n = 12$ (the coefficients a_P^{HO} obtained from equations (117) and (138), which practically coincides with the black solid line showing the Hermite expansion at order 6 according to equation (148).

discussion on the perturbative model with hierarchical ordering, we refer the reader to 8.5).

5.2.6 The Minkowski Functionals $\boldsymbol{v}_1(\nu)$ and $\boldsymbol{v}_2(\nu)$

According to Hadwiger's theorem [19], there are three independent MFs on $\mathcal{S}^2$. The simplest case V_0, respectively v_0 has already been discussed in subsection 5.2.3. In

this section, we discuss the remaining two which are defined again with respect to the excursion set $\mathcal{Q}_\nu$, see equation (106), and are given in their normalized form by

$$v_1(\nu) := \frac{1}{4\pi} V_1(\nu) = \frac{1}{4\pi}\frac{1}{4}\int_{\partial\mathcal{Q}_\nu} \mathrm{d}s = \frac{1}{16\pi}\,\text{length}\,(\partial\mathcal{Q}_\nu) \quad , \tag{150}$$

$$v_2(\nu) = \frac{1}{4\pi} V_2(\nu) = \frac{1}{4\pi}\frac{1}{2\pi}\int_{\partial\mathcal{Q}_\nu} \kappa(s)\;\mathrm{d}s \quad , \tag{151}$$

where $\mathrm{d}s$ denotes the line element along $\partial\mathcal{Q}_\nu$, and $\kappa(s)$ the geodesic curvature of $\partial\mathcal{Q}_\nu$. The *Gaussian prediction* for the MFs, $v_k(\nu), k = 1, 2$, have been computed by Tomita [21–23] (we set $\mu = 0$):

$$v_1^{\mathrm{G}}(\nu) := \frac{1}{8\sqrt{2}}\frac{\sigma_1}{\sigma_0}\,\mathrm{e}^{-\nu^2/2} \quad ; \quad v_2^{\mathrm{G}}(\nu) = \frac{1}{2(2\pi)^{3/2}}\frac{\sigma_1^2}{\sigma_0^2}\,\nu\,\mathrm{e}^{-\nu^2/2} \quad . \tag{152}$$

Here, σ_0 denotes again the standard deviation of the CMB temperature anisotropy $\delta T(\hat{\boldsymbol{n}})$ on $\mathcal{S}^2$, where $\hat{\boldsymbol{n}} = \hat{\boldsymbol{n}}(\vartheta, \varphi)$ denotes a unit vector on $\mathcal{S}^2$ dependent on the coordinates $x^1 = \vartheta \in [0, \pi]$ and $x^2 = \varphi \in [0, 2\pi]$. Then, the line element on $\mathcal{S}^2$ is given by $\mathrm{d}s^2 = \gamma_{ij}\mathrm{d}x^i\mathrm{d}x^j$ with $\gamma_{11} = 1$, $\gamma_{22} = \sin^2\vartheta$, $\gamma_{ij} = 0$ otherwise, and $\gamma_{ik}\gamma^{kj} = \delta_i{}^j$. Furthermore, σ_1^2 is the *variance of the gradient field* $\boldsymbol{\nabla}\delta T = (\nabla^1\delta T, \nabla^2\delta T)$, i.e.,

$$\langle \nabla_i \delta T(\hat{\boldsymbol{n}}) \nabla_j \delta T(\hat{\boldsymbol{n}}) \rangle = \frac{\sigma_1^2}{2}\,\gamma_{ij} \quad . \tag{153}$$

From the MFs v_1 and v_2 one can form, by a linear combination, two further interesting measures, the *Euler characteristic* $\chi(\nu)$, respectively the *genus* $g(\nu) := 1 - \frac{1}{2}\chi(\nu)$. On the excursion set $\mathcal{Q}_\nu$ with smooth boundary $\partial\mathcal{Q}_\nu$ the *Gauss–Bonnet theorem* holds ($K = 1/R^2 \equiv 1$ is the Gaussian curvature on the unit sphere with radius $R = 1$):

$$\int_{\mathcal{Q}_\nu} K\,\mathrm{d}a + \int_{\partial\mathcal{Q}_\nu} \kappa(s)\mathrm{d}s = V_0(\nu) + 2\pi V_2(\nu) = 2\pi\,\chi(\nu) \quad , \tag{154}$$

which gives

$$\chi(\nu) = 2v_0(\nu) + 4\pi v_2(\nu) \quad \text{and} \quad g(\nu) = 1 - v_0(\nu) - 2\pi v_2(\nu) \quad . \tag{155}$$

As a measure of possible non–Gaussianities based on the MFs $v_k(\nu), k = 1, 2$, we define, in analogy to the discrepancy functions $\Delta_P(\nu)$ (equation (97)) and $\Delta_0(\nu)$ (equation (113)), the following *discrepancy functions* (we here include also the case $k = 0$):

$$\Delta_k(\nu) := \frac{v_k(\nu) - v_k^{\mathrm{G}}(\nu)}{N_k} \quad (k = 0, 1, 2) \quad , \tag{156}$$

with $N_0 = 1/\sqrt{2\pi}$, $N_1 = \max\{v_1^{\mathrm{G}}\} = [1/(8\sqrt{2})]\sigma_1/\sigma_0$, and $N_2 = [1/(2(2\pi)^{3/2})]\sigma_1^2/\sigma_0^2$. Under the same assumptions made before (for Δ_P respectively Δ_0, see 8.5), we can expand the Δ_k's into a convergent *Hermite expansion*,

$$\Delta_k(\nu) = \mathrm{e}^{-\nu^2/2}\sum_{n=n_k}^{\infty}\frac{a_k(n)}{n!}\,\mathrm{He}_n(\nu) \quad ; \quad k = 0, 1, 2 \quad , \tag{157}$$

with the dimensionless NG–coefficients $a_k(n)$ and $n_0 = 2$, $n_1 = n_2 = 0$. With the help of (103) we obtain the integral representation:

$$a_k(n) = \frac{1}{\sqrt{2\pi}}\int_{-\infty}^{\infty}\Delta_k(\nu)\,\mathrm{He}_n(\nu)\,\mathrm{d}\nu \quad . \tag{158}$$

Again, it is assumed that the series (157) can be truncated at a low value $n = N$, where N may depend on k. In the following, we shall again compare the general expansion (157) with the one derived under the assumption of hierarchical ordering ($k = 0, 1, 2$),

$$\Delta_k^{\mathrm{HO}(J)}(\nu) = \mathrm{e}^{-\nu^2/2} \sum_{n=n_k}^{M_k(J)} \frac{a_k^{\mathrm{HO}}(J,n)}{n!} \mathrm{He}_n(\nu) \quad , \tag{159}$$

for which the second order NG–coefficients $a_k^{\mathrm{HO}}(2,n)$ have also been calculated by Matsubara [51, 59] for $k = 1$ and $k = 2$. The highest degree of the Hermite polynomials contributing for $J = 2$ is given by $M_1(2) = 6$ and $M_2(2) = 7$.
The NG–coefficients are then given for $\Delta_1^{\mathrm{HO}(J)}(\nu)$ as follows:
$J = 2, M_1(2) = 6$:

$$\begin{aligned}
a_1^{\mathrm{HO}}(2,0) &= -\frac{K_3}{16} \\
a_1^{\mathrm{HO}}(2,1) &= -\frac{S_1}{4} \\
a_1^{\mathrm{HO}}(2,2) &= -\frac{1}{6}(K_1 + \frac{3}{8}S_1^2) \\
a_1^{\mathrm{HO}}(2,3) &= \gamma_1 \\
a_1^{\mathrm{HO}}(2,4) &= \gamma_2 - \gamma_1 S_1 \\
a_1^{\mathrm{HO}}(2,5) &= 0 \\
a_1^{\mathrm{HO}}(2,6) &= 10\gamma_1^2 \quad .
\end{aligned} \tag{160}$$

and for $\Delta_2^{\mathrm{HO}(J)}(\nu)$:
$J = 2, M_2(2) = 7$:

$$\begin{aligned}
a_2^{\mathrm{HO}}(2,0) &= -S_2 \\
a_2^{\mathrm{HO}}(2,1) &= -\frac{1}{2}(K_2 + S_1 S_2) \\
a_2^{\mathrm{HO}}(2,2) &= -S_1 \\
a_2^{\mathrm{HO}}(2,3) &= -K_1 - \gamma_1 S_2 \\
a_2^{\mathrm{HO}}(2,4) &= 4\gamma_1 \\
a_2^{\mathrm{HO}}(2,5) &= 5\gamma_2 - 10\gamma_1 S_1 \\
a_2^{\mathrm{HO}}(2,6) &= 0 \\
a_2^{\mathrm{HO}}(2,7) &= 70\gamma_1^2 \quad .
\end{aligned} \tag{161}$$

Here, we introduced the three dimensionless skewness parameters γ_1, S_1, S_2 and the four dimensionless kurtosis parameters γ_2, K_1, K_2 and K_3 using the notation $\tau = \tau(\hat{\boldsymbol{n}}) := \delta T(\hat{\boldsymbol{n}})$ (γ_1 and γ_2 as in equations (88) and (89), respectively):

$$\begin{aligned}
S_1 &:= \frac{\left\langle \tau^2 \boldsymbol{\nabla}^2 \tau \right\rangle_C}{\sigma_0 \sigma_1^2} \quad ; \quad S_2 := \frac{\left\langle |\boldsymbol{\nabla}\tau|^2 \boldsymbol{\nabla}^2 \tau \right\rangle_C \sigma_0}{\sigma_1^4} \quad ; \\
K_1 &:= \frac{\left\langle \tau^3 \boldsymbol{\nabla}^2 \tau \right\rangle_C}{\sigma_0^2 \sigma_1^2} \quad ; \quad K_2 := \frac{2\left\langle \tau |\boldsymbol{\nabla}\tau|^2 \boldsymbol{\nabla}^2 \tau \right\rangle_C + \left\langle |\boldsymbol{\nabla}\tau|^4 \right\rangle_C}{\sigma_1^4} \quad ; \quad K_3 := \frac{\left\langle |\boldsymbol{\nabla}\tau|^4 \right\rangle_C}{\sigma_1^4} \, .
\end{aligned} \tag{162}$$

(Note that the products of the field $\tau(\hat{\boldsymbol{n}})$ respectively of its derivatives are taken at the same point $\hat{\boldsymbol{n}}$ on $\mathcal{S}^2$.)

Table 7 shows the coefficients $a_1(n)$ and $a_2(n)$ calculated from (158).

ΛCDM sample Full individual map range, no mask, 2°fwhm, bin 13μK *c.f.* 8.2									
n	0	1	2	3	4	5	6	7	8
$a_1(n)$	-2.21×10^{-6}	-2.808×10^{-5}	3.97274×10^{-3}	-5.0873×10^{-4}	-5.823×10^{-5}	-6.643×10^{-5}	-1.97922×10^{-3}	5.059×10^{-5}	6.37408×10^{-3}
$a_2(n)$	1.927×10^{-5}	-2.148×10^{-5}	-1.7313×10^{-4}	1.183631×10^{-2}	-1.53488×10^{-3}	-4.8941×10^{-4}	-1.20822×10^{-3}	-9.58844×10^{-3}	-7.33397×10^{-3}

Table 7: Table of coefficients $a_1(n)$ and $a_2(n)$.

Figure 17 shows the second Minkowski Functional, and figure 18 the discrepancy function Δ_1 together with the Hermite expansion to order 8. The third Minkowski Functional is shown in figure 19, and the discrepancy function Δ_2 together with the Hermite expansion to order 8 in figure 20.

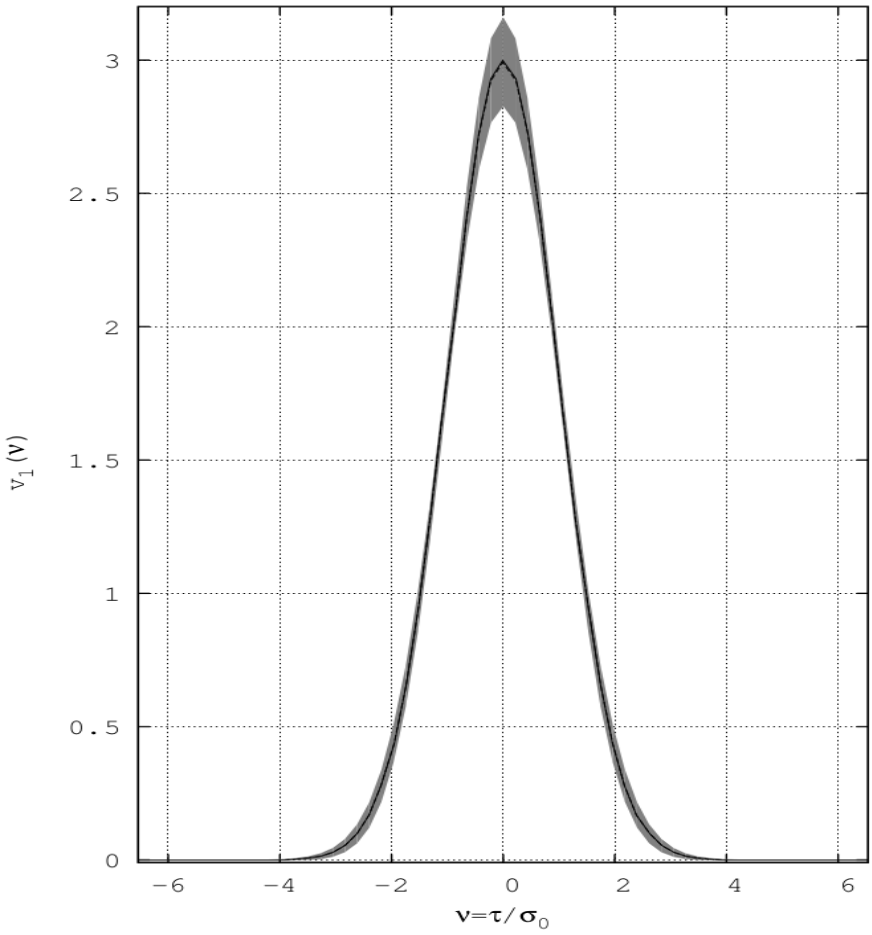

Figure 17: ΛCDM map sample, $N_{\rm side}$=128, $\ell_{\rm range}$=[2,256] without mask, 2° fwhm, for a 13μK temperature bin width over the largest temperature range of the sample ($\pm 396.5 \mu K$). We plot the second Minkowski Functional $v_1(\nu)$ as a black dashed line with its Gaussian premise as a black solid line (almost coincident). The 1σ cosmic variance is the grey shaded area. (We use $\sigma^2_{\rm 0px}$ and $\sigma^2_{\rm 1px}$ – see, respectively, 2^{nd} equation in (186) and equation (188) as well as table 8.)

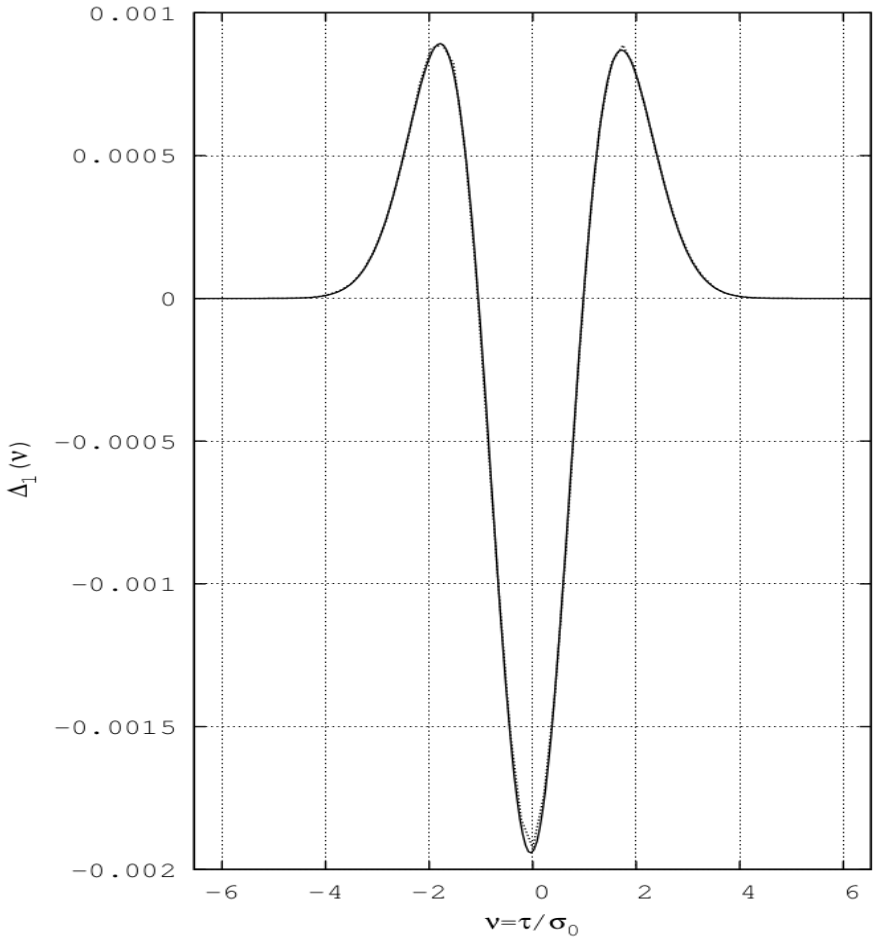

Figure 18: We plot $\Delta_1(\nu)$, the discrepancy function of v_1 as a dotted line, and as a solid line the Hermite expansion to order 8. (For the $\sigma-$values used, see caption to figure 17.)

5.2.7 Discrepancy functions and Df−differences

GAUSSIAN random fields have a specific signature (the Gaussian prediction) depending only on the choice of the descriptor. Non–Gaussian processes may generate strong departures from the Gaussian prediction as in the formation of large–scale structure; however, attempts to find general and specific analytic signatures of a statistical property sufficiently far away from Gaussianity are most of the time unsuccessful in the context of CMB analyses. It is clear that the values $\sigma_{0C\ell}$ and $\sigma_{1C\ell}$ are model–dependent and that their use in the formulae for the Gaussian prediction, equations (92), (111) and (152), biases the reference of Gaussianity in general, so that the $\sigma-$values from the moments of pixels (denoted by subscripts px, x) or from the moments of the PDF should rather be used in the *discrepancy functions* $\Delta_k(...)$ we defined above. As a reminder, we list here the whole set of *discrepancy functions*:

$$\Delta_P(\tau) := \frac{P(\tau) - P^{\rm G}(\tau)}{N_{\rm P}}, \quad \text{with} \quad N_{\rm P} = \frac{1}{\sigma_0\sqrt{2\pi}}\,; \tag{163}$$

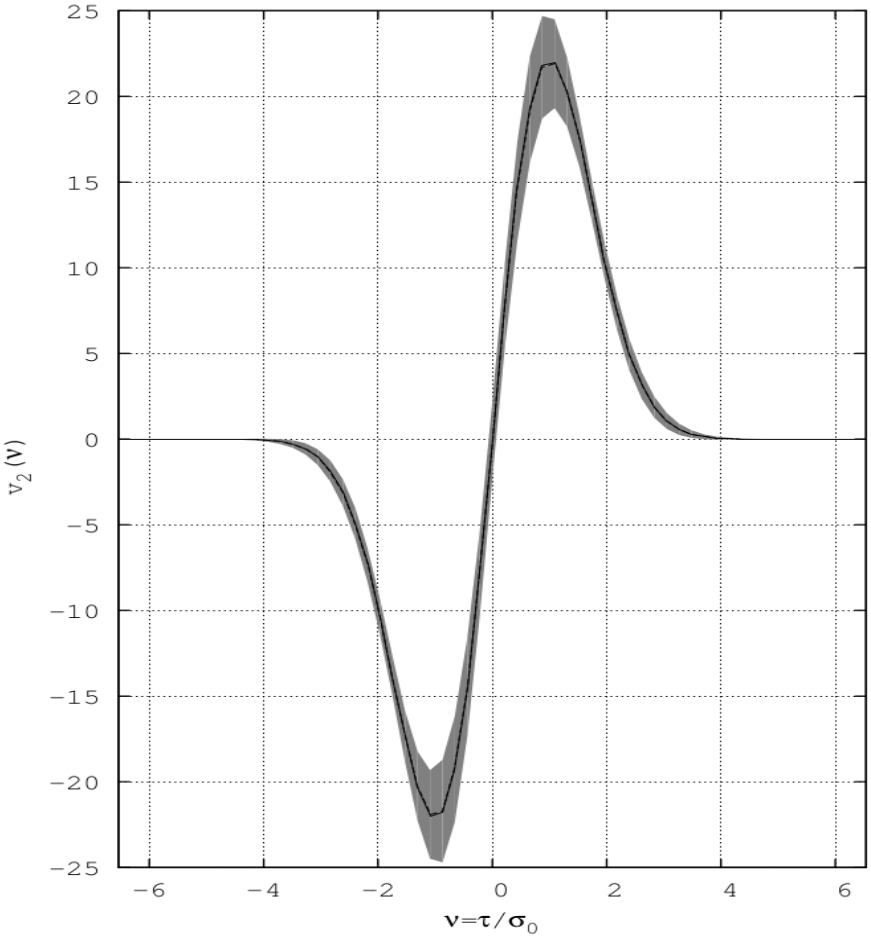

Figure 19: ΛCDM map sample, $N_{\rm side}$=128, $\ell_{\rm range}$=[2,256] without mask, 2° fwhm, for a 13μK temperature bin width over the largest temperature range of the sample ($\pm 396.5 \mu K$). We plot the third Minkowski Functional $v_2(\nu)$ as a black dashed line with its Gaussian premise as a black solid line (almost coincident). The 1σ cosmic variance is the grey shaded area. (For the $\sigma-$values used, see caption to figure 17.)

$$\Delta_0(\nu) := \frac{v_0(\nu) - v_0^{\rm G}(\nu)}{N_0}, \quad \text{with} \quad N_0 = \frac{1}{\sqrt{2\pi}}, \qquad \nu = \frac{\tau}{\sigma_{0\rm px}}\ ; \qquad (164)$$

$$\Delta_1(\nu) := \frac{v_1(\nu) - v_1^{\rm G}(\nu)}{N_1}, \quad \text{with} \quad N_1 = \frac{1}{8\sqrt{2}}\frac{\sigma_{1\rm px}}{\sigma_{0\rm px}}, \qquad \nu = \frac{\tau}{\sigma_{0\rm px}}\ ; \qquad (165)$$

$$\Delta_2(\nu) := \frac{v_2(\nu) - v_2^{\rm G}(\nu)}{N_2}, \quad \text{with} \quad N_2 = \frac{1}{2(2\pi)^{3/2}}\frac{\sigma_{1\rm px}^2}{\sigma_{0\rm px}^2}, \quad \nu = \frac{\tau}{\sigma_{0\rm px}}\ . \qquad (166)$$

These discrepancy functions are self–consistent and model–independent given that the terms used, $\sigma_{\rm S}$ and $\sigma_{\rm Spx}$ are model–independent; these four formulae ($\Delta_k(...)$) are straightforwardly applicable to a single data or sample map. In the case of determination

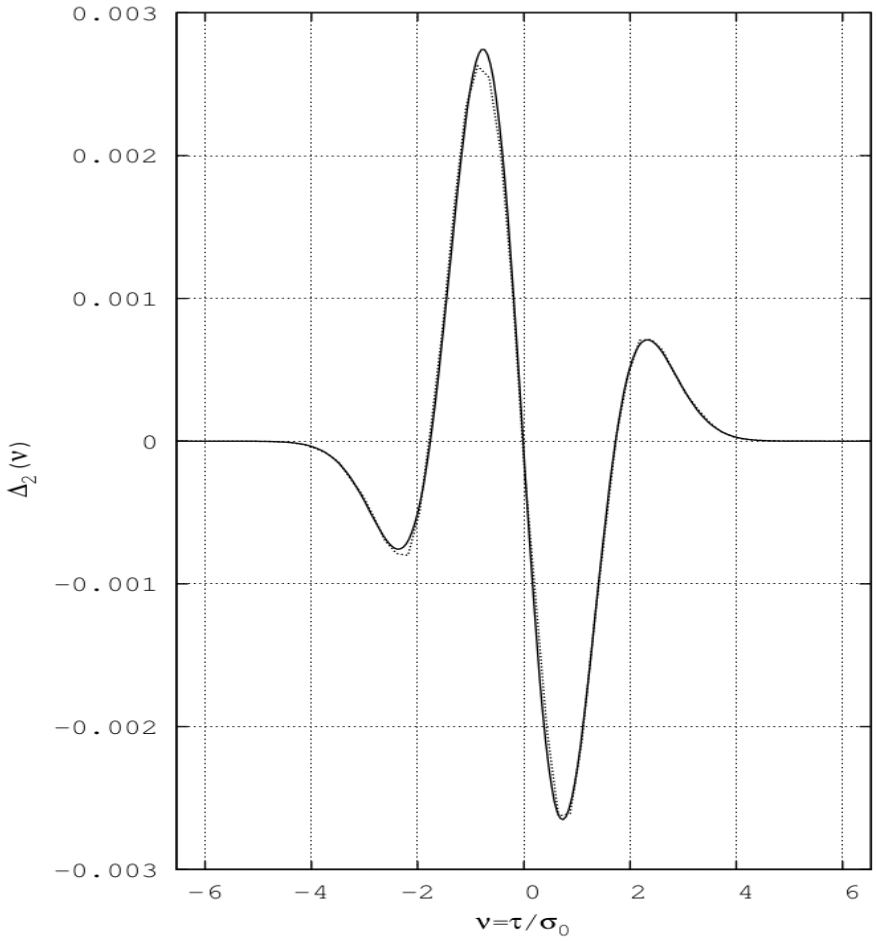

Figure 20: We plot $\Delta_2(\nu)$, the discrepancy function of v_2 as a dotted line, and as a solid line the Hermite expansion to order 8. (For the $\sigma-$values used, see caption to figure 17.)

for a sample S of maps, we define the *sample discrepancy functions* this way:

$$P_{\mathrm{S}}^{\mathrm{G}}(\tau) := P^{\mathrm{G}}\left(\langle\mu\rangle_{\mathrm{S}}\,, \sqrt{\langle\sigma_0^2\rangle_{\mathrm{S}}},\ \tau\right), \tag{167}$$

$$v_{i\mathrm{S}}^{\mathrm{G}}(\nu) := v_i^{\mathrm{G}}\left(\langle\mu_{\mathrm{px}}\rangle_{\mathrm{S}}\,, \sqrt{\left\langle\sigma_{1\mathrm{px}}^2\right\rangle_{\mathrm{S}}}\,, \sqrt{\left\langle\sigma_{0\mathrm{px}}^2\right\rangle_{\mathrm{S}}}\,,\ \nu\right)\ . \tag{168}$$

As mentioned at the end of the introductory section 5.1, the *Planck* collaboration applies a different method of calculation for the non–Gaussianity. While the analytic formulae are not given in the various papers [51–56], we can rebuild them here from the explicit formulations in the text. In the case of a single data map d, the *differences* of the normalized MFs (denoted Df) are given by

$$\mathrm{D}f_i^d(\nu) := \frac{v_i^d(\nu)}{N_i^d} - \left\langle\frac{v_i(\nu)}{N_i}\right\rangle_{\mathrm{S}}\ , \tag{169}$$

where the reference map sample S is Gaussian by construction. Compared with the discrepancy functions, the Df's measure the distance to a Gaussian premise which may

be different in amplitude and shape from our analytical one. The Df's may, under certain conditions, provide a direct statistical measure of the departure from a given cosmological model statistics, which is an interesting feature.

Let us make some remarks on this methodology addressing some important issues. The variance terms σ_S, entering the left and right denominators of equation (169), may differ in the sample map generation, if no special precaution is taken. We have compared the results of this Df−method (using Gaussian ΛCDM map samples) with our discrepancy functions method, using the analytical Gaussian premises, and found no significant difference of non–Gaussianity. But, obviously, the dependence on the statistical properties of the map sample and the number of maps may yield different results. It is not clear how the non–Gaussianity of the reference map sample is calculated as the direct application of the formula (169) gives zero and in this case, the analytic Gaussian premise is probably used. If instead our discrepancy functions are applied to the sample, we do not employ different methods for comparing the non–Gaussianity of a CMB data map with a CMB map sample.

5.2.8 Comparing the ΛCDM map sample to the *Planck* map

The next figures, figure 21, figure 22, figure 23 and figure 24 show the statistical and morphological behaviour of each of the 10^5 sample maps in the ΛCDM model compared with the four *Planck* maps $NILC$, $SEVEM$, $SMICA$ and *Commander—Ruler*, all with the $U73$ mask and a bin width of 6μK. The average quantities μ, σ_0 and σ_1, as well as the discrepancy functions are calculated over the largest common and centered (on $\nu = 0$) temperature range $[-201\mu\text{K}, +201\mu\text{K}]$, as given by the *Planck* 2015 $SMICA$ map. In these figures, clearly, the non–Gaussianity of the average sample is weak. For each descriptor, many ΛCDM sample maps show a strong non–Gaussianity; several individual sample maps lying well beyond the 5σ cosmic variance limit.

The benchmark study of *Planck* maps and the ΛCDM sample with U73 mask (figures 21 to 24) compares all the different maps over the same temperature range ($\pm 201\mu K$) for a $6\mu K$ binning, and shows very populated (almost saturated) 4σ–sample envelopes for each of the four discrepancy functions. In the case of Δ_P we count 240 maps (among 100000) peaking beyond the 6σ–envelope. Peaking beyond 6σ we also count 354 maps for Δ_0.

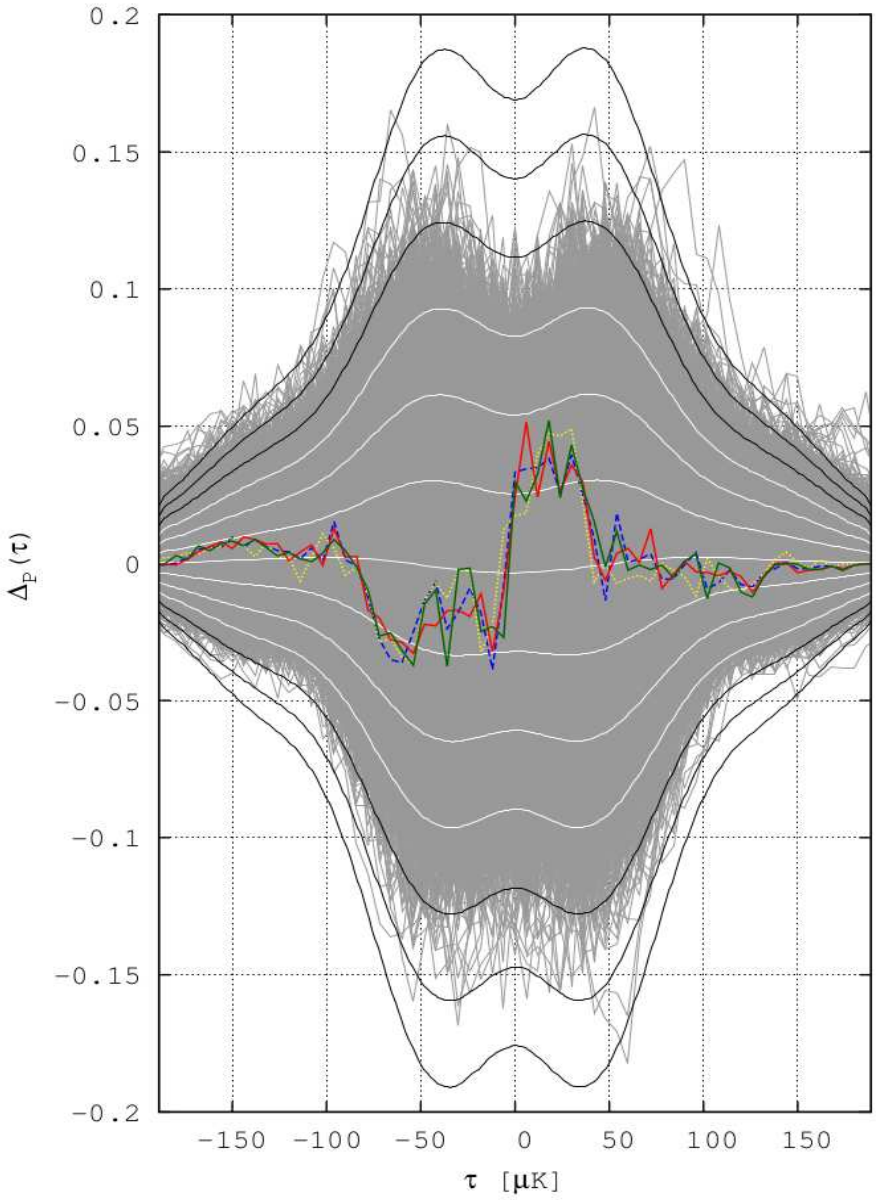

Figure 21: Envelope of each Δ_P function in grey, 1σ to 6σ cosmic variances in white or black solid lines. The central and almost horizontal white line is the discrepancy function of the average sample. *Planck* maps are in blue dashed line for $NILC$, yellow dotted line for $SEVEM$, in red solid line for $SMICA$, and green solid line for *Commander–Ruler*, as calculated for the ΛCDM map sample, $N_{\rm side}$=128, $\ell_{\rm range}$=[2,256] with $U73$ mask, 2° fwhm, for a 6μK temperature bin width over the equal temperature range ($\pm 201 \mu K$).

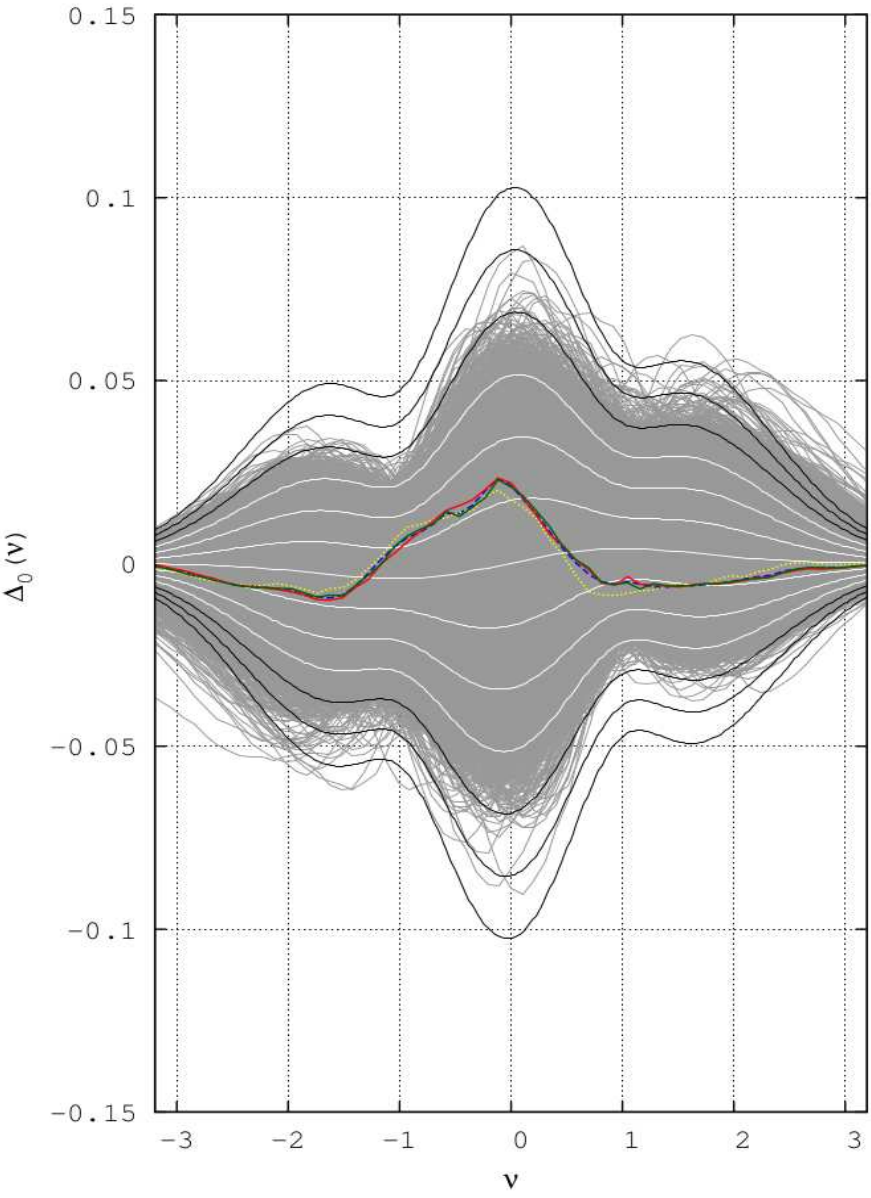

Figure 22: Envelope of each Δ_0 function. Same figure caption as in figure 21.

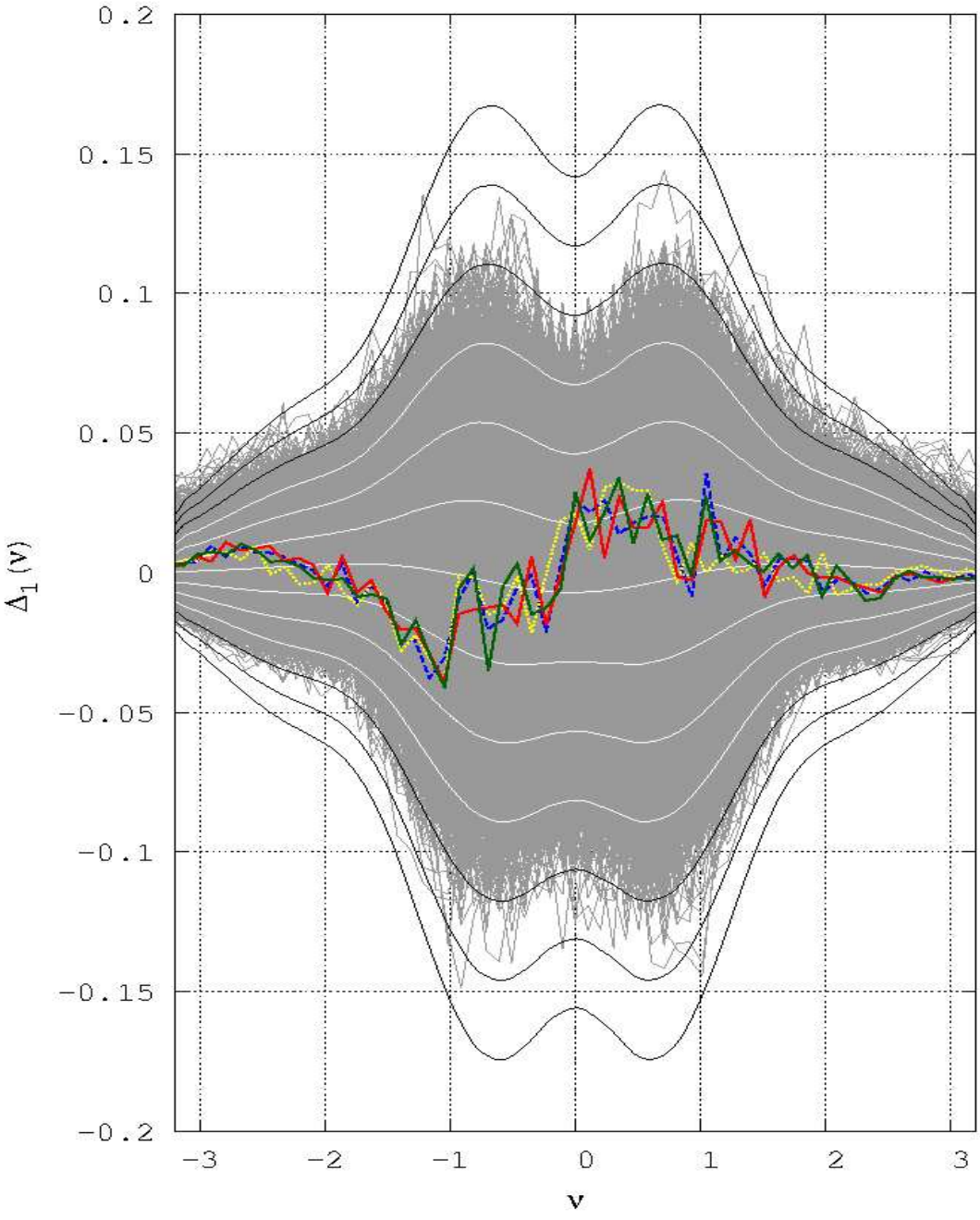

Figure 23: Envelope of each Δ_1 function. Same figure caption as in figure 21.

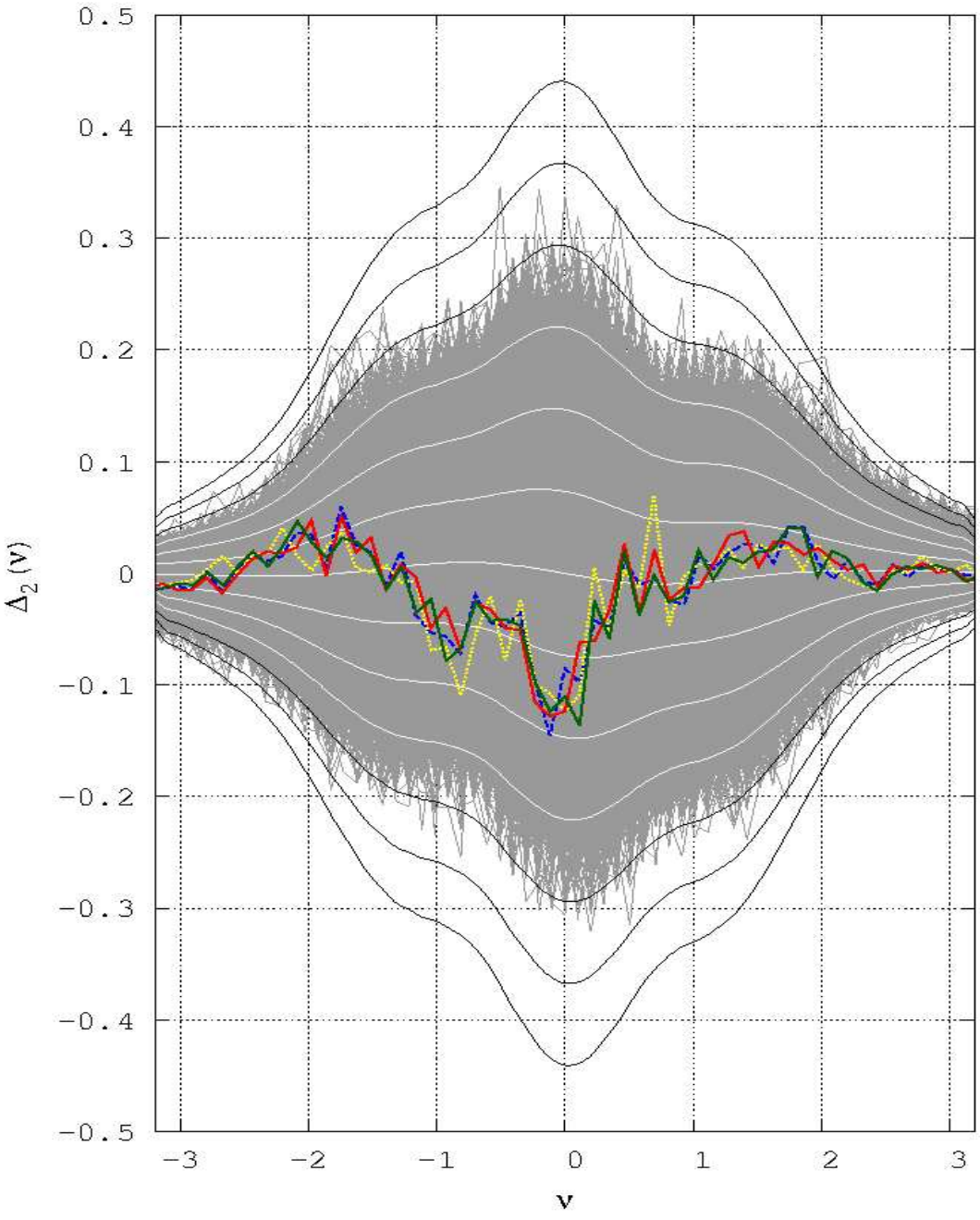

Figure 24: Envelope of each Δ_2 function. Same figure caption as in figure 21.

5.3 Three brief discussions about the CMB non–Gaussianity

5.3.1 Origin of non–Gaussianities

CONTRARY to other works to unveil CMB non–Gaussianity, no specific model of non–Gaussianity has been put into the 100000 maps of the ΛCDM sample probed all along this study (see 8.2). However, already without mask, as in the initial analysis of the sample explored in this chapter, we find that the four discrepancy functions show small but clear departures from Gaussianity, and this for a map ensemble that is supposed to be highly if not completely Gaussian, since it is computed from the ΛCDM model using purely Gaussian initial conditions. What is the origin of these NGs? For a given ensemble of realizations one expects several extraneous mechanisms that generate supplementary NG such as: an increasing smoothing scale beyond the 1° horizon angular scale on the surface of last scattering increases the NG amplitude (increasing the dependence between neighbouring pixels acts in the sense of enlarging the causal horizon radius); we also checked that smoothing leaves the shape of the discrepancy functions unaffected, while rising the amplitude of NG. Our present study shows that these numerical NGs are of non-negligible amplitude even for a 100000 map sample without mask. Our previous analyses using different parameters $N_{\rm side}$, $l_{\rm max}$, fwhm, without or with mask leave the shape of the descriptors Δ_1 and Δ_2 invariant, but with different amplitudes (we have no such invariance for Δ_P and Δ_0, they detect the mask). We reached the same conclusion using different cosmological parameters (e.g. $WMAP$ 7yr) for the generation of the power spectrum to get a 100000 map sample. The comparison with the NG of the observed CMB (figures 21 to 24) shows that numerous individual ΛCDM maps can possibly be of the same amplitude and shape of NG than the *Planck* data map. These assessments would say that without any addition of supplementary NGs in each sample map, some sources of non–Gaussianity existing in the power spectrum used to generate the maps may well be detected by the discrepancy functions. The census of components is in 8.2.3. Among them, probably some cannot be detected because we limit the l–range to $[2, 256]$, but the Sachs–Wolfe effect, the Doppler effect and the integrated Sachs–Wolfe effect would contribute to the non–Gaussianity detected in the individual maps of the ensemble. A systematic study is needed to disentangle the NG effects of the various components.

5.3.2 The case of σ_0

WHEN μ, σ_0, and σ_1 are evaluated over $[-\tau_m, \tau_m]$, while the discrepancy functions are calculated over a smaller interval in τ (resp. in ν), this leads to an error on their shape and to an overestimate of the magnitude of NG, as we tested for the 100000 map sample. Such a problem may arise when one works with the normalized temperature $\nu = \tau/\sigma_0$. While $\sigma_0(\tau_{max1})$ is known for the temperature range τ_{max1} giving $\nu_{max1} = \tau_{max1}/\sigma_0(\tau_{max1})$, the need to impose a ν–range (ν_{max2}) different from ν_{max1} (e.g. for comparing with another map sample) is equivalent to solve for an implicit function f, $\sigma_0(\nu_{max2}) = f(\sigma_0(\nu_{max2}))$, simply because two different map samples or two different

maps will have in general different variances and variances of the gradient, even if they are explored over the exactly same temperature range. The estimation of the unknown σ_0 corresponding to the new ν–range can be made using iterative methods, or by referring to a model that predicts the behaviour of σ_0 for given changes of the range. For the comparison (with U73 mask) of *Planck* maps to the ΛCDM sample, $P(\tau)$ and $\Delta_P(\tau)$ show no difficulties as abscissas are in τ and impose the same range to data and to the simulation maps.

For $\Delta_{0,1,2}$ we first calculated μ's and σ's over the full τ–range ($\pm$ 201 μK) of the four different *Planck* maps. For each of these we obtain the following σ_0 values: *NILC* 51.532μK, *SEVEM* 51.750μK, *SMICA* 51.576μK, *Commander—Ruler* 51.794μK, while we obtain σ_0 =59.294μK for the ΛCDM simulations over exactly the same ($\pm$ 201 μK) range! This illustrates well the "anomalously" low variance of *Planck* data already observed with *WMAP* compared to a ΛCDM model map ensemble (see [11,80–85] and [56, 86]). When not treated correctly, the impact of this anomaly is significant for the calculation of the Gaussian premises $P^{\rm G}$, equation (92), and $v_k^{\rm G}$, equations (110) and (152), as they are functions of the standard deviation σ_0. Regarding v_1 and v_2 we made two interesting observations: firstly, the Gaussian premises $v_1^{\rm G}$ and $v_2^{\rm G}$ are functions of the ratio $\rho = \sigma_1/\sigma_0$ in the prefactor of the exponential, and we verified that this ratio is very similar for the four *Planck* maps, $\rho = 36.658^{+0.030}_{-0.032}$, even if the σ_0's are not very similar, $\sigma_0 = 51.663\mu{\rm K}^{+0.131}_{-0.131}$. For the simulation sample, $\rho_{\Lambda CDM}$ has a much smaller value: 34.162. Secondly, we observed that the ratio ρ is very stable for the sample with U73 mask and for *Planck* maps with U73 mask when passing from the largest common temperature range ($\pm$ 201 μK) to the smallest temperature range covering all the maps ($\pm$ 396.5 μK). On the other hand we noticed (see at the beginning of 8.2) that the ratio ρ is no more stable but increasing when passing from no mask to U73 mask.

In summary, in the present work, the issue of the fair comparison of different CMB maps, (i) is treated by using exactly the same temperature range for P, $P^{\rm G}$ and Δ_P, (ii) for v_0, $v_0^{\rm G}$ and Δ_0 it required some iterations upon different temperature ranges to reach close to the $\nu_{\rm max}$ values, and (iii) is simplified for v_1, $v_1^{\rm G}$, v_2, $v_2^{\rm G}$, Δ_1 and Δ_2 by assuming $\rho = \sigma_1/\sigma_0$ to be constant for the given change of temperature range.

5.3.3 The f_{NL} results

Non–linear correction terms within the standard perturbation approach are commonly investigated by constraining the coefficients (bi–spectrum with $f_{\rm NL}$ and tri–spectrum with $g_{\rm NL}$). Applied to Bardeen's curvature these constraints allow to decide whether inflation models such as with single slow–roll scalar field are rejected or not. A scalar random field of the primordial period, the gravitational potential $\Phi(\hat{\boldsymbol{n}})$ ($\hat{\boldsymbol{n}} = \hat{\boldsymbol{n}}(\vartheta, \varphi)$), is commonly expanded in real space around a Gaussian random field $\phi(\hat{\boldsymbol{n}})$ (of vanishing mean), using the expansion:

$$\Phi(\hat{\boldsymbol{n}}) = \phi(\hat{\boldsymbol{n}}) + f_{\rm NL}^{\rm (local)}(\phi^2(\hat{\boldsymbol{n}}) - \left\langle \phi^2(\hat{\boldsymbol{n}}) \right\rangle) + g_{\rm NL}^{\rm (local)}(\phi^3(\hat{\boldsymbol{n}}) - \left\langle \phi^3(\hat{\boldsymbol{n}}) \right\rangle) + \cdots . \tag{170}$$

In 2010, the limit derived from *WMAP* 7yr was $f_{\rm NL}^{\rm (local)} \approx 30 \pm 20$ at 1σ, a very small non–Gaussianity almost compatible with a zero value allowing for single–scalar fields [1]. *Planck* 2013 data, expected to give smaller error bars, have narrowed this to $f_{\rm NL}^{\rm (local)} = 2.7 \pm 5.8$, $f_{\rm NL}^{\rm (equilateral)} = -42 \pm 75$, and $f_{\rm NL}^{\rm (orthogonal)} = -25 \pm 39$ [88]. Then,

Planck 2015 temperature data provided $f_{\rm NL}^{\rm (local)} = 2.5 \pm 5.7$, $f_{\rm NL}^{\rm (equilateral)} = -16 \pm 70$, and $f_{\rm NL}^{\rm (orthogonal)} = -34 \pm 33$ [4]. All these very similar outcomes are consistent with a vanishing f_{NL}, which is itself consistent with a very weak primordial non–Gaussianity. However, the interpretation of this characterization of CMB Gaussianity depends on the cosmological model and, in particular, on the type of inflation mechanism that is assumed in this model.

5.4 **Conclusion**

DETECTING non–Gaussianity in the CMB temperature maps is still a great challenge. Whatever the descriptor, the discrepancy functions of the CMB by *Planck* 2015 data are not zero but stay within 1σ or slightly leak into the 2σ cosmic variance band of current (model–dependent) ensembles. In our search for CMB non–Gaussianities we find systematic signatures of weak non–Gaussianity which would be of importance if the ensemble cosmic variance would be re-evaluated at smaller amplitudes. Compared to the *Planck* maps we find that the ΛCDM simulations commonly used offer a systematically larger value for the variances σ_0^2 and σ_1^2 as observed in [11, 80–85] and [56, 86]. This anomaly of the variances and its interpretation has to be explored in more detail in the prescriptions of model simulations. Furthermore, after the first main mask is applied, further different possible superimposed foreground and source masks have a big impact upon the magnitude of non–Gaussianities, showing that numerous tiny field sources contribute to residual foreground contamination and may imply a noticeable change in the values of the variances [87]. Several possible strategies should be explored to select ensembles on the basis of the actually observed statistical parameters within a constrained random field approach, in order to reach a deeper understanding of a statistical comparison with a single realization, or to accordingly constrain cosmological models.

References

[1] Komatsu E 2010 Hunting for primordial non–Gaussianity in the Cosmic Microwave Background *Class. Quantum Grav.* **27** 124010 (*Preprint* arXiv:1003.6097)

[2] Martin J, Ringeval C and Vennin V 2014 Encyclopaedia Inflationaris *Elsevier* **5-6** 75–235 (*Preprint* arXiv:1303.3787)

[3] Martin J 2016 What have the Planck data taught us about inflation? *Class. Quantum Grav.* **33** 034001 (https://doi.org/10.1088/0264-9381/33/3/034001)

[4] Ade P A R et al. 2016 Planck 2015 results. XVII. Constraints on primordial non–Gaussianity *Astron. Astrophys. Special feature* **594** A17 (*Preprint* arXiv:1502.01592)

[5] Renaux–Petel S 2015 Primordial non–Gaussianities after Planck 2015: an introductory review *Comptes rendus – Physique* **16** 969–985 (*Preprint* arXiv:1508.06740)

[6] Brandenberger R H 2015 String gas cosmology after Planck *Class. Quantum Grav.* **32** 234002 (*Preprint* arXiv:1505.02381)

[7] Ijjas A and Steinhardt P J 2016 Implications of Planck 2015 for inflationary, ekpyrotic and anamorphic bouncing cosmologies *Class. Quantum Grav.* **33** 044001 (*Preprint* arXiv:1512.09010)

[8] Durrer R 2008 The Cosmic Microwave Background *Cambridge, Cambridge University Press* (https://doi.org/10.1017/cbo9780511817205)

[9] Meerburg P D, Meyers J, van Engelen A and Ali–Haïmoud Y 2016 On CMB B–Mode non–Gaussianity *Phys. Rev. D* **93** 123511 (*Preprint* arXiv:1603.02243)
[10] Seljak U and Hirata C M 2004 Gravitational lensing as a contaminant of the gravity wave signal in CMB *Phys. Rev. D* **69** 043005 (*Preprint* arXiv:astro-ph/0310163)
[11] Schwarz D J, Copi D J, Huterer D and Starkman G D 2016 CMB anomalies after Planck *Class. Quantum Grav.* **33** 184001 (*Preprint* arXiv:1510.07929)
[12] Aurich R, Janzer H S, Lustig S and Steiner F 2008 Do we live in a "small Universe"? *Class. Quantum Grav.* **25** 125006 (*Preprint* arXiv:0708.1420)
[13] Aurich R and Lustig S 2013 A search for cosmic topology in the final WMAP data *Mon. Not. Roy. Astr. Soc.* **433** 2517–2528 (*Preprint* arXiv:1303.4226)
[14] Aurich R 2008 A spatial correlation analysis for a toroidal universe *Class. Quantum Grav.* **25** 225017 (*Preprint* arXiv:0803.2130)
[15] Bolejko K, Nazer M A and Wiltshire D L 2016 Differential cosmic expansion and the Hubble flow anisotropy *J. Cosmol. Astropart. Phys.* JCAP06(2016)035 (*Preprint* arXiv:1512.07364)
[16] Notari A and Quartin M 2016 CMB all–scale blackbody distortions induced by linearizing temperature *Phys. Rev. D* **94** 043006 (*Preprint* arXiv:1603.02996)
[17] Steiner J 1840 Über parallele Flächen. *Monatsbericht Akad. Wiss. Berlin, Springer*pp 114–8 Steiner J 1971 Ges. Werke II, 2nd edn *Providence, RI: AMS Chelsea*pp 171–6 (https://doi.org/10.1515/9783111611716.171)
[18] Minkowski H 1903 Volumen und Oberfläche *Mathematische Annalen* **57** 447 (https://doi.org/10.1007/978-3-7091-9536-9)
[19] Hadwiger H 1957 Vorlesungen über Inhalt, Oberfläche und Isoperimetrie *Berlin, pringer* (https://doi.org/10.1007/978-3-642-94702-5)
[20] Santaló L A 1976 Integral Geometry and Geometric Probability *Reading, MA: Addison–Wesley* (https://doi.org/10.1017/cbo9780511617331)
[21] Adler R J 1981 The Geometry of Random Fields *Philadelphia, PA: SIAM* (https://doi.org/10.1137/1.9780898718980)
[22] Tomita H 1986 Statistical properties of random interface system *Prog. Theor. Phys.* **75** 952 (https://doi.org/10.1143/PTP.75.482)
[23] Tomita H 1986 Curvature invariants of random interface generated by Gaussian fields *Prog. Theor. Phys.* **76** 4 (https://doi.org/10.1143/ptp.76.952)
[24] Groemer H 1977 Minkowski addition and mixed volumes *Springer, Geometriae Dedicata* **6** **2** 141–163 (https://doi.org/10.1007/bf00181456)
[25] Schneider R 1993 Convex bodies: the Brunn–Minkowski Theory *Encyclopedia of Mathematics and its Applications* **44** *Cambridge, Cambridge University Press* (https://doi.org/10.1017/cbo9780511526282)
[26] Mecke K R 2000 Additivity, convexity, and beyond: applications of Minkowski Functionals in Statistical Physics *Springer, Lecture Notes in Physics* **554** 111–184 (http://www.theorie1.physik.uni-erlangen.de/mecke/papers/additivity00.pdf) (https://doi.org/10.1007/3-540-45043-2)
[27] Bond J R and Efstathiou G 1987 The statistics of cosmic background radiation fluctuations *Mon. Not. Roy. Astr. Soc.* **226** 655–687 (http://articles.adsabs.harvard.edu/full/1987MNRAS.226..655B)
[28] Aurich R, Janzer H S, Lustig S and Steiner F 2011 Ellipticity of structures in CMB sky maps *Int. J. Mod. Phys. D* **20** 2253 (*Preprint* arXiv:1007.2722)
[29] Pogosyan D, Pichon C and Gay C 2011 Non–Gaussian extrema counts for CMB maps *Phys. Rev. D* **84** 083510 (*Preprint* arXiv:1107.1863)
[30] Gay C, Pichon C and Pogosyan D 2012 Non–Gaussian statistics of critical sets in 2D and 3D: Peaks, voids, saddles, genus, and skeleton *Phys. Rev. D* **85** 023011 (*Preprint* arXiv:1110.0261)

[31] Codis S, Pichon C, Pogosyan D, Bernardeau F and Matsubara T 2013 Non–Gaussian Minkowski Functionals and extrema counts in redshift space *Mon. Not. Roy. Astr. Soc.* **425** 2187–2196 (*Preprint* arXiv:1305.7402)
[32] Mecke K R, Buchert T and Wagner H 1994 Robust morphological measures for large–scale structure in the Universe *Astron. Astrophys.* **288** 697–704 (*Preprint* arXiv:astro-ph/9312028)
[33] Kerscher M, Schmalzing J, Buchert T and Wagner H 1998 Fluctuations in the IRAS 1.2 Jy catalog *Astron. Astrophys.* **333** 1–12 (*Preprint* arXiv:astro-ph/9704028)
[34] Kerscher M, Mecke K R, Schmalzing J, Beisbart C, Buchert T and Wagner H 2001 Morphological fluctuations of large–scale structure: the PSCz survey *Astron. Astrophys.* **373**, 1–11 (*Preprint* arXiv:astro-ph/0101238)
[35] Wiegand A, Buchert T and Ostermann M 2014 Direct Minkowski Functional analysis of large redshift surveys: a new high–speed code tested on the luminous red galaxy Sloan Digital Sky Survey–DR7 catalog *Mon. Not. Roy. Astr. Soc.* **443** 241–259 (*Preprint* arXiv:1311.3661)
[36] Kerscher M 2000 Statistical analysis of large–scale structure in the Universe *Springer, Lecture Notes in Physics* **554** 36–71 (*Preprint arXiv:astro-ph/9912329)*
[37] Schmalzing J and Buchert T 1997 Beyond genus statistics: a unifying approach to the morphology of cosmic structure *Astrophys. J.* **482** L1–L4 (*Preprint* arXiv:astro-ph/9702130)
[38] Schmalzing J and Górski K M 1998 Minkowski Functionals used in the morphological analysis of Cosmic Microwave Background anisotropy maps *Mon. Not. Roy. Astr. Soc.* **297** 355–365 (*Preprint* arXiv:astro-ph/9710185)
[39] Tomita H 1990 Statistics and geometry of random interface systems *In: Formation, Dynamics and Statistics of Patterns* **1** 113–157 (Editors K Kawasaki, M Suzuki, A Onuki)*Singapore, World Scientific Publishing* (https://doi.org/10.1142/9789814368223)
[40] Schmalzing J 1999 On Statistics and Dynamics of Cosmic Structure *PhD thesis; supervisor T. Buchert.* Ludwig–Maximilians–Universität München, Germany (https://edoc.ub.uni-muenchen.de/449/)
[41] Schmalzing J, Buchert T, Melott A L, Sahni V, Sathyaprakash B S and Shandarin S F 1999 Disentangling the cosmic web. I. morphology of isodensity contours *Astrophys. J.* **526** 568–578 (*Preprint* arXiv:astro-ph/9904384)
[42] Hikage C, Schmalzing J, Buchert T, Suto Y et al. 2003 Minkowski Functionals of SDSS Galaxies I: analysis of excursion sets *P.A.S.J.* **55** 911–931 (*Preprint* arXiv:astro-ph/0304455)
[43] Beisbart C, Buchert T and Wagner H 2001 Morphometry of spatial patterns *Physica A* **293** 592–604 (*Preprint* arXiv:astro-ph/0007459)
[44] Beisbart C, Valdarnini R and Buchert T 2001 The morphological and dynamical evolution of simulated galaxy clusters *Astron. Astrophys.* **379** 412–425 (*Preprint* arXiv:astro-ph/0109459)
[45] Winitzki S and Kosowsky A 1998 Minkowski Functional description of Microwave Background Gaussianity *New Astronomy* **3** 75–99 (*Preprint* arXiv:astro-ph/9710164)
[46] Novikov D I, Schmalzing J and Mukhanov V F 2000 On non–Gaussianity in the Cosmic Microwave Background *Astron. Astrophys.* **364** 17–25 (*Preprint* arXiv:astro-ph/0006097)
[47] Takada M, Komatsu E and Futamase T 2000 Gravitational Lensing Effect on the Two–Point Correlation of Hot Spots in the Cosmic Microwave Background *Astrophys. J.* **533** L83–L87 (*Preprint* arXiv:astro-ph/9908284)
[48] Schmalzing J, Takada M and Futamase T 2000 Effects of weak lensing on the topology of CMB maps *Astrophys. J. Letter* **544** L83–L86 (*Preprint* arXiv:astro-ph/0008502)
[49] Munshi D, Hu B, Matsubara T, Coles P and Heavens A 2016 Lensing–induced morphology changes in CMB temperature maps in modified gravity theories *J. Cosmol. Astropart. Phys.* JCAP04(2016)056 (*Preprint* arXiv:1602.00965)

[50] Zhao W 2014 Probing CMB Cold Spot through Local Minkowski Functionals *Research in Astronomy and Astrophysics* **14** 625 (*Preprint* arXiv:1209.4021)
[51] Komatsu E et al. 2003 First Year Wilkinson Microwave Anisotropy Probe (WMAP) observations: tests of Gaussianity *Astrophys. J. Suppl.* **148** 119–134 (*Preprint* arXiv:astro-ph/0302223)
[52] Eriksen H K, Novikov D I, Lilje P B, Banday A J and Górski K M Testing for non–Gaussianity in the WMAP data: Minkowski Functionals and the length of the Skeleton 2004 *Astrophys. J.* **612** 64–80 (*Preprint* arXiv:astro-ph/0401276)
[53] Ducout A et al. 2012 Non–Gaussianity and Minkowski Functionals: forecasts for Planck *Mon. Not. Roy. Astron. Soc.* **429** 2104–2126 (*Preprint* arXiv:1209.1223)
[54] Modest H I et al. 2013 Scale dependent non–Gaussianities in the CMB data identified with Minkowski Functionals and scaling indices *Mon. Not. Roy. Astron. Soc.* **428** 551–562 (*Preprint* arXiv:1209.5106)
[55] Ade P A R et al. Planck 2014 results. XXIII. Isotropy and statistics of the CMB 2014 *Astron. Astrophys.* **571** A23 (*Preprint* arXiv:1303.5083)
[56] Ade P A R et al. 2016 Planck 2015 results. XVI. Isotropy and statistics of the CMB *Astron. Astrophys.* **594** A16 (*Preprint* arXiv:1506.07135)
[57] Matsubara T 2003 Statistics of smoothed cosmic fields in perturbation theory. I. formulation and useful formulae in second–order perturbation theory *Astrophys. J.* **584** 1–33 (*Preprint* arXiv:astro-ph/0006269)
[58] Matsubara T 2010 Analytic Minkowski Functionals of the Cosmic Microwave Background: second–order non–Gaussianity with bispectrum and trispectrum *Phys. Rev. D* **81** 083505 (*Preprint* arXiv:1001.2321)
[59] Hikage C and Matsubara T 2012 Limits on second–order non–Gaussianity from Minkowski Functionals of WMAP 7–year data *Mon. Not. Roy. Astr. Soc.* **435** 531–564 (*Preprint* arXiv:1207.1183)
[60] Juszkiewicz R, Weinberg D H, Amsterdamski P, Chodorowski M J and Bouchet F R 1993 Weakly non–linear Gaussian fluctuations and the Edgeworth expansion *Astrophys. J.* **442** 39–56 (*Preprint* arXiv:astro-ph/9308012)
[61] Blinnikov S and Moessner R 1997 Expansions for nearly Gaussian distributions *Astron. Astrophys. Suppl.* **130** 193–205 (*Preprint* arXiv:astro-ph/9711239)
[62] Bernardeau F, Colombi S, Gaztañaga E and Scoccimarro R 2002 Large–scale structure of the Universe and cosmological perturbation theory *Physics Reports* **367** 1–248 (*Preprint* arXiv:astro-ph/0112551)
[63] Abramowitz M and Stegun I A 1965, Handbook of Mathematical Functions, *New York, Dover* (Handbook of Mathematical Functions)
[64] Magnus W, Oberhettinger F and Soni R P 1966 Formulas and Theorems for the Special Functions of Mathematical Physics **52** p.253 *Berlin, Springer* (eBook ISBN, 978-3-662-11761-3)
[65] Comtet L 1974 Advanced combinatorics: the art of finite and infinite expansions *Dordrecht, Reidel Publishing Company* (eBook ISBN, 978-94-010-2196-8)
[66] Courant R and Hilbert D 1953 Methods of Mathematical Physics Vol. **1** *New York, Interscience Publications* (ISBN, 978-0-471-50447-4)
[67] Boas R P and Buck R C 1958 Polynomial expansions of analytic functions *Ergebnisse der Mathematik und ihrer Grenzgebiete. Neue Folge* **19** *Berlin, Springer* (eBook ISBN, 978-3-662-25170-6)
[68] Erdélyi A 1956 Asymptotic Expansions *New York, Dover* (ISBN, 0486603180, 9780486603186)
[69] Cramér H 1970 Random Variables and Probability Distributions, 3rd edn, *Cambridge, Cambridge University Press* (https://doi.org/10.1017/cbo9780511470936)
[70] Cramér H 1999 Mathematical Methods of Statistics *Nineteenth printing Princeton, NJ,*

Princeton University Press (https://doi.org/10.1214/aoms/1177730503)
[71] Cramér H 1972 On the history of certain expansions used in mathematical statistics *Biometrika* **59** 205–207 (https://doi.org/10.1093/biomet/59.1.205)
[72] Aurich R and Steiner F 2001 The Cosmic Microwave Background for a nearly flat compact hyperbolic Universe *Mon. Not. Roy. Astron. Soc.* **323** 1016–1024 (*Preprint* arXiv:astro-ph/0007264)
[73] Aurich R, Lustig S, Steiner F and Then H 2004 Hyperbolic Universes with a horned topology and the CMB anisotropy *Class. Quantum Grav.* **21** 4901–4925 (*Preprint* arXiv:astro-ph/0403597)
[74] Ade P A R et al. 2016 Planck 2015 results. XIII. Cosmological parameters *Astron. Astrophys.* **594** A13 (*Preprint* arXiv:1502.01589)
[75] Patrignani C et al. Review of Particle Physics (Particle Data Group) 2016 Chin. Phys. C (**40** 100001)
[76] Marozzi G, Fanizza G, Di Dio E and Durrer R 2016 CMB–lensing beyond the Born approximation *J. Cosmol. Astropart. Phys.* JCAP09(2016)028 (*Preprint* arXiv:1605.08761)
[77] Lim E A and Simon D 2012 Can we detect hot or cold spots in the CMB with Minkowski Functionals? *J. Cosmol. Astropart. Phys.* JCAP01(2012)048 (*Preprint* arXiv:1103.4300)
[78] Vorobyev Y V and Seckler B 1965 Methods of Moments in Applied Mathematics *New York, Gordon and Breach*
[79] Reed M and Simon B 1975 Methods of Modern Mathematical Physics, vol. II: Fourier Analysis, Self–Adjointness *San Diego, CA, Academic Press*
[80] Monteserín C, Barreiro R B, Vielva P, Martínez-González E, Hobson M P and Lasenby A N 2008 A low Cosmic Microwave Background variance in the Wilkinson Microwave Anisotropy Probe data *Mon. Not. Roy. Astr. Soc.* **387** 209–219 (*Preprint* arXiv:0706.4289)
[81] Cruz M, Vielva P, Martínez-González E and Barreiro R B 2011 Anomalous variance in the WMAP data and galactic foreground residuals *Mon. Not. Roy. Astr. Soc.* **412** 2383–2390 (*Preprint* arXiv:1005.1264)
[82] Bennett C L et al. 2011 Seven–year Wilkinson Microwave Anisotropy Probe (WMAP) observations: Are there Cosmic Microwave Background anomalies? *Astrophys. J. Suppl.* **192** 19 (*Preprint* arXiv:1001.4758)
[83] Bennett C L et al. 2013 Nine–year Wilkinson Microwave Anisotropy Probe (WMAP) observations: Final Maps and Results *Astrophys. J. Suppl.* **208** 20 (*Preprint* arXiv:1212.5225)
[84] Hinshaw G et al. 2013 Nine–year Wilkinson Microwave Anisotropy Probe (WMAP) observations: Cosmological Parameter Results *Astrophys. J. Suppl.* **208** 19 (*Preprint* arXiv:1212.5226)
[85] Gruppuso A, Natoli P, Paci F, Finelli F, Molinari D, De Rosa A and Mandolesi N 2013 Low variance at large scales of WMAP 9 year data *J. Cosmol. Astropart. Phys.* JCAP07(2013)047 *Preprint* arXiv:1304.5493)
[86] Addison G E, Huang Y., Watts D J, Bennett C L, Halpern M, Hinshaw G and Weiland J L 2016 Quantifying discordance in the 2015 Planck CMB spectrum *Astrophys. J.* **818** 132 (*Preprint* arXiv:1511.00055)
[87] Chingangbam P and Park C 2013 Residual foreground contamination in the WMAP data and bias in non–Gaussianity estimation *J. Cosmol. Astropart. Phys.* JCAP02(2013)031 (*Preprint* arXiv:1210.2250)
[88] Ade P A R et al. 2014 Planck 2013 results. XXIV. Constraints on primordial non–Gaussianity *Astron. Astrophys.* **571** A24 (*Preprint* arXiv:1303.5084)

6 Is the Cosmic Microwave Background Gaussian?

In connection with our 2017 paper on the model-independent analyses of the CMB non-Gaussianity, the editorial board of Classical and Quantum Gravity proposed us to give insights presented here, regarding this question, in the CQG online review Focus issue: Planck and fundamental of cosmology [27].

A challenging question touching upon the initial conditions of the primordial Universe, on modeling assumptions, on statistical ensembles of the Cosmic Microwave Background, and on the quest for model-independent approaches being one of the underlying guidelines of my work all along my PhD thesis. There is a heuristic issue concerning all the observational cosmology which is that no physical experiment allows to "run" the Universe evolution at will to obtain ensembles of observed patterns, nor one can communicate with observers everywhere in spacetime to get an overview of our Universe. This remains the conundrum that hampers any statistically valuable modeling endeavor. The efforts to understand and construct the Cosmic Microwave Background (CMB) maps, built from raw data of the Planck satellite, are based on a large number of hypotheses, i.e. observer independence if the cosmological principle holds, data reduction and modeling assumptions that, however for some of them can be tested on the grounds of an ensemble of statistical realizations of the same model. The question can then be answered as to whether there is a single realization of the chosen model that agrees with what is observed, but we better extend the answer to judge the probability of finding this single realization within the ensemble of patterns that our model offers. However, for this we have to select the statistical average properties of the model and those of its initial conditions. The key-assumption (i) is that initial conditions are drawn from a Gaussian random field with a power spectrum that is built on further assumptions on the energy content of the model. Cosmology traces back the Gaussian hypothesis to some generality of predictions from the inflationary paradigm.

The essential further hypotheses underlying models and that are commonly adopted to construct CMB maps are (ii) to idealize the global event of last scattering of the CMB radiation as an ideal surface without thickness, (iii) to idealize this surface as an exact 2-sphere by adopting the hypothesis (iv) that the cosmological model is homogeneous and isotropic with—according to the concordance model of cosmology—a vanishing constant curvature at this surface; of course this hypothesis on the curvature can be extended to test a variety of constant-curvature models, (v) the assumption that the observed dominant dipole pattern (generally not included in the analyses of CMB anisotropies) has no global cause and is solely the result of our proper motion with respect to the global reference frame, and (vi) an assumption on the global topology that can also be extended to test a variety of topological space forms. Combined with hypotheses on the preparation of ideal CMB maps (e.g. recipes of how to mask the galactic emission and foreground contamination) finally furnishes statistical ensembles of model maps as candidates for the comparison with the data.

In view of the large number of hypotheses, it may appear plausible that the anomalies observed in the Planck maps (like the Cold Spot, see [1]) are a result of violation of one or

[27] **CQG+ https://cqgplus.com/2017/04/18/is-the-cosmic-microwave-background-gaussian/**

some of the assumptions made. A surprising result of our studies is, however, that we do have to be cautious about rapid conclusions on abandoning the above hypotheses: already inspection by eye of some maps show "anomalous patterns" in realizations of Gaussian random fields, and an important part for future work should be dedicated to asking as to whether these anomalies may be compatible with all of the assumptions currently made: realizing 100000 maps we found likelihood envelopes on various statistical characteristics of CMB maps that allow single maps in excess of 6σ from the averaged assumed Gaussian distribution. Indeed, it is true that the characteristics of the Planck maps do not lie close to the average characteristics of the model ensemble: the average variance of the maps created from the standard concordance model of cosmology is bigger than the variance of the Planck maps, but individual members of the ensemble offer compatible values. Constrained random samples will have to be analyzed, with characteristics around those of the Planck maps, to narrow the ensemble and to understand more about what we will be able to get with realizations of a Gaussian random field. Despite the disclaimers made above, there are alternative hypotheses which provide "natural" explanations of some of the anomalies. As an example I mention the anomaly of missing power on large scales (studied and discussed in the chapter 4) in the observed CMB maps. The standard concordance model assumes infinite space sections with perturbations on all scales up to infinity. The assumption on the global topology can be altered to closed space sections. Having a finite volume, closed spaces offer an explanation of missing power on large scales, since perturbations at spatial scales larger than the cutoff length are missing. A variety of topological space forms has been analyzed earlier at Ulm University. Some models like $3-$tori are compatible with flat space sections, some are not. However, on the scale of the CMB, curvature is small but non-vanishing, widely opening the door to an infinity of possible, spherical or hyperbolic space forms.

The issue of cosmic topology has attracted scientists from another angle: could we dig deeper into the topology by analyzing CMB maps (now that we have provided a new CMB signature of non-trivial topology)? The answer is likely, yes. These efforts have to assume and analyze a space form. Then, out of a wealth of possible space forms, only those that have a finite size below the CMB scale have a chance to be observed: observing the CMB then may create "circles-in-the-sky" along which the pixels of the CMB data should have comparable properties. On the other hand, it turned out that finite volume space forms should be closed on a scale that is comparable for a variety of space forms analyzed (and are of the order of 4 times the Hubble length for best- fits to the two-point correlation function of the observed maps). However, even extreme situations like the construction of CMB maps for observers who look into a horn of a hyperbolic and closed space form (the Poincaré dodecahedron space) did not reveal significant observable differences to the standard models for CMB maps. So far, the most conservative way to advance our understanding of the Planck maps is to first keep the assumptions listed above. This already provides a starting point of rich and unforeseen consequences, as our results show.

We are attempting to go another route—from the standard list of hypotheses on the model and the assumed average statistical distribution—aiming at critically examining further model-dependencies in the analysis of the deviations from the assumed Gaussian distribution (named non-Gaussianities). It is here, where model-independent strategies can be developed and compared with current perturbative models of the CMB

perturbations: we employ discrepancy functions to measure the drifts from Gaussianity for the univariate descriptors (i) probability density function PDF, and (ii) the complete set of three Minkowski Functionals MFs. The latter method, exploiting the wealth of results of integral geometry, has been developed over the last 27 years, after their introduction into cosmology by [2], and is nowadays used by many teams worldwide including the Planck team. In particular, the family of Minkowski Functionals provide a robust set of morphological valuations which supersedes the power of correlation analyses. A small number of functionals is needed to completely characterize the morphology of the CMB, a characterization that contains all orders of the correlation functions in integrated form. Deviations from Gaussianity are then expanded into Hermite polynomials of these discrepancy functions, a method that appears to fit well the behaviour of non-Gaussianities even for masked model maps that are expected to show large deviations from a Gaussian (large deviations are also expected, e.g., in string gas cosmologies (see [3]) and multi-field inflation models (see [4]). Hermite expansions rely on coefficients obtained by integration over limited temperature ranges and eventually large bin widths, corrections that we can control. Non-Gaussianities can thus be parametrized by those coefficients, which are calculated in the case of the PDF as functions of normalized cumulants (using the moment and cumulant generating functions and the complete Bell polynomials which have integer coefficients). Any drift from Gaussianity is unveiled by non-vanishing higher cumulants (order ≥ 3) and impacts directly on the expansion coefficients of the discrepancy functions. This general characterization of the CMB non-Gaussianities is compared with model-dependent procedures commonly employed.

Among the models of inflation many predict the hierarchical ordering (HO) of the normalized cumulants: in standard perturbation theory one usually expands in powers of σ_0 (standard deviation of the field). By virtue of the central limit theorem, such an expansion should be exactly Gaussian if its argument σ_0 would decrease with the sample size, but this is not the case. Moreover, σ_0 is not a small parameter. To compare the two approaches, one has to perform numerical tests. The result of our tests are that, at comparable orders of the expansions (we had to go to fourth order in σ_0), the HO-expansion yields satisfactory results, but the full Hermite expansion provides a better fit. In our paper we also found a stable signature of non-Gaussianity in the ensemble of map realizations despite the Gaussian assumption underlying their construction. This calls for systematic further analyses that disentangle the various secondary effects that go into the production of maps. And, to add a fresh remark, there are issues related to general-relativistic modeling of the CMB that have not yet been addressed: there might be inhomogeneity effects—named cosmological backreaction—hints coming from the reality of inhomogenous expansion (see [5]), as well as related problems such as the current assumption of a single universal frame for the description of all energy sources in the model, contradicting basic principles of a cosmological model in a space+time foliation within general relativity. To understand these effects is one of the headlines of our future work.

References

[1] Schwarz D J, Copi D J, Huterer D and Starkman G D 2016 CMB anomalies after Planck *Class. Quantum Grav.* **33** 184001 (*Preprint* arXiv:1510.07929)

[2] Mecke K R, Buchert T and Wagner H 1994 Robust morphological measures for large–scale structure in the Universe *J. Astrophys. Astr.* **288** 697-704 (*Preprint* arXiv:astro-ph/9312028)

[3] Brandenberger R H 2015 String gas cosmology after Planck *Class. Quantum Grav.* **32** 234002 (*Preprint* arXiv:1505.02381)

[4] Martin J, Ringeval C and Vennin V 2014 Encyclopaedia Inflationaris *Phys. Dark Univ.* **Elsevier 5-6** 75–235 (*Preprint* arXiv:1303.3787)

[5] K Bolejko, M Ahsan Nazer and D L Wiltshire 2016 Differential cosmic expansion and the Hubble flow anisotropy *J. Cosmol. Astropart. Phys.* **JCAP06(2016)035** (*Preprint* arXiv:1512.07364)

7 General Conclusions and Outlook

This PhD thesis, under the supervision of Thomas Buchert and Laurence Tresse, investigates some of the topological, geometrical and dynamical properties of the Universe that can be predicted or derived from the physics and statistical analysis of the primordial CMB temperature anisotropy map. Firstly I review: the construction of the General Relativistic Cosmology; the Universe observed according to the ΛCDM model; and the key-principles of GR, cosmology and the construction of the FLRW model. This manuscript explores two fields of research in cosmology, cosmic topology: the CMB in a multiply connected Universe (in chapter 4) and morpho-statistics with Minkowski Functionals: a model-independent analysis of the CMB non-Gaussianity (in chapter 5).

A Universe with multiply connected topology such as the 3−torus, flat, homogeneous and globally anisotropic could dictate specific physical properties to our observable Universe. Indeed, we verify that any CMB map in the ΛCDM model displays a different 2-point correlation function once the toroidal topology is assumed. In the first case the 2-pcf shows non-vanishing correlations at all angles, in the second case all correlations vanish beyond an angular scale depending on the torus sidelength (20° for a small cubic torus of $0.5L_H$ and 30° for $3.0L_H$). The CMB observed by the radiotelescopes Planck, WMAP and others displays also a lack of correlation, in fact beyond ∼60°. Should we conclude that our Universe is spatially finite? It would be a bold and early conclusion, since e.g. the CMB, bigger by its diameter of $6.3L_H$ than the (nearly optimal in term of the 2-pcf) torus at $3.0L_H$, exists and is observable nevertheless. Also there are not yet identified connections between the cut-off angle of the CMB 2-pcf in a Universe with toroidal topology and the infrared cut-off due to the finite spatial size of the torus. The 2 signatures of the 2-pcf and ρ I presented and discussed in the chapter 4 prove that the physics of our Universe is, at a certain degree of magnitude, affected by the finite size of: matter distribution at large scale and, or physical processes affecting chiefly the Sachs-Wolfe effect on the CMB. Cosmology doesn't have yet obvious clues on the causes of the toroidal-like, or multiply connected-like behavior of our Universe. The signature of the 2-pcf and our new signature ρ are compatible with a spatially finite physical Universe. Our observable Universe remains spatially finite and presents two typical signatures of finite and boundless topologies. But cosmology should make progresses to prove that our physical Universe could be finite.

(i) Our results are in contradiction with the Concordance model, i.e. the ΛCDM model which is spatially infinite and shows angular correlations everywhere in the 2-pcf. Furthermore, a spatially infinite Universe addresses the question of the validity of Mach's principle, essential to GR, unless the infinite Universe is populated by an infinite number of heavenly bodies. This hypothesis leading to the issue of an infinitely energetic (or massive) Universe. Numerically, it seems out of reach to simulate an infinite Universe showing the properties of our Universe. Does this technical impossibility correspond to the physical reality of our Universe at large scale? Besides, numerical simulations of finite or multiply connected Universe are only limited by the complexity (increasing with the spatial size) of the calculations of modes and the inherent but ever improving computing durations.

(ii) The spatial finiteness of the torus fundamental domain has certainly many other consequences on the physical properties of the observable Universe. It is up to us in

future studies to predict, to model, to observe or to rediscover certain of the specific properties and signatures of non-trivial topologies. As a matter of fact, the question of the unexplained CMB anomalies and the ΛCDM model tensions, chiefly on H_0 and σ_8, should be investigated in a global universe model with multiply connected topology (MCU). Such a Universe, as discussed in this thesis, answers to the question of the anomalous lack of correlation at large angular scale observed on the CMB. Is it possible that this MCU alleviates other anomalies and tensions?

(iii) We re-verify the known result that the CMB angular 2-point correlation function presents a hierarchical signature of the size of the universe topology; the larger the cubic torus, the higher the angular cut-off of the 2-pcf. In addition, the 2-pcf of the primordial CMB is compatible with the 2-pcf of model Universes with non trivial topology (finite without boundary) and incompatible with the 2-pcf of the infinite ΛCDM Universe.

(iv) We show that the statistical quantity ρ which is the normalized standard deviation of the CMB temperature gradient field is a hierarchical signature for a Universe with cubic 3−toroidal topology. We also observe a linear relation between ρ and L/L_H. A large number of CMB temperature maps is generated, 100 000 by model, at a resolution of $\mathrm{N}_{\mathrm{side}}$=128 i.e. 196 608 pixels, over the multipole range l=[2,256]. The computing time of a CMB map in the infinite ΛCDM Universe is short, however, this is not the case for the CMB with toroidal topology. Indeed, in comparison with an infinite Universe, homogeneous and isotropic, the discrete spectrum of the torus vibrational modes (of spatial frequencies) has to be calculated. In addition, the torus has an anisotropic impact on CMB physics and this has to be calculated since the orientation of the 3−torus does matter. Even limited to $l_{\max}$=256 the computation of the CMB temperatures in a Universe with toroidal topology is time consuming. Therefore, we have limited our present investigations to 5 ensembles of 100 000 torus maps at 0.5, 1.0, 1.5, 2.0 and 3.0 Hubble lengths. However, it will be important to confirm our results with other torus sizes, to satisfy the hierarchical and linear laws we observe and to refine the provisional comoving size of 3 Hubble lengths for our Universe. Two other aspects could be investigated. The first concerns the detection of torus orientation which I already study in connection with the signature ρ. The second aspect is to calculate the CMB signature ρ for other kinds of universe topologies over various sizes, such as the simply connected spherical Universe $\mathcal{S}^3$.

Interesting properties of $\mathrm{P}(\sigma_0)$, $\mathrm{P}(\sigma_1)$ and $\mathrm{P}(\rho)$ have been observed during our studies or appear in our ρ paper. In fact, $\mathrm{P}(\sigma_0)$ presents a systematic important skewness. In relation with this skewness of $\mathrm{P}(\sigma_0)$, $\mathrm{P}(\rho)$ presented in our paper displays also a persistent skewness. This skewness is under scrutiny since, as a consequence, the property of CMB Gaussianity in terms of these PDFs should be re-visited. At last, for the variance of the gradient σ_1, $\mathrm{P}(\sigma_1)$ shows no pronounced skewness.

Also, as I said above, ρ plays an important role in the Minkowski functionals since it is the prefactor in the Gaussian premise of the second MF v_1 and ρ^2 is the prefactor for the Gaussian premise of the third MF v_2. I already work on a comprehensive study of the MFs for the CMB in multiply connected Universes.

What is the origin of the properties of ρ, as hierarchical signature of a MCU and the linear law $\mathrm{L}/\mathrm{L}_H \sim$-0.3$\rho$+14? For the moment, none of our analytical attempts to connect ρ and L/L_H, a monotonic way, through another physical or statistical quantity, e.g. the Gaussian smoothing of the CMB, is valid or brings significant results.

(v) What about the primordial physical Universe beyond the CMB, i.e. beyond our observable Universe? It has been proven that the asymptotic limit of a toroidal Universe

model is not L$\rightarrow \infty$ but L$\sim$1.1 CMB comoving diameter. It is important that we verify this limit in terms of ρ with tori of sizes larger than 3 Hubble length. We know that our Universe is compatible with a torus of size L $\sim 3\mathrm{L}_H$ in the sense of both the CMB angular 2-pcf and ρ.

(vi) One difficulty arises from the absence of observation of the circle-in-the-sky patterns expected on the CMB as complementary signature of a multiply connected Universe. As it is discussed in the ρ-paper, it is likely that the CITS signal is drowned out by the strong integrated Sachs-Wolfe effect observed and recently confirmed. It is therefore very important that our ρ signature actually verifies the multiply connected nature of the Universe measured before by only the 2-point correlation function.

(vii) The Gaussianity of the primordial CMB, in the sense of the MFs is verified in the second article developed in this thesis. This weak level of non-Gaussianity goes along with an angular power spectrum and its associated 2-pcf which are compatible with a multiply connected Universe. As illustrated in the ρ-paper, the level of isotropy and homogeneity (IH) of the CMB in a toroidal Universe is very high and at the level of IH of the ΛCDM in the sense of ρ. This property is very interesting since we are able to propose a challenging universe model, multiply connected but where the CMB displays the IHG properties of the CMB in the ΛCDM Universe.

In view of these results, important for cosmology since ρ brings a new signature reinforcing the hypothesis of a Universe with finite topology, the future prospects of this PhD thesis open toward a better understanding of the mechanisms connecting the statistical quantity ρ to the underlying physical properties of the CMB in a MCU. Thus, the property of global anisotropy of the 3$-$torus will be used in an attempt to discriminate different multiply connected Universe models in function of their global orientation. A modified implementation of ρ would make possible the detection of the topology, differentiating e.g. the spherical Universe $\mathcal{S}^3$ from the infinite Universe, or from a multiply connected Universe. Some of my researches going in this sense are in progress.

Besides, the perspectives of application of solution to the EFE of General Relativity in a multiply connected Universe have to be deepened and explored theoretically first devising toy-models and to extend the studies with a geometrisation of gravity at non-infinitesimal scales. There are important difficulties to constrain a MCT in the resolution of the EFE even in the case of a static black hole. The non trivial first order solutions found by Steiner and e.g. the exact solution for a static black hole in a slab space (1994, [1, 2]) are promising. However, it would be very interesting to progress in the description of the metric properties of a MC Universe more densely populated.

The CMB, because of its good properties, projected over the 2$-$sphere $\mathcal{S}^2$ brings a diagnosis synoptic tool of any universe model. Proceeding to more realistic cosmological models (finite and with inhomogeneous matter and curvature distributions), we might see, whether these models would also reveal other anomalies detected in the observed CMB.

References

[1] Korotkin D and Nicolai H 1994 The Ernst equation on a Riemann surface *Nucl. Phys. B* **429** 229-54 (arXiv:gr-qc/9405032)

[2] Korotkin D and Nicolai H 1994 A Periodic Analog of the Schwarzschild Solution (arXiv:gr-qc/9403029)

8 Appendices

8.1 The truncated Gaussian probability density function

The construction of the truncated Gaussian PDF is based on the standard unconditional normal distribution (also called in this context the "parent distribution" by statisticians) defined on the whole line in terms of the mean μ and the variance σ^2. The *truncated Gaussian* PDF $P_+(\rho)$ is defined as the normalized conditional PDF restricted to the half-line $[0, \infty[$ by

$$P_+(\rho) := \frac{N}{\sqrt{2\pi}\sigma} \exp\left(-\frac{(\rho-\mu)^2}{2\sigma^2}\right)\Theta(\rho) \ , \tag{171}$$

where $\Theta(\rho)$ is the Heaviside step function ($\Theta(\rho) = 1$ for $\rho \geq 0$, $\Theta(\rho) = 0$ for $\rho < 0$). N is a normalization constant determined by the parent parameters $\mu > 0$ and $\sigma > 0$ and is given by

$$N := \frac{2}{1 + \mathrm{erf}(\frac{\mu}{\sqrt{2}\sigma})} \ , \tag{172}$$

satisfying $1 < N < 2$. It follows that $P_+(\rho)$ is unimodal of mode μ having the same shape as the standard normal distribution whose peak height b at $\rho = \mu$ is, however, larger by the factor N. The important new properties of $P_+(\rho)$ are that the mean $\langle\rho\rangle$ is no more equal to the mode μ and is also different from the median, and that the variance Σ^2 is different from the parent variance σ^2. Actually, all higher moments are different from the well-known Gaussian moments, in particular the odd moments and all higher cumulants are non-zero. As an example we give the values for $\langle\rho\rangle$ and Σ^2:

$$\langle\rho\rangle = \mu + \sigma\lambda > \mu \ ; \tag{173}$$

$$\Sigma^2 := \left\langle(\rho - \langle\rho\rangle)^2\right\rangle = \sigma^2 - \sigma^2\lambda\left(\lambda + \frac{\mu}{\sigma}\right) < \sigma^2 \ , \tag{174}$$

with

$$\lambda := \frac{N}{\sqrt{2\pi}} \exp\left(-\frac{\mu^2}{2\sigma^2}\right) \ . \tag{175}$$

Note that $\langle\rho\rangle$ and Σ^2 can be directly computed from the histograms. But in order to compare the histograms with the truncated (continuous) Gaussian $P_+(\rho)$, one has to know the *a priori* unknown parent parameters μ and σ. In principle, it is straightforward to get them. μ is directly determined by the position of the maximum of the histogram, and σ is obtained from the numerical solution of the equation (see equations (171) and (172)),

$$\sigma + \sigma\,\mathrm{erf}\left(\frac{\mu}{\sqrt{2}\sigma}\right) = \sqrt{\frac{2}{\pi}}\,\frac{1}{b} \ , \tag{176}$$

once the previously obtained value for μ and the peak height b have been inserted. The actual determination of μ and σ is, however, rendered more difficult, since the accuracy of the histograms depends on the binning and, thus, the correct position of the maximum (and of b) is not well-defined (see figures 3 and 4).

From equations (172)–(176) one infers that the relevant parameter determining the size of the deviations of the truncated Gaussian PDF from the standard (parent) Gaussian PDF is given by the positive parameter

$$\beta := \frac{\mu}{\sqrt{2}\sigma} \quad . \tag{177}$$

The figures 3 and 4 show that the modes of all histograms are much larger than the associated variances and thus we have $\beta \gg 1$ for the tori considered. For $\beta \gg 1$, one obtains for N and λ from (172) and (175):

$$N = \frac{1}{1-\epsilon} = 1 + \epsilon + \mathcal{O}(\epsilon^2) \ , \tag{178}$$

with

$$\epsilon := \frac{1}{2}\mathrm{erfc}(\beta) = \frac{1}{2\sqrt{\pi}}\frac{e^{-\beta^2}}{\beta}\left(1 + \mathcal{O}\left(\frac{1}{\beta^2}\right)\right) \ , \quad \text{and} \quad \lambda = \frac{1}{\sqrt{2\pi}}e^{-\beta^2} + \mathcal{O}\left(\frac{e^{-2\beta^2}}{\beta}\right) \ , \tag{179}$$

which gives e.g. for $\beta = 10$ the extremely small values $\epsilon = \mathcal{O}(10^{-45})$ and $\lambda = \mathcal{O}(\beta\epsilon)$=$\mathcal{O}(10^{-44})$. Thus, it is justified to use for a comparison of the histograms with a Gaussian PDF the Gaussian PDF (171) with $N = 1$. Since a precise determination of the parent parameters μ and σ from the histograms is rendered with difficulties, as discussed before, we show in figures 3 and 4 the standard Gaussian PDF determined by the mean values $\langle\rho\rangle$ and the variances Σ^2 of the histograms given in tables 1 and 2 for the cases without mask and with U73 mask, respectively. The ratio β is then given by $\langle\rho\rangle/2\Sigma$, which varies in the unmasked case between 12.340 and 15.494, and in the U73 mask case between 12.938 and 14.532.

8.2 Definitions and notations for the CMB analysis

Statistical and morphological descriptors of a random field are *a priori* based on model–independent definitions for a given support manifold. But these descriptors are bias– and error–dependent according to the impact they have on the amplitude and shape of the non–Gaussianity, problems we shall touch upon in this appendix. Numerical biases and errors originate from the pixelation and finite–temperature resolution of the CMB data maps and sample maps, but also from the way infinitesimal calculations are translated into discrete algorithms. These numerical issues affect the descriptors, the fundamental quantities of the field and also the Gaussian predictions.

In what follows we recall some fundamental quantities of the CMB random field as they are used in the numerical analysis. The temperature anisotropy δT we use in this thesis is dimensionful, $\delta T := T - T_0$ in units of μK with T the absolute local temperature, and $T_0 = 2.7255 \pm 0.0006$K, is the mean CMB temperature, which can be considered as the monopole component of the CMB maps. The dimensionless CMB temperature anisotropy $(T - T_0)/T_0$ is used in linear perturbation theory, in the Sachs–Wolfe formula (see for instance [72, 73]). The temperature anisotropy δT derives from the measure of the spectral radiance $I(\nu(\mathrm{GHz}))$ by the instruments HFI and LFI of the *Planck* probe [16], and depend on the modelling of several effects: relativistic Doppler–Fizeau, and Sunyaev–Zel'dovich. The magnitude of these effects is a function of the

cosmological model, therefore, the CMB spectral radiance and consequently the CMB temperature rest–frame estimations are model–dependent. The suffixes, $_{\rm px}$ or $_{{\rm C}\ell}$ apply to the quantities calculated: from the moments of the probability distribution function (no suffix), $P(\tau)$, directly from the pixels, or from the angular power spectrum, respectively.

8.2.1 Basic quantities of the CMB random field

We consider a Gaussian window function with smoothing scale $\theta_{\rm fwhm}(^\circ)$,

$$\sigma_{\rm G} := \theta_{\rm fwhm}\frac{\pi}{180}\frac{1}{\sqrt{8\ln 2}} \ . \tag{180}$$

For $\sigma_{\rm G}^2 \ll 1$ the Gaussian kernel is approximated by

$$\mathrm{W}_\ell = \exp\left(-\frac{\sigma_{\rm G}^2}{2}\ell(\ell+1)\right) \ , \tag{181}$$

and once the $a_{\ell,m}$ coefficients of the expansion of δT on $\mathcal{S}^2$ in spherical harmonics are calculated from the map, given the pixelation correction $\mathrm{pxc}(\ell)$, the corrected multipole moments are given by

$$\mathrm{C}_\ell := \left\langle \frac{1}{2\ell+1}\sum_{m=-\ell}^{+\ell}|a_{\ell,m}|^2 \right\rangle \ , \tag{182}$$

$$\mathrm{Cw}_\ell = \mathrm{C}_\ell \ \mathrm{pxc}(\ell)^2 \exp\left(-\ell(\ell+1)\sigma_{\rm G}^2\right) \ , \tag{183}$$

and the angular power spectrum by

$$(\delta \mathrm{T}_\ell)^2 := (\ell(\ell+1)/2\pi)\mathrm{Cw}_\ell. \tag{184}$$

We consider the mean values,

$$\mu := \alpha_1 \ ; \ \mu_{\rm px} := \langle \delta T \rangle_{\rm px} \ , \tag{185}$$

and the variances,

$$\sigma_0^2 := \alpha_2 - \mu^2 \ ; \ \sigma_{0\rm px}^2 := \left\langle (\delta T)^2 \right\rangle_{\rm px} - \langle \delta T \rangle_{\rm px}^2 \ . \tag{186}$$

For a homogeneous and isotropic Gaussian random field, $\sigma_{0{\rm C}\ell}^2$ is independent of the absolute direction of light provenance; the variance ensemble average is

$$\sigma_{0{\rm C}\ell}^2 := \sum_{\ell=2}^{\ell_{\rm max}} \mathrm{Cw}_\ell \frac{(2\ell+1)}{4\pi} \ . \tag{187}$$

The variance of the local gradient is (compare the definition in equation (153))

$$\sigma_{1\rm px}^2 := \left\langle (\nabla_1 \delta T(\hat{\boldsymbol{n}}))(\nabla^1 \delta T(\hat{\boldsymbol{n}})) + (\nabla_2 \delta T(\hat{\boldsymbol{n}}))(\nabla^2 \delta T(\hat{\boldsymbol{n}})) \right\rangle \ , \tag{188}$$

and, only in a homogeneous and isotropic model, for a Gaussian random field, the ensemble average of $\sigma_{1{\rm C}\ell}^2$ is

$$\sigma_{1{\rm C}\ell}^2 := \sum_{\ell=2}^{\ell_{\rm max}} \mathrm{Cw}_\ell \frac{(2\ell+1)\ell(\ell+1)}{4\pi} \ . \tag{189}$$

The measures of the variance and variance of the local gradient, equations (186) and (188), contain an averaged statistical, respectively, morphological information of the random field. Since the model–dependent expressions, equations (187) and (189), are

valid only for homogeneous–isotropic Gaussian fields, any significant difference between these two methods indicates a preliminary detection of non–Gaussianity and the degree of comformity with the model for the CMB. For the ΛCDM sample we notice such a difference between the variances calculated from the pixels and the variances calculated from the angular power spectrum. Model–dependent predictions for $\sigma_{0C\ell}$ and $\sigma_{1C\ell}$ and further discussions can be found in [28].

Table 8 shows the averaged values of μ, σ_0 and σ_1 over the CMB map sample in the ΛCDM model. Two cases are shown in this table and all the further tables for our ΛCDM 10^5 map sample at $N_{\rm side} = 128$, $\ell_{\rm max} = 256$, 2°fwhm: without mask at bin width 13μK and over the full temperature range of the sample; with $U73$ mask subtraction at bin width 6μK and over the limited temperature range fixed by the *Planck SMICA* map. The effect of passing from no mask to the mask $U73$ is upon μ, σ_0 and σ_1. And the variation of the ratio σ_1/σ_0 is noticeable (e.g. 34.16218/33.93190 = 1.006787) and affects the magnitude of the Gaussian premise of the Minkowski Functionals v_1 and v_2.

(Units of μK) ΛCDM sample Full individual map range, no mask, 2°fwhm, bin 13μK			
μ_{px}	σ_{0px}	σ_{1px}	$\sigma_{1px}/\sigma_{0px}$
-3.4×10^{-7}	59.53348	2020.08398	33.93190
(Units of μK) ΛCDM sample Equal temperature range (ETR ± 201μK), U73 mask, 2°fwhm, bin 6μK			
μ_{px}	σ_{0px}	σ_{1px}	$\sigma_{1px}/\sigma_{0px}$
-1.4534×10^{-3}	59.13275	2020.10372	34.16218

Table 8: Table of μ and σ values.

8.2.2 The Cosmic Microwave Background in the ΛCDM model

The six-parameter (see e.g. the article by de Valentino [1]) ΛCDM model is based on a choice of six cosmological parameters selected to limit degeneracies when fitting to the observation dataset. An example is to find the best fit of a ΛCDM model variant to the observational data using the 2-point CMB power spectrum (see the article by Callin [2] on the calculation of the CMB spectrum and the associated algorithms and programs CAMB and CMBFAST).

An example of 6-parameter setting:

physical baryon density, $\Omega_b h^2$
physical cold dark matter density, $\Omega_c h^2$
age of the Universe, t_0
scalar spectral index, n_s
curvature fluctuation amplitude, σ_8
reionization optical depth, τ

The 2 articles developed in my Manuscript make use of the same ΛCDM model cosmological parameters to get the CMB temperature map ensemble. The ΛCDM CMB maps are generated with the software library *HEALPix synfast*. Its interface takes as input the CMB angular power spectrum calculated with **CAMB** using the cosmological parameters of the ΛCDM model according to *Planck* 2015 (see [3], p.31, table 4, last column, and Review of particle physics [75]:

$H_0 = 67.74 \pm 0.46$ kms^{-1}Mpc^{-1}, the Hubble constant today
$h = H_0/(100\text{kms}^{-1}\text{Mpc}^{-1}) = 0.6774$, the normalized Hubble constant today
$T_0 = 2.7255 \pm 0.0006$ K, present–day CMB temperature
$\Omega_b h^2 = 0.02230 \pm 0.00014$, baryon density
$\Omega_c h^2 = 0.1188 \pm 0.0010$, Cold Dark Matter density
$\Omega_\nu h^2 = 0.00209$, neutrino density
$\Omega_k = 0$, constant–curvature density parameter
$Y_P = 0.249^{+0.025}_{-0.026}$, helium fraction
$N_{\text{eff}} = 3.04 \pm 0.33$, number of massless neutrinos
$\sum m_\nu < 0.194$ eV, neutrino mass eigenstates
τ=0.066 $\pm$ 0.012, reionization optical depth
z_{re}=8.8 $^{+1.2}_{-1.1}$, redshift of the reionization
n_S=0.9667 $\pm$ 0.0040, scalar spectral index
x_e=1, ionization fraction
z_*=1089.90 $\pm$ 0.23, redshift of decoupling
Ω_Λ=0.6911 $\pm$ 0.0062, cosmological constant density
Ω_m=0.3089 $\pm$ 0.0062, total matter density
Age= 13.799 $\pm$ 0.021 Gyr, age of Universe

The recent investigation (August, 2021) made by Efstathiou updates the cosmological parameters after a reanalysis of the Planck HFI maps (see in [50]) .

A few important definitions

– Elastic Thomson scattering and CMB regime out of equilibrium

Thomson scattering of charged particles (free electrons of mass m_{e-}) by incident photons of energy $h\nu_{\text{inc}}$ is the main process at the origin of CMB radiation. Before recombination, at a temperature $>$ 3000K electrons and protons are statistically decoupled while electrons and photons are coupled. As a consequence, elastic collisions between free electrons and photons occur very frequently. This is the Thomson scattering obtained if $h\nu_{\text{inc}} << \text{m}_{e-}\text{c}^2$. Photons are then in regime of thermodynamic equilibrium at the temperature T_{equ}. The number of CMB photons at a given energy $\text{E}_i = h\nu_{\text{inc,i}}$ is proportional to the Bose-Einstein statistics

$$\Phi(h\nu_{inc,i}) = \left(e^{\frac{h\nu_{inc,i}}{kT_{equ}}} - 1 \right)^{-1} \quad , \tag{190}$$

where h is the Planck constant and k being the Boltzmann constant. During the recombination of electrons with protons, the mean free path of photons overcomes the comoving radius while the number density of free electrons drops down. In the phase of decoupling between photons and electrons, the CMB thermodynamic system is no more in state of thermal balance. Collisions photon-electron or of completely different particles occur now occasionally and abruptly. The statistical evolution of this thermodynamic system is described by the collision integral taking the form of the non-linear integro-differential Boltzmann's equation. This equation allows a global and statistical description of the evolution of a complex thermodynamical system made of various kinds of particles in collision in a regime now out of equilibrium. Nevertheless, the CMB is extremely close to the ideal blackbody i.e. equivalent to a body with an absorption coefficient nearly of

1 at temperature today 2.7255±0.0006K. Mathematical developments on the Boltzmann equation and the mechanisms of CMB primordial radiation can be found in the books by Carlo Cercignani [4] and Ruth Durrer [5].

– Harrison-Zel'dovich spectrum

A weak level of inhomogeneity, anisotropy and non-Gaussianity is observed all over the CMB. However, the extreme CMB temperature uniformity ($\Delta T/T \sim 10^{-5}$) at angular scales beyond 7° cannot be explained physically since the causal horizon at the epoch of last scattering underlies an angular size of ∼0.6° measured in the ΛCDM model. Also, the extremely high level of CMB Gaussianity that we confirm at angular scales >0.6° is compatible with a statistical and physical independence of small CMB regions physically decoupled. Inflation (see e.g. the book by Giovannini [6]) is a phenomenological theory that proposes a scenario of mechanisms able to

- produce the CMB temperature uniformity,
- account for a CMB patched by small regions physically decoupled,
- account for the high level of inhomogeneity observed in the large scale structure distribution of our Universe.

The properties of inhomogeneity of the primordial Universe are characterized by a statistical tool, the 2-point distance correlation function. Given the 2-point correlation function (which is an auto-correlation function) denoted 2pcf_d of the density fluctuations in the primordial Universe, the 2-point distance spectrum is defined as the Fourier transform of the 2pcf_d (see e.g. the reference book by Lyth and Liddle [7]). In the framework of the ΛCDM model of a Universe homogeneous, isotropic and Gaussian, the fluctuations around the homogeneous density ρ_d are considered as adiabatic perturbations $\delta(\rho_d)$. The 2pcf_d is calculated as the mean value of the density contrast of all the pairs of points separated by the distance r

$$2pcf_d(r) = \left\langle \frac{\delta(\rho_d, x_0)}{\rho_d} \frac{\delta(\rho_d, x_0 + r)}{\rho_d} \right\rangle . \tag{191}$$

No specific location x_0 enters this equation (191) given the properties of homogeneity and isotropy of the ΛCDM Universe. The spectrum P(k) as a function of the wave-vector k (the wavelength l verifying $l = 2\pi/\text{k}$) is

$$P(k) = \frac{k^3}{2\pi^2} \int 2pcf_d(r) dx^3 . \tag{192}$$

In the case of adiabatic perturbations verifying purely Gaussian statistics, the properties of these perturbations are completely given by the power spectrum.

– Δ^2_R is the amplitude of the primordial power spectrum specified at a comoving scale of 0.002Mpc h^{-1} or 0.05Mpc h^{-1}. Δ^2_R is denoted A_s in previous studies on the primordial density perturbation. In the tables of cosmological parameters, Δ^2_R is used generally under the form $\log_e(10^{10}\ \Delta^2_R)$ or $\Delta^2_R\ 10^9$ or $\Delta^2_R\ 10^{10}$.

– n_s, the scalar spectral index quantifies how the density fluctuations vary with scale, having scale invariant fluctuations for n_s=1 corresponding to the peculiar case of an Harrison-Zel'dovich spectrum. The primordial Harrison-Zel'dovich spectrum is, in the ΛCDM model, the spectrum able to account for the evolution to the inhomogeneity and

anisotropy observed in our Universe today. In this scenario, the relation between Δ^2_R, amplitude of the primordial power spectrum, and its scalar spectral index n_s is given by the power law

$$\Delta^2_R(k) = \Delta^2_R(k_*) \left[\frac{k}{k_*}\right]^{n_s - 1} , \tag{193}$$

where k_* is an arbitrary wave-vector.

– σ_8 is the root mean square of perturbations of density at a comoving scale of 8Mpc h^{-1}. How the Universe is clumped at a given redshift? Thus, σ_8 is measured, (i) on the CMB temperature map, (ii) in large-scale structures distributions such as spatial distributions of galaxies or galaxy clusters. A slight and persistent tension is signalled between the values of σ_8 measured in the CMB temperature map and in LSS data such as the SZ (Sunyaev-Zel'dovich) clusters.

– τ, the reionization optical depth quantifies how much CMB radiation has been absorbed or scattered between CMB and receiver during the reionization era taking place in a ΛCDM Universe old of ∼13Gy, i.e. at redshift z∼9. At scales smaller than the horizon size at reionization (l≥10 i.e. angle ≤ 18°) free electrons generated during the reionization scatter and damp the CMB anisotropies. This implies a scale independent suppression of CMB radiation power within this angular range. τ is dimensionless and given by

$$\tau = n_H(z=0)\ c\ \sigma_{Th} \int_{z=0}^{z_{max}} x_e(z) \frac{(1+z)^2}{H(z)} dz , \tag{194}$$

where n_H is the fractional number of hydrogen nuclei, σ_{Th} is the Thomson scattering cross section and x_e the number density of free electrons (or ionization fraction).

8.2.3 The CMB radiation components

The full Boltzmann physics is implemented in the $CAMB$ software; thus, the maps of the CMB sample in the ΛCDM model include the following effects: ordinary Sachs–Wolfe effect / Doppler effect / Silk damping / Reionization / Polarization of photons / Neutrinos / Integrated Sachs–Wolfe effect (ISW) / Lensing. The weak lensing effect upon the CMB is treated in [5] and in [8] beyond the Born approximation, which is usually applied at first–order of perturbation theory. For a second–order treatment the deflection angles, still assumed small[28] if $\ell \leqslant 2500$, are no more Gaussianly distributed, but the post–Born corrections would be weakly detectable in low noise CMB temperature maps merging the contributions of hundreds of ℓ–values between $\ell = 1000$ and $\ell = 2500$. Our present study uses an ℓ–range [2,256], well below $\ell = 1000$. One notices that an evaluation of the Sunyaev–Zeldovich effect (SZ) on the CMB radiation is not implemented in $CAMB$, the sources responsible of the SZ effect being more or less excluded when using an appropriate foreground mask. It is clear that, in this list, some of the effects are not primordial but depend on model–dependent knowledge of the matter distribution and the physical assumptions in the concordance model, i.e., mainly the ISW effect, the lensing and the neutrinos.

[28] Two times the typical angular deviation equals 4 arc minutes (CMB lensing due to structures at $z < 20$ in a flat $FLRW$ model); this corresponds to $\ell_{max} = 180°/(4/60) = 2700$.

8.2.4 Map ensemble and statistical stability

From the power spectrum we generate with *synfast* a 10^5 map ensemble. Given the map resolution ($N_{\rm side} = 128$, $\ell_{\rm max} = 256$, and 2°fwhm), the number of 10^5 maps allows a statistical stability in the sense of the second averaged MF v_1, which becomes smooth and stable around 10^5 maps, a second different sample of 10^5 maps gives very similar results and doubling the sample brings no visible improvement in the shape of v_1. A number of 10^5 maps is satisfactory in the sense of the statistical stability for the MFs themselves, but less for the PDF. However, once we come to the discrepancy functions, the stability is definitely impaired when using a smaller number of maps, and 10^5 maps must be considered as a minimum requirement. We shall not develop more on these studies in the present work.

8.2.5 Discretization: definition of the τ–lattice

One observes that in the case of 10^5 realizations there is an interval in τ, $[\tau_-, \tau_+]$ such that $P(\tau) = 0$ *for all* realizations, if $\tau \notin [\tau_-, \tau_+]$. In order to simplify the problem, we use a symmetric interval $[-\tau_m, +\tau_m]$, where $\tau_m = \max\{|\tau_-|, \tau_+\}$. The interval $[-\tau_m, +\tau_m]$ is divided into $2L+1$ bins of equal bin width $\Delta\tau := 2\tau_m/(2L+1)$, where the mid–points of the bins are given by the "$\tau-$lattice", $\tau_l = -\tau_m + (2l-1)(\Delta\tau/2)$, $l = 1, 2, \cdots, (2L+1)$, in such a way that the $(L+1)^{\rm th}$ bin is centered at $\tau_{L+1} = 0$. (Example: $\tau_m = 396.5\ \mu$K, $L = 30$, $\Delta\tau = 13\mu K \Rightarrow (2L+1) = 61$ bins.) Then, the *discretized PDF* for a given realization, which is now a step–function, i.e. piecewise continuous, can be represented as a *histogram* that is defined by ($l = 1, 2, \cdots, (2L+1)$):

$$P(\tau_l) := \frac{\#\text{pixels}\{\delta T \in [\tau_l - \frac{\Delta\tau}{2}, \tau_l + \frac{\Delta\tau}{2})\}}{N_{\rm tot}\Delta\tau} \quad , \tag{195}$$

with $N_{\rm tot}$ the total number of pixels, and for τ within the $l^{\rm th}$ bin, i.e., $\tau \in \left[\tau_l - \frac{\Delta\tau}{2}, \tau_l + \frac{\Delta\tau}{2}\right)$ (half open interval!).

The *ensemble average (mean)* $\langle P(\tau)\rangle$ is given by the arithmetic mean of all the PDFs of the 10^5 realizations. $\langle P(\tau)\rangle$ is still constant in a given bin, denoted by $\langle P(\tau_l)\rangle$ in the $l^{\rm th}$ bin and, thus, the derivative $\mathrm{d}\langle P(\tau)\rangle/\mathrm{d}\tau$ is zero almost everywhere, but $\langle P(\tau)\rangle$ will have, in general, $(2L+2)$ jumps, namely at the points $\tau_l + \Delta\tau/2$, $l = 1, 2, \cdots 2L$ and at the points $\mp\tau_m$ (iff $\langle P(\tau)\rangle$ possesses this special property!) In general, there will be a *first jump* at a value $\tau_0 \in [-\tau_m, \tau_1 + \Delta\tau/2)$, and a *last jump* at a value $\tau_{2L+2} \in (\tau_{2L+1} - \Delta\tau/2, \tau_m]$, and these contributions have to be treated separately.

If we ignore the last subtlety, the expectation value (79) of a given random field $f(\delta T)$ is exactly given by the finite sum

$$\langle f(\delta T)\rangle = \sum_{l=1}^{2L+1} \langle P(\tau_l)\rangle \int_{\tau_l - \Delta\tau/2}^{\tau_l + \Delta\tau/2} f(\tau)\,\mathrm{d}\tau \quad . \tag{196}$$

As an important example, this yields with $f(\tau) = \tau^n$ the *exact formula for the moments* α_n *of* δT (see equation (80) for $n = 0, 1, 2, \cdots$):

$$\alpha_n = \frac{1}{n+1} \sum_{l=1}^{2L+1} \langle P(\tau_l)\rangle \left[(\tau_l + \Delta\tau/2)^{n+1} - (\tau_l - \Delta\tau/2)^{n+1}\right] \quad . \tag{197}$$

For $n = 0$ and $n = 1$ one obtains the expected values

$$\alpha_0 = \sum_{l=1}^{2L+1} \langle P(\tau_l)\rangle \, \Delta\tau = 1 \quad \text{(normalization)} \ , \tag{198}$$

$$\alpha_1 = \mu = \sum_{l=1}^{2L+1} \tau_l \langle P(\tau_l)\rangle \, \Delta\tau = 0 \ , \tag{199}$$

whereas, for $n \geq 2$, one gets a decomposition into a "main term" and an "exact correction" in the form of a finite series in the bin width $\Delta\tau$:

$$\alpha_n = \sum_{l=1}^{2L+1} \tau_l^n \langle P(\tau_l)\rangle \, \Delta\tau + \frac{2}{n+1} \sum_{k=1}^{[n/2]} \left(\begin{array}{c} n+1 \\ 2k+1 \end{array} \right) \sum_{l=1}^{2L+1} \tau_l^{n-2k} \langle P(\tau_l)\rangle \left(\frac{\Delta\tau}{2}\right)^{2k+1} \ . \tag{200}$$

(Example for $n = 2$: $\sigma_0^2 := \alpha_2 = \sum_{l=1}^{2L+1} \tau_l^2 \langle P(\tau_l)\rangle \Delta\tau + (\Delta\tau)^2/12$.)

In many papers on MFs the integral in equation (79) and similar integrals are approximated by the "main term" and, thus, the results suffer from an *error*, which is exactly given (in the case of (79)) by the "correction" in (200), if it is not taken into account. For a discussion of the correction term in the case of the MFs v_1 and v_2, see [77]. This error can be made small, iff $\Delta\tau$ or $\Delta\nu$ is chosen small enough in principle, which is not the case, i.e., for $\Delta\tau = 13\mu K$. Looking at the "main term" (mentioned above) without correction,

$$\alpha'_n = \sum_{l=1}^{2L+1} \tau_l^n \langle P(\tau_l)\rangle \, \Delta\tau \ , \tag{201}$$

we obtain that $\sigma'_0 = \sqrt{\alpha'_2} = 59.6516\mu$K to be compared with $\sigma_{0\mathrm{px}} = 59.5335\mu$K (second equation in (186) and see also table 8).

8.3 Generating functions of the moments and cumulants

From the definition (96) of the discrepancy function $\Delta_P(\tau)$ and the Hermite expansion (97), one obtains with (82) for the generating function $M(x)$ of the moments α_n (with $\alpha_0 = 1$, $\alpha_1 = \mu = 0$, $\alpha_2 = \sigma_0^2$):

$$M(x) = \sum_{n=0}^{\infty} \frac{\alpha_n}{n!} x^n = \langle \mathrm{e}^{x\delta T}\rangle = \int_{-\infty}^{\infty} e^{x\tau} \left[P^{\mathrm{G}}(\tau) + \frac{1}{\sqrt{2\pi}\sigma_0} \Delta_P(\tau) \right] \mathrm{d}\tau =: M^{\mathrm{G}}(x) + M^{\Delta}(x), \tag{202}$$

with

$$M^{\mathrm{G}}(x) := \frac{1}{\sqrt{2\pi}\sigma_0} \int_{-\infty}^{\infty} \mathrm{e}^{x\tau - \tau^2/2\sigma_0^2} \, \mathrm{d}\tau \ = \ \mathrm{e}^{\sigma_0^2 x^2/2} \ , \tag{203}$$

and

$$\begin{aligned} M^{\Delta}(x) &:= \frac{1}{\sqrt{2\pi}\sigma_0} \sum_{n=3}^{\infty} \frac{a_P(n)}{n!} \int_{-\infty}^{\infty} \mathrm{e}^{x\tau - \tau^2/2\sigma_0^2} \, \mathrm{He}_n(\tau/\sigma_0) \, \mathrm{d}\tau \\ &= \frac{1}{\sqrt{2\pi}} \mathrm{e}^{\sigma_0^2 x^2/2} \sum_{n=3}^{\infty} \frac{a_P(n)}{n!} \int_{-\infty}^{\infty} \mathrm{e}^{-\nu^2/2} \mathrm{e}^{(\sigma_0 x)\nu - \frac{1}{2}(\sigma_0 x)^2} \mathrm{He}_n(\nu) \, \mathrm{d}\nu \ . \end{aligned} \tag{204}$$

Using the generating function of the Hermite polynomials [64],

$$\mathrm{e}^{z\nu-\frac{1}{2}z^2} = \sum_{m=0}^{\infty} \mathrm{He}_m(\nu)\frac{z^m}{m!} \ ,$$

equation (204) can be rewritten as

$$M^{\Delta}(x) = \frac{1}{\sqrt{2\pi}}\mathrm{e}^{(\sigma_0 x)^2/2}\sum_{n=3}^{\infty}\frac{a_P(n)}{n!}\sum_{m=0}^{\infty}\frac{(\sigma_0 x)^m}{m!}\int_{-\infty}^{\infty}\mathrm{e}^{-\nu^2/2}\,\mathrm{He}_m(\nu)\,\mathrm{He}_n(\nu)\,\mathrm{d}\nu \ ,$$

which leads with the orthogonality relation (103) to

$$M^{\Delta}(x) = M^{\mathrm{G}}(x)\sum_{n=3}^{\infty}\frac{a_P(n)}{n!}(\sigma_0 x)^n \ , \tag{205}$$

and, thus, with (202), (203), to the *factorization*

$$M(x) = M^{\mathrm{G}}(x)K(x) \ , \tag{206}$$

with

$$K(x) := 1 + \sum_{n=3}^{\infty}\frac{a_P(n)}{n!}\,(\sigma_0 x)^n \ . \tag{207}$$

The cumulant generating function, defined in (83), is then *additive*,

$$C(x) = \sum_{n=2}^{\infty}\varkappa_n\frac{x^n}{n!} = C^{\mathrm{G}}(x) + \Delta C(x) \ , \tag{208}$$

as given in equations (98) and (99) of the main text. It is convenient to write $\Delta C(x) := \ln K(x)$ in terms of the dimensionless variable $z := \sigma_0 x$,

$$\Delta C\left(\frac{z}{\sigma_0}\right) = \ln\left[1 + \sum_{n=3}^{\infty}\frac{a_P(n)}{n!}\,z^n\right] = \sum_{n=3}^{\infty}\frac{C_n}{n!}\,z^n \ , \tag{209}$$

where $C_n := \varkappa_n/\sigma_0^n$ are the *normalized* (dimensionless) *cumulants*. To obtain closed expressions for the NG–coefficients $a_P(n)$ in terms of the cumulants C_n, we recall the *generating function of the complete Bell polynomials* B_n [65] ($B_0 = 1$):

$$\exp\left[\sum_{n=1}^{\infty}\frac{x_n}{n!}\,z^n\right] = 1 + \sum_{n=1}^{\infty}\frac{B_n(x_1, x_2, \cdots, x_n)}{n!}\,z^n \ . \tag{210}$$

By expanding the exponential and comparing in (210) the terms of the same power in z, it is not difficult to obtain, e.g., the first four Bell polynomials: $B_1(x_1) = x_1$, $B_2(x_1, x_2) = x_1^2 + x_2$, $B_3(x_1, x_2, x_3) = x_1^3 + 3x_1x_2 + x_3$, $B_4(x_1, x_2, x_3, x_4) = x_1^4 + 6x_1^2x_2 + 4x_1x_3 + 3x_2^2 + x_4$. A comparison between (209) and (210) yields the closed expression ($x_1 = x_2 = 0, x_3 = \gamma_1, x_4 = \gamma_2, x_n = C_n$ for $n \geq 5$):

$$a_P(n) = B_n(0, 0, \gamma_1, \gamma_2, C_5, \cdots, C_n) \ , \quad n \geq 3 \ , \tag{211}$$

as given in the main text in equation (102). The explicit expressions for B_3 and B_4 give $a_P(3) = B_3(0, 0, \gamma_1) = \gamma_1$, $a_P(4) = B_4(0, 0, \gamma_1, \gamma_2) = \gamma_2$, in agreement with (101). In order to obtain the higher Bell polynomials, one can either use the *recurrence relations*,

$$B_{n+1}(x_1, x_2, \cdots, x_{n+1}) = \sum_{m=0}^{n}\binom{n}{m}\,B_{n-m}(x_1, x_2, \cdots, x_{n-m})\,x_{m+1} \ , \tag{212}$$

or the *combinatorial expression*

$$B_n(x_1, x_2, \cdots, x_n) = \sum_{\pi(n)} \frac{n!}{a_1! a_2!, \cdots, a_n!} \left(\frac{x_1}{1!}\right)^{a_1} \left(\frac{x_2}{2!}\right)^{a_2} \cdots \left(\frac{x_n}{n!}\right)^{a_n} \quad .(213)$$

Here, the sum is over all partitions $\pi(n)$ of n, i.e., over all positive integers a_m such that $\sum_{m=1}^{n} m\, a_m = n$. The multinomial coefficients

$$(n; a_1, a_2, \cdots, a_n)' := \frac{n!}{(1!)^{a_1} a_1! (2!)^{a_2} a_2! \cdots (n!)^{a_n} a_n!} \quad , \tag{214}$$

are given, for $n = 1, 2, \cdots, 10$, in table 24.2 in [63]. The Bell polynomials have the nice property that their coefficients are integers and, therefore, the NG coefficients $a_P(n)$ of the PDF discrepancy function are linear combinations of the normalized cumulants with integer coefficients, as seen in equation (101). Since the NG–coefficients $a_0(n)$ of the discrepancy function Δ_0 are related to the $a_P(n)$'s by $a_0(n) = \frac{a_P(n+1)}{n+1}, n \geq 2$, it follows that the coefficients of the $a_0(n)$'s are, in general, rational numbers (see equation (118)).

8.4 A closed expression for the NG–parameters $\mathbf{a_P(n)}$

Finally, we give an alternative closed formula for the expansion coefficients $a_P(n)$, which does not express them in terms of the cumulants C_n as in equation (211), but rather in terms of the *normalized moments* $\hat{\alpha}_n$ (see equation (80)),

$$\hat{\alpha}_n := \frac{\alpha_n}{\sigma_0^n} = \left\langle \left(\frac{\delta T}{\sigma_0}\right)^n \right\rangle \quad . \tag{215}$$

Replacing Δ_P in equation (104) by its definition (96), we obtain:

$$a_P(n) = \int_{-\infty}^{\infty} [P(\tau) - P^{\mathrm{G}}(\tau)]\, \mathrm{He}_n(\tau/\sigma_0)\, \mathrm{d}\tau \quad , \tag{216}$$

which gives, with the definition (79) and the orthogonality relation (103), $(n = 0, 1, 2, \ldots)$:

$$a_P(n) = \langle \mathrm{He}_n(\delta T/\sigma_0) \rangle - \delta_{n0} \quad . \tag{217}$$

From (217) follows immediately $a_P(0) = 0$, $a_P(1) = \hat{\alpha}_1 = \mu/\sigma_0 = 0$, and $a_P(2) = \alpha_2/\sigma_0^2 - \hat{\alpha}_0 = 0$, and for the required $a_P(n)$'s with $n \geq 3$ using the expansion [63],

$$\mathrm{He}_n(x) = n! \sum_{k=0}^{[n/2]} \frac{(-1)^k}{2^k k! (n-2k)!}\, x^{n-2k} \quad , \tag{218}$$

the closed expression

$$a_P(n) = n! \sum_{k=0}^{[n/2]} \frac{(-1)^k}{2^k k! (n-2k)!}\, \hat{\alpha}_{n-2k} \quad (n \geq 3) \quad . \tag{219}$$

By virtue of this formula, the integral in the original definition (104) is replaced by a finite sum and, thus, one obtains in combination with the formula (80) for the moments simple closed expressions for the Hermite expansion coefficients.

8.5 General Hermite and Edgeworth expansions

Here, we summarize some well–known mathematical facts (see, e.g., [66–71]), which are used in section 5.2.3 for expanding the various discrepancy functions $\Delta_P(x)$, $\Delta_0(x)$, etc., in terms of Hermite polynomials.

Let $f(x)$, $\mathbb{R} \to \mathbb{R}$, be square integrable with respect to a positive weight function $w(x)$, i.e., $f(x) \in \mathbb{H} := L^2(\mathbb{R}, w(x)\mathrm{d}x)$. For $f, g \in \mathbb{H}$, we define the *inner product*

$$(f, g) := \int_{-\infty}^{\infty} w(x) f(x) g(x) \mathrm{d}x \quad , \tag{220}$$

which satisfies the Schwarz inequality $|(f, g)| \leq ||f|| \cdot ||g||$, where $||f||$ denotes the *norm of* f, $||f|| := \sqrt{(f, f)}$. Let $\psi_0(x), \psi_1(x), \cdots \in \mathbb{H}$ be an *orthonormal system* satisfying the *orthogonality relation* $(m, n \in \mathbb{N}_0)$,

$$(\psi_m, \psi_n) = \delta_{mn} \quad , \tag{221}$$

and let $f \in \mathbb{H}$ be any function. Then, the numbers

$$b_n := (f, \psi_n) \quad (n \in \mathbb{N}_0) \tag{222}$$

are called the *expansion coefficients* ("Fourier coefficients") of f with respect to the ψ_n's. From the relation

$$0 \leq \int_{-\infty}^{\infty} w(x) \left(f(x) - \sum_{n=0}^{N} b_n \psi_n(x) \right)^2 \mathrm{d}x = ||f||^2 - \sum_{n=0}^{N} b_n^2 \quad , \tag{223}$$

one obtains $\sum_{n=0}^{N} b_n^2 \leq ||f||^2$, and since the right–hand–side of the last inequalities is independent of N, we obtain *Bessel's inequality*

$$\sum_{n=0}^{\infty} b_n^2 \leq ||f||^2 \quad . \tag{224}$$

This proves that the sum of the squares of the expansion coefficients b_n always converges.

Consider now, for a given function $f(x) \in \mathbb{H}$ the following linear combination:

$$F_N(x) := \sum_{n=0}^{N} \gamma_n \psi_n(x) \quad , \tag{225}$$

with constant coefficients γ_n and fixed N. Then, there arises the question under which conditions the approximation (225) can be considered as an *approximation "in the mean"* such that the *mean square error*

$$\mathcal{E}_N := ||f - F_N||^2 \tag{226}$$

is as small as possible. From the identity

$$\mathcal{E}_N = ||f||^2 + \sum_{n=0}^{N} (\gamma_n - b_n)^2 - \sum_{n=0}^{N} b_n^2 \tag{227}$$

it follows immediately that $\mathcal{E}_N$ takes on its least value for $\gamma_n = b_n$ $(n = 0, 1, \cdots, N)$. If the error $\mathcal{E}_N$ converges for every *piecewise continuous* function $f \in \mathbb{H}$ to zero as N goes to infinity, then the orthonormal system $\{\psi_n\}$ is said to be *complete*, i.e., it provides a

complete basis of $\mathbb{H}$, and Bessel's inequality (224) becomes an equality for every piecewise continuous function f,

$$\sum_{n=0}^{\infty} b_n^2 = ||f||^2 \ , \tag{228}$$

which is known as *completeness relation* (also called *Parseval's equation*).

It is important to note that the completeness of the system $\{\psi_n\}$, expressed by the equation

$$\lim_{N\to\infty} \int_{-\infty}^{\infty} w(x) \left(f(x) - \sum_{n=0}^{N} b_n \psi_n(x) \right)^2 \mathrm{d}x = 0 \ , \tag{229}$$

does not necessarily imply that $f(x)$ can be expanded in a series in the functions $\psi_n(x)$. The expansion

$$f(x) = \sum_{n=0}^{\infty} b_n \psi_n(x) \tag{230}$$

is, however, valid if the series in (230) converges *uniformly* and, thus, the limit in (229) can be carried out under the integral.

In this thesis, our main concern is not the *theoretical problem* to find an expansion (230) of $f(x)$, but rather the *practical problem* to obtain a representation (225) of $f(x)$ with $\gamma_n = b_n$ with a small number of terms, $N < 10$, say, which provides a fairly good approximation by minimizing the error (226). To this end, it is convenient to choose an orthogonal basis $\{\phi_n(x)\}$ in $\mathbb{H}$, where each $\phi_n(x)$ is a polynomial of degree n. For the Gaussian weight function $w^{\mathrm{G}}(x) := \exp(-x^2/2) = \sqrt{2\pi} P^{\mathrm{G}}(x)$, it turns out that the polynomials are uniquely determined (up to a multiplicative constant in each polynomial) by the *Hermite polynomials* $\mathrm{He}_n(x)$ (*c.f.* [63]),

$$\phi_n(x) := \mathrm{He}_n(x) \ , \tag{231}$$

which provide a complete orthogonal (not orthonormal) system in $\mathbb{H} = L^2(\mathbb{R}, \exp(-x^2/2)\,\mathrm{d}x)$, satisfying the orthogonality relation (see (103))

$$(\phi_m, \phi_n) := h_n\, \delta_{mn} \quad (m, n = 0, 1, 2, \cdots) \ , \tag{232}$$

with $h_n := \sqrt{2\pi} n!$. In order that the piecewise continuous function $f(x)$ satisfies $||f|| < \infty$ in $\mathbb{H}$, it must obey the asymptotic condition

$$f(x) = O\left(\frac{\mathrm{e}^{x^2/4}}{|x|^{1/2+\epsilon}} \right) \ , \quad \epsilon > 0 \ , \quad |x| \to \infty \ . \tag{233}$$

The approximation (225) becomes then the *polynomial approximation*

$$F_N(x) = \sum_{n=0}^{N} \frac{a(n)}{n!} \mathrm{He}_n(x) \ , \tag{234}$$

where the expansion coefficients $a(n) = \frac{1}{\sqrt{2\pi}}(f, \phi_n)$ are explicitly given by

$$a(n) = \frac{1}{\sqrt{2\pi}} \int_{-\infty}^{\infty} \mathrm{e}^{-x^2/2} f(x) \mathrm{He}_n(x)\, \mathrm{d}x \quad (n = 0, 1, 2, \cdots) \ . \tag{235}$$

The *completeness relation* (228) then reads:

$$\sum_{n=0}^{\infty} \frac{a^2(n)}{n!} = \frac{1}{\sqrt{2\pi}} \int_{-\infty}^{\infty} e^{-x^2/2} f^2(x)\, \mathrm{d}x \ , \tag{236}$$

which implies the asymptotic behaviour

$$\frac{|a(n)|}{n!} = O\left(\frac{1}{n^{1/2+\delta}\sqrt{n!}}\right) \quad , \quad \delta > 0 \quad , \quad n \to \infty \quad . \tag{237}$$

It is important to bear in mind that, even in the case when the series (230) is uniformly convergent, it by no means follows that the N^{th} partial sum (234) is the best selection of N terms for representing the function $f(x)$. Even though (234) gives the best fit in the sense of *least squares* by minimizing the error (226), it may be that some other measure of approximation is better suited for a given problem [67]. All the more this may be the case if the series (230) is divergent, in which case one may ask whether there exists an *asymptotic expansion* in the sense of Poincaré (*c.f.* [68]).

In the particular case of the Hermite expansion (234), many authors have worked on asymptotic expansions since quite a long time, mainly in the context of probability theory, statistics, number theory, and mathematical aspects of insurance risk (*c.f.* [67, 69–71], and references therein). The results relevant to us in this thesis are connected with the attempts to give a refinement of the classical *central limit theorem* in probability theory, and are often, historically incorrect, referred to as *Charlier* or *Gram–Charlier A–series* and *Edgeworth expansion*, although they had been introduced by Tchebychev already before [71]. Since Matsubara's expansion of the MFs in [57, 58] (see also [60] and [61]), based on the assumption of hierarchical ordering (HO), is formally closely related to the Edgeworth expansion, we shall summarize the main properties of the latter. It turns out that the Edgeworth expansion furnishes, in the case of the central limit theorem, a genuine asymptotic expansion with a well–defined remainder term.

Let $x_1, x_2, \cdots, x_n$ be independent and identically distributed random variables with a common continuous distribution function, such that every x_k has zero mean, standard deviation σ, and a third absolute moment $\beta_3 = \langle|\delta T|^3\rangle$. Consider the standardized sum variable

$$y_n := \frac{x_1 + x_2 + \cdots + x_n}{\sqrt{n}\sigma} \quad , \tag{238}$$

and let $P_n(x)$ be the PDF of y_n. The central limit theorem then asserts that, as $n \to \infty$, under appropriate conditions, $P_n(x)$ tends to the Gaussian (normal) PDF, $P^{\mathrm{G}}(x) = \frac{1}{\sqrt{2\pi}} \exp\left(-x^2/2\right)$. The Edgeworth expansion is a refinement of this by giving also the *rate of convergence* to the Gaussian limit. Define the *discrepancy function*

$$\delta_n(x) := \sqrt{2\pi}\left(P_n(x) - P^{\mathrm{G}}(x)\right) \quad . \tag{239}$$

Then, the *Edgeworth (E) expansion* [67, 69–71] is the following *asymptotic expansion*:

$$\delta_n^E(x) = \mathrm{e}^{-x^2/2}\left[\sum_{k=1}^{K} \frac{q_k(x)}{n^{k/2}} + \mathcal{O}\left(\frac{1}{n^{(K+1)/2}}\right)\right] \quad (n \to \infty) \quad , \tag{240}$$

where $q_k(x)$ is a polynomial of degree $3k$, which only depends on the normalized cumulants C_n ($n \geq 3; C_3 = \gamma_1, C_4 = \gamma_2$), and which can be expressed as a linear combination of the Hermite polynomials $\mathrm{He}_n(x)$. For $k = 1, \cdots, 4$ they are explicitly given by:

$$\begin{aligned}
q_1(x) &= \frac{\gamma_1}{3!}\mathrm{He}_3(x) \quad ; \\
q_2(x) &= \frac{\gamma_2}{4!}\mathrm{He}_4(x) + \frac{10\gamma_1^2}{6!}\mathrm{He}_6(x) \quad ; \\
q_3(x) &= \frac{C_5}{5!}\mathrm{He}_5(x) + \frac{35\gamma_1\gamma_2}{7!}\mathrm{He}_7(x) + \frac{280\gamma_1^3}{9!}\mathrm{He}_9(x) \quad ; \\
q_4(x) &= \frac{C_6}{6!}\mathrm{He}_6(x) + \frac{35\gamma_2^2 + 56\gamma_1 C_5}{8!}\mathrm{He}_8(x) + \frac{2100\gamma_1^2\gamma_2}{10!}\mathrm{He}_{10}(x) + \frac{15400\gamma_1^4}{12!}\mathrm{He}_{12}(x)
\end{aligned} \tag{241}$$

The expansion (240), $\delta_n^E(x)$, taking the first K terms into account, is an asymptotic expansion of $\delta_n(x)$ in powers of $1/\sqrt{n}$ with a remainder of the same order as the first term neglected (i.e., it is an "asymptotic expansion to K terms" as defined by Poincaré, *c.f.* [68]). Thus, it gives a correction to the central limit theorem, with a well–defined error of order $n^{-(K+1)/2}$, in the case where n is finite but large ($1 \ll n < \infty$). Due to the Hermite expansions (241) of the polynomials $q_k(x)$, the Edgeworth expansion (240) can be interpreted as a particular rearrangement of the following polynomial approximation:

$$\delta_{n,3K}(x) := \mathrm{e}^{-x^2/2}\left[\sum_{m=3}^{3K}\frac{a^E(m)}{m!}\mathrm{He}_m(x) + \mathcal{O}\left(\frac{1}{n^{(K+1)/2}}\right)\right] \quad (n\to\infty)\,, \tag{242}$$

where the ordering is not with respect to powers of $1/\sqrt{n}$, but rather according to the order of the Hermite polynomials. (The $n-$dependence of the coefficients $a^E(m)$ is not explicitly noted.) By a comparison of (242) with (240,241) one immediately reads off the first 12 expansion coefficients (here we choose $K = 4$):

$$\begin{aligned}
&a^E(3) = \frac{\gamma_1}{\sqrt{n}} \quad ; \quad a^E(4) = \frac{\gamma_2}{n} \quad ; \quad a^E(5) = \frac{C_5}{n^{3/2}} \quad ; \quad a^E(6) = \frac{10\gamma_1^2}{n} + \frac{C_6}{n^2} \quad ; \\
&a^E(7) = \frac{35\gamma_1\gamma_2}{n^{3/2}} \quad ; \quad a^E(8) = \frac{56\gamma_1 C_5 + 35\gamma_2^2}{n^2} \quad ; \quad a^E(9) = \frac{280\gamma_1^3}{n^{3/2}} \quad ; \\
&a^E(10) = \frac{2100\gamma_1^2\gamma_2}{n^2} \quad ; \quad a^E(11) = 0 \quad ; \quad a^E(12) = \frac{15400\gamma_1^4}{n^2} \quad .
\end{aligned} \tag{243}$$

(Note that the coefficients $a^E(m)$, $m \geq 7$, change if one goes to higher order in $1/\sqrt{n}$, e.g., for $K = 5$ they receive additional contributions of order $n^{-5/2}$ and n^{-3}.) If the coefficients (243) are compared with the coefficients $a_P(m)$ in equation (101), derived for a *general* Hermite expansion for the non–Gaussianities as in (97), it is not difficult to derive the law that governs the size, with respect to powers of $1/\sqrt{n}$, of the coefficients $a^E(m)$ associated with the asymptotics (240) of the central limit theorem. It simply says that every cumulant C_r in (101) has to be replaced by $C_r/n^{(r-2)/2}$ (for fixed $n \gg 1, r \geq 3$).

This is precisely the law, rigorously proven for the central limit theorem, which in some models of inflation is built in as *hierarchical ordering* (HO). But then, the role of the small dimensionless expansion parameter $1/\sqrt{n}$ is played by the standard deviation σ_0 which, for the CMB anisotropy, has a fixed value and cannot be made arbitrarily small as in the case of the central limit theorem. It is, thus, important to perform numerical checks, as done in this thesis. Furthermore, one should keep in mind that the Edgeworth expansion, applied to a given PDF, can suffer from the fact that the PDF is not correctly normalized and it can exhibit undesirable properties such as negative probabilities. In particular, the approximation deteriorates in the tails.

References

[1] E Di Valentino, A Melchiorri and J Silk 2015 Beyond six parameters: extending ΛCDM *Class. Quantum Grav.* **92** 121302 (*Preprint* arXiv:1507.06646)

[2] P Callin 2006 How to calculate the CMB spectrum (*Preprint* arXiv:astro-ph/0606683)

[3] Ade P A R et al. 2016 Planck 2015 results. XIII. Cosmological parameters *Astron. Astrophys.* **594** A13 (*Preprint* arXiv:1502.01589)

[4] C Cercignani 1988 The Boltzmann Equation and Its Applications *Springer-Verlag* ()

[5] Durrer R 2008 The Cosmic Microwave Background *Cambridge, Cambridge University Press* (https://doi.org/10.1017/cbo9780511817205)

[6] M Giovannini A Primer on the Physics of the Cosmic Microwave Background 2008 *World Scientific Publishing Co.* (https://doi.org/10.1142/6730)

[7] D H Lyth and A R Liddle 2009 The Primordial Density Perturbation (ISBN:9780521828499)

[8] Marozzi G, Fanizza G, Di Dio E and Durrer R 2016 CMB–lensing beyond the Born approximation *J. Cosmol. Astropart. Phys.* **JCAP09(2016)028** 1-26 (*Preprint* arXiv:1605.08761)